PKD
914j/KAP

SLE
Ref.

A STUDY OF HEAT AND MASS TRANSFER CHARACTERISTICS OF JET IMPINGEMENT

by

Shabir F Kapasi, BSc (Hons), AMIMechE

Thesis submitted in partial fulfilment of the requirements of The Nottingham Trent University for the Degree of Doctor of Philosophy

June 1994

A study of heat transfer and mass transfer characteristics of jet impingement

Shabir F Kapasi

Submitted for Degree of Doctor of Philosophy

Abstract

Experimental and numerical mass/heat transfer data for a semi-confined axisymmetric jet impingement for laminar and turbulent flow and a range of nozzle to plate spacings has been completed. The experimental mass transfer results have been correlated into useful design equations with quoted uncertainties, thus making a valuable contribution to extending existing data.

The experimental programme involved measurement of mass transfer coefficients due to a laminar 4.93 mm diameter jet impinging on a flat surface. The test mass transferring surface was a silicon rubber swollen with ethyl salicylate. Deformations caused by convection on the polymeric surface was measured using holographic interferometry. The tests were conducted for Reynolds numbers of $500 < Re < 2000$ with corresponding nozzle to plate spacings of $2 < z/d < 12$. The same geometric configuration was investigated for turbulent flow ranging $3000 < Re < 60000$ with the same nozzle to plate spacings.

PHOENICS was adapted to produce numerical predictions initially for the semi-confined axisymmetric laminar impinging jet for $100 < Re < 2000$ with nozzle to plate separation of $2 < z/d < 12$. Further predictions using the same technique for turbulent flow have been made using a standard κ - ϵ model for jet flow rate range of $3000 < Re < 60000$ with the same spacings.

The experimental laminar wall jet Sherwood numbers are shown to compare well with analytical and predicted results. The turbulent wall jet results also show good agreement with predicted values and available data. However errors in the mass transfer coefficients are exacerbated by the uncertainties in the physical properties of materials used in the experimental method. The confidence interval of the derived correlation equations are estimated to be ± 30 per cent. Although the effect of nozzle to plate separations on the wall jet mass transfer is shown to be insignificant within the investigated range, semi-confinement lowers the mass transfer rates by suppressing entrainment and turbulence. The wall jet heat transfer coefficients are independent of the inlet jet velocity profiles. The consequences of the flow patterns due to the semi-confinement boundary on the heat transfer coefficients are discussed.

An experimental jet impingement rig was designed for ease of replication and associated computer software for data analysis is described. Recent developments in computer hardware, processing speeds and optical equipment can be used for automatic analysis of this technique so that it can be used more easily.

Experimental measurements of the diffusion coefficients of the swelling agent into air have never before been obtained at the working temperature are estimated to have an uncertainty of ± 50 per cent. The refractive index and swelling properties of the silicon rubber agree well with published data and have been correlated into usable equations for convenience. The vapour pressure data of the swelling agent used has an uncertainty of 15 per cent which contributes to an uncertainty level in the mass transfer calculations to about 5 per cent.

Acknowledgement

I would like express my most sincere gratitude to Dr Krishnamoorthy Jambunathan, my Director of studies, who has been a continual source of help, encouragement and enthusiasm with my research work and many other activities.

I am specially grateful to Eur Ing Professor Bryan Button, my second supervisor, for employing me as research assistant on his SERC grant and of late giving his time to read the thesis.

I am greatly indebted to all my friends and colleagues past and present. My most sincere thanks goes to Dr Geoff Tansley a dear friend, and colleague, whose genuine encouragement with continual confidence building has been my inspiration to undertake a higher degree. Many friends and colleagues who have made studying a pleasure and enriched the working environment are listed alphabetically. They are Mr Brian Dobbins, Dr R J Edwards, Associate Prof Shiping He, Dr Mehran Pasdari, Mr John Pritchard, Dr C L Saluja, Dr F Shemirani and Mr S Zangeneh and others too numerous to mention. I would like to thank them all sincerely for being whom they are and appreciate having had the opportunity of working with them.

To my most recent friends and colleagues Stuart Hartle and Shirley Ashforth-Frost, whom I like to thank for many enjoyable hours of fruitful discussions about work among many other things.

I am grateful to the following technician staff in Mechanical engineering for being always helpful and for manufacturing many specialist items when required. Thanks goes to Mr Ralph James, Mr Tony Maides and his staff and Mr Alan Crisp principal technician and his numerous crew who have helped in setting up and maintaining the holographic laboratory.

The excellent services provided by the library staff, in particular Mr Jim Corlett the Engineering Librarian is acknowledged. I also appreciate the assistance of Mrs Doreen Corlett whose endless searches of literature have made my task a little easier.

I dedicate this thesis to my parent's Fidahusen and Rubab, my bother Talib and his wife Duriaya and my sister Sakina without whose unending support and enduring patience, I could not have completed my studies.

I am grateful to the Department of Mechanical Engineering for providing the main facilities, equipment and labour used during the research. Acknowledgement is given to the SERC for providing initial financing for my project.

List of contents

List of figures

List of tables

Nomenclature

Symbol	Description
b,B	Width of slot jet
C_o	Optical arrangement constant
C_1,C_2	Constants
d,D	Diameter of nozzle
D_f	Diffusion coefficient of the swelling agent
g'	Function of Schmidt number
H	Non-dimensional nozzle to plate distance
h_m	Local mass transfer coefficient
i_1,i_2	Incidence and reflection angles of the laser beam
k	Local mass transfer coefficient
KE	Turbulent kinetic energy
L/D	Non-dimensional length of nozzles
M_s	Mass swelling percentage of polymer
M_w	Molecular weight of the swelling agent
n	Fringe number
N	Mass transfer flux
Nu	Nusselt number $(h\ d\ /\ k)$
Nu_o	Stagnation point Nusselt number
Nu_{av}	Average Nusselt number
Nu_d	Average Nusselt number on disk
$P1$	Predicted pressure
P_s	Vapour pressure of swelling agent

p	Atmospheric pressure
Pr	Prandtl number
R	Radius of nozzle
r	Radial distance from stagnation point
$r/d,R/d$	Non-dimensional radial distance from stagnation point
Re,Re_j	Reynold number of the jet ($U\,d\,\mu\,/\,\rho$)
Re_r	Reynold number of the rotating disk
R_f	Refractive index of swollen polymer
Rn	Random number
S	Swirl number
Sc	Schmidt number
Sh	Sherwood number ($k\,d/D_f$)
Sh_o	Sherwood number at stagnation point
t	Duration time of the mass transfer experiment
T	Temperature of the air
T_{jet}	Temperature at the jet exit
U	Error estimate of the physical quantity
U_{suct}	Suction velocity at the impingement plate
u_{max}	Maximum velocity in the wall jet
$V1$	Predicted radial velocity (y - direction)
V_{jet}	Radial jet velocity at the nozzle exit
V_{ps}	Vapour pressure of the swelling agent at the surface
V_{pj}	Vapour pressure of the swelling agent at the jet exit
V_{po}	Vapour pressure of the swelling agent at the jet exit
$W1$	Predicted axial velocity (z direction)
W_{jet}	Axial velocity at the nozzle exit

X_{max}	Maximum confinement plate distance
x/b,X/B	Non-dimensional distance from stagnation point (2 - D)
X/D	Non-dimensional distance from stagnation point
z/b,z/B	Non-dimensional nozzle to plate distance (2 - D)
z/d	Non-dimensional nozzle to plate distance
zx	Axial distance from the jet exit

Greek

Symbol	**Description**
α	Refracted angle of incidence
β	Relected angle of beam
Δ	Optical path length difference
δ	Shrinkage of the swollen polymer
δ_i	Initial polymer thickness
ϵ	Turbulent kinetic energy dissipation rate
η	Refractive index of the swollen polymer
κ	Turbulent kinetic energy
λ	Wavelength of He-Ne laser beam
μ	Absolute viscocity of the air
ν	Kinematic viscocity of the air
ρ	Density of the air
σ	Boundary layer thickness
τ	Shear stress at the wall
Φ	Oblique angle of the jet
Φ_i	Independent variable to be solved
ψ	Function of Re and r/d

List of publications

- Jambunathan, K., Kapasi, S., Button, B.L. and Bland, J.A., 1989. Numerical study of flow field for confined laminar jet impingement. Third International PHOENICS User Conference, Dubrovnik, Yugoslavia, 28 August - 1 September, 1989. PHOENICS Journal, 3 (2), 156-169.

- Dobbins, B.N., He, S.P., Jambunathan, K., Kapasi, S., Wang, L.S. and Button, B.L., 1991. Measurement of temperature field in confined jet impingement using phase-stepping video holography. Proceedings of SPIE International Symposium on Optical Applied Science and Engineering, San Diego, California, USA, 21-26 July, Volume 1554B Part Two, 586-592.

- Button, B.L., Dobbins, B.N., Jambunathan, K. Kapasi, S., He, S.P., and Wang, L.S., 1991. The measurement of temperature distribution in semi-confined jet impingement using ESPI and Holography. 112th ASME WAM, Atlanta, Georgia, USA, 1-6 December, FED-Vol. 128, 41-46.

- Wang, L.S., Kapasi, S., Jambunathan, K., and Dobbins, B.N., 1994. Application of phase stepping speckle interferometry and swollen polymer technique to mass transfer measurements. Optical Methods and Data Processing in Heat and Fluid Flow, 14-15 April, City University, London, 207-211.

CHAPTER 1

INTRODUCTION

1.1 Background

Impinging jets of countless configurations are used in industrial equipment because of their wide ranging heat and mass transfer characteristics surveyed by Hrycak (1980), Wilcock and Button (1978), Button and Jambunathan (1989). Many varied applications of impinging jets are cooling of turbine blades, electronic components, heat treatment of glass or metal sheets, drying of textiles and paper.

There are important advantages in investigating the jet impingement geometry:

- it has a simple geometry arrangement and can be easily duplicated
- the basic flow regimes exist within its bounds, namely, free stream, boundary layer, stagnation and mixing zones

Some of these industrial applications already mentioned would gain some benefit from studies of the heat or mass transfer characteristics in single impingement jets, which may ultimately lead to savings in energy and running costs of the equipment. Improved transport of heat or mass can also mean reductions in size of the equipment which in turn mean reductions in manufacturing cost and consequently overall costs. The ultimate benefit is to the world eco-system and our future generations because economical use of fuels now means less pollution into the environment.

Most industrial applications involving jet impingement flow are unconfined and

turbulent. Consequently most of the published research is about unconfined jet impingement flow and little attention has been given to confined jet impingement in past research. In nearly all real impingement equipment some form of confinement exists, although it is limited in extent and with no doubt this additional boundary must affect the flow. A major disadvantage with unconfined jet impingement is the unknown inflow condition associated with that boundary region and therefore even similar experimental results would lead to greater uncertainties.

The jet impingement configuration has been proposed as an important bench-mark test case for studying new and modified turbulent models in numerical codes. Unfortunately previous cases were modelled with an unknown unconfined condition next to the jet, which gave significant uncertainties to the comparisons made. This uncertainty is eliminated when a semi-confinement boundary is imposed with either some two-dimensional or axisymmetric impinging jet models.

Numerous experimental correlations are available for unconfined jet impingement heat transfer but only handfuls are ever quoted with any estimates of uncertainty in the data or correlations. Designers who use jet impingement heat and mass correlations for design of equipment, need to use correlations with error estimates for their design. Unfortunately this is not possible with the current state of the information. New heat/mass transfer correlations with uncertainty limits need to be obtained, which will help minimise uncertainty in future designs of jet impingement equipment.

The work described in the thesis is part of a wider study into the comparisons of

the full-field heat and mass transfer techniques. The following heat transfer measurements were investigated using;

- liquid crystals
- phase change paints
- infra-red thermography

and mass transfer measurements using

- swollen polymer technique with holography is reported in this thesis
- swollen polymer technique with electronic speckle pattern interferometry

and flow measurements and predictions using

- a finite volume method is reported in this thesis
- laser doppler anemometry

1.2 Aims

To investigate mass transfer experimentally and heat transfer numerically on a flat surface due to a single semi-confined laminar impinging jet and gain a better understanding of the transport process.

To widen the experimental and numerical mass/heat transfer investigation to include a semi-confined turbulent impinging jet flow and gain a better understanding of the transport process.

To obtain correlation equations with uncertainties from the experimental data.

1.3 Objectives

To achieve the described aims the following objectives have been completed.

To complete a comprehensive review of available jet impingement literature in English and to contribute to the development of a computer database.

To determine physical and geometrical quantities for the semi-confined jet impingement experiments.

To install, commission and validate an experimental mass transfer measurement technique and an appropriate profilometric technique.

To design, develop and commission a jet impingement rig with appropriate boundary conditions based on the literature survey.

To plan an experimental test programme based on statistical approach that will help obtain the transfer coefficients with their measurement errors and find overall errors due to a semi-confined impinging jet flow.

To verify independently any physical property quantities needed for the analysis of experimental data.

To identify from the literature survey a computational approach for producing the numerical predictions of the impingement flow.

To optimise grid structure for the semi-confined jet impingement models with a grid independent study for the laminar flow conditions.

To undertake a numerical flow and geometrical parametric study of heat transfer in a semi-confined laminar jet impinging geometry.

To carry out a numerical flow and geometrical parametric study of heat transfer in a semi-confined turbulent jet impinging geometry using a standard turbulence model.

To compare the laminar and turbulent experimental mass transfer results with available experimental or analytical data.

To correlate the experimental data into appropriate correlation equations with estimated uncertainties using the Monte-Carlo error analysis methodology.

1.4 Chapter contents

Chapter one describes introductory background to the current research programme. The aims and objectives of the work are listed and the scope of the research is given. The principle quantities to be investigated in the experimental and numerical programmes are also identified.

Chapter two contains a chronological appraisal of the literature listed in the several sub-headings. The sub-headings are heat and mass transfer for laminar and

turbulent flow, both for experimental and numerical techniques. An additional sub-heading is included in this chapter which summarises the conclusion from the literature review.

Chapter three reports on the experimental apparatus and techniques used for the current research. These are :

- the swollen polymer mass transfer method
- the jet impingement rig
- the optical arrangement for obtaining the profilometric measurements
- the statistical approach used for establishing the error within the obtained results
- the properties used in the calculations of mass transfer.

Chapter four gives a brief description of the numerical method and the structure of PHOENICS. The boundary conditions activated in the numerical model are explained. The PHOENICS command language PIL is described and the syntax required is explained. A grid dependency study with its findings are discussed. Description of the user interface program for calculating the heat transfer coefficient from the predictions is included.

Chapter five contains the validation of the wall jet mass transfer technique using an unconfined laminar jet impingement configuration. The semi-confined laminar impingement mass transfer data obtained from the experimental study are presented and discussed. Correlations of the experimental data are tabulated with estimates of their uncertainty limits quantified. Results are presented from a numerical study of the heat transfer due to a laminar semi-confined impinging jet.

The effects of inlet jet velocity profile on the impingement heat transfer together with the effects of *z/d* spacings are discussed. Implications of the flow behaviour within the semi-confinement region with implications to the heat transfer are discussed.

Chapter six contains the experimental wall jet mass transfer results for a turbulent semi-confined jet impingement. Correlations of the experimental data are tabulated with estimates of their uncertainty limits. Results of the numerical studies of turbulent heat transfer due to a semi-confined impinging jet are presented. The effects of inlet jet velocity profile and turbulence energy levels and the effect of *z/d* spacing on heat transfer due to mixing of the jet are discussed.

Chapter seven contains major conclusions drawn from the achievements of the initial objectives set out.

Chapter eight contains the suggested further work and recommendations for future developments from the experiences of the current research project.

Appendix A contains the results of the experimental work done using Stefan's technique for measuring the diffusion for ethyl salicylate and n-tetradecane.

Appendix B contains the description of the experimental method used to measure refractive index and mass swelling properties of the swollen polymer and swelling agent used in the current experimental work.

CHAPTER 2

REVIEW OF LITERATURE

2.1 Introduction

The following review reports on the most relevant publications to the current research work. A brief background description of the impingement flow configuration and the terminology used is presented. The survey is done under main subject headings with individual reference papers listed chronologically to assist the reader to assimilate the erratic nature in research within this topic. An added bonus to the structured review made the comprehension of the individual papers easier.

Investigations of flow field, heat and mass transfer due to single and multiple impinging jets within unconfined regimes are abundant in open literature. The difficulty with this vast amount of data is in identifying data for particular flow and geometric condition which is being used in a particular application. This predicament is due to an infinite number of variants that exist for the test conditions and hence only islands of information are available for interrogation purposes. The current literature review could not possibly cover all the aspects that are possible for the jet impingement geometry, therefore no attempt is made to achieve this task. Instead the current review is to cover detailed information on the most relevant papers for a single unconfined and semi-confined impinging jet Figure 3.1 with either heat or mass transfer occurring on the impingement surface. The review includes experimentally obtained data and numerically predicted results

for the single jet impingement flow.

This research is based entirely on a semi-confined submerged impinging jet flow, where the jet fluid and the surrounding fluid are composed of the same constituent medium i.e. air to air. The effect of entrainment due to a submerged jet flow is substantially greater when compared to a liquid jet flowing into a gas surrounding. This flow type is known as a "free jet", where the entrainment is considered to be negligible and a free surface is formed at the boundaries of the flow. Mainstream research is concentrated into the investigation of turbulent submerged jets, because the results are immediately relevant to industrial applications.

Many investigations have been conducted for single axisymmetric jets for both laminar and turbulent flows, section 1.3 to 1.8. Both heat and mass transfer processes were investigated for various nozzle sizes, *Re* and *z/d* spacings. For comprehensive reviews of this subject the reader is directed to reviews by Gaunter et al (1970), Arganbright and Resch (1971), Mujumdar and Douglas (1972), Livingood and Hrycak (1973), Becko (1976), Hrycak (1980), Downs and James (1987), and comprehensive literature surveys by Wilcock and Button (1976), Button and Jambunathan (1989) and Jambunathan et al (1992). Only one review of the numerical predictions in the impingement flow has been undertaken by Polat et al (1989).

An infinite number of variants are possible for flows involving impinging jets, the commonly studied configurations are for multiple jet flows with assorted spacings between jets and *z/d* spacings with a view to identifying the effects due to the

individual quantities. The other main impingement flow being studied is with cross flow and the aim being to single out the effect on heat or mass transfer due to single independent quantities, which are *z/d* spacing, jet flow rate and the imposed cross flow. The ultimate aim of the research investigations are to optimise the transport efficiency of the mass and energy from the working surface without increasing the input energy requirements. The input energy normally is the pumping power of the working fluid, if the pressure drop generated in the nozzle is increased then more energy is required as input and therefore the overall efficiency is not achieved. The current work does not address this overall energy efficiency of the impingement flow but only considers the local transport process at the impingement surface.

2.2 Description of the flow domains within a single laminar impinging jet

The characteristics of a single impinging jet can be viewed as being structured of three flow regions, whether the jet is laminar or turbulent,

- free jet region
- the stagnation flow region
- the wall jet region

The fundamental importance between laminar and turbulent flow is defined by Hrycak et al (1970), where $Re < 1000$ is fully laminar and $Re > 3000$ is fully turbulent. The flow field of a single jet which is unconfined can be represented schematically by Figure 3.1. Practically all the literature deals with unconfined impingement jet flows, therefore no boundary restrictions exist to the entrained flow into the regime from beyond the region under consideration. The variations

this undefined boundary creates are numerous and therefore comparisons between results cannot be made without some uncertainty due to effect of this uncontrolled boundary.

2.2.1 The free jet flow

The free jet is considered to be that part of the jet flow which has not been affected by the impingement surface. The jet as it emerges from the nozzle is immediately affected by the surrounding fluid and a mixing region is formed around the jet, this zone increases continuously as the jet progresses forward until it is wide enough to have reached the jet centre line. The region upstream of the point where the jet centre line velocity is reduced by this mixing zone is called the "potential core". For an axisymmetric laminar jet the decay velocity has been obtained by Schlichting (1968) using boundary layer theory.

$$\frac{W1}{W_{jet}} = c \left(\frac{d}{z}\right) \qquad (2.1)$$

The normal definition given to core length is where the centre line velocity decreases to 98 per cent of the initial velocity or its pressure head is 95 per cent of the initial value. The potential core lengths have been obtained for turbulent axisymmetric submerged jets by various researchers and found to vary from about 4.7 to 7.7 *d* summarised by Gaunter et al (1970). The increased turbulence enhances the mixing and hence the core length is drastically reduced. For laminar axisymmetric jets according to Hrycak et al (1970) the core length is between 15 d to a maximum of 20 d depending on the jet Reynolds number.

2.2.2 The stagnation flow region

The axial centre line velocity is decelerated as it approaches the impingement plate until it reaches a point at or near the plate where the velocity attains a value of zero and the pressure is a local maximum. The stagnation region is defined from where the axial velocity begins to decrease below 98 per cent of the jet centre line velocity. For axisymmetric turbulent jets this is found by Giralt et al (1977) to be about 1.2 d above the impingement plate.

2.2.3 The wall jet flow region

The wall jet occurs as a consequence of the jet being deflected when passing through the stagnation region. The wall jet radial velocity is initially linearly accelerated in the stagnation region, where it attains a maximum velocity downstream of the stagnation point and begins eventually to decelerate. For laminar axisymmetric jets the maximum velocity occurs just beyond *r/d* of one from the stagnation point. For a fully developed wall jet, the radial velocities at the impingement surface and the outer jet surface are both zero. This necessitates a maximum radial velocity within these two bounding points. The structure of the wall jet is composed of two flow types, firstly the flow nearest the impingement surface is regarded as being similar to a boundary layer flow, the other half is considered as being a mixing zone region not dissimilar to the submerged jet flow. The most common independent quantities that are used to analyse wall jets are the decay of maximum radial velocities and boundary layer thickness of the wall jet. Glauert has reported a complete theoretical analysis of a laminar axisymmetric wall

jet that is summarised in equations (2.2) and (2.3)

$$\frac{u_{max}}{W_{jet}} = C_1\left(\frac{d}{r}\right)^{1.1} \quad \textbf{(2.2)}$$

$$\frac{\sigma}{d} = C_2\left(\frac{r}{d}\right)^{1.25} \quad \textbf{(2.3)}$$

where C_1 and C_2 are constants and σ is the wall jet boundary layer thickness.

2.3 Mass transfer with laminar jets

A laminar unconfined radial wall jet on a flat plate is analysed theoretically and experimentally by Scholtz and Trass (1963). An exact solution of the mass transport equation as well as an approximate solution of the integral mass balance equation with assumed velocity and concentration profiles is obtained. The theoretical mass transfer function is reduced into the following

$$Sh = 0.159\ Sc^{1/3}\ Re^{3/4}\ (r/d)^{-1.25} \quad \textbf{(2.2.1)}$$

Their own experimental data agreed closely with the above correlation. The above function is quoted as a practical expression for a gaseous system for *Sc* greater than one. For the present system, the *Sc* = 2.76 and the expected error from the exact solution is about five per cent. Their mass transfer experiments for *Re* range of 1000 - 3000 are conducted with a water jet exposed to a soluble mass transfer coating of acetanilide and benzoic acid and the resulting surface contour is measured by profilometry, a stylus coupled to a displacement transducer. The data

for *Re* below 1000 has a systematic deviation from equation (2.2.1). This is shown via dye streak visualisation that separation is occurring at around *r/d* of 5.66 for *Re* of 300. This phenomena reduces the experimental mass transfer results when compared to the theory, but for increasing $Re > 700$ the significance of the deviation is very small.

Scholtz and Trass (1970) is an analytical work which is often cited, they derived a theoretical solution for impingement flow with a non-uniform inlet jet velocity profile. For $z/d < 0.5$, $r/d \leq 0.7$ and *Sc* in the range $1 < Sc < 10$ the general form of the expression is

$$Sh = a\, Re^{0.5}\, Sc^{0.361} + b\, Re^{0.5}\, Sc^{0.386} \left(\frac{r}{d}\right)^2 + c\, Re^{0.5} Sc^{0.408} \left(\frac{r}{d}\right)^4 + \ldots \qquad (2.2.2)$$

The coefficients a, b and c are tabulated in the paper for $0.05 < z/d < 0.5$. They examined the mass transfer around the stagnation point for $r/d < 0.1$ between $0.05 \leq z/d \leq 0.5$ and found no significant dependence on radial position. Hence equation (2.2.2) can be used with only the first term being included to deduce mass transfer. For radial positions between $0.1 < r/d \leq 0.5$, it is found that the mass transfer distribution increased monotonically with separation of $z/d < 0.25$, but for larger separation $z/d > 0.25$ the mass transfer decreases with *r/d*. The flow issuing is considered to be a wall jet when the separation is under *z/d* of 0.25 a more detailed discussion is found in Scholtz and Trass (1970).

Experimental results of the flow field and surface mass transfer using an air/naphthalene sublimation technique are compared to their theoretical results. They concluded that the mass transfer is independent of *z/d* separations between 0.25 to 6. They proposed an empirical correlation in the transition region .

$$Sh = 0.757\ Sc^{-0.0361}\ Re^{0.5} \left(\frac{r}{d}\right)^{-0.86} \qquad \textbf{(2.2.3)}$$

From the theoretical transfer rate calculations for a uniform jet profile the transfer rate at the stagnation point is found to be half the value when compared to results for a nonuniform jet profile. This is assigned to the higher acceleration present within the developed velocity profile.

Kapur and Macleod (1972) are the first to publish an article to describe the use of the swollen polymer method for the measurements of convective mass transfer combined with holographic interferometry. Results compared with those of Scholtz and Trass's correlation showed good agreement. A correlation is obtained for radial locations $r/d > 2.9$ and for the range $1000 < Re < 2000$.

General principles of using holographic interferometry with three different optical setups are described in Kapur and Macleod (1974) and how this is used as a profilometric method for mass transfer experiments. They presented detailed discussions on optimum test and optical parameters and recommended procedures for photographic processing of the holographic plates used to record the interferogram. They tested a swollen polymer mass transferring surface as the target surface, which had some major advantages over the traditional mass

transferring surfaces. They investigated unconfined jet impingement and wall jet arrangements to validate this technique and had compared their results to those of Scholtz and Trass (1970). Their main conclusion was the consistency and reproducibility of the holographic technique to the order of one per cent and the speed with which the profilometric information is extracted. The nature of the holographic method revealed the entire deformation field in a single image and hence provided comprehension of the data immediately. The main problem they identified is the assignment of the zeroth fringe for the fringe pattern, especially when it did not appear in the field of study. The solutions to this very difficult problem are being considered by the authors. To date no conclusive method has been established for assigning the zeroth fringe, but various approaches have been proposed for particular situations.

Masliyah and Nguyen (1976) investigated a square impingement jet using a swollen polymer/holographic interferometry technique for various flow rates. Unfortunately, they only conducted qualitative interpretation of the mass transfer distributions which they found to be completely unexpected and no definite conclusions could be drawn because of the limited amount of data.

Kapur and Macleod (1975) obtained mass transfer coefficients for laminar submerged water jet impingement for $1000 < Re < 3000$. They found for the low *Re* investigated the agreement with the theory from Scholtz and Trass in the wall jet is satisfactory, but for high *Re* the discrepancy increased to seventeen per cent. The cause for the deviation is explained as the violation of the constant rate period which from the prediction from Macleod and Todd (1973) is found to be three

times greater than they identified experimentally. The ratio of the experimental time to constant rate period of 0.55 gave an error in the mass transfer coefficients of three per cent, but when the ratio increased to 0.72 the deviation increased to seventeen per cent. They showed the Scholtz and Trass wall jet theory is valid for a wide range of *Sc*. Their *Sc* for water is approximately 1000 and good agreement is shown with theory and Scholtz and Trass's (1970) experimental results with air, where the *Sc* is approximately equal to unity.

Sparrow and Wong (1975) used naphthalene sublimation to measure transfer coefficient for a laminar slot air jet impingement configuration for $150 < Re < 950$ with slot to plate separation of $2 < z/b < 20$. A detailed account of the experimental procedure and analysis of the results is included in the paper. From their results they showed correlations with $Re^{0.6}$ dependence within the stagnation region but a radial dependence of $(x/b)^{-0.51}$, which are valid for $z/b = 5$. The radial profile of the transfer coefficients they obtained showed humps which they have smoothed over with monotonic curves. However, for large spacings insufficient data is available for an accurate correlation to be made.

Kapur and Macleod (1976) reversed their developed technique for mass transfer measurement using holographic interferometry and the swollen polymer method to measure vapour pressures for various esters using a laminar normal impingement air jet with its established correlation. They obtained vapour pressures for ethyl salicylate, methyl salicylate and isobutyl benzoate from which two of the esters agreed closely to data that had been published before, the other ester is found to be largely dependent on its age and therefore had been found to be lower in value

during measurement. The results had been correlated in standard form for vapour pressures and are valid for limited temperature ranges. The equation (2.2.4) for the ethyl salicylate is said to be within three per cent of the extrapolated data from published work.

$$\ln p_s \ (mmHg) = -\frac{6790.7}{T} + 20.318 \qquad \textbf{(2.2.4)}$$

Masliyah and Nguyen (1977) quantified their 1976 investigation of local mass transfer rates for a laminar impinging square jet on a flat surface using the swollen polymer technique and holographic interferometry. The investigated *Re* were 710, 980, 1325, 1810 and they postulated correlations for the wall jet to lie in between the two limiting theoretical wall jet cases, namely a circular and a slot jet. The distribution of the transfer coefficient was found to be highly dependant on the angular direction about the centre of the jet, and they presented correlation for 0 and 45° for both wall jet and stagnation regions.

Masilyah and Nguyen (1977) again utilised the swollen polymer/holographic technique to investigate mass transfer due to a rectangular impinging jet tube with $770 < Re < 1800$. They reduced the experimental results by regression and derived several correlations for *Sh* for the following angular positions of 0°, 45°and 90° relative to the horizontal with radial bounds of the stagnation region and others for the wall jet region. These are the first correlations for this particular nozzle configuration. It is concluded from their work that local heat transfer due to non-circular jets are significantly higher than comparative circular jets with similar

conditions. The overall rates however are similar in magnitude for the non-circular and circular nozzles assuming the flow area and volumetric flow rates are same the for both nozzles types.

Harper and Macleod (1978) communicated a novel setup for measuring real-time mass transfer within complex flow regimes using a glass prism coated with the swollen polymer. Total internal reflection of the illuminating beams occurs at polymer/fluid interface and using either a single or double exposure holographic technique a record of the contours could be obtained. The advantage of using this real-time technique makes possible the counting of the fringe order numbers and hence the absolute deformation which is not readily possible with the double exposure holography technique.

Masliyah and Nguyen (1979) looked at two dimensional laminar impinging jets using the double exposure holographic technique. The regression equation (2.2.5)

$$Sh = 0.7 \left(\frac{x}{b}\right)^{-0.73} Re^{0.55} \qquad \textbf{(2.2.5)}$$

is derived for the *Re* between $180 \leq Re \leq 600$ and $1 \leq x/b \leq 30$ with the *Sc* of 2.85. They noted that the edge surface finish on the nozzle caused fluctuations in the fringe pattern which is eliminated by polishing the edge. The correlation agreed with experimental data of Sparrow and Wong (1975). The exponents of their research are compared with the theoretical analysis of Schwarz and Caswell (1961), the *x/b* exponents are compatible but the *Re* exponents disagreed.

Four objectives were undertaken by Law (1982), firstly he experimentally investigated mass transfer in a laminar two-dimensional confined jet impingement geometry with varying conditions, using the swollen polymer and holographic techniques. The conditions studied are $100 < Re < 400$, $2 < z/b < 4$. He evaluated the effects of confinement on the mass transfer with direct comparisons with unconfined experimental results. Then he numerically modelled the experimental conditions to verify the computations which could be subsequently used for further case studies. The significance of inlet velocity profile on the mass transfer rates is investigated which he showed to have a dramatic effect on the stagnation point transfer rate. A parabolic inlet velocity jet produced twice the transfer rate when compared to a flat inlet velocity jet. The predictions compare very favourably with their experimental results for the two-dimensional confined jet impingement flow.

Law and Masliyah (1984) summarised Law's (1982) work on local mass transfer in confined laminar air jet impingement using double exposure and real time holography and also simulated the geometry numerically. Typical experimental duration times of air jet subjected to the mass transfer surface are from 120 to 480 seconds. A regression equation for $x/b = 2$ and 4 is given by (2.2.6)

$$Sh = 0.34\ Re^{0.66} \left(\frac{x}{b}\right)^{-0.78} \qquad \textbf{(2.2.6)}$$

The numerical simulations conducted utilised a geometry grid network of 55 x 25. The two dimensional momentum and transport equation are reduced to vorticity - stream function form with specific boundary conditions. The model with the

upstream weighted differencing scheme is found to predict mass transfer successfully for the same flow regime. The *Sh* are found to exhibit local minima and maxima at a distance from the stagnation point which is shown to be due to separation and re-attachment flows along the wall.

2.4 Mass transfer with turbulent jets

Rao and Trass (1964) studied mass transfer due to a turbulent wall jet using a trans-cinnamic acid surface and water as the working fluid with $Sc = 900$, from which the following correlation (2.3.1) is obtained

$$Sh = 1.3\ Re^{0.94} \left(\frac{r}{d}\right)^{-1.27} \qquad \textbf{(2.3.1)}$$

for $25000 < Re$ 125000 and $r/d > 4.5$. The coefficients for the impingement zone showed very complex behaviour and therefore have been correlated into two equations as averages over this domain for $z/d > 6.5$ and $z/d < 6.5$. Erosion is found to enhance the mass transfer at the impingement region $r/d < 4.5$, hence the analogy between heat and mass transfer is of limited use within this area. They also observed that the optimal range for the nozzle $z/d = 6$ to 7 from the impingement plate.

Dawson and Trass (1966) analysed theoretically the transfer coefficients by analogy for a radial wall jet using the momentum integral technique. A plot is given from which all the theoretically derived indices of *Re* and *r/d*, for $1 \leq Sc \leq 100$ can be obtained. The *Sh* correlation (2.3.2) for $Sc = 1$

$$Sh = 0.0509\ Re^{0.832} \left(\frac{d}{r}\right) \qquad \textbf{(2.3.2)}$$

For $Sc = 2.76$ equation (2.3.3) is formulated and the exponent and constant are found from the plot given in the reference.

$$Sh = 0.044\ Re^{0.88} \left(\frac{d}{r}\right) \qquad \textbf{(2.3.3)}$$

The experimental work backed up the theoretical work for Re of $10000 \leq Re \leq 60000$ with two mass transfer methods; air impinging on a naphthalene surface and water impinging on a cinnamic acid surface. Surface roughness for high Sc is suspected to enhance the transfer rates when the results are compared with the theoretical predictions.

Ward et al (1972) used Naphthalene sublimation with the Chilton-Colburn analogy to show the feasibility for determining average heat transfer coefficients due to confined jet impingement on the walls of furnaces. The analogy given in (2.3.4)

$$Nu = Sh \left(\frac{Sc}{Pr}\right)^{\frac{2}{3}} \qquad \textbf{(2.3.4)}$$

was used for converting mass transfer into heat transfer data with nozzle to plate spacing varied from $z/d = 2$ to 12. They concluded that the recirculatory flow from the impingement plate to the nozzle plate contribute to the turbulence and hence a natural increase in heat transfer when the separation distance is decreased.

Chia, Giralt and Trass (1977) incorporated effects of z/d and turbulence into a laminar concentration boundary layer equation to predict mass transfer. Experimental transfer coefficients using naphthalene sublimation are obtained and the effect of turbulence is incorporated into the theoretically derived solution. The resultant equation is in good agreement with the experimental data up to a maximum deviation of five per cent, such an equation is thought to be a useful design tool.

Vallis et al (1978) applied a novel electrolytic mass transfer technique to find by analogy the heat transfer in turbulent impingement jet for $3880 < Re < 230000$ with $5 < z/d < 20$. The correlation coefficients are given with plots of Sh. Considerable difference is shown to exist at the stagnation and impingement region when compared with heat transfer measurement methods. It is only at the fully developed wall jet that agreement is obtained between heat and mass data. The correlation produced for the wall jet was

$$Sh = 0.078\, Re^{0.82}\, Pr^{\frac{1}{3}} \left(\frac{r}{d}\right)^{-1.05} \qquad \textbf{(2.3.5)}$$

where the exponent for Re agreed with that of Rao and Trass (1964) who suggested 0.84 and the r/d exponent matches the theoretically predicted of -1 by Dawson and Trass (1966).

Pokusaev and Volkov (1980) experimented with a similar electrochemical method to measure transfer rates both for one and two phase flows and obtained the

following correlation

$$Nu = 0.038\ Re^{0.8}\ Pr^{0.33} \qquad \textbf{(2.3.6)}$$

Rao (1980) analytically solved velocity and concentration profiles for a plane and radial wall jets. The agreement between the analytical and experimentally measured velocity is good beyond an inner layer next to the wall. Experimental measurements using a porous surface used to evaporate methanol into the turbulent wall jet and concentrations are measured using gas chromatography. The analytically derived concentration profiles agreed with measurements.

Button and Wilcock (1982) measured velocities and turbulence values using hot-wire anemometry for circular impinging jets with Re = 15000, 25000 and 35000 at various distance from the jet z/d = 2, 4, 6, 8 and 10. Using conditions discussed above the naphthalene sublimation technique is used to obtain mass transfer coefficients, which are correlated into equations (2.3.7) and (2.3.8) for the stagnation Nu for two different impingement areas of radius $0.5D$ and $3D$.

$$Nu = 1.276\ Re^{0.456} \left(\frac{L}{D}\right)^{-0.012} e^{\left(0.160\left(\frac{X}{D}\right) - 0.021\left(\frac{X}{D}\right)^2\right)} \qquad \textbf{(2.3.7)}$$

$$Nu = 0.839\ Re^{0.524} \left(\frac{L}{D}\right)^{-0.035} e^{\left(-0.221\left(\frac{X}{D}\right) - 0.380\left(\frac{X}{D}\right)^2\right)} \qquad \textbf{(2.3.8)}$$

A review of the cause of the secondary peaks observed in their own research is discussed.

Kataoka et al (1982) acquired local mass transfer using an electrochemical procedure and local surface pressures using piezoelectric pressure transducers for $4000 < Re < 15000$. They found that the stagnation mass transfer is a maximum when the $z/d = 6$. The velocity gradient fluctuations near the stagnation region had extremely large values and decreased slightly in spite of the negative pressure gradient. Large scale eddies are formed by disintegration of vortices of the oncoming jet and these created local velocity turbulence near the wall. This is thought to be the reason for enhanced local mass transfer at the wall due to the increased velocity turbulence.

Sonin (1983) adapted the limiting current electrochemical method to acquire transfer data for multiple impingement jets, which he had applied to depositing material rather than eroding the surface. He extracted correlations specifically for electroplating and stated that the liquid jet or gas jet transfer coefficients are different because of their respective *Sc*. The electroplating rate is increased but at the expense of pumping power, a 17 to 26 per cent increase in transfer rate is achieved by doubling the input power.

Hyne and Macleod (1984) used ESPI and the swollen polymer surface to observe mass transfer in turbulent jet impingement. They identified local maxima and minima which had been observed by previous workers using conventional heat transfer methods. Real-time ESPI observations of the transfer process showed any

local deviations from a monotonic behaviour, but the difficulties in maintaining stability with constant monitoring and long warm up periods made this technique arduous to use. The resolution of the fringe pattern produced some uncertainty in the quantification of the experimental data.

Chin and Hsueh (1986) used the electrochemical limiting current method to quantify mass transfer correlations for circular impinging jets on a flat plate. They experimented in the range $2500 < Re < 20000$ with $0.1 < z/d < 5$ and $0 < r/d < 5$. The Chilton-Colburn analogy is used to obtain the average experimental mass transfer correlations.

For the impingement region $r/d < 0.8$

$$Sh = 0.9\, Re^{\frac{1}{2}}\, Sc^{\frac{1}{3}} \left(\frac{z}{d}\right)^{-0.09} \qquad \textbf{(2.3.9)}$$

For the wall jet region $0.8 < r/d < 5$

$$Sh = 0.77\, Re^{\frac{1}{2}}\, Sc^{\frac{1}{3}} \left(\frac{r}{d}\right)^{-\frac{1}{2}} \qquad \textbf{(2.3.10)}$$

Popiel and Boguslawski (1986) using the naphthalene technique investigated two nozzles, a bell shape nozzle and orifice nozzle used for turbulent jet impingement. The flow ranged from $6000 < Re < 44000$ with $1.2 < z/d < 16$. The sharp ended orifice gave a greater mass transfer rate for the same conditions due to the phenomena of contraction of the jet, hence shortening the core length. Stagnation

point transfer attained a maximum when the z/d separation is beyond the core region. Correlations for stagnation point mass transfer are given for the two different jet types.

Sparrow, Xu and Azevedo (1987) used the naphthalene sublimation technique and obtained transfer rates for a confined impingement geometry with annular collection of spent air. The conditions tested are $7000 < Re < 80000$, $1 < z/d < 5$ and $1.51 < r/d < 2.20$. The Chilton Colburn heat/mass transfer analogy is suggested for determining the Nu. The transfer rate is found to be sensitive with area ratios of the jet tube to impingement area. Variation of jet separation distances is significant i.e. the transfer rate increased for the smaller jet to a maximum at separation distance $z/d = 2.5$ and then decreased for larger separations. For the larger tube the transfer decreased montonically with separation.

Gholizadeh (1992) used a real time holographic technique in conjunction with the swollen polymer technique to make profilometric measurements of the mass transfer from a flat plate due to normal impingement of an isothermal axisymmetric submerged jet of air. Two nozzle types; plain and contoured are used with spacings ranging from $0.26 \leq z/d \leq 24.0$ and flow Re in the range $700 \leq Re \leq 29600$. The Sc are varied in the range $2.64 \leq Sc \leq 3.62$ to assess their influence on the mass transfer process, this is achieved by using three swelling agents namely; ethyl salicylate, 1-methyl naphthalene and n-tetradecane. The transfer coefficients for a laminar jet within the impingement zone $0 \leq r/d \leq 0.6$ and Re between $700 \leq Re \leq 1700$ with separation distance $0.26 \leq z/d \leq 5.0$ are found to be in agreement

with the Scholtz and Trass equation (2.2.2) to within ± three per cent. The coefficients for transition region of $0.6 \leq r/d \leq 2.0$ has been correlated as

$$Sh = 0.93\ Re^{0.5}\ Sc^{0.361} \left(\frac{r}{d}\right)^{-0.8} \qquad \textbf{(2.3.11)}$$

The constant and the exponent of r/d in equation (2.3.11) are quoted to have experimental uncertainties of four per cent and six per cent respectively. The author found his data to be 20 per cent higher than the values obtained from equation (2.2.3) determined by Scholtz and Trass.

The data within the radial range $2.0 < r/d \leq 5.0$ had been correlated as

$$Sh = 1.18\ Re^{0.5}\ Sc^{0.361} \left(\frac{r}{d}\right)^{-1.1} \qquad \textbf{(2.3.12)}$$

This data is found on average to be 40 per cent higher than the values derived from the wall jet theory equation (2.2.1) of Scholtz and Trass. The coefficients found beyond $r/d = 6$ agreed with the wall jet theory of Scholtz and Trass, which the author deduced as implying that the theory can only be applied beyond $r/d = 6$. The vapour pressure data from Paterson et al (1987) for the three swelling agents are confirmed by the independence of the mass transfer data from the agent by the Sc in the form of $Sc^{0.361}$.

The dependence of the transfer coefficient at the stagnation point is found to be unaffected by the z/d spacing within the range $0.26 \leq z/d \leq 12.0$. Beyond this range and between $12.0 < z/d \leq 20.0$ the stagnation data is reduced to the

following correlation (2.3.13) with five per cent uncertainty in the constant and exponent of *r/d*.

$$Sh_o = 34.7\ Re^{1/2}\ Sc^{1/3} \left(\frac{r}{d}\right)^{-5/4} \qquad \textbf{(2.3.13)}$$

A nonuniform mass transfer field is viewed to be evidence of transition from laminar boundary layer to turbulent in this research within the radial region $1 < r/d < 2$ at $z/d \leq 4.0$ for $Re \geq 10300$ and is present for both plain and contoured nozzles. The plain tube nozzle had no effect on mass transfer in the impingement zone, yet the contoured nozzle generated a non-uniform transfer distribution which is dependent on *z/d* spacing but independent of *Re*.

For the plain tube nozzle with $2400 < Re < 13550$ and $z/d = 2$, the stagnation point mass transfer distribution is correlated

$$Sh_o = 1.22\ Re^{1/2}\ Sc^{1/3} \qquad \textbf{(2.3.14)}$$

The transfer coefficients for $Re = 10300$ and $z/d > 1$ are judged to be comparable with available data in literature, similar trends as would be expected are obtained i.e. between $z/d = 1$ to 6 the stagnation point coefficients increased by 26 per cent and beyond $z/d = 6$ the values decreased.

The stagnation mass transfer for the plain tube nozzle is represented by the following correlation (2.3.15) for $10.0 \leq z/d \leq 24.0$ and $7000 < Re < 13550$,

$$Sh_o = 0.80 \left(\frac{z}{d}\right)^{0.83} Re^{3/4} Sc^{1/3} \quad \textbf{(2.3.15)}$$

The transfer data for the contoured nozzle has also been correlated (2.3.16) however only for one spacing $z/d = 2$ and for $900 < Re < 29600$.

$$Sh_o = 1.12\, Re^{1/2} Sc^{1/3} \quad \textbf{(2.3.16)}$$

2.5 Numerical predictions with laminar jets

Marple et al (1974) carried out numerical predictions and experimental tests on the flow patterns on both a round and rectangular laminar jet in a partially confined space. The authors were not concerned with the transport phenomena at the impingement plate but concluded that whether or not this confinement boundary is present, it did not greatly affect the flow field in the impaction region below the jet. The observed effect of the confinement boundary on the flow field is an associated increase in size of the recirculation bubble with a related increase in the *Re* from 700 to 2300.

Saad (1975) presented in his thesis results from numerical simulations he had undertaken of a semi-confined axisymmetric jet impinging on a flat surface. He studied the effect of the confinement plate on the impingement region and found it to be negligible, but the flow pattern of the recirculation zone is dramatically altered by the change in the *z/d* spacing. The jet velocity profile emitted from the nozzle had a significant effect on the transfer coefficients on the impingement

surface. He simulated a porous target surface with suction and observed the enhancement of heat transfer coefficient due to this modification to the boundary condition.

Van Heiningen, Mujumdar and Douglas (1976) used a similar numerical finite difference technique to model for flow field and impingement transfer due to a laminar slot jet on a permeable impingement surface with suction. An interesting observation they made is a contraction in the jet with a parabolic velocity profile which as a consequence had higher momentum, steeper velocity and temperature gradients as compared with a flat inlet jet velocity profile. A proportionality with respect to $Re^{0.5}$ lead to a collapse of all the results for the range of Re investigated onto a single curve on the dimensionless graph of transfer coefficient against position from the stagnation point. This dependence on the $Re^{0.5}$ is found to be more pronounced for heat transfer than for the skin friction on the target surface. Applying suction to the impingement surface lead to an enhanced transfer rate with minimal effect on the stagnation region. The inclusion of variable properties to the numerical model had minor significance to the Stanton number distribution on the impingement surface.

Huang (1977) simulated a swirling laminar jet with both weak and strong swirl imposed on the flow. There is no difference found in the heat transfer characteristics of the weak swirl flow when compared to the non-swirl flow case. Increasing the swirl created an increased jet spreading which had thus generated a recirculation region adjacent to the impingement zone which had the effect of insulating the heat transfer. The spacings between the confining surfaces had very

little effect on the transfer coefficients within the imposed swirled jet flow. The author had modelled suction/blowing at the impingement surface, from his results he concluded, that suction had enhanced heat transfer but blowing had suppressed it.

Saad, Douglas and Mujumdar (1977) predicted numerically heat transfer coefficients under an axisymmetric laminar impinging jet in a semi-confined region with a permeable surface to which suction is applied. Their presentation focused on the transport phenomena, chiefly heat transfer, occurring at the impingement surface. The Stanton number did not vary with z/d over the range $1.5 < z/d < 12$. The effect of jet exit velocity profile (i.e. parabolic or flat) on heat transfer is found to be important because the transfer rate due to the flat velocity profile is significantly less over the entire impingement plate as compared to the parabolic jet. This effect is a consequence of the higher momentum at the stagnation point when inlet jet profile is parabolic. The addition of suction to the impingement surface is observed to produce an enhancement in the transfer rate.

Huang, Douglas and Mujumdar (1978) modelled a confined laminar swirling jet and analysed the heat transfer characteristics. They made a parametric study on the model with the following: z/d, r/d, Re, S, $W1$, U_{suct}. The results of which are previously published in Huang (1977).

Mujumdar, Li and Douglas (1980) simulated coupled heat and mass transfer characteristics under round laminar jet impinging on a plane wall. The addition of coupled mass transfer to the surface resulted in lowering the heat transfer rate. A

semi-empirical correlation which allowed for evaporation showed close agreement with their numerical predictions.

Huang, Mujumdar and Douglas (1981) predicted the flow field of partially confined normally impinging laminar jet, with the following parameters being investigated; *Re*, *z/d*, *W1*, Swirl and *r/d* of the confinement plates. The results are presented for both flat and parabolic velocity profiles and swirl number varied from 0 to 0.4, and for $950 < Re < 1950$. The velocity profile is shown with the effect of swirl superimposed. For swirl numbers below 0.2 no difference is apparent compared with the non swirling flow of the jet. Predictions for swirl greater than 0.5 indicated a recirculation zone at the stagnation region which caused degradation of heat transfer at that point.

Schneider et al (1987) solved analytically flow field for laminar axisymmetric jet issuing from plane infinite walls at large distances from the wall. The main flow region is a toroidal eddy. Numerical analysis was carried out using the finite volume program TEACH, whose results compare favourably with the analytical results.

Deshpande and Vaishnav (1982) wanted to obtain shear stresses on the wall which is impinged on by an air jet as a means of measuring the mean strength of arterial endothelium membranes of dogs arteries. They conducted parametric numerical studies and reviewed the following results; streamlines, vorticity, centre of eddy, radial/axial velocity profiles and pressures on the surface. A purpose written code is used and comparison with Saad et al's (1977) shear stress values are made which

showed good agreement.

Law and Masliyah (1984) obtained contours of stream functions with specific computer code written specifically for a two dimensional laminar jet impingement flow. The variables modelled were $z/b = 4$ and $Re = 400$ for several confinement distances $X_{max} = 42$, where as the critical region in the flow field is $X_{max} = 24$ to 34. They presented plots of vortex centres against Re for $z/b = 4$ and the following $Re = 100, 200, 300, 400$ with $X_{max} = 40$. They concluded that long confinement plates produced recirculating flows which dominated, whereas for shorter confinement plates these vortices disappeared and inflow is established which then dominated the flow.

Jassaud et al (1984) studied heat and mass transfer under an oblique laminar impinging slot jet in cross flow, specifically for evaporation from a wet surface impinged on by a drying air jet which is one of the main configuration used in industry.

Ravi and Deshpande (1986) generated numerical models of a plane jets impinging on a flat surface, with a non-dimensional height $z/b = 4$. The results for streamlines, velocities, wall shear stress, and pressure profile are presented.

Despande et al (1988) presented in this note results of their numerical predictions and flow visualisation pictures of their experiments and they concluded a qualitative agreement in their findings.

Jambunathan et al (1990) generated a numerical model of the semi-confined jet impingement geometry and study the grid independent solutions for this configuration. Skin friction factor were calculated which compared well with other published data.

2.6 Numerical predictions with turbulent jets

Ravuri and Tabakoff (1975) devised a numerical scheme for calculating heat transfer between a heated plate and an axisymmetric jet. The calculated heat transfer values are found to be a little lower than some experimentally determined values by themselves.

Vallis, Bacon and Patrick (1979) applied a two equation turbulence model for predicting numerically an impinging jet flow and assessed the heat transfer present within a convective heating furnace. They commented that the model showed qualitative agreement with their own experimental results but the equations used required further work before this method would be used as a design tool with any confidence.

Rubel (1980) simplified his numerical simulations by imposing an incompressible, inviscid rotational flow condition onto an axisymmetric and oblique two dimensional impinging jet on a flat surface. He found that the centre line decay velocity and ground plane pressures compared well with available observations.

Agarwal and Bower (1982) used a κ - ϵ turbulence equations to model the jet

impingement configuration which would be applied for VTOL aircraft design. An augmented central difference scheme is used and it is found that the kinetic energy had a large overshoot at the ground plane.

Amano and Jensen (1982) studied axisymmetric turbulent jet impingement both experimentally and numerically. The *Re* investigated are 10000, 20000 and 40000 with $z/d = 4$, 7 and 10. They used a finite difference algorithm with refined wall functions for κ and ϵ in their program and they claimed better agreement with their own experimental results.

Amano (1983) predicted characteristics of a turbulent submerged impinging jet. A secondary peak for skin friction is observed for $z/d < 2$, its magnitude is dependant on the *Re*, z/d and kinetic energy. The radial position of the second maximum moved away from the stagnation point with an increase in turbulence intensity and *Re*.

Guo and Maxwell (1984) simulated turbulent flow using the κ - ϵ turbulence equations to predict flow for plane impingement jet. The predicted wall shear stresses for the impingement zone are in good agreement with their own experimental data and are found to be somewhat lower in the wall jet region. The maximum kinetic energy is found to be in the impingement zone and in the vortex like region.

Amano and Brandt (1984) studied the effect of flow characteristic of jet impingement using the finite difference method with the κ - ϵ turbulence equations,

which are said to have achieved five per cent accuracy in the flow variables. The calculated skin friction coefficients are within 25 per cent of the experimentally measured values and similar findings are found to that of Amano (1983).

Polat, Mujumdar and Douglas (1985) modelled turbulence with the κ - ϵ equations and obtained the heat transfer and flow behaviour of a slot jet impinging on a flat surface. They looked at the effects of *z/d* spacing, turbulence level, jet *Re* which compared favourably with available data. They suggested enhancement of *Nu* on the impingement surface is possible with higher turbulence from a nozzle with smaller *z/d* spacing, but this would be at the expense of pumping power required.

Paullay, Melnik, Rubel, Rudman and Siclari (1985) solved by numerical integration of ordinary differential equation using similarity solutions of radial and plane jets utilising the κ - ϵ turbulence equations. Results are not compared with any experimental data, but are assessed with asymptotic solutions and found to be undervalued by six per cent.

Amano and Sugiyama (1985) numerically modelled heat transfer for an axisymmetric normally impinging jet with the κ - ϵ model. Their findings showed that the maximum heat transfer predictions are much improved when a refined wall function for the ϵ equation is used in the near wall region. They recommended further modifications to the wall functions to improve heat transfer predictions before embarking on the use of a multi-equation model approach to the simulations.

Rakadjiev, Ennoji and Asanuma (1987) simulated flow variables for a normally impinging axisymmetric jet on a flat wall. A range of *Re* are investigated with good agreement being shown for *Re* of 100000 with both their experimental data and inviscid flow computations.

2.7 Heat transfer with laminar jets

Vickers (1959) experimentally found heat transfer coefficients on a target plate placed in an oven, impinged on by a laminar jet. The jet flow ranged from $550 < Re < 1200$. The transfer coefficients for $Re = 550$ are lower due to the uncertainties associated with their experimental measurement method.

Wolfshtein and Stotter (1964) used an analytical approach and derived an equation for heat transfer using Glauerts analytical solution of flow equations for laminar impinging air jets on a flat surface. The equation is summarised as

$$Nu = 0.208\ Re^{1/4} \left(\frac{r}{d}\right)^{-5/4} \qquad \textbf{(2.6.1)}$$

Brdlik and Savin (1965) applied an integral method and derived an analytical solution for heat transfer coefficients on a flat surface due to an axisymmetric laminar impinging jet. They undertook a testing program and validated their analysis. They quoted this data to a ten per cent uncertainty which is scattered around their theoretical predictions to be within twelve per cent.

Miyazaki and Silberman (1972) used a combined numerical and analytical approach

and obtained solutions for flow and heat transfer for a two dimensional impingement jet. They observed friction factors attained a maximum when the $z/b = 1$ and increased to 3.5 times greater when z/b is larger. This is found to be true for Nu, but the factor is 1.7 times the value. The Nu is shown to be proportional to $Pr^{0.373}$ at the impingement region.

Sparrow and Lee (1975) analysed the fluid flow and heat transfer characteristics within a slot jet with an initial non-uniform velocity profile. Stagnation transfer coefficients for non-uniform jets are predicted to be twice that of flat jet profiles. They compared their theoretical solutions against previous experimental coefficients, which they found to be lower than their theory as would be expected from any assumptions made at the beginning of the analysis.

Lipsett and Gilpin (1978) utilised a finite element method for solving the potential flow region and subsequently an integral method for the boundary layer flow, which allowed determination of the transfer coefficients for the impingement domain. The technique described above is potentially applicable to a large class of this type of problems. The inclusion of phase changes and surface curvature could be allowed for very effectively within this method.

Ero (1978) used flow models he had developed to obtain transfer coefficients for an impinging slot jet in close proximity to the surface. He studied two jet profiles, a Gaussian and parabolic from which he summarises that the Gaussian attained a higher centre line velocity, he also observed that the entrainment did not penetrate the wall jet region in his predictions.

Popiel et al (1980) experimentally studied heat transfer from a hot gas jet impinging on an isothermal surface. The investigated Re = 1860 and 1050. Turbulence intensity measured showed no increase due to combustion at the jet centre line. They identified three domains in the flow namely laminar layer, transitional region and turbulent region.

Hrycak's (1980) reviewed literature on the state-of-the art of heat transfer due to impinging jets. He summarised the flow characterisations and analytical approaches contained within 70 references which he had cited. A conclusion he made was that further investigations of turbulence are needed for a better understanding of its effect on the heat transfer. Another observation from this review is for obtaining maximum heat transfer, the impingement surface should be placed at the end of the potential core, because the turbulence is greatest there. The final comment made was that there was a need for considerable work to achieve a through understanding of the impingement flow regime.

Gaunter, Livingwood and Hrycak (1970) reviewed the flow characteristics which are the governing conditions present in a single turbulent impinging jet. The authors made 11 concluding remarks about this type of flow and these are found to be an important summary of the conditions that dominate the flow geometry.

Downs and James (1987) reviewed 47 publications as part of background work relating to the their research. This paper summarised the findings from the literature, covering the main aspects of heat transfer within impinging jets. They discussed the following topics as the most important to be considered in this

research i.e geometry effects, temperature effects, interferences and cross flow, turbulence levels, incidence, surface roughness, externally applied factors, jet outlet conditions and non uniformity of jet arrays. Their tabulated summary of correlations and available equations would be an excellent source for any one researching into this field.

Raj (1987) applied variational mathematics to solve for the stagnation point heat transfer for boundary layer flow.

2.8 Heat transfer with turbulent jets

Smirnov, Verevochkin and Brdlick (1961) measured heat transfer between a (water) liquid jet and flat surface using a calorimeter method. Their equation for heat transfer is presented and agrees well with other recognised investigations. The authors separate the heat transfer results into three z/d ranges for Re = 1600 to 50000. The experimental data for $0 < z/d < 10$ is summarised in equation (2.7.1) with an error of ± eight per cent.

$$Nu = C\ Re^{0.64}\ Pr^{1/3}\ e^{(-0.037\ z/d)} \qquad \textbf{(2.7.1)}$$

$$Nu_o = 13\ \sqrt{Re}\ D/z \qquad \textbf{(2.7.2)}$$

Gardon and Cobonpue (1962) directly measured heat transfer for both single and multiple jets impinging on an isothermal surface. A new heat flow transducer enabled localised heat transfer to be measured for $d < 0.001$ (m). A correlation

they produced for stagnation point heat transfer for $z/d > 20$ is given in equation (2.7.2)

For $z/d > 10$ a characteristic bell shape heat transfer profile is present, but for $z/d < 6$ an annular hump developed around the central peak at $r/d = 1.9$. These secondary peaks enlarged with narrowing spacing and for $z/d < 3$ above the surface the secondary maximum was established. This is explained to be due to either a transition point in the flow from laminar to turbulent and/or a point of flow separation at the surface.

Gardon and Akfirat (1965) re-examined heat transfer in two- dimensional jet impingement with consideration being given to turbulence measurements which are used to explain some anomalous phenomena. The heat transfer at the stagnation point could be significantly altered by initial turbulence levels within the jet when the $z/b < 8$. The radial variation of heat transfer with the secondary peaks at $x/b = \pm 7$, is explained to be due to transition of the boundary layer from laminar to turbulent flow. The upper limit of $z/b = 8$ is identified and influence of induced turbulence had no effect and the secondary peak no longer existed. The inner heat transfer peaks at $x/b = \pm 0.5$ only existing when $z/b < 0.5$ is explained to be due to increased velocity caused by the narrow exit gap formed by the z/b. However, similar inner peaks are present in heat transfer in axisymmetric flows for $z/d = 3$, their appearance is regarded to be due to the existence of thinning of the boundary layer at $r/d = 0.5$. The authors advised that when designing impingement heat transfer equipment with short $z/b < 8$, consideration should be given to turbulence levels upstream of the nozzle.

Gardon and Akfirat (1966) determined experimentally local and averaged heat transfer coefficients for a two dimensional jet. The main conclusions are summarised in Gardon and Akfirat (1965), however, correlations are determined for stagnation point *Nu* as equation (2.7.2) when $z/b > 14$ and $Re > 2000$. The error in the equation is said to be ± five per cent.

$$Nu_o = 1.2\ Re^{0.58}\ (z/b)^{0.62} \qquad \textbf{(2.7.3)}$$

For multi slot jets with $Re > 2000$ and $z/b > 8$, the average *Nu* correlation is given as equation (2.7.3) with

$$Nu_{av} = 0.36\ Re^{0.62} \qquad \textbf{(2.7.4)}$$

Wolfshtein (1966) collated experimental data from other workers, for both two dimensional and axially symmetric jets which he compared by plotting them on a non-dimensionalised graph. The Stanton number could be estimated from the figures to an accuracy of ± 30 per cent.

Vlachopoulos and Tomich (1971) defined a new method for determining heat flux from a hot impinging jet on to a flat plate.

Cadek and Zerkle (1974) theoretically analysed two-dimensional impingement and showed good agreement with their own experimental results using an electrically heated constant temperature surface. The wall jet region gave the best agreement, but the stagnation heat transfer is increased by turbulence present within the jet,

mainly for $z/b > 6$.

Obot, Majumdar and Douglas (1979) made a detailed study of impingement heat transfer due to a round nozzle with different inlet shapes for $15000 < Re < 60000$ with $z/d = 2$ to 12. The effect on velocity and turbulence and hence heat transfer due to a short nozzle length is the most significant. Beyond $z/d = 12$, neither the shape nor the length of the nozzle had any effect on the heat transfer characteristics. However, it is significant at $z/d < 6$.

Obot, Douglas and Mujumdar (1982) looked at the effect of confinement on the heat transfer at the impingement surface. For $z/d = 2$ greatest reduction in heat transfer was noticed outside the central impingement region. The difference in heat transfer is less between confined and unconfined jet impingement for $4 < z/d < 6$, but the difference increases at $z/d = 8$. Doubling the confinement distance had no effect on the transfer rates.

Pamadi and Belov (1980) had shown the mechanism to explain the inner peaks due to non-uniform turbulence generated by mixing within the jet and therefore could not agree with Gardon and Akfirat proposal that boundary layer thinning caused this inner peak. The outer peak is still attributed to transitional flow in wall boundary layer from laminar to turbulent.

Goldstein and Behbahani (1982) studied cross flow in normal jet impingement and they found for a $z/d = 12$, the heat transfer coefficient diminished, however at $z/d = 6$ the peak heat transfer is increased. Correlation in absence of cross flow is

given as

$$Nu = \frac{Re^{0.6}}{\left(A + B \left(\frac{x}{d} \right)^{n} \right)} \qquad \textbf{(2.7.5)}$$

where A = 3.329, B = 0.273 and n = 1.3

Hrycak (1983) made direct heat transfer measurements for two types of nozzles, which he correlated for stagnation point values. He concluded that the heat transfer peaks at about $z/d = 7$ from the nozzle exit. The stagnation *Nu* showed a dependence on *Re* to the power 1/2, however the average over the target surface is *Re* to the power 0.7 showing a wall jet dominance.

Hollworth and Gero (1985) had shown with direct measurements using a heat flux sensor, that the heat transfer at the impingement surface is reduced due to non-isothermal impingement, caused by a mixing of jet with its surrounding of different temperatures. They also obtained recovery temperatures of the jet and used these to determine new heat transfer data and found there is no difference from an isothermal jet with similar conditions.

Kataoka (1985) studied high temperature gas jets impinging on flat surfaces, they found the maximum stagnation heat transfer occurs at the end of the potential core region. A generalised model is used to calculate the optimum spacing for various initial conditions, so that the heat transfer is optimised.

Carper et al (1986) experimentally obtained average heat transfer coefficients on a rotating disk due to liquid oil jet impinging normally onto the disk. Correlation for an axisymmetric jet is

$$Nu_d = 0.097\ Re_r^{0.384}\ Re_j^{0.459}\ Pr^{0.448} \qquad \textbf{(2.7.6)}$$

and for $Pr = 270$ the following correlation was obtained

$$Nu_d = 3.4\ Re_r^{0.413}\ Re_j^{0.250} \qquad \textbf{(2.7.7)}$$

For an asymmetric jet

$$Nu_d = 0.57\ Re_r^{0.272}\ Re_j^{0.442}\ Pr^{0.381}\ \left(1-\frac{2r}{d}\right)^{0.255} \qquad \textbf{(2.7.8)}$$

Goldstein and Franchett (1988) used liquid crystals on the impingement surface of an oblique surface to measure heat transfer coefficients. Empirical correlation equations for the *Nu* were obtained, typically of the form of

$$Nu = A\ Re^{0.7}e\left[-(B + C\cos\phi)\left(\frac{r}{d}\right)^m\right] \qquad \textbf{(2.7.9)}$$

Jambunathan et al (1992) have collated data from available sources and produced an appropriate form of correlation equation suggested by the latest empirical data. A comprehensive review of literature to date was carried out and the information extracted shows the lack of data there is on jet impingement with all its variations.

Moss (1993) has collated heat transfer data from available literature and produced an expert system to aid the designer in selecting the most relevant correlation data for his particular application.

2.9 Conclusions

Unconfined laminar impingement jet flow has been analysed theoretically by Schlichting (1968), Glauert (1956), Scholtz and Trass (1970) but their analysis is limited to either within the wall jet or the impingement zone. As the analytical approaches are found to be limiting, numerical methods are utilised for analysing flow and heat/mass transfer within the impinging configuration. The following had all studied the semi-confined impingement geometry using a numerical method, Marple et al 1974, Saad (1975), van Heiningen et al (1976), Huang et al (1977, 1978, 1981), Li (1977), Saad et al (1977), Mujumdar et al (1980), Law and Masliyah (1984), Jassaud et al (1984), but others such as Schneider et al (1987), Deshpande and Vaishnav (1982, 1988), and Ravi and Despande (1986) studied the unconfined impingement geometry. Their predictions are for numerous different boundary conditions such as flat or non-uniform jet velocity profiles for either an axisymmetric or two-dimensional systems. The ease with which any or all the boundary conditions could be modified demonstrated the power and usefulness of these predictive techniques. The uncertainties associated with these predictions are of the same order as those expected from the analytical solutions.

The measured laminar heat transfer coefficients for the unconfined impingement geometry are plentiful, Vickers (1959), Brdlik and Savin (1965), Popiel at al (1980)

but because of the infinite possibilities in the boundaries, it is by no means complete and the uncertainty in these measurements are not always quantified. However, no experimental data is available for the semi-confined impingement flows because the available heat transfer measurement techniques are laborious and difficult to use. Therefore, analogous mass transfer methods are extensively used, for the study of the unconfined geometry by Scholtz and Trass (1963, 1970), Kapur and Macleod (1972, 1975, 1976), Masliyah and Nguyen (1976, 1977, 1979), Harper and Macleod (1978) and Golizadeh (1992) but only Law (1982), Law and Masliyah (1984) had studied the geometry with the imposed semi-confinement boundary. Nevertheless they produced some useful and functional mass transfer correlation for the unconfined geometry but none of them estimated the associated uncertainties for their equations. The semi-confined geometry has largely been neglected by the experimenters because of the assumed insignificance of the confinement boundary to the impingement heat transfer and therefore a void exists in the data and as such the potential for making an important contribution exist with the current research.

Most industrial processes that utilise the impingement geometry operate with turbulent flow conditions, but only simplistic analytical solutions are possible Schlichting (1968), Dawson and Trass (1966). Hence computational methods became increasingly important and a review by Polat et al (1989), provide a ready means of predicting the heat transfer trends even though the uncertainty in the absolute solutions are high due to approximate nature of modelling the turbulence. Numerous studies with the high Re κ-ϵ turbulence model had been done but the predictions showed significant difference between them and the experimental

measurements. These discrepancies are associated with the turbulence equations and the way the near wall boundary is modelled, Ravuri and Tabakoff (1975), Vallis et al (1979), Rubel (1980), Agarwal and Bower (1982), Amano and Jensen (1982), Amano (1983), Guo and Maxwell (1984), Amano and Brandt (1984), Polat et al (1985), Paullay et al (1985), Amano and Sugiyama (1985) and Rakadjiev et al (1987). The semi-confined turbulent impingement simulation has largely been neglected by the research community. The inclusion of the semi-confinement boundary in the predictions would have provided some commonality between the many examples in literature. But the numerous ways these boundaries have been specified makes the uncertainty in comparisons large. Recently, the semi-confined single jet impingement has been recommended as a future bench mark test case for validating new developments in turbulence models since the geometry provides a simple domain and stringent flow conditions for purposes of comparison.

Experimental measurements of unconfined turbulent jet impingement are plentiful even though the experimental methods used are laborious and only provided data at discrete points, Smirnov et al (1961), Gardon and Cobonpue (1962), Gardon and Akfirat (1965, 1966), Wolfshtein (1966), Vlachopoulos and Tomich (1971), Cadek and Zerkle (1974), Obot et al (1979, 1982), Pamadi and Belov (1980), Hrycak (1981, 1983), Goldstein and Bebahani (1982), Hollworth and Gero (1985), Kataoko (1985), Carper et al (1986) and Goldstein and Franchett (1988). Some excellent reviews are compiled on the flow and heat transfer characteristics by Gaunter et al (1970), Arganbright and Resch (1971), Mujumdar and Douglas (1972), Livingwood and Hrycak (1973), Becko (1976), Hrycak (1980), Downs and James (1987) and Jambunathan et al (1992). The heat transfer in a semi-confined regime is studied

by Obot et al (1982) and he concluded that there is a significant effect in the stagnation heat transfer for $z/d < 2$ and also when $8 < z/d < 12$.

Analogous methods have also been used to investigate the mass transfer in turbulent unconfined impingement jets Rao and Trass (1964), Ward et al (1972), Chia et al (1977), Vallis et al (1978), Pokusaeu and Volkov (1980), Button and Wilcock (1982), Kataoko et al (1982), Sonin (1983), Hyne and Macleod (1984), Chin and Hsueh (1986), Popiel and Boguslawski (1986) and Golizadeh (1992).

A tremendous number of sources of jet impingement information exist for interrogation, but unfortunately the results vary widely and this is mainly due to the error sources in experimental methods used and simplifying assumption made about the physical condition of the flow i.e turbulence, compressibility, viscosity effects, conduction and radiation. The final conclusion of this review is that, although the flow and heat transfer process for the jet impingement geometry is abundantly documented with fairly reasonable understanding of the transfer process, only 7 percent of the available literature has accounted for some form of confinement. This low percentage shows a clear gap in the available knowledge about the effect of confinement on the transport properties in impingement flows and therefore it is proposed that the current work is to address this deficiency and the need to produce a universal functional model for all relevant variants at the boundaries.

CHAPTER 3
EXPERIMENTAL TECHNIQUE, INSTALLATION AND VALIDATION

This chapter reports the background and overview of the physical arrangement and experimental procedure used in the current research. This research is first gleaned by Button and Mohamad (1983), who investigated the available convective heat transfer measurement techniques. They found there is no definitive work in literature that compared existing experimental heat and mass transfer techniques for a particular application. Subsequently, an SERC grant awarded to Button & Wykes in 1987 entitled 'The investigation of the full-field heat and mass transfer techniques for measurements of the jet impingement heat and mass transfer'. The current research work is part of this wider study into the various heat and mass transfer techniques.

Several techniques are available for measurement of heat and mass transfer, but most are of limited use when the application geometries become complex.

The following direct heat transfer measurement techniques are studied with a jet impingement geometry as part of this research. They are;

- Phase change paint thermography both transient and steady state procedures
- Infra-red thermography
- Liquid crystal thermography both transient and steady state analysis methods.
- Thermocoupled test surface with constant flux heating

Alternative indirect mass transfer techniques used are;

- Swollen polymer used with holographic interferometry
- Swollen polymer used with Electronic Speckle Pattern Interferometry (ESPI)
- Naphthalene sublimation with Moire interferometry

Experimental and numerical flow visualisation using

- Finite volume numerical analysis
- Laser doppler anemometry

All the above techniques mentioned have the following important features associated with their use;

- Full-field data and visualisation
- Non-intrusive nature
- Data to examine the heat and mass transfer analogy

The current research project is selected from the above programme with the aim of obtaining mass transfer data for semi-confined jet impingement using the swollen polymer and holographic interferometric technique. Following sections report on the swollen polymer technique, arrangement of the jet impingement rig, optical system used and a detailed account of the experimental procedure. A section on the analysis procedure with associated formula for data reduction is included. The Monte-Carlo statistical analysis method for uncertainty in the measured quantities is described. The physical properties used in the analysis of the mass transfer data are also presented.

3.1 The swollen polymer technique

A brief historical background and limitations of the swollen polymer technique is presented in this following section. An innovative technique first proposed by Macleod and Todd (1973), used a polymeric mass transfer surface capable of absorbing a volatile organic liquid, which replaced a commonly used naphthalene coating for mass transfer experiments. The mass transfer rate is determined from the shrinkage in the polymer coating as the mass of the volatile liquid is allowed to convect away from the surface. Shrinkage of the coating is of the order of 10^{-6} m and most mechanical methods of measurement become very intricate at this level of accuracy. It is therefore proposed to use a non-contact holographic interferometric technique with the swollen polymer transfer surface proposed by Kapur and Macleod (1974). The principal advantages of this combined method are the non-intrusive nature of the profilometry and the results are given as full-field images.

The main objectives of current research are the measurement of local mass transfer

distributions in semi-confined, normal axisymmetric impingement jet for laminar and turbulent *Re*, using the swollen polymer and the double exposure holographic system. Mass transfer coefficients for the target surface within a semi-confined impinging jet region are correlated in an appropriate and useful functional equation.

The following criteria for using the swollen polymer technique are first proposed by Macleod and Todd (1973) who envisaged a few advantages over the conventionally used materials for the mass transfer experimental methods. The main benefit to this inventive combination of materials is, that the test surface fabrication needs to be prepared only once, as compared with other types of subliming surfaces such as naphthalene. Naphthalene surfaces have to be recast after each mass transfer experiment. Polymeric surfaces need only be restocked by immersion into the volatile fluid, which restores the volatile fluid and the transfer surface to its saturated homogeneous state ready for further experiments. The second significant advantage of using this polymer surface is by changing the swelling agent, a wider choice of *Sc* can be created so that different experimental conditions may be applied. Applicability of this system to the determination of mass transfer coefficients in air is made with the following assumptions.

- The reduction in swollen polymer surface thickness is proportional to the mass of swelling agent lost during an exposure to a convective flow.
- The vapour pressure of the ester is assumed to remain constant at/or above the polymer surface during the period of transfer called the 'constant rate period'.
- The diffusion resistance of the ester is mainly in the gas phase therefore the ester is always assumed to be available at the polymeric surface for convection.
- Lateral distortions to the polymeric surface are regarded to be insignificant when compared with the local deformations that are due entirely to the mass convection.
- The initially dry polymer coating thickness is assumed to have no bias on shrinking rates at any point on the transfer surface.

The swollen polymer technique is to be used in the current work to measure mass transfer in semi-confined jet impingement, the arrangement of which is discussed in the following section.

3.2 Semi-confined axisymmetric jet impingement arrangement

The survey of literature in Chapter 2 revealed various jet impingement arrangements in the numerous studies available. The current design is chosen to be compatible with the geometric dimensions and flow conditions used in literature. A semi-confinement boundary provides control on the flow from the boundary adjacent to the nozzle and this is not normally present in other numerous studies. Air is chosen as the fluid medium and therefore a submerged jet flow arrangement is to be investigated.

The exact geometry studied is an axisymmetric air jet impinging on a flat target surface with in a semi-confined region shown in Figure 3.1. Full details of the geometric arrangement and dimensions are provided in Appendix M. A semi-confinement plate is located flush with the exit of the nozzle. Two adjacent supporting pillars are fixed parallel to the target plate and aligned with the front-face of the surface. These pillars are detached from the test plate to isolate vibrations that may be transmitted during handling of the confinement plate. Four threaded bars are secured to these legs that are used to mount the confinement plate at a known distance from the impingement plate with the use of spacers. The confinement plate is fastened onto these pillars and the spacers ensured parallel alignment of the two bounding surfaces.

The air flow system used is represented schematically in Figure 3.1. The air jet is generated from a compressed air supply, which is pressurised to a nominal value of 1,160.00 N/m^2. This pressure is regulated down through a valve to 145.00 N/m^2. A Platon rotameter or British standard orifice flowmeter is positioned between the regulating valve and plenum chamber, which facilitates measurement of the air flow into the nozzle. A simple precaution is necessary downstream of the plenum, which is never to restrict the outlet. This is because the pressure in the plenum

will rise to the regulated pressure, which could have an extremely dangerous consequence because the plenum is made of perspex and will not withstand high pressures. The aperture to the nozzle is always left unrestricted, and thus only a small pressure is ever produced in the plenum chamber.

A fully developed velocity profile is created at the exit of the nozzle because a pipe length of 60 diameters is part of the nozzle design, so that the outlet condition is controlled. The plenum chamber and pipe provide sufficient settling time for the turbulence level to be fully developed at the nozzle exit.

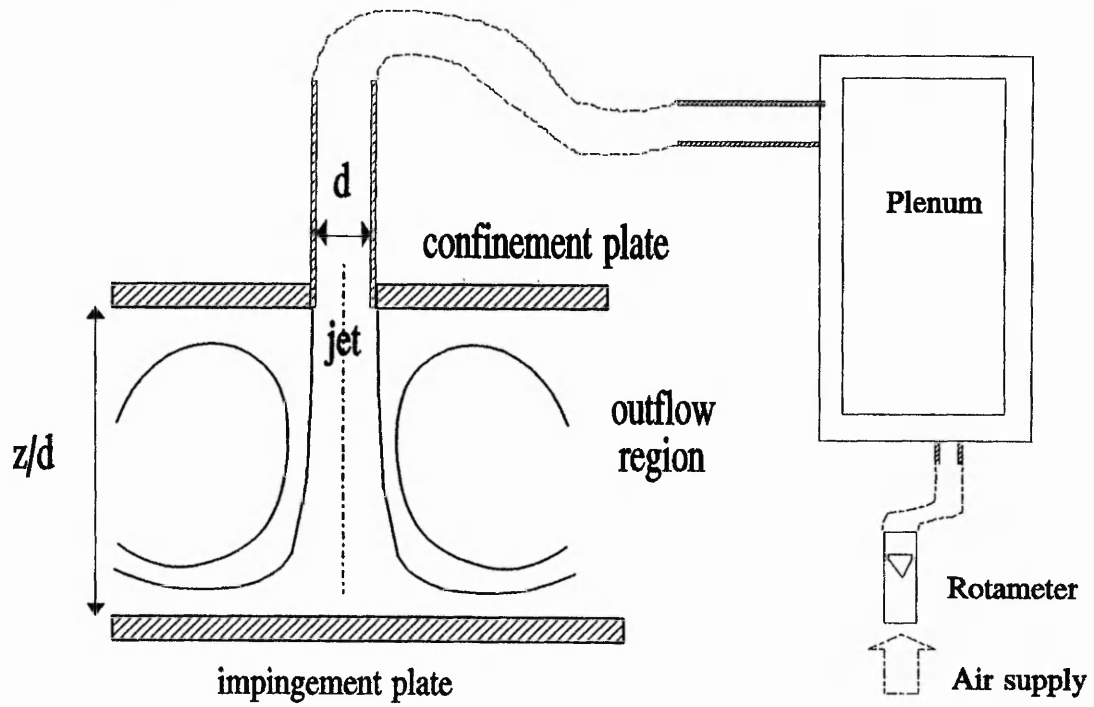

Figure 3.1 Schematic of jet impingement geometry

3.3 Holography

In this section only the basic principles of double exposure holography are presented for an understanding of the profilometric technique. Detailed principles of holography can be found in Wykes (1980), Vest (1972). The first ever hologram was produced in 1948 by Gabor and the image gave both amplitude and phase information of the original light wavefronts from the object. The production of a hologram required a source of highly coherent light, which became readily available some thirty years ago with the arrival of the LASER. This now makes holography a commonly used technique for the measurement of engineering quantities.

The essentials of making a hologram are simple, where a single beam from a LASER is split into two beams. One beam is known as the object beam, which illuminates the object and the scattered wavefront is captured on a photographic plate. The second beam called the reference proceeds directly from the LASER to the photographic plate. Since both the beams are mutually coherent, they combine and form an interference pattern on the photographic plate. The interference pattern is stored by chemically processing the image on the photographic glass plate which leaves 1000 fringes per millimetre and this is given the name "hologram". The amplitude of light from the object is recorded as the contrast of the fringes since the intensity at the photographic plate is the square of the sum of the amplitudes of the object and reference waves. The phase information is also recorded on the photographic plate as the variation in spacing of the fringes. When the phase difference between the object and reference waves is half a wavelength, the waves cancel and no light is recorded on the emulsion.

To reconstruct the hologram only the reference beam wave is required with the hologram being used as a diffraction grating. The two first-order diffracted waves generated by the grating produces a virtual and a real image. The scattered light from a point on the object is recorded in every part of the hologram and therefore may be viewed from different angles. The reconstruction is therefore a truly three-dimensional image as it contains both the amplitude and phase information of the original beams.

A unique feature of being able to record multiple images on one photographic plate and reconstructing the image only with the reference beam is a powerful concept. Any changes between multiple exposures are identified as correlation fringes. These fringes are the basis behind double exposure holographic interferometry.

3.3.1 Double exposure holographic interferometry

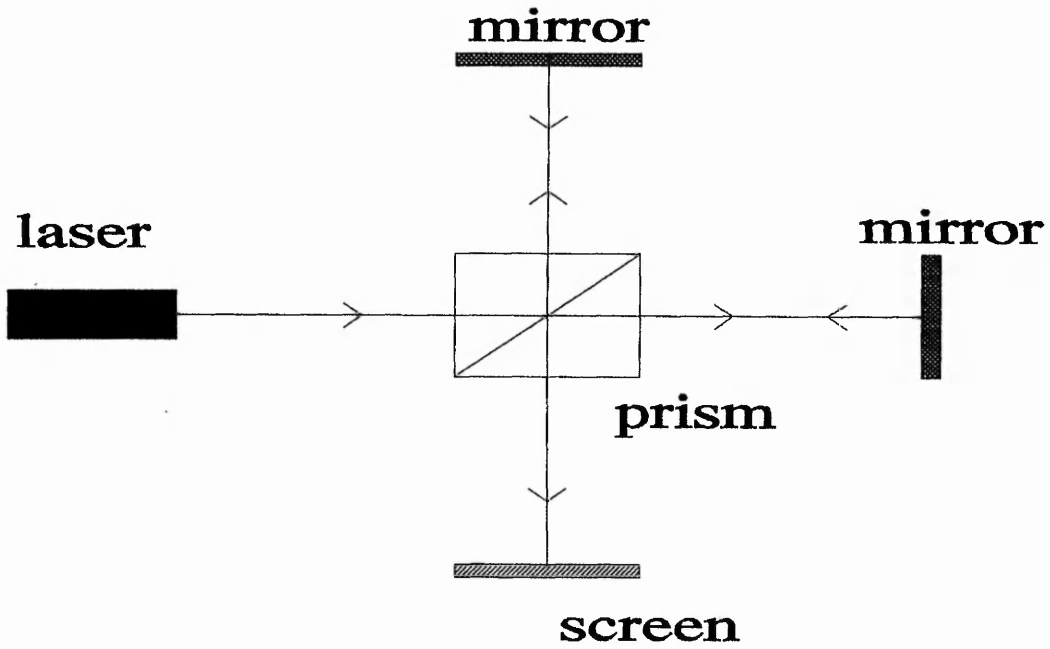

Figure 3.2 Schematic arrangement of the Michelson interferometer

The following description is of the equipment used to produce the holographic interferometer. The stable base for the optics is a table designed for isolation from ground born vibrations. It consists of a large cast iron surface plate placed on concrete pillars that are cast in-situ as it was difficult to transport the assembled table because of its bulky size. The foundation of the table legs is flexible rubber shock absorbers that isolate the table from any vibrations. Vibration characteristics of the table are verified by using a Michelson interferometer Figure 3.2. This set up is placed on the table and any movement of the table is detectable in the interference pattern produced by this arrangement. During the experiments no vibrations are observed confirming a very stable platform for the other optical

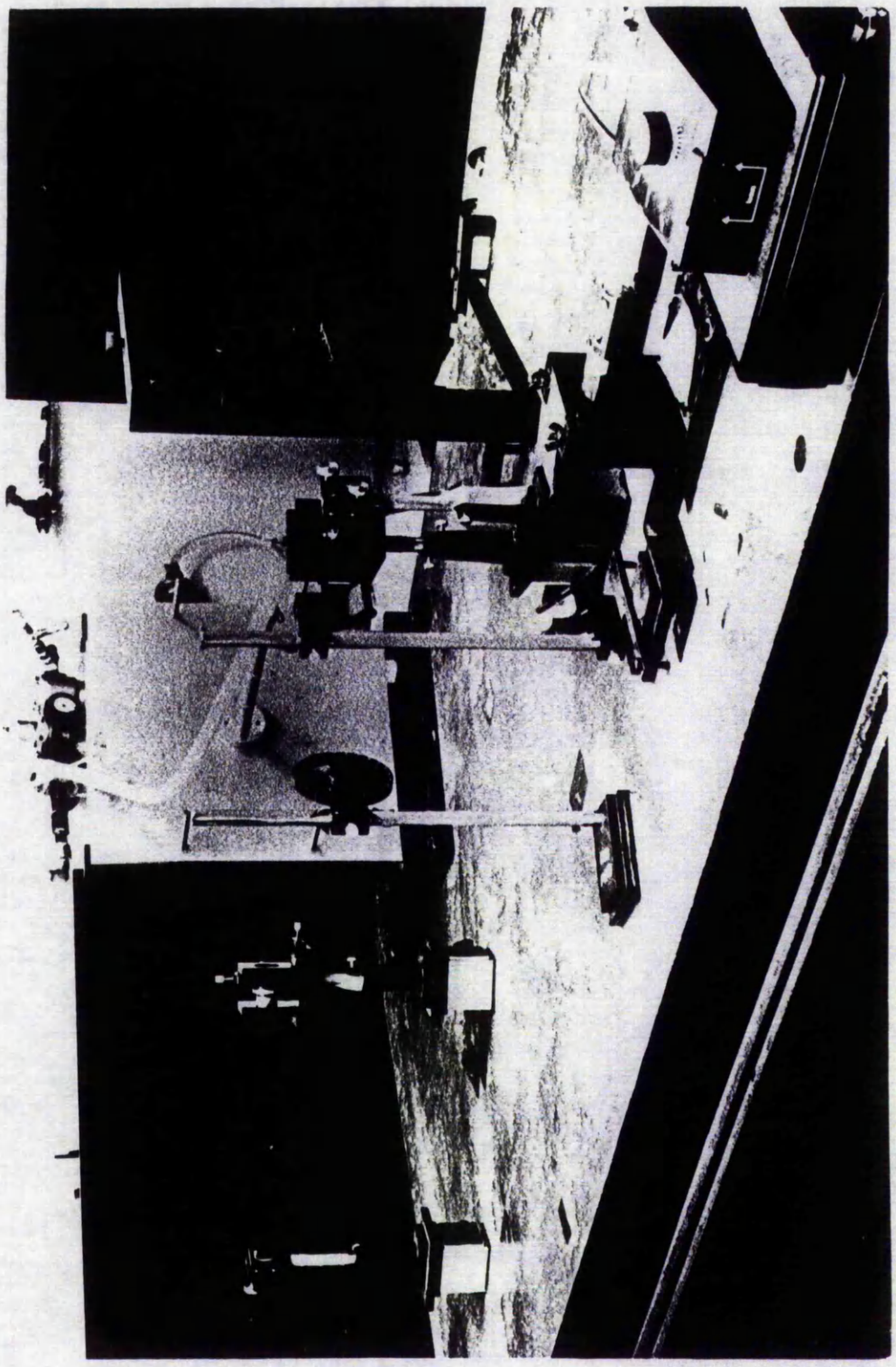

Figure 3.3 Photograph of the double exposure holographic system set up on an optical table

arrangements to be placed on the table.

The present optical layout shown in a photograph in Figure 3.3, Figure 3.4 and schematically in Figure 3.4 for making holograms consists of a Spectra Physics 15 Mw He-Ne LASER mounted horizontally on the table. An Ealing beam steering device is used to alter the working plane of the beams such that the plane is raised to the central height of the vertical test surface. Splitting the beams into two components, an Ealing variable mirrored beam splitter is used so that the beams are split into two beams with varying intensity ratios. After the beams are divided, an Ealing adjustable mirror is placed so that the beams are directed to their appropriate destinations. The reference beam is directed onto the Agfa-Gevaert 10E74 AH photographic plate through an Ealing spatial filter so that any spatial noise in the laser light is filtered. The object beam is directed to the centre of the test plate again through another spatial filter where it is also expanded so that the area of interest on the surface of the test plate is illuminated. The positions of the optical components are determined according to the holo-diagram technique proposed by Abramson (1969,1970). The positioning of the test plate is such that the light reflected back from the surface is incident onto the photographic plate where interference with the reference beam occurs to generate a correlation fringe pattern. The optical paths of the two laser beams from the splitter to the photographic plate are constrained to be of equal lengths. Maximum coherence length of the LASER is utilised and maximum depth of field of the object is obtained. The detailed procedure for producing the fringes and analysing them will be described in the following section.

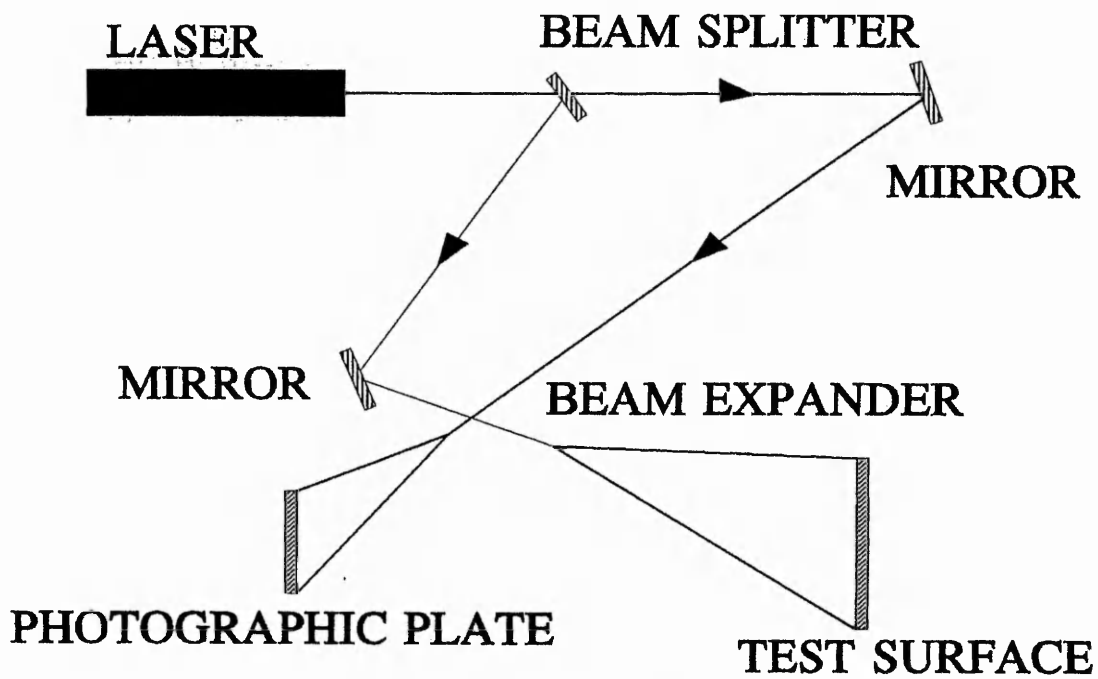

Figure 3.4 Schematic of optical arrangement for double exposure holography

3.4 Experimental procedure

The following sections describe the preparation of the polymer surface and the detailed laboratory procedure needed for producing and reconstructing the interferograms and subsequently making photographs for the analysis stage.

3.4.1 Preparation of swollen polymer surface

The polymer used in the present experimental work are a two part silicon rubber, RTV-615A and the related catalyst RTV-15B both from General Electric. Its composition ratio is 9 parts resin to 1 part catalyst mixed very thoroughly. The test aluminium plate surface is cleaned and prepared by immersion to caustic soda (sodium hydroxide) which etched the surface and created a diffusively reflective texture on the surface, which is ideal for the optical method. To manufacture and cast the polymeric surface, a recess is machined into the aluminium plate to a depth of 0.001 m. The volume of this recess is calculated and with the known density of the polymer material an appropriate mass of polymer is mixed in a

disposable cup. The machined test plate is levelled horizontally on a flat surface table with the aid of three jacking screws and an electronic levelling instrument. The polymer mix is poured into the levelled recess of the plate and with the aid of a spatula the polymer is encouraged to spread uniformly over the flat surface. If air bubbles are created within the poured surface they could be removed by piercing with a sharp tool. The polymer mix requires about 7 days to cure at room temperature. However, the curing process could be accelerated by increasing the temperature of the polymer mix to 65°C, after an initial period of 10 hours at room temperature for the surface to flatten and semi-harden. The time taken for curing is reduced from 7 days to 24 hours. When the polymer has cured to a solid mass it is ready to be used for mass transfer experimentation and is prepared by initial immersion into a chosen swelling agent for 10 hours. This is to ensure that the coating does not detach from the host metal surface and the polymer is swollen to saturation.

The refractive index property of the swollen polymer with temperature has been also been investigated and the findings are presented in Appendix B.

3.4.2 Making a hologram of the impingement plate

A detailed experimental procedure for producing the double exposure holograms is outlined in this section. The optics is arranged as shown in Figure 3.4, uniformly illuminated beam is directed onto the object surface and an adequate reflected illumination from object is collected on the photographic film. The reference beam is expanded by a spatial filter to illuminate the photographic plate with a uniform beam. The limiting intensity ratio of the reference to object beams are reported by Kapur (1973), and is quoted to be less than 16:1 at the photographic plate and this is found to produce satisfactory results. To produce a good hologram, the object surface is positioned so that reflected light is scattered onto the recording plate. The following settings used during the present research are obtained by trial and error. The LASER exposure time of 15 seconds is set on the timer, this is found to produce the right level of illumination on the light sensitive emulsion. The beam splitter is set to give the correct beam ratio necessary for obtaining good

contrast holograms.

To begin the experiment, the impingement plate is removed from the swelling agent and dried thoroughly with lint free tissue and placed on its provided supports. The following procedure is conducted in virtual darkness and therefore familiarity with the operation is essential. Temperature of the laboratory is measured and the room is darkened. An unexposed photographic plate is taken from its light proof storage box and placed into its holder. The apparatus is allowed to reach equilibrium with the laboratory temperature as transient temperature gradients are caused due to handling of the components. The timer toggle switch is engaged and the LASER source is energised for the set amount of time, exposing the light sensitive emulsion. To obtain an interferogram, it is essential to remain motionless during the recording process, so that any disturbance does not register on the interferogram. When the LASER time set expired, it deenergises and the first exposure is completed and recorded on the photographic plate. Next, the confinement plate is placed on its supports and secured in position without the lights in the laboratory. The air flow is started and the convective mass transfer is allowed to take place for the allotted period. When this period is completed, the air flow is stopped. Confinement plate is removed from its supports and the test plate is ready for the second exposure, which is made by energising the laser for the same preset period as the first exposure. The laboratory is kept in darkness when the doubly exposed recording emulsion plate is removed from its holder and developed as described in detail in the following section.

3.4.3 Photographic processing

The photographic processing procedure is described for the holographic plate exposed to the light from the laser and object. A resulting image plate is then developed and fixed so that a permanent record of the image is stored on the emulsion. In the darkened laboratory the photographic plate is removed from its holder and taken to the chemical baths, which have been prepared before the experiment is commenced. The following sequence of processing the photographic negative was found to produce satisfactory results;

- The glass plate is placed in KODAK D19 developer for 2.5 minutes, constant agitation of the developer is necessary so that fresh liquid is introduced to the emulsion. The developer is available commercially in two forms - diluted or powder, the powder is mixed with a 1 to 9 ratio with water at 35°C and allowed to dissolve for a few hours before use. Diluted developer has to be stored in a concertina bottle so that air is eliminated from the bottle before the lid is secured. This is done because the developer oxidises rapidly with air and therefore the shelf life is reduced dramatically if this simple precaution is not taken. The chemical is used with caution as it is harmful and therefore requires disposable gloves to be worn when using these chemicals.
- The next step is to remove the plate from the D19 and wash it in a bath of distilled water for 30 seconds to stop the development process and remove any active developer.
- The plate is removed from the water and placed in a KODAK Universal fixer for 4 minutes again agitating the liquid to distribute the active fluid onto the surface of the emulsion.
- After bathing the plate in the fixer for the allotted time it is again washed in another tray of fresh distilled water for 30 seconds.
- Finally the glass plate is withdrawn from the water and dipped in methyl alcohol for 30 seconds which assists in the removal of unused film from the surface and repels water from the emulsion surface and aids the drying process. The negative plate is allowed to dry in free air for a few minutes for the emulsion to harden and stabilise.

3.4.4 Reconstructed image

A stored image on the holographic negative is reconstructed once the film is allowed to dry, this is done by placing the glass plate back into its holder on the table. The schematic for the optical arrangement shown in Figure 3.5 is used for reconstructing the image.

- The beam splitter is set such that the maximum amount of light is transmitted to the reference beam.

- The object test plate is concealed with dark material so no reflections from it are visible and the beam directed to it is blocked, so that only the reference beam is incident on the photo plate. Viewing the photo plate from the opposite side produces a three-dimensional image of the object.

This reconstructed image is recorded on a photograph as discussed in the next section that is subsequently used for analysis.

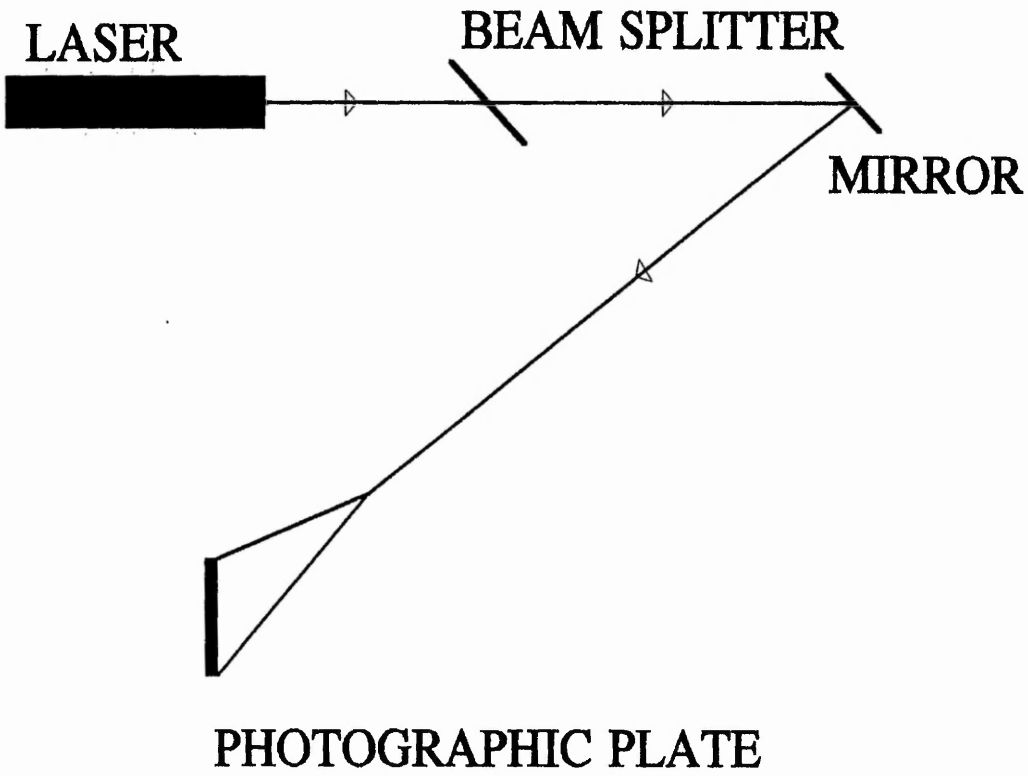

Figure 3.5 Schematic of optical arrangement for reconstruction of double exposure holograms

3.4.5 Photograph of the impingement surface from the hologram

The object image is only visible while the reference beam is directed to the hologram, therefore an ordinary photograph of the image is obtained for the convenience of the analyst for precise spatial measurement of fringe positions. A FUJICA ST705 35mm camera fitted with a 55mm lens is used. It is at a distance of a few centimetres from the holographic plate and the image being about 80 cm distance from the plane of the camera. The camera settings are for 100 ASA film

and the B shutter control setting which allows manual operation of the shutter via a remote trigger. An optimum exposure time is determined to be approximately 30 seconds for the conditions that prevail. It has been found and confirmed in literature that a zoom lens used at 3-4 metres from the holographic plate provides higher magnification pictures of a small area. With a standard lens a larger area is captured with sufficient magnification for the analysis. A typical fringe pattern picture shown in Figure 3.6 is for a laminar jet impingement.

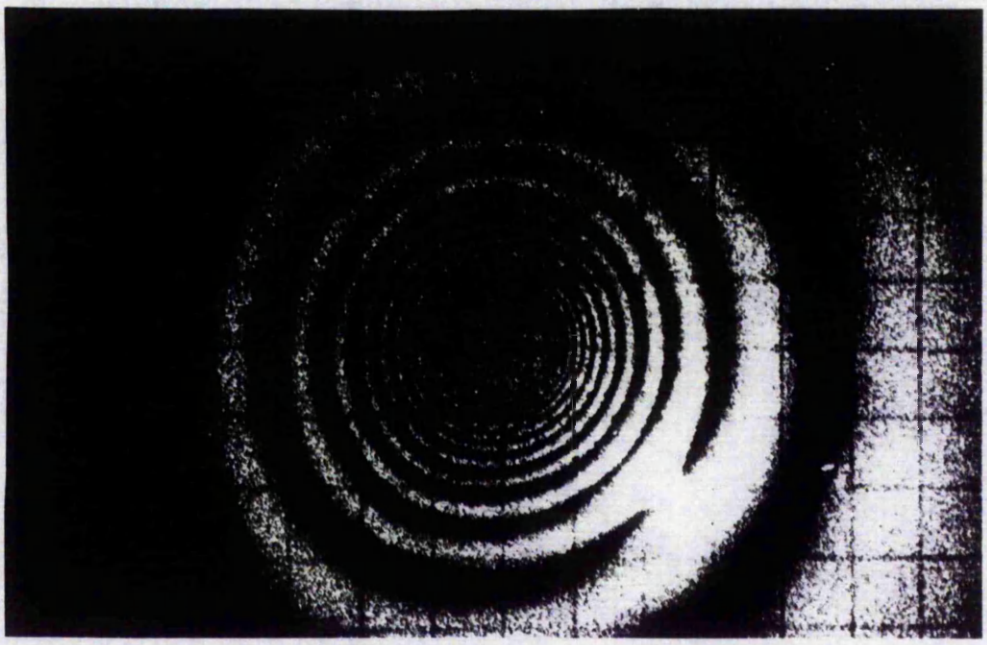

Figure 3.6 Fringe pattern obtained from double exposure holography for laminar jet impingement

3.4.6 Mass transfer coefficient from optical measurements

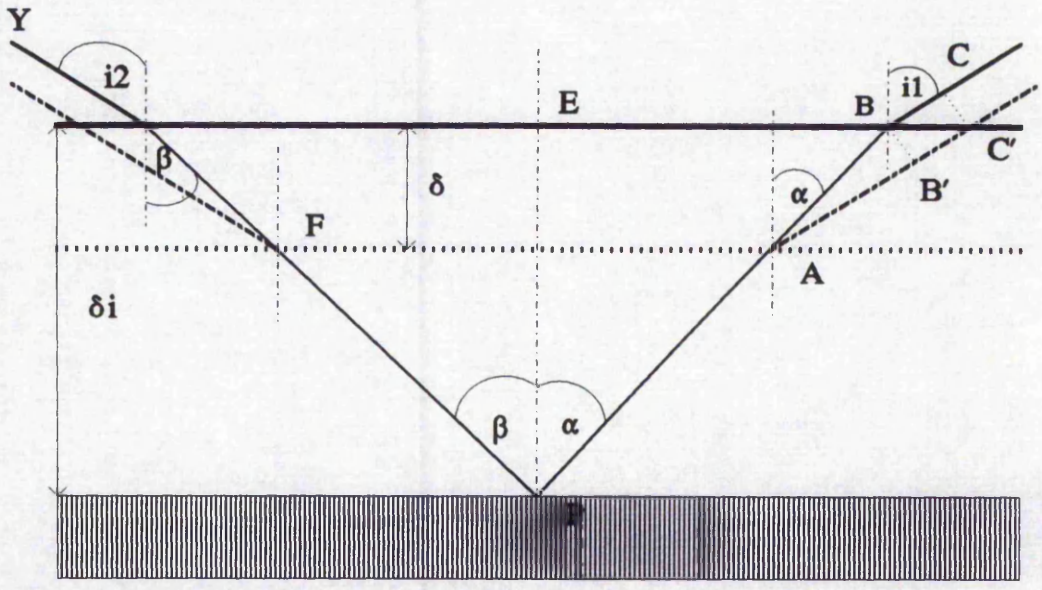

Figure 3.7 Schematic of the optical path through the polymer coating

Analysis of the optical path length and changes of thickness for a transparent coating is shown in Figure 3.7. The equations obtained are summarised from Kapur (1973) as

$$\Delta = \frac{\delta}{\cos\alpha}\left\{ \eta - \cos(i_1 - \alpha)\right\} + \frac{\delta}{\cos\beta}\left\{ \eta - \cos(i_2 - \beta)\right\} \qquad (3.1)$$

where

$$\sin\alpha = \frac{\sin i_1}{\eta} \qquad (3.2)$$

and

$$\sin\beta = \frac{\sin i_2}{\eta} \qquad (3.3)$$

Change in path length is given by $n\,\lambda/2$ where integer n is the fringe order number. Therefore

A fringe order number is given to both light and dark fringes. Each fringe is due to a phase difference of half a wavelength between the two interfering beams of the

$$\Delta = n\frac{\lambda}{2} = \frac{\delta}{\cos\alpha}\left\{\eta - \cos(i_1 - \alpha)\right\} + \frac{\delta}{\cos\beta}\left\{\eta - \cos(i_2 - \beta)\right\} \qquad \textbf{(3.4)}$$

$$n\,\lambda = \delta\,C_o$$

laser light. The identification of fringe numbers is simplified if the surface with no displacement is within the bounds of the illuminated area of the holographic image. For the jet impingement case the time allowed for mass transfer to take place is shortened to ensure that the zero displacement region stays within the field of view. For some tests carried out for longer periods the fringes went beyond the outer region of the polymer surface that made it difficult to identify the order number of the outer most fringes. Rather than guessing the order number, Scholtz and Trass (1963) suggested the method of estimating the recession of the surface at a largest radial distance. This is then substituted into the expression for optical path difference from which n is calculated. The theory is applicable only for the laminar radial wall jet region and is validated by the unconfined wall jet flow. Although the calculated results are not for a confined flow, it is a consistent method rather than just arbitrarily assigning a value to the outer most fringe. Once the outer fringe is designated the rest of the fringes can be consecutively assigned fringe numbers and mass transfer coefficients determined.

The local mass transfer coefficient is given by

$$N = \frac{k\left(V_{ps} - V_{pj}\right)\rho\,M_w}{P} \qquad \textbf{(3.5)}$$

where N is the mass flux, ρ is the molar density

3.5 The experimental test range

The axisymmetric semi-confined jet impingement geometry described in section 3.2 has the following parameters summarised in Table 3.1

- The nozzle diameter is 3.1 and 4.9 mm.
- The nozzle to plate separations *z/d* of 2, 4, 6, 8, 10 and 12.
- The laminar jet *Re* are 500, 1000, 1500 and 2000
- The turbulent nozzle *Re* are 3000 to 60000.

- Preliminary test to identify the duration times for the mass transfer experiments, a series of trials is undertaken for the 4.9 mm nozzle with *Re* of 1500 and duration times of 2, 3, 4, 6, 8 minutes.

	z/d	*z/d*	*z/d*	*z/d*	*z/d*
Re	2	4	6	8	12
500	+	+			
1000	+	+	+		+
1500	+	+	+	+	
2000	+	+	+	+	
3000	+	+	+		+
5000	+	+	+		+
6000	+	+	+		+
8000		+	+		+
10000	+	+	+		+
12000	+		+		+
15000	+				
20000			+		
21000	+		+		+
35000	+		+		+
42000	+				+
52000	+		+	+	+
60000	+		+	+	+

Table 3.1 Range of tests that have been completed using swollen polymer and Holography

The analysis is carried out using a computer program presented in Appendix G for calculating the mass transfer coefficients from the fringe pattern by using the equations and available physical properties Appendices A and B.

3.6 Estimation of uncertainty in measured physical quantities

Measurement uncertainties are estimated for all the experimental quantities measured in the current experimental work.

- The estimated errors encountered are for the measurement of the laminar flowrates and these are read on the flowmeter to an accuracy of a quarter unit on the scale.
- The flow metering used for the turbulent flow from the nozzle is an orifice meter, which has an uncertainty of one unit of the water manometer used to measure the pressure differential generated on either side of the orifice restriction.
- The uncertainty associated with the spatial determination of the fringe position from the photographic record of the fringe pattern, has an uncertainty of 0.5 $x10^{-3}$ m in the radial direction.

The calculation of the mass transfer coefficient for the radial fringe data measured by holography requires the following physical properties of the swelling agent.

- The vapour pressures for a temperature range from 18° to 35°C for ethyl salicylate has been determined by Zangeneh (1990). The uncertainty quoted for the technique used is about 15 per cent.
- The air side diffusion coefficient for ethyl salicylate in air is obtained from the Lennard-Jones equation, which has been used by Kapur and Macleod (1975) and Golizadeh (1992) with an uncertainty of 10 per cent.
- The diffusion coefficients obtained in the current research are documented in Appendix A. However the uncertainty band for these values are estimated to be ± 50 per cent. Therefore using these highly uncertain results is not justified and so for the calculation purposes the theoretical data is used from Kapur (1973).

These estimated error are used in the error analysis method described in the following section.

3.7 The Monte-Carlo method for estimation and calculation of error for the physical quantities

All derived quantities from the experimentally measured values have been assigned estimated uncertainty limits, determined by a numerical simulation technique called the Monte-Carlo method. This statistical analysis is chosen because both the mean and the uncertainty limits are obtained using the data reduction equation, which is simulated with the estimated tolerances randomly distributed within this tolerance band. The reduction equation is repeatedly simulated with these random tolerances until a sufficient number of data populations have been obtained. This sample population is plotted on a frequency histogram. Uncertainty limits with 95 per cent confidence can be obtained by taking 2.5 percentiles from either end of the distribution tail. The benefits of the method are;

- No knowledge of the distributions of the final calculated values is assumed.
- No terms have to be neglected as required by the Taylor series.
- The effect on the results due to the inter-relationships of the independent variable are taken care of automatically.
- The significance of one or more of the independent quantities is identified.
- The statistical analysis coding is completely independent from the main data reduction procedure.

3.7.1 The Monte-Carlo method

The Monte-Carlo statistical method is utilised in the following way. A larger number of random samples are generated for each of the measured quantities within its own randomly distributed tolerance.

Histograms of these samples are plotted and these present the overall distribution type. The uncertainty limit is obtained from the histogram by finding the resultant quantities from either end of the distribution curve. The practical way to adopt this method is to store the calculated quantities in a vectored memory array. Then sort this array in an ascending order and choose the desired confidence limit from the top or the bottom of the array. Although this is a highly ineffective use of

computing power and memory, it is the most convenient.

3.7.2 The Monte-Carlo simulation equation

A random number R is generated between 0 and 1, using which two values of the measured quantity with an error of ± U, where U is the estimated error in the measured quantity.

x_i = R * 2 * U + measured value - U

x_i+1 = (1-R) * 2 * U + measured value - U

Mean value of sample simulation is calculated from

$$x_m = \sum_{i=1}^{i=n} \frac{x_i}{n} \tag{3.6}$$

where n is the number of samples

The standard deviation of statistical samples is

$$s = \sqrt{\left(\frac{\left(\Sigma x_i^2 - n x_m^2 \right)}{n} \right)} \tag{3.7}$$

The following methodology is used in two programs generated to estimate the uncertainty in the measured quantities and the derived mass transfer correlation equations. Both programs are presented in Appendices H and I.

3.8 Correlation equation of the mass transfer coefficients

The experimental results had been correlated in the form established from a non-dimensional analysis of the flow type first determined by Schlichting (1966), namely

$$Sh = a\ Re^{\,b} \left(\frac{r}{d}\right)^{c} \left(\frac{z}{d}\right)^{d} \tag{3.8}$$

where (the *Sh* is a function of *Re*, *r/d* and *z/d)*. The mass transfer data is converted using the Chilton-Colburn analogy to heat transfer data by the relationship *Nu* =

$Sh\ (\ Pr\ /\ Sc\ )^{1/3}$. Both heat and mass transfer convection in boundary layer flows is controlled by the same mechanism. Therefore, the *Nu* correlation equation is of the same functional type and the proportionality constant is the only quantity affected

$$Nu = f\ Re^{\ b} \left(\frac{r}{d}\right)^{c} \left(\frac{z}{d}\right)^{d} \tag{3.9}$$

where f = c $(\ Pr\ /\ Sc\ )^{1/3}$

3.9 Physical properties for the analysis of the mass transfer coefficients

3.9.1 Vapour pressure of ethyl-salicylate in air

The following property equations are found from various publications. Dominant property is the vapour pressure of ethyl salicylate which have been investigated by various researchers, with the most recent being Zangeneh (1990) who used an UV absorption spectrophotometry technique to obtain the vapour pressure correlation. The spread in data by various workers is large but Zangeneh's results are the closest to the widely recognised results of Paterson et al (1987). This affirms confidence in the results because the two methods used by each worker are completely different. From Zangeneh (1990)

$$\ln V_p \left(\frac{N}{m^2}\right) = 27.8 - \frac{7650}{T} \tag{3.10}$$

Paterson et al (1987) gives

$$\ln V_p \left(\frac{N}{m^2}\right) = 24.6 - \frac{6706}{T} \tag{3.11}$$

Kapur (1973) gives

$$\ln V_p \left(\frac{N}{m^2}\right) = 22.4 - \frac{6567}{T} \quad \textbf{(3.12)}$$

Law (1984) uses the following as originally provided by Masilyah (1974, 1976, 1979).

$$\ln V_p \left(\frac{kN}{m^2}\right) = 7.897 - \frac{2931.6}{T} \quad \textbf{(3.13)}$$

3.9.2 Diffusion coefficient of ethyl-salicylate in air

$$D_f \left(\frac{cm^2}{\text{sec}}\right) = -0.516 + 0.000367 * T \quad \textbf{(3.14)}$$

The coefficients have been obtained from Kapur (1973) which are calculated using the Lennard-Jones expression and the results are correlated into the above equation (3.14).

3.9.3 The density and refractive index of the polymer swollen with ethyl-salicylate

The density given by the manufacturer for unswollen polymer that has not been immersed in ethyl salicylate is 1.02 kg/m^3. The immersion into ethyl salicylate of density of 1.131 kg/m^3 does not increase the combined density significantly and therefore the value used in the analysis of the mass transfer data is 1.02 kg/m^3.

Refractive index was measured experimentally and the results are presented in Appendix B, summarised here by the correlation equation (3.15) obtained from the experiments and used for the analysis of mass transfer coefficients. The equation for the refractive index is determined with respect to the temperature only.

$$R_f = 1.48 - 0.00017 * T \quad \textbf{(3.15)}$$

CHAPTER 4
INTRODUCTION TO NUMERICAL PREDICTIONS

For the laminar impingement flows Sholtz and Trass (1970), Glauert (1956), and Schlichting (1966) have produced analytical solutions of the transfer rates for the laminar impingement and wall jet regions. However, it is not possible to solve the whole flow domain with these analytical approaches. Therefore, numerical techniques to solve the differential equations are the only other feasible alternative.

This chapter reports a brief introduction into the numerical approach used in the current research. The preparation of the model and solution method of the algebraic equations are discussed. A brief review of the software language used, is included. Finally the convergence technique employed and the grid independency study with calculation of the transfer rates is shown.

The flow field within the two confinement surfaces arising from both laminar and turbulent incompressible jets issuing from the upper confinement surface and impinging normally on the lower impingement surface are numerically investigated using PHOENICS. The heat transfer distributions in the impingement region are predicted for a fully developed exit jet velocity profile for Re = 100 to 60000 and z/d = 2 to 12.

An survey of numerical packages available showed PHOENICS to be the most adaptable for the current research. The PHOENICS input language proved to be most versatile when setting up the model. Another advantage with the package was that a number of turbulence models already existed within the main core of the code and access was also available to the user to add further models if he so desired. The main use for the current work was the potential for adding self written coding to the package, which would allow the output to be manipulated in any desired form. The fundamental equations being modelled numerically by the package are presented in the next section.

4.1 Governing differential equations

The governing equations for a steady axisymmetric flow are

Continuity:

$$\frac{1}{r}\frac{\partial}{\partial r}(rv) + \frac{\partial w}{\partial z} = 0 \tag{4.1}$$

Momentum :

$$\rho\left(v\frac{\partial v}{\partial r} + w\frac{\partial v}{\partial z}\right) = -\frac{\partial p}{\partial r} + \mu\left(\frac{\partial^2 v}{\partial r^2} + \frac{1\partial v}{r\partial r} + \frac{\partial^2 v}{\partial z^2} - \frac{v}{r^2}\right) \tag{4.2}$$

$$\rho\left(v\frac{\partial w}{\partial r} + w\frac{\partial w}{\partial z}\right) = -\frac{\partial p}{\partial z} + \mu\left(\frac{\partial^2 w}{\partial r^2} + \frac{1\partial w}{r\partial r} + \frac{\partial^2 w}{\partial z^2}\right) \tag{4.3}$$

Energy:

$$\frac{1}{r}\left[\frac{\partial}{\partial r}(\rho rvT) + \frac{\partial}{\partial z}(\rho ruT) - \frac{\partial}{\partial r}\left(r\frac{K}{C_p}\frac{\partial T}{\partial r}\right) - \frac{\partial}{\partial z}\left(r\frac{K}{C_p}\frac{\partial T}{\partial z}\right)\right] = 0 \tag{4.4}$$

Turbulence: Kinetic energy

$$\rho\frac{Dk}{Dt} = \frac{1}{r}\left\{\frac{\partial}{\partial z}\left[r\left(\mu + \frac{\mu_T}{\sigma_k}\right)\right] + \frac{\partial}{\partial r}\left[r\left(\mu + \frac{\mu_T}{\sigma_k}\right)\frac{\partial k}{\partial r}\right]\right\} + G - \rho\epsilon \tag{4.5}$$

Dissipation of kinetic energy

$$\rho\frac{D\epsilon}{Dt} = \frac{1}{r}\left\{\frac{\partial}{\partial z}\left[r\left(\mu + \frac{\mu_T}{\sigma_\epsilon}\right)\frac{\partial \epsilon}{\partial z}\right] + \frac{\partial}{\partial r}\left[r\left(\mu + \frac{\mu_T}{\sigma_\epsilon}\right)\frac{\partial \epsilon}{\partial r}\right]\right\} + C_1\frac{\epsilon}{k}G - C_2\rho\frac{\epsilon^2}{k} \tag{4.6}$$

where

$$G \equiv \mu_T \left\{ \left(\frac{\partial w}{\partial r} + \frac{\partial v}{\partial z} \right)^2 + 2 \left[\left(\frac{\partial w}{\partial z} \right)^2 + \left(\frac{\partial v}{\partial r} \right)^2 + \left(\frac{v}{r} \right)^2 \right] \right\} \quad (4.7)$$

The above equations are transformed into more generalised form for a universal approach to be utilised for the solution procedure. The general form of the transport equation is

$$\frac{1}{r} \left[\frac{\partial}{\partial r}(\rho r v \phi) + \frac{\partial}{\partial z}(\rho r u \phi) - \frac{\partial}{\partial z}\left(r \Gamma \frac{\partial \phi}{\partial z} \right) - \frac{\partial}{\partial r}\left(r \Gamma \frac{\partial \phi}{\partial r} \right) \right] = S_\phi \quad (4.8)$$

4.2 Computational geometry

A brief description of the jet impingement model provided here consists of an axisymmetric nozzle of diameter d, the exit plane of which is flush with the confinement plate shown in Figure 4.1. The jet emerges from the nozzle with a mean velocity w_{jet} and impinges perpendicularly on to an impingement plate. This is parallel with the confinement plate and at a non-dimensionalised distance of *z/d*. Both the confinement and impingement walls extend radially to $r/d = 7$ to the outflow region. The whole flow domain is symmetric about the nozzle centre line.

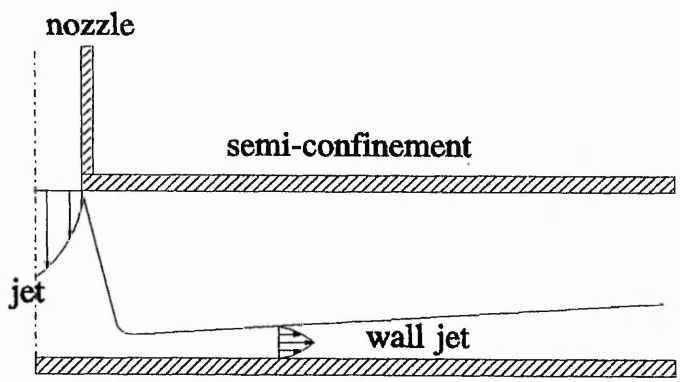

Figure 4.1 Jet impingement geometry

4.3 Computational boundary conditions

The following boundary conditions are applied to simulate the semi-confined jet impingement flow field.

Boundary I - The impingement wall. Type of condition imposed at this surface is impermeability and constant temperature.

$W1 = 0$, $V1 = 0$, $T = T_w$, $K = 0$ and $\epsilon = 0$ at $z/d = z_{max}$

Boundary II -

The nozzle exit. The definition of the characteristic isothermal fully developed or flat jet velocity profiles at exit of the nozzle are applied.

Developed

$$w_{jet} = \frac{2Re\mu}{\rho d}\left(1-\frac{4r^2}{d^2}\right) \qquad (4.9)$$

or for a flat jet profile

$W1 = w_{jet}$, $T = T_{jet}$,

$K = w_{jet}^2 * 0.01 / 4$ and $\epsilon = K^{3/2} / (d * 0.1643 / 2)$ at $z/d = 0$

Boundary III -

The axis of symmetry at the nozzle centre line

$V1 = 0$ at $r/d = 0$

Boundary IV -

The semi-confinement wall

$W1 = 0$, $V1 = 0$ at $z/d = 0$ $K = 0$ and $\epsilon = 0$ at $z/d = 0$

Boundary V -

The domain outflow region

$p = 0$ at $r/d = 7$

4.4 Discretisation methodology

Differential equations (4.1) to (4.8) are solved numerically using a commercially available finite volume software. The integration of the equations leads to following form of finite difference equations (FDE's)

$$a_P\Phi_P = a_N\Phi_N + a_S\Phi_S + a_E\Phi_E + a_W\Phi_W + a_H\Phi_H + a_L\Phi_L + a_T\Phi_T + b \quad (4.10)$$

To close the above set of equations, specific boundary conditions are imposed to complete the FDE's. These are inserted by the software as additional contribution to the source term. A system of algebraic equations is generated then solved using slab wise linear solver. The solution algorithm used, is a modified version of SIMPLE, which is given the acroymn SIMPLEST. A description of the basic methodology is provided by Patankar (1980) with the modifications amplified in the lecture notes CFDU HTS/80/1. A brief summary of SIMPLE is given here, with the essential steps

- The pressure field is guessed
- The velocity is determined
- The continuity errors are calculated from the velocity
- These errors give some guidance to the corrections required for the velocity and pressure fields
- The pressure corrections are obtained by solution of a set of equations
- The coefficients represent dependence of mass flow rates on pressure differences

4.5 The solution

A solution of the jet impingement model is carried out using a propriety finite volume software named PHOENICS. The software is developed primarily to solve Computation Fluid Dynamic (CFD) problems for industrial and commercial users because no other comparative system was available. Recent developments in computer power, storage and generalisation of the mathematical approach, has

brought forth other numerical techniques in CFD. These are finite element methods and boundary element methods, which are still in their infancy with respect to CFD. The codes are developing very rapidly and are generally more accomplished for preprocessing. The code allows the model mesh to be generated in a superior way compared with the structured mesh requirements for the finite volume technique. Fortunately, the current jet impingement configuration under study is rather simple to setup with a structured grid generator.

The input to the package until recently required an experienced programmer of the software. This is because the software has its own programming language known as (PIL) PHOENICS Input Language. The structure of the language and the set up of the complete package makes it possible to model an enormous variety of numerical simulations and therefore the necessary complexity of the input language. A diagrammatic representation of the PHOENICS computer code is shown in TR/100 beginners guide. The boundary conditions are activated by inclusion of command lines and these boundaries have to be defined precisely, i.e. the type of boundary and how it is to be simulated within the software.

The software package has an on-line help facility that provides a series of lecture panels on CFD modelling and a comprehensive dictionary of all the PIL commands. This program is called "GUIDE" and contains a library of test cases that is to be used as a starting point for new models to be created.

The input commands could be generated in two ways, with the ultimate objective of creating a series of command lines stored in an ASCII format file called the "Q1" file. The first method for generating a "Q1" file is by using the interactive mode of a program called "SATLIT". Alternatively, the other method is to use an external ASCII text editor. This latter method is normally used by experienced PHOENICS users, who do not require on-line help with the commands. The "Q1" text file cannot be submitted to the "EARTH", the PHOENICS solver. It must first be transformed into a form, which the solver can accept. The converted file is produced by the "SATLIT" program and is given the name "EARDAT.DAT". The equation solver "EARTH" cannot be accessed directly by the user and therefore

changes cannot be made to the solution algorithm. Specialist features can be added via a user interface "GROUND" subroutine or existing ones can be used. The user can create his own FORTRAN coding to manipulate the solved variables that are accessible from the "EARTH" core. After performing numerous solution iterations to satisfy convergence, the final output from the solver is stored in two files. The first is an ASCII file, "RESULT.DAT" and the second is a condensed machine code file, "PHIDA.DAT". The latter file is used for post processing of the results that can be presented in text or graphical forms. This is done with either "PHOTON" or "AUTOPLOT", these are a further two integrated parts of the software contained within the PHOENICS package.

4.6 Pre-processing

To create the numerical model the first task was to define a model by its geometric grid arrangement, material properties and boundary conditions. For the current model an axisymmetric geometry is generated by creating a structured nonuniform mesh by defining the number of Y and Z direction cells with their appropriate dimensions, using the commands "YFRAC", "ZFRAC" or the "GRDPWR" commands. These commands allow geometric progression of the grid spacing within the requested ordinal direction. A detailed description of the PIL grid generation commands is obtained from the TR/200 PHOENICS user manual. The axisymmetric coordinate system is initialised by using the command "CARTES = FALSE" in the command file. This signals to the PHOENICS software that a non-Cartesian geometry is being initialised and therefore the alternative Cylindrical coordinate system is activated. The grid defined is a structured mesh because of the limitation of the finite volume technique. Fortunately, the geometry of the axisymmetric impingement jet and its associated boundary conditions are relatively simple to specify. For curved and complex geometries the Body Fitted Coordinate system needs to be used allowing curvilinear boundaries of the geometries to be modelled. The structured grid still needs to be maintained for the finite volume method.

For the current axisymmetric jet impingement geometry, the grid cells are

generated using the PIL command language, using the coordinate variables "YFRAC", "ZFRAC". These commands are used in combination known as the method of pairs. The odd numbered "YFRAC" array contain the number of Y cells and the even number "YFRAC" array contains the width of the cells. This method allows some flexibility in variation of the cell spacing which is totally at the discretion of the users.

Fluid medium and its physical properties are set by the following system variables "ENUL", "RHO1", "PRNDTL()", which are respectively viscosity, density and Prandtl number. The input values to these variables are in SI units.

The PIL commands used for setting the inflow, outflow and wall boundary conditions are "PATCH" and "COVAL". The "PATCH" command defines the region of the mesh that is to be assigned a particular boundary condition. It also defines the type specification of boundary, e.g. "INLET", "OUTLET", "WALL" etc. The corresponding "COVAL" command imposes a coefficient and a constant to that "PATCH" command. For example the coefficient may be "FIXP", "FIXFLU", "FIXVAL", "ONLYMS" etc. these being reserved constants pre-defined within PIL.

The PIL commands described above are common to both laminar and turbulent modelling of the impingement flow. However turbulent flow model requires two further variables to be simulated, namely kinetic energy (k) and dissipation of kinetic energy (ϵ). There are choices of using two other turbulence models but the one chosen here is considered to be the best for mixing flows of the kind being simulated. The PIL command to activate the turbulence modelling is "TURBMOD(KE)", which is translated by SATLIT into several commands which store and solve the two variables k and ϵ. The values given to the inlet nozzle have been obtained from separate numerical predictions of pipe flows for long lengths so that full-developed conditions are simulated. These predictions near the exit of the pipe are used as the input state for the nozzle in the impingement model. The turbulent Prandtl number is specified by the command "PRT()". Typical commands files are presented in Appendices C and D for laminar and turbulent semi-confined

jet impingement models respectively. The following section describes the approach used for obtaining the solutions from the PHOENICS code.

4.7 Model solution (Solution phase)

Once the model is generated with the input language it is compiled and submitted to be processed by the solver "EARTH". The ranges of model test parameters to be solved are numerous and therefore cannot be run interactively on the available VAX 8000 series mainframe computer. The solutions are obtained by overnight runs in batch queues. Large numbers of solution iterations are required to obtain convergence and require vast amounts of computer time. To avoid wastage of computer time with wrong or erroneous solutions, preliminary runs using the interactive approach are used with limited numbers of iteration. The solutions are then interrogated for stability, divergence and continuity. Once satisfied that the solution is converging further solution iterations are submitted to the batch queue. A further method for reducing the computer usage time is to use converged solutions as a starting point for all similar models, rather than starting the solution from an initially guessed pressure and velocity field. This accelerates the solution process because the starting flow field is almost converged and therefore the solution process is minimised. If the models are approaching a solution, it is necessary to implement some convergence criteria discussed in the following section.

4.8 Convergence criteria for the numerical solution

The algebraic equations have been solved using an iterative approach as the variables are all coupled. As the solution process requires a large number of iterations it is necessary to monitor convergence regularly to avoid unnecessary usage of computer time. When the model is submitted to the VAX for interactive runs, the monitoring output from the solver is displayed on the visual display unit. The output is echoed to a log file if the job is run on the batch queue. The following monitoring information is provided, i.e. residual sums of the pressure and temperature equations and the residual sums of the velocity equations. The

residual sum of the pressures has a physical significance namely the volumetric continuity error of each cell summed over the whole field. Observation of the changing value of this residual during every iteration sweep and defining the tolerance setting can give an indication of convergence. Using the following PIL command as an example to set the tolerance for convergence of pressure is "RESREF(P1) = 10^{-4} ". The solution of the variable is stopped when the sum of the residuals reaches this value. When the residual sums for all the variables being solved fall below their pre-defined tolerance values, the solution of the system of equations is terminated. The required continuity of all the flow quantities is taken to be satisfied for the flow domain when all the tolerances have been reached. Some similar criteria to the convergence of the velocity and temperature equations are applied.

4.9 Grid independency study for laminar jet impingement

Numerical predictions are only as accurate as the input conditions used when setting up the model. The grid distribution is one important condition that contributes to the inaccuracy and therefore a grid dependency study is necessary to minimise its effect on the solution .

Predictions for jet impingement flow are obtained for the grid dependency study using a nonuniform, 15 x 158 grid arrangement, 15 cells parallel to the plates, 158 cells parallel to the jet centre line. A nonuniform grid spacing allows a finer grid spacing in region of steeper gradients, i.e. near the impingement wall and adjacent to the jet centre line, a typical grid distribution for the laminar case is given in Figure 4.2.

The grid dependence is assessed by studying wall friction factors on the impingement surface with grid size at the near wall region of the flow see Jambunathan et al (1989). This optimised grid size is then used for further predicted work. If the grid size has to be changed to accommodate alterations in the geometry then this change cannot affect the predictions of the flow. The flow and geometric conditions chosen to assess grid independency are Re = 1000, z/d =

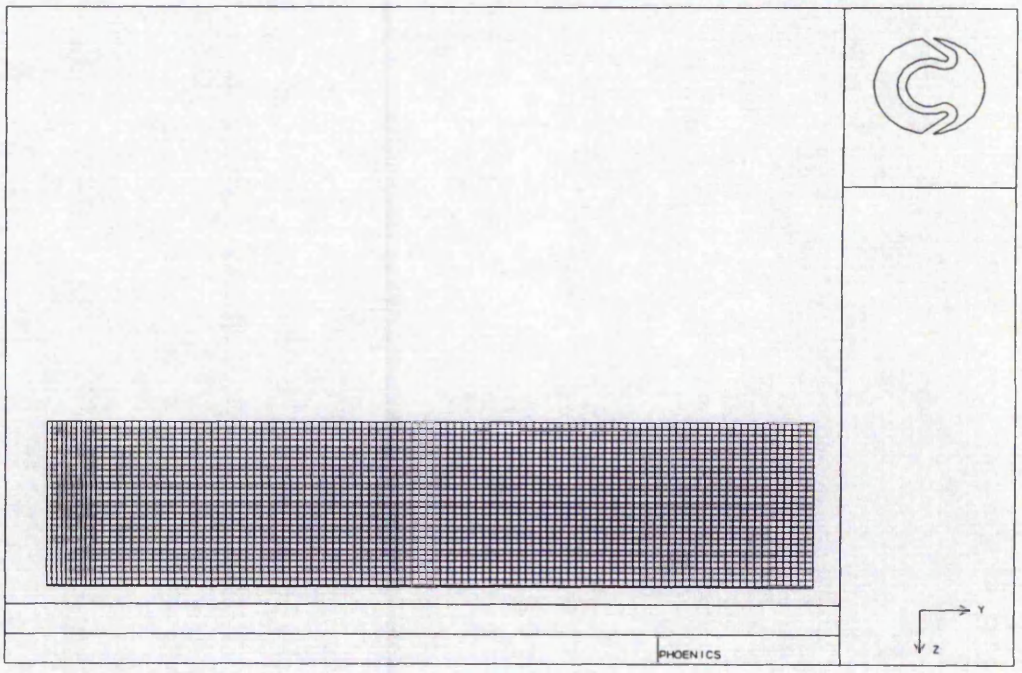

Figure 4.2 Grid distribution used in modelling

2 and the out flow boundary distance or semi-confinement bounds at $r/d = 37.5$ from the jet centre line. The grid spacing at the wall is modified as it is the critical region of the flow. The following ranges of grid spacings at the wall are selected for the analysis and they range from 0.00125 to 0.125 non-dimensionalised with a nozzle size $d = 4$ mm. The optimum size is assessed to be 0.0075 d which had a 3 per cent maximum error in the wall friction factor that is obtained from Figure 4.3.

The optimum grid size chosen at the wall interface of the impingement surface from all further analysis work in the laminar flow regime is in the range of 0.005 to 0.0075 d. The grid size in the main stream flow areas away from the walls are varied over a greater range to accommodate the various z/d spacings that have to be imposed for the parametric study. One important condition that is adhered to is that of the cell aspect ratio which is not to exceed a 1 : 10 ratio limit as this is the suggested maximum in TR/100 PHOENICS beginners user guide. This outflow

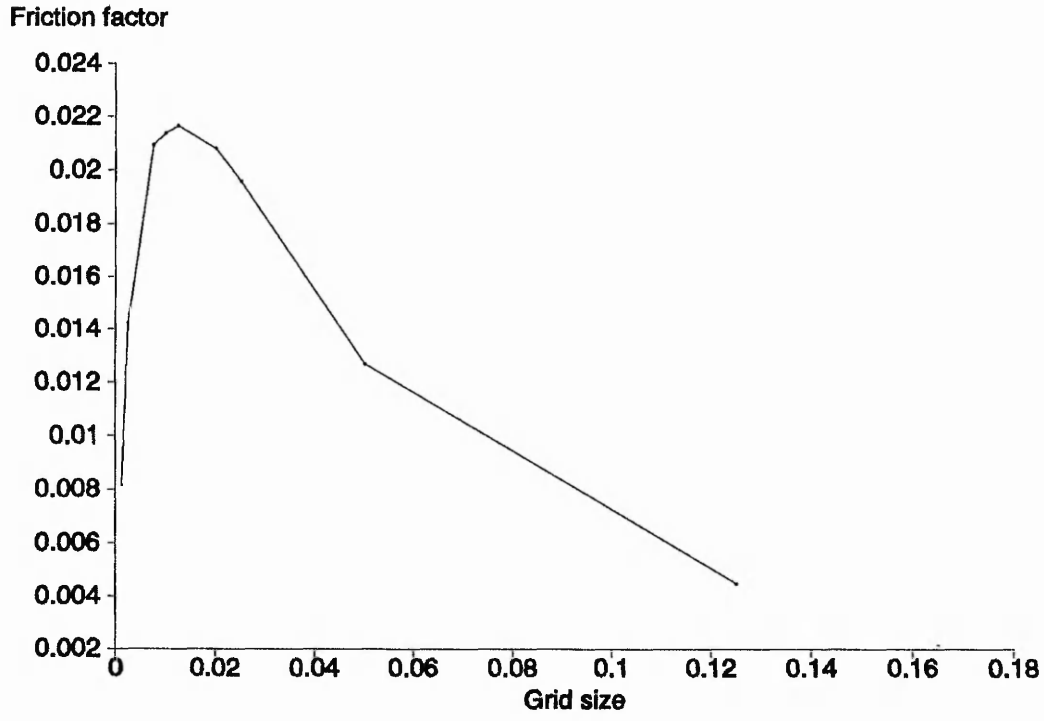

Figure 4.3 Friction factor against grid size, for Reynold number of 1000 and z/d = 2

region condition is met by shortening the model for both the laminar and turbulent flow conditions to 8 *d* from the nozzle centre. If this is not implemented the computational size of the model would have been significantly increased to meet the aspect ratio condition. The associated computer time and memory resources would have proportionately had to increase to get a converged solution.

4.10 GROUND code calculation of heat transfer coefficient

The standard flow velocities, pressures and temperatures can be obtained from the "EARTH" solver. If however, derived quantities are needed from the standard flow variables a postprocessing code has to be included into the "GROUND" subroutine specifically to calculate the shear stresses and heat transfer coefficients at the wall boundary, listed in Appendix E. Two calculation methods are proposed for evaluation of the heat transfer coefficient at the wall surface. The first method is an energy balance method applied to the wall interface. To calculate the heat

transfer coefficient at the wall by equating the heat conducted into the fluid to the heat convected away by the fluid on a cell by cell basis along the wall boundary. The second method which is again based on energy balance, but here the energy transfer to the fluid is calculated by the difference in summation of the heat energies in adjacent slabs. This would then be equated to convected heat transfer from the surface. The latter method would only be used in the parabolic type flows as the main flow direction and the heat energy convection is known. For the current situation of a semi-confined impingement jet the former method needs to be adopted as the flow within the wall is highly elliptic and therefore the heat energy convection is multi-directional.

For this approach the conducted heat transfer at the wall is calculated at the first cell adjacent to the wall. Using Fourier's law for one dimensional conduction the required thermal gradient is determined from the temperature difference between the first cell node next to the wall and the constant wall temperature divided by half the cell width. A function is provided within PHOENICS code for calculating the thermal gradient, but this is not used. The gradient is averaged in all directions and therefore an underestimated value is obtained when compared to the thermal gradient existing at the wall interface.

A skeleton "GROUND" subroutine is provided in the PHOENICS code in which the user can interface with the "EARTH" solver. The above mentioned calculation approach is coded using FORTRAN programming language and the necessary flags within the skeleton code changed so that the user code is used. It is only necessary to calculate the heat transfer values at the final iteration sweep of the temperature equations. Therefore, a flag for the sweep number and variable being solved is monitored to indicate which sweep the solver is currently operating at. When it has entered the last sweep, then only does the user interface activate. This helps reduce, the CPU time used and any unnecessary calculations that have to take place in the earlier sweeps.

For the laminar impingement flow, shear stresses are defined at the wall interface by $\tau = \mu$ (dv/dz). The PHOENICS system provides a standard "GREX1"

activated function "FNDVDZ". This function "FNDVDZ" calculates an averaged gradient around the cell faces, which gives an underestimated value of the velocity gradient at the wall interface. The velocity gradient dv/dz is obtained from the user "GROUND" subroutine written specifically for that purpose. The coding has been implemented in the same manner as the coding for heat transfer coefficient. The velocity control cells are staggered by half a cell due to the velocities being located at the cell faces. To model the wall in PHOENICS, the velocity at the high node is set to zero and the velocity *V1* on the north face of the control cell is solved. The velocity gradient at the wall is then determined by dividing *V1* by half the cell height.

Access to all the geometric and flow variables from user "GROUND" code is possible using the standard subroutine provided such as "GETYX" and "SETYX". This has been updated in the latest PHOENICS version 1.6 by allowing direct access to the F-array. This F-array is a single array that stores all the "EARTH" solved variables. The approach to accessing the variables is not used as the coding has already been written using the functions provided in the earlier version 1.4 of the code. The user has total control over the variables once retrieved from the F-array which means that the user code can output the data in any format that is desired by the user. Therefore all the derived quantities are written to formatted ASCII files that are then read directly into a graph plotting package.

The heat transfer data for the turbulent flow is extracted from the numerical model by interrogating the F-array for the wall Stanton number at the wall "PATCH" and using this value to calculate the *Nu*. The coding is listed in Appendix E within the same ground code used as for the laminar flow.

CHAPTER 5
EXPERIMENTAL AND NUMERICAL RESULTS FOR LAMINAR FLOW

5.1 Laminar unconfined jet impingement

5.1.1 Theoretical background to mass transfer for laminar flow

This section reports on the validation of the experimental and optical arrangements by studying mass transfer in an unconfined laminar impingement surface using the swollen polymer surface and the holographic interferometry techniques. These techniques are used to obtain mass transfer data in semi-confined jet impingement and further tests are conducted to confirm repeatability of the experimental procedure. The following physical quantities are investigated for the semi-confined flow;

- Re = 500 to 2000
- z/d = 2 to 12

The resulting experimental mass transfer data are regressed into the most appropriate type of correlation equations found by the nondimensional analysis of the flow by Schlichting (1968). Since the flow regimes that exist show boundary layer characteristics, the correlation equation proposed is of the form Sh = func (Re, r/d, z/d, Sc). The experimental mass transfer data are statistically regressed to obtain correlations equations of the form discussed earlier. These equations are subjected to the Monte-Carlo uncertainty analysis to quantify the uncertainty limits in the equation.

Comparisons are made with results obtained by a theoretically exact solution derived by Glauert and is given in Scholtz and Trass.

$$h_m = 0.426 \left(\frac{D_f}{r}\right) Re^{3/4} [-g'(0)] \left(\frac{d}{r}\right)^{1/4} \psi \qquad \textbf{(5.1.1)}$$

Equation (5.1.1) is a theoretically derived solution and is corroborated by Scholtz and Trass with experimental tests for limited test conditions. Their experimental Sc is significantly different from the present experimental value. A more practical

$$\psi = \left[1 + 0.2337\ x\ 10^{-3}\ Re\ \left(\frac{d}{r}\right)^3\right]^{-0.75} \quad \textbf{(5.1.2)}$$

equation (5.1.3) is obtained using an approximate solution and is only valid within the wall jet region for a radial range of $2.5 < r/d < \infty$.

$$Sh = 0.159\ Sc^{1/3}\ Re^{3/4}\ \left(\frac{r}{d}\right)^{-5/4} \quad \textbf{(5.1.3)}$$

The region between $0.7 < r/d < 2.5$ is called the transition region and is given some consideration and correlation (5.1.4) is obtained by Scholtz and Trass (1970).

$$Sh = 0.757\ \left(\frac{r}{d}\right)^{-0.86}\ Re^{0.5}\ Sc^{-0.361} \quad \textbf{(5.1.4)}$$

For the stagnation point region $r/d < 0.7$ the following equation (5.1.5) is derived from a theoretical analysis.

$$Sh = 1.648\ Re^{0.5}\ Sc^{0.361} - 1.081\ Sc^{0.025}\ \left(\frac{r}{d}\right)^2\ Re^{0.5}\ Sc^{0.361} \quad \textbf{(5.1.5)}$$

The mass transfer *Sh* are transformed into heat transfer *Nu* by invoking the established Chilton/Colburn analogy for stagnation flows, namely

$$Nu = \left(\frac{Pr}{Sc}\right)^{\frac{1}{3}} \quad \textbf{(5.1.6)}$$

5.1.2 Validation of the optical setup and the swollen polymer technique

The following section reports on the comparison between the current experimental tests for laminar unconfined jet impingement and theoretical solutions available. This is to validate the experimental technique and use it to investigate different geometric arrangements.

$$Sh = \frac{k\ d}{D_f} \quad \textbf{(5.1.7)}$$

Mass transfer coefficients in the wall jet region due to an unconfined impingement jet were obtained and transformed into *Sh* using the definition given in equation (5.1.7)

The local mass transfer k is defined by

$$N = \frac{k\,(V_{ps} - V_{pj})\rho M_w}{P} \qquad \textbf{(5.1.8)}$$

where N is the mass flux from the surface due to convection, ρ is the molar density of the gas mixture, M_w is the molecular mass of the swelling agent and P is the atmospheric pressure. The partial vapour pressures of the swelling agent, V_{ps} and V_{pj} are at the polymer surface and at the exit of the nozzle respectively.

If both semi-confined and unconfined air jet impingement is considered, then V_{pj} = 0 and the V_{ps} are the partial vapour pressure of the swelling agent V_{po} during the so called "constant rate period" and equation (5.1.8) simplifies to equation (5.1.9)

$$N = \frac{k\,V_{po}\,\rho\,M_w}{P} \qquad \textbf{(5.1.9)}$$

The mass flux N, is also determined from the coating shrinkage given by

$$N = \frac{\delta\,\rho_s}{t} \qquad \textbf{(5.1.10)}$$

where δ is the change in coating thickness, ρ_s is the density of the swollen polymer and t is the duration time of the mass transfer experiment. It is also shown from equation (3.4) that $\delta = n\,C_o\,\lambda$, therefore substitution into equation (5.1.10) gives

$$N = \frac{n\,C_o\,\lambda\,\rho_s}{t} \qquad \textbf{(5.1.11)}$$

Defining $A = C_o\,\lambda\,\rho_s$ then equation (5.1.11) is transformed into

$$N = A\left(\frac{n}{t}\right) \qquad \textbf{(5.1.12)}$$

where A is a calibration constant for a particular optical and experimental arrangement. The definition of *Sh* is defined in equation (5.1.7) and combining

with equations (5.1.9) and (5.1.12) gives

$$Sh = \left(\frac{A\,P}{\rho_o\,V_{po}\,M_w}\right)\left(\frac{d}{D_f}\right)\left(\frac{n}{t}\right) \qquad \textbf{(5.1.13)}$$

To evaluate the *Sh* using equation (5.1.13) the following physical quantities are required; the properties of the working fluid, the calibration constant A, the local fringe numbering and the duration time of the mass transfer experiment.

5.1.3 Discussions of results

The following section reports on the comparison of experimental mass transfer data for unconfined wall jets and comparable results obtained from theoretical solutions for similar flows. This comparison is to validate the experimental technique for more mass transfer experiments. By determining the calibration constant, A the experimental arrangement is corroborated. The unique value of the constant, A in equation (5.1.13) is dependent on the optical arrangement and is obtained by studying mass transfer in unconfined laminar impinging jet. The constant A, is obtained by equating the theoretical wall jet *Sh* of Scholtz and Trass (1963) equation (5.1.3) with the current reduced experimental equation (5.1.13). When equations (5.1.3) and (5.1.13) are equated the following expression (5.1.14) for an unconfined wall jet is produced, which is used to obtain the value for constant A. The graph of n against $t^*Re^{0.75}*(r/d)^{-1.25}$ is plotted for the experimental results, the gradient for the line obtained is 0.000185 and by substituting the physical properties that can be found in Appendices A and B, the value of A is calculated to be 3.72e-4.

$$0.159\,Sc^{1/3}\,Re^{0.75}\,(r/d)^{-1.25} = \left(\frac{A\,P}{\rho_o\,V_{po}\,M_w}\right)\left(\frac{d}{D_f}\right)\left(\frac{n}{t}\right) \qquad \textbf{(5.1.14)}$$

Alternatively, another approach is used to find the value for A by using the optical arrangement, i.e. the angles of the beams, laser wavelength and density of the swollen polymer. The value for C_o in equation (3.4) is calculated as 0.57 and therefore using the definition $A = C_o\,\lambda\,\rho_s$, the value for A is equal to 3.62 e-4.

The values for the constant A are within 3 per cent of each other. The main reason for the discrepancy is due to the uncertainty associated with the determination of the gradient from the graph.

A plot of the current experimental *Sh* for nozzle *Re* = 1000 with two nozzles of 3.1 mm and 4.9 mm for an unconfined axisymmetric impingement jet shown in Figure 5.1.1 are compared to the theoretical wall jet and transition region solutions of Scholtz and Trass equations (5.1.3), (5.1.4) and the experimental results obtained by Gholizadeh (1992). Gholizadeh used real time holography and the swollen polymer technique, to obtain mass transfer data for *Re* = 1055 to 1200. Gholizadeh's wall jet *Sh* are 30 to 40 per cent higher when compared to the Scholtz and Trass's correlation equation (5.1.3). The present mass transfer results for the two different nozzles investigated, are within 10 to 15 per cent of Scholtz and Trass's wall jet correlation equation (5.1.3). The *Sh* within the transition region are 10 to 15 per cent lower in value when compared with equation (5.1.4). Transition region results from Gholizadeh's work are consistently 10 to 30 per cent higher than the theoretical predictions. Gholizadeh's stagnation point results are within 3 per cent when compared with Scholtz and Trass's equation (5.1.5) .

A plot of the present *Sh* for unconfined impingement with different *Re* = 1000 and 2000 with nozzle sizes of 3.1 mm and 4.9 mm are shown in Figure 5.1.2. The present wall jet *Sh* shows good agreement when compared with equation (5.1.3) but underestimates the theoretical within the transition region. It can be concluded that the current results confirm the experimental technique being validated with the widely accepted theory, which is regarded as the reference work by numerous researchers in the literature.

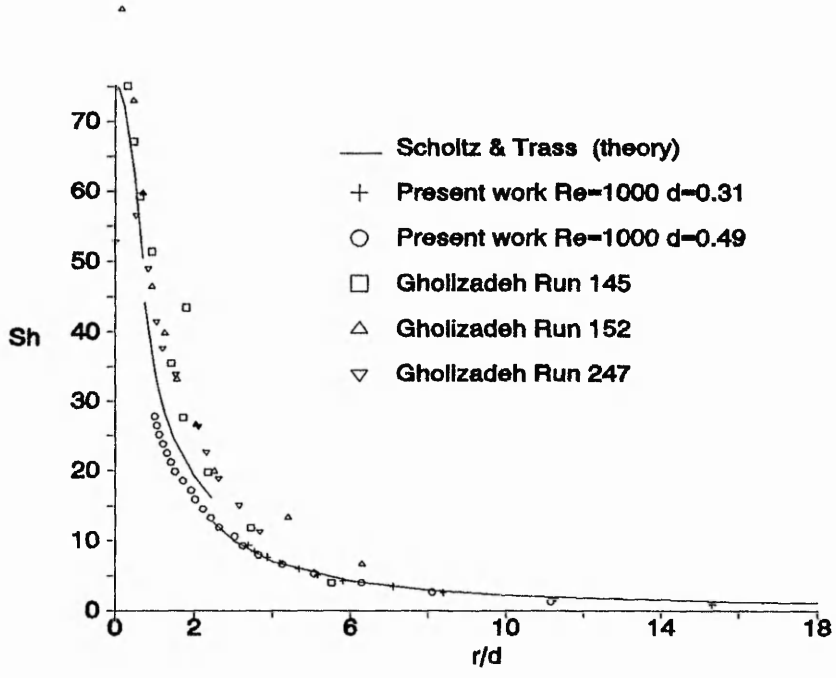

Figure 5.1.1 *Sh* versus *r/d*, *Re* = 1000 and *z/d* = 2 for unconfined jet impingement

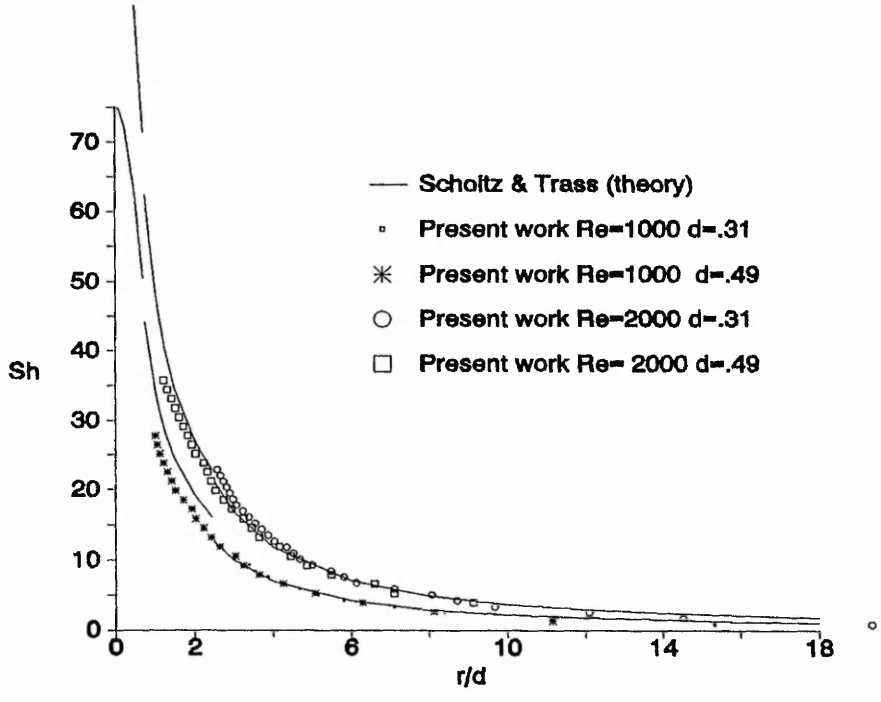

Figure 5.1.2 *Sh* versus *r/d*, *Re* = 1000 and 2000 for unconfined jet impingement with nozzle diameters = 3.1 mm and 4.9 mm

5.2 Laminar semi-confined jet impingement

5.2.1 Repeatability of experimental results

The following section reports on a set of experimental trials to confirm the repeatability of the experimental technique and that the mass transfer mechanism does not change with the duration times of the experiments. The physical geometry used for the current tests is the semi-confined impingement configuration and is to be used for all subsequent tests. Physical quantities selected for testing are, Re = 1500, z/d = 4 and the nozzle size d = 4.9 mm. Two replicate sets of the current experiments are carried out. The Sh obtained are plotted in Figure 5.2.1 and Figure 5.2.2 compared to the theoretical solutions of Scholtz and Trass (1970) equations (5.1.3), (5.1.4) and (5.1.5). The following experimental duration times of 120, 180, 240, 360 and 480 seconds are investigated. Results are plotted to show Sh against the radial position for which the trends of the mass transfer distributions are unaffected by the time span of experiment, although the quantities are scattered due to the uncertainty in the experimental technique. The plot of fringe order number against radial position on log scales shown in Figure 5.2.3 and Figure 5.2.4 demonstrate that the mechanism of the mass transfer is unchanged for the longer duration experiments and that the fringe order numbering of the fringe patterns is consistent.

5.2.2 Mass transfer distribution

The following section reports the experimental mass transfer in a semi-confined jet impingement flow for various z/d spacing and laminar Re. The range of nozzle Re investigated are 500, 1000, 1500 and 2000 which are all assumed to be laminar in nature.

The Sh distribution for Re = 500 is shown in Figure 5.2.5 with z/d = 2 and 4, it shows that the experimental values for z/d = 2, are different from the corresponding theoretical values calculated from equations (5.1.3), (5.1.4) and (5.1.5). In the wall jet region, r/d > 2.5, the Sh are up to 67 per cent higher when

compared to the correlation (5.1.3). For the transition region, $0.7 < r/d < 2.5$, the experimental *Sh* are 9 per cent lower than the values of equation (5.1.4). The radial *Sh* distribution obtained for $z/d = 4$ produce similar trends to those discussed for the $z/d = 2$ case but the percentage difference from the theory is about 30 per cent in the wall jet region.

Sh distribution for $Re = 1000$ is shown in Figure 5.2.6 for $z/d = 2$, 4, 6, and 12 with the equations (5.1.3), (5.1.4) and (5.1.5). The experimental wall jet, *Sh* for $z/d = 2$ is 30 per cent lower when compared to the theory. The *Sh* distribution for the other z/d presented shows a definite link with separation distances. Increasing z/d seems to reduce the difference to 10 per cent less than theory in the wall jet region and in the transition region the difference is 20 per cent lower than the theory.

Sh distributions for $Re = 1500$ and $z/d = 2$, 4, 6 and 8 are plotted in Figure 5.2.7. For higher $z/d = 6$ and 8, it is found in the wall jet region that the *Sh* are lower by as much as 50 per cent compared to the theory. For $z/d = 2$ the wall jet *Sh* are 29 per cent higher than the theoretical values, this difference reduces to 10 per cent in the transition region. The *Sh* distributions for all z/d are asymptotic to the wall jet theory from $r/d > 4$ from the stagnation point. The transition region, *Sh* distribution for all the z/d shows good comparison to be within 5 per cent of the theory.

The results of the experimental *Sh* distributions for $Re = 2000$ and for $z/d = 2$, 4, 6 and 8 is shown in Figure 5.2.8. These results show that for the $z/d = 2$ the wall jet *Sh* are 50 per cent lower than theory. This changes to over prediction from theory in the transition region by about 7 per cent. For $z/d = 6$ and 8, the wall jet *Sh* distributions are 30 per cent lower which changes to 15 per cent in the transition region.

5.2.3 Correlation equation from experimental data

The *Sh* obtained from the mass transfer experiments are transformed into heat transfer *Nu* using the Chilton/Colburn analogy $Nu = (Pr/Sc)^{0.4}\, Sh$. The *Nu* are

then entered into a statistical computer package called MINITAB, where a multiple regression technique is used to produce correlations of the *Nu* with the following predictors of *Re*, *r/d* and *z/d*. The data is also selectively regionalised into three parts such that the correlations reflect whether radial location is in the wall jet or the transition region. The following general form of the correlation is produced.

$$Nu = a\ Re^{\,b} \left(\frac{r}{d}\right)^{c} \left(\frac{z}{d}\right)^{d} \qquad \textbf{(5.2.1)}$$

Multiple variations on the correlation equations extracted from the experimental results are summarised in the Table 5.1. The main radial categories are the wall jet $r/d > 2.5$, the transition region, $r/d < 2.5$, and whole field, $0 < r/d < \infty$. The other variations selected for subsequent correlations are listed in Table 5.1. Most practical and useful correlation produced from the experimental results is for the wall jet region and transition region. The wall jet correlation is plotted on a $\log(Nu/(0.254*Re^{0.734}\ (z/d)^{-0.139}))$ against $\log((r/d)^{1.42})$ scale with the corresponding experimental data in Figure 5.2.9, this shows all the experimental data is unbiased and well scattered around the correlated line. Figure 5.2.10 contains the same data but with a different scale $\log(Nu/(Re^{0.734}))$ against $\log((r/d)^{1.42})$. This serves to show the effect due to *z/d* separation on the correlation equation. The spread of data from each other shows there is some functional dependence of *z/d* on the *Nu*.

The exponent of the *Re* within the wall jet varies from 0.323 to 0.831, which encompasses the theoretically predicted value of 0.75. It should be noted that the *Re* exponent is approaching the value of 0.8 found for boundary layer flow, but it must be made clear that the *Re* is based on the nozzle diameter and not the distance from the a datum point as it is in boundary layer flow. The high *Re* and large *z/d* tends to reduce the exponents value. The radial variation exponent varies from -1.36 to -1.66 and supports the theoretical value of -1.25. The larger the *z/d* the greater is the deviation from the expected values.

Reynolds	r/d	z/d	a	b	c	d
500-2000	0 - ∞	2 - 12	0.21	0.714	-1.24	-0.122
500-2000	< 2.5	2 - 12	0.156	0.714	-0.811	-0.121
500-2000	> 2.0	2 - 12	0.252	0.718	-1.36	-0.130
500-2000	> 2.5	2	0.177	0.757	-1.39	-
500-2000	> 2.5	2 - 12	0.254	0.734	-1.42	-0.139
500-1000	0 - ∞	2 - 12	0.119	0.779	-1.25	-0.019
500-1000	> 2.5	2 - 12	0.252	0.708	-1.44	0.01
500-1000	< 2.5	2 - 12	0.1	0.761	-0.772	-0.055
1500-2000	> 2.5	2 - 12	3.94	0.384	-1.42	-0.225
1500-2000	< 2.5	2 - 12	2.57	0.341	-0.796	-0.137
1500-2000	0 - ∞	2 - 12	1.95	0.425	-1.24	-0.176
500-2000	0 - ∞	8 - 12	219.2	-0.059	-1.35	-0.665
500-2000	> 2.5	8 - 12	6.35	0.323	-1.66	-0.089
500-2000	< 2.5	8 - 12	692.3	-0.137	-0.818	-1.11
500-2000	0 - ∞	2 - 4	0.0898	0.811	-1.22	0.0235
500-2000	> 2.5	2 - 4	0.099	0.831	-1.38	0.066
500-2000	< 2.5	2 - 4	0.079	0.799	-0.844	-0.007

Table 5.1 Table of heat transfer correlations for the various regions and parametric limits

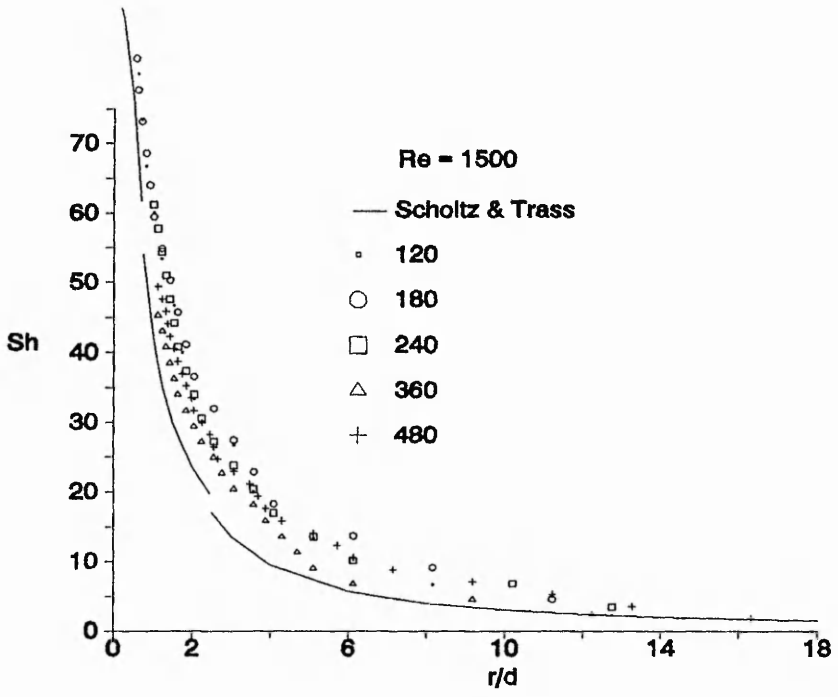

Figure 5.2.1 *Sh* versus *r/d*, *Re* = 1500 and *z/d* = 4 for experiment time t = 120, 180, 240, 360 and 480 s for semi-confined jet impingement

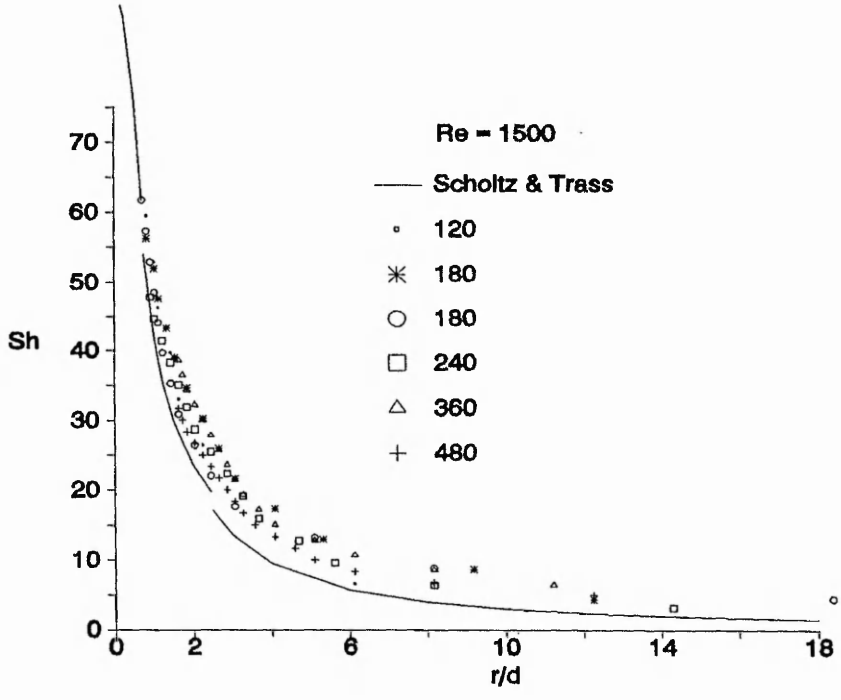

Figure 5.2.2 *Sh* versus *r/d*, *Re* = 1500 and *z/d* = 4 for experiment time t = 120, 180, 240, 360 and 480 s for semi-confined jet impingement (repeat)

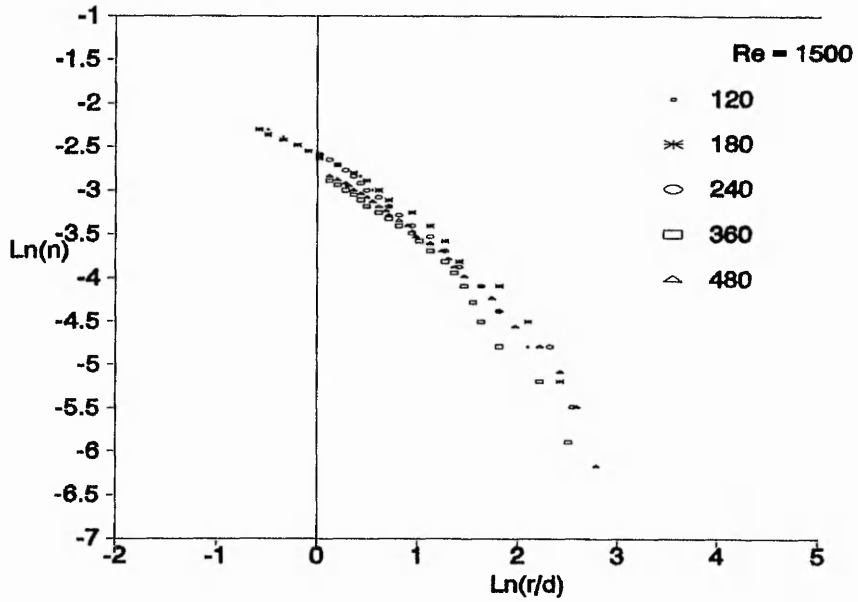

Figure 5.2.3 Fringe order number versus *r/d*, *Re* = 1500 and *z/d* = 4 for experiment time t = 120, 180, 240, 360 and 480 s for a semi-confined jet impingement

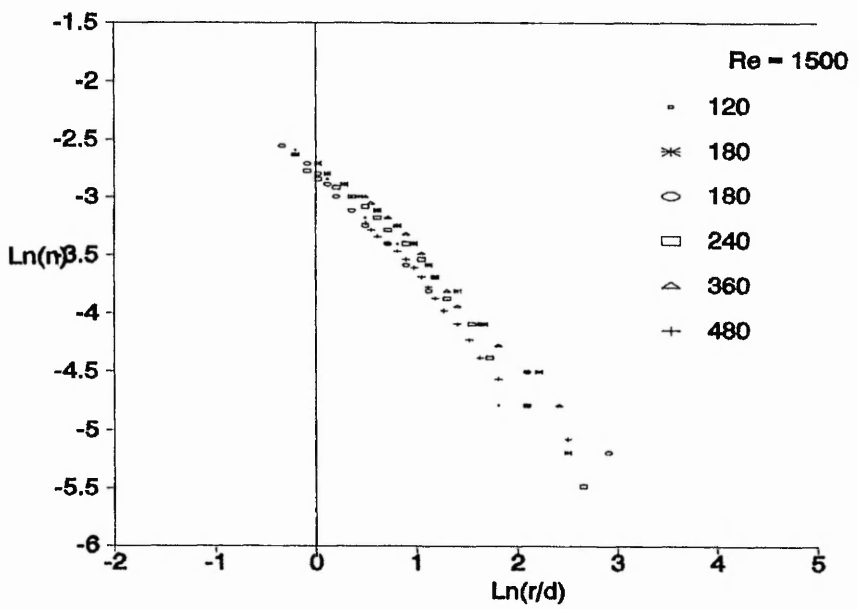

Figure 5.2.4 Fringe order number versus *r/d*, *Re* = 1500 and *z/d* = 2 for semi-confined jet impingement (repeat)

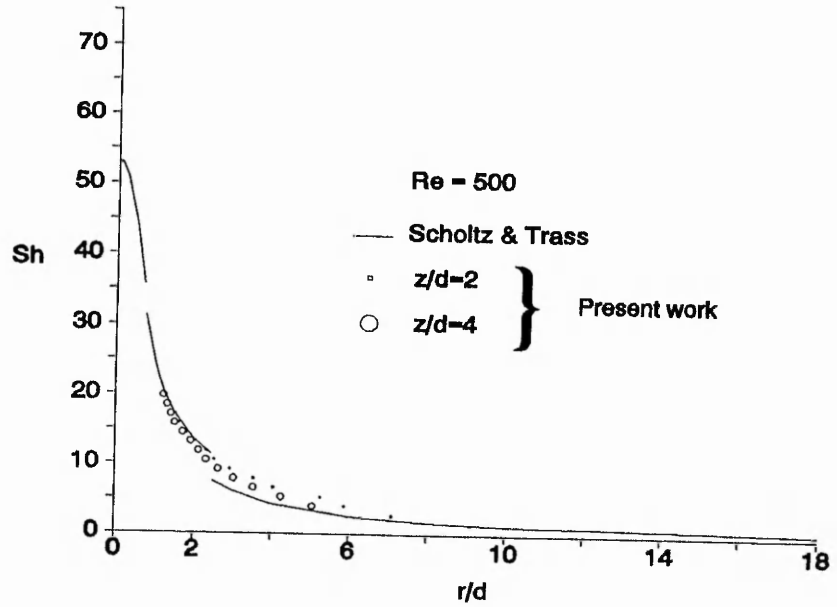

Figure 5.2.5 *Sh* versus *r/d*, *Re* = 500, *z/d* = 2 and 4 in semi-confined jet impingement

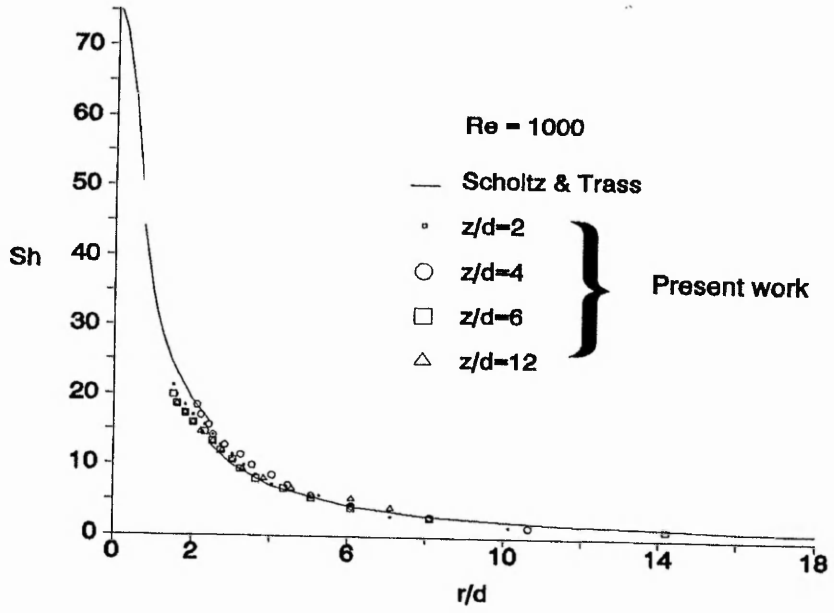

Figure 5.2.6 *Sh* versus *r/d*, *Re* = 1000 and *z/d* = 2, 4, 6 and 12 in semi-confined jet impingement

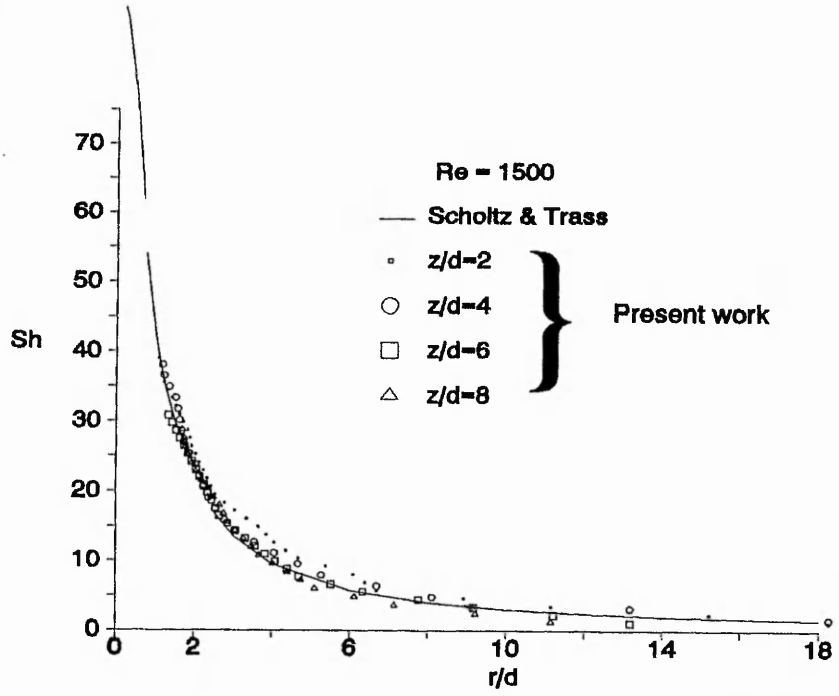

Figure 5.2.7 *Sh* versus *r/d*, *Re* = 1500 for *z/d* = 2, 4, 6 and 8 in semi-confined jet impingement

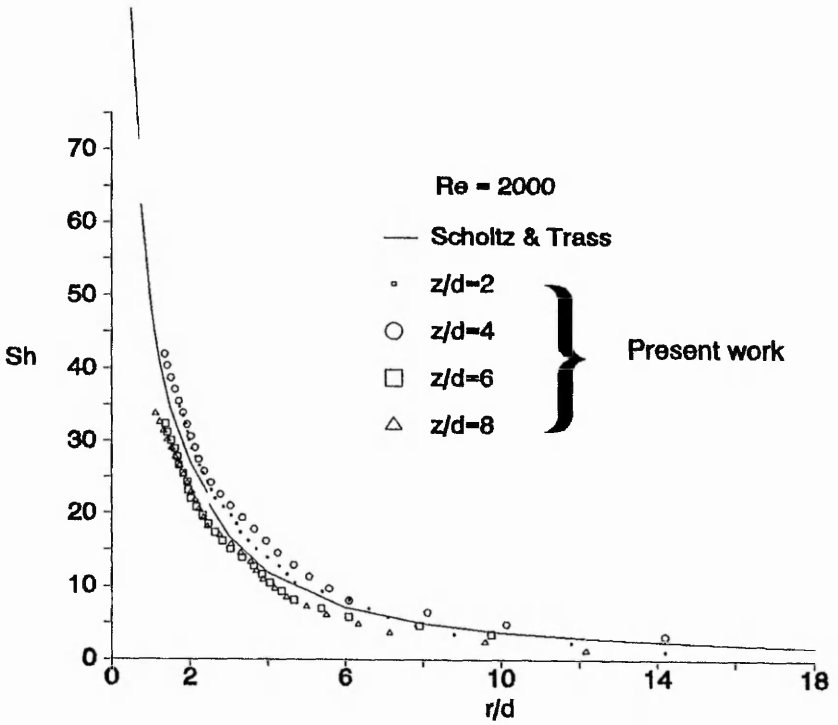

Figure 5.2.8 *Sh* versus *r/d*, *Re* = 2000 for *z/d* = 2, 4, 6 and 8 in semi-confined jet impingement

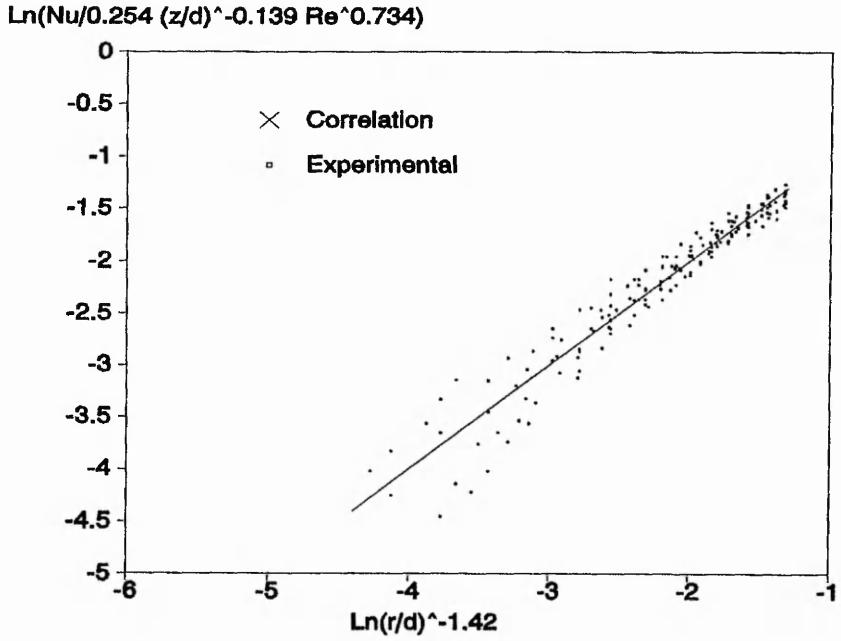

Figure 5.2.9 Experimental wall jet *Nu* versus *r/d* with regression equation for laminar semi-confined jet impingement

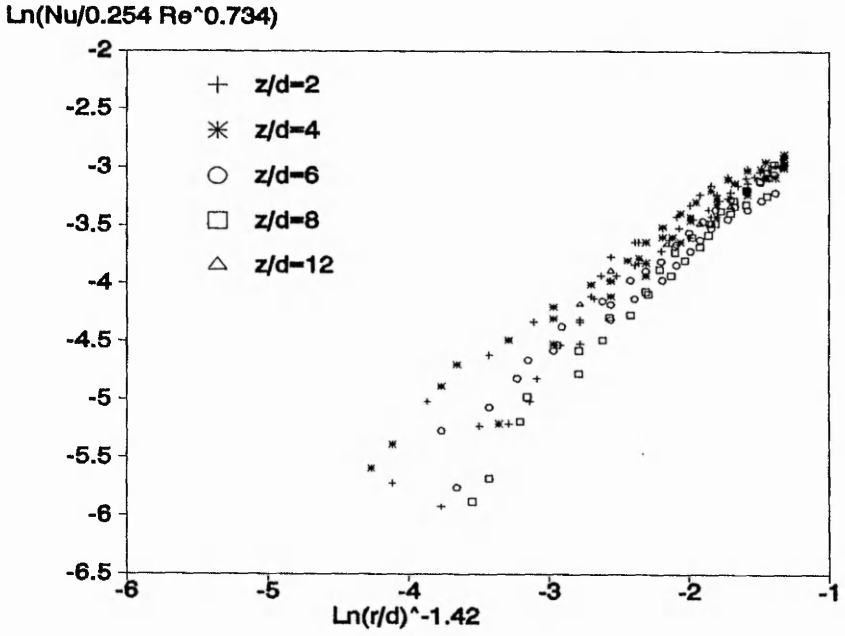

Figure 5.2.10 Experimental wall jet *Nu* versus *r/d* with regression equation without the *z/d* correlated for semi-confined jet impingement

5.2.4 Uncertainty analysis of the correlation equation

The correlation equations obtained in the Table 5.1 for the laminar flow conditions are subjected to error analysis using the Monte-Carlo technique. Ninety-five per cent confidence limits are quoted in the resulting *Sh* as ± 37 per cent, when the exponents of the correlation are kept constant during the simulation. If the uncertainty limits for the exponents are incorporated into the error analysis then the uncertainty limits increased to ± 83 per cent at *r/d* of 18.5 and to ± 53 per cent at *r/d* of 2.5. Therefore, in the worst case the *Sh* correlations can be used to an accuracy of ± 83 per cent with 95 per cent confidence. These uncertainties are largely due to the form of the correlation equation which is assumed to fit the experimental data well. It should be noted that this uncertainty is independent of the experimental uncertainty. The uncertainty of the correlation equation can be reduced by chosing a better form of the equation which will fit the experimental data more precisely. Lower uncertainty in the experimental data will improve the fit of the correlation equation and this can be done by more experimental measurements with reduced uncertainties in the data. A further implementation for reducing the uncertainty in the data and hence producing a better fit of the correlation equation is by applying an automated image analysis procedure to interrogate the interferograms. The current approach is to manually allocate fringe locations, the uncertainty in the precise location adds to the overall uncertainty in the result. Developments in recent image processing technology and computer power should be used to automate this process and this should help eliminate uncertainties of the manual process.

5.3 Numerical predictions for semi-confined jet impingement

In this section the flow and heat transfer results obtained from the numerical predictions for a laminar semi-confined jet impingement are reported. The boundary conditions imposed on the model are summarised in chapter four and an example of the PHOENICS Q1 input file for the laminar case is in Appendix C. The results from these predictions are used to obtain an insight into the trends that show themselves due to various boundary conditions being imposed.

Fluid flow and heat transfer predictions are carried out for laminar Re = 100, 500, 1000, 1500 and 2000. The corresponding Nu on the impingement surface are calculated from the resulting data. These heat transfer predictions are obtained for both flat and parabolic exit velocity profiles from the nozzle.

5.3.1 Predicted flow field

This section discusses typical pressure (*P1*), and velocities (*V1*, *W1*) predictions to obtain an understanding of the heat transfer mechanism. Flow data for Re = 500 is chosen as typically representative for a range predicted of Re = 100, 500, 1000, 1500 and 2000. The effects of jet diffusion are still significant for this Re and therefore a greater understanding of the flow interaction can be obtained.

Figure 5.3.1 and Figure 5.3.2 show *P1* on the impingement wall for z/d = 2 and 12 respectively with both flat and paraboloic jet profiles. Results show that the parabolic jet with the higher axial momentum produces a significantly higher *P1* distribution than the flat jet. This causes an increased acceleration of the flow and thus an increased transfer rate at the wall. The *P1* distribution for the flat jet is notably flat which suggests a much lower momentum change and consequently reduced transfer rates. The *P1* distribution decreases with increasing z/d and therefore a related reduction in momentum is observed. The *P1* distribution extends radially till $r/d \approx 1$, and outside this region the *P1* decreases to the datum *P1* of zero.

Figure 5.3.3 and Figure 5.3.4 shows the *V1* for Re = 500 at r/d = 0.0 and 0.5 and z/d = 2 and 12. In Figure 5.3.3 z/d = 2 and the maximum *V1* at r/d = 0.5 for the parabolic jet is twice that for the flat jet and therefore higher transfer rates are observed for the parabolic jet. The maximum *V1* at r/d = 0.0 is also shown in Figure 5.3.3, the flat jet *V1* is lower and consequently transfer rates are lower. In Figure 5.3.4 for z/d = 12, a significantly reduced maximum *V1* is obtained compared to the results of z/d = 2 for both r/d = 0.0 and 0.5. This will again reduce the transfer rates. The *V1* for the flat jet is well developed and the profile shape is similar to that obtained for the parabolic jet, suggests that by increasing

z/d, the development of the flat jet will take place. Maximum $V1$ for $z/d = 12$ at $r/d = 0.0$ is lower than that for the $z/d = 2$ and this should further lower the transfer rate.

Figure 5.3.5 and Figure 5.3.6 show $W1$ for $z/d = 2$ and 12 with both jets, at $r/d = 0.0$ and 0.5 respectively. Values of $W1$ are significantly different and are affected by the wall at $zx/d \approx 1$ for the parabolic jet and $zx/d \approx 1.5$ for the flat jet. Development of $W1$ has insufficient length before the wall has its effect. For $z/d = 12$, the $W1$ are developing and the parabolic jet shows a gradual reduction in the $W1$ but both jets begin to be affected by the wall at the same distance above the wall. In Figure 5.3.6 the $W1$ profiles at $r/d = 0.5$ are shown for $z/d = 2$ and 12 for both the flat and parabolic jets. The developed jet for $z/d = 2$ shows some development of the jet before the presence of the wall causes the reduction of $W1$. The flat jet with $z/d = 2$ shows an immediate decrease in the $W1$ as it emerges from the nozzle because proximity of the wall does not allow further velocity development. $W1$ for $z/d = 12$ shows gradual development of the outer region of the jet until both the flat and parabolic jets acquire similar $W1$ profiles. Presence of the wall on the flow is observed at the same location above the wall.

Streamline plots for the laminar semi-confined jet impingement show similar characteristics for all the Re investigated. A typical streamline figure for $Re = 500$ is shown in Figure 5.3.7. The figure shows a large circulation bubble attached to the jet and confined between the two boundary walls. Downstream of the wall jet, the flow becomes similar to flow between parallel plates. For higher Re the circulation bubble bursts out into the out-flow region pushed further downstream by the higher momentum of the jet. This requires part of the outflow region to have inflow due to entrainment induced by the jet flow. The wall jet established by the impingement flow stays attached to the impingement wall until the outflow is reached.

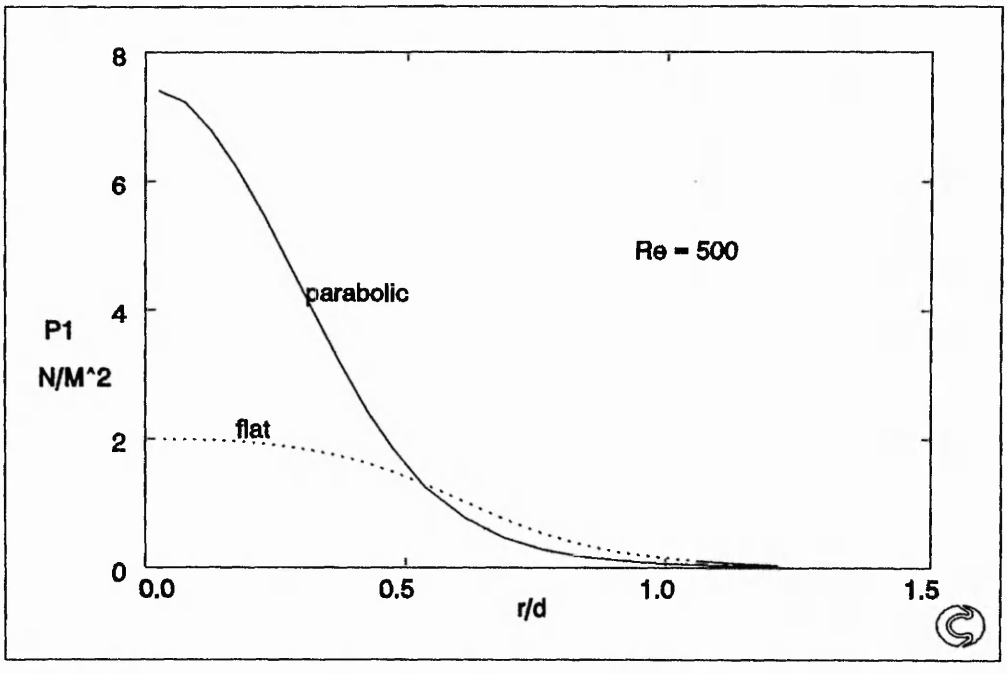

Figure 5.3.1 P1 on the impingement surface versus r/d, $Re = 500$, $z/d = 2$ and W_{jet} (flat and parabolic)

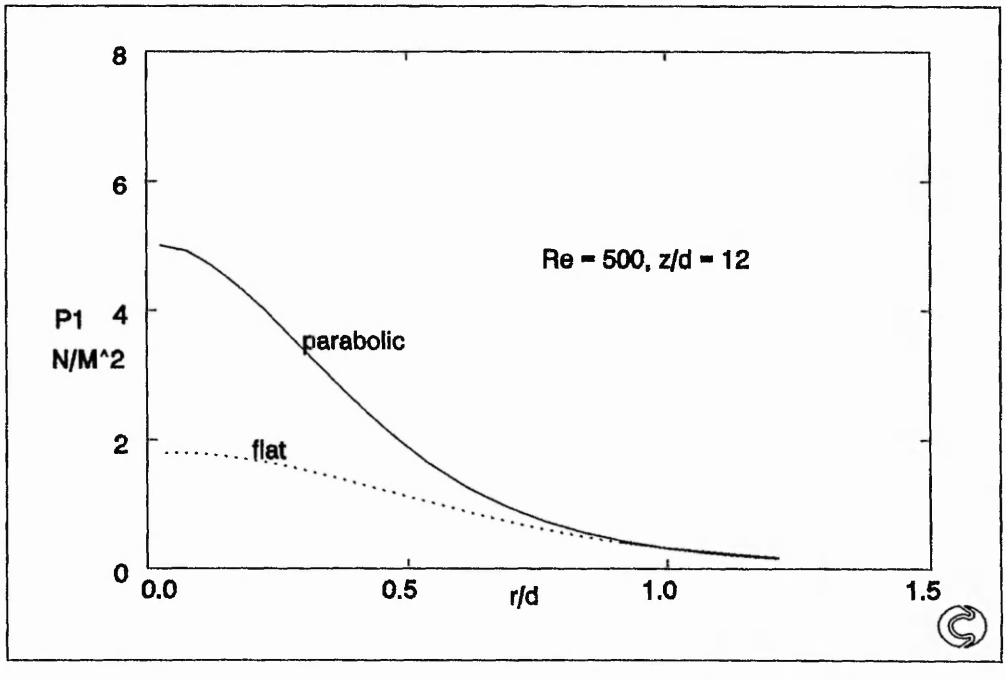

Figure 5.3.2 P1 on the impingement surface versus r/d, $Re = 500$, $z/d = 12$ and W*jet* (flat and parabolic)

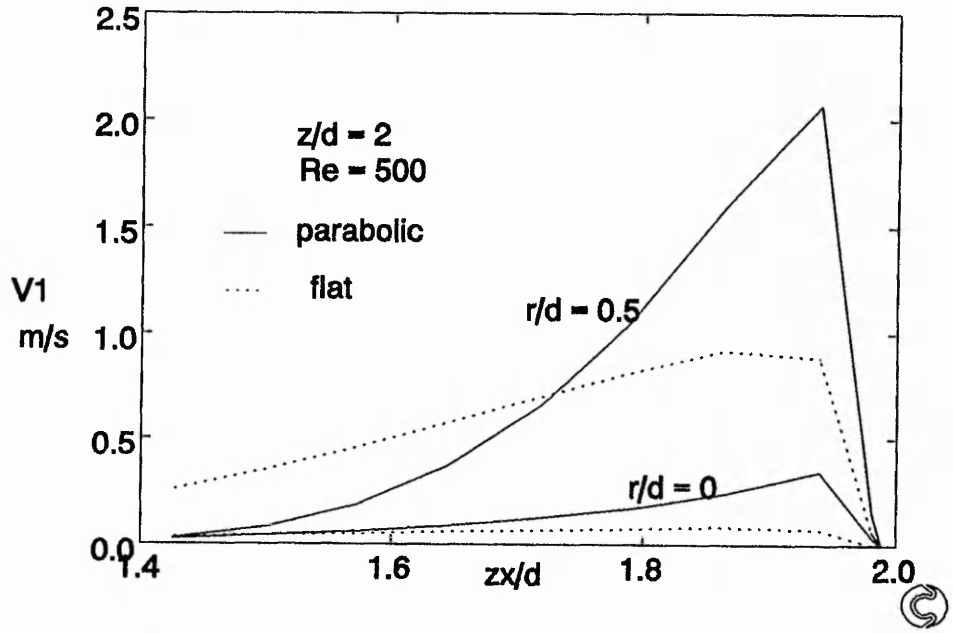

Figure 5.3.3 V1 versus zx/d, r/d = 0.0 and 0.5, Re = 500, z/d = 2 and W_{jet} (flat and parabolic)

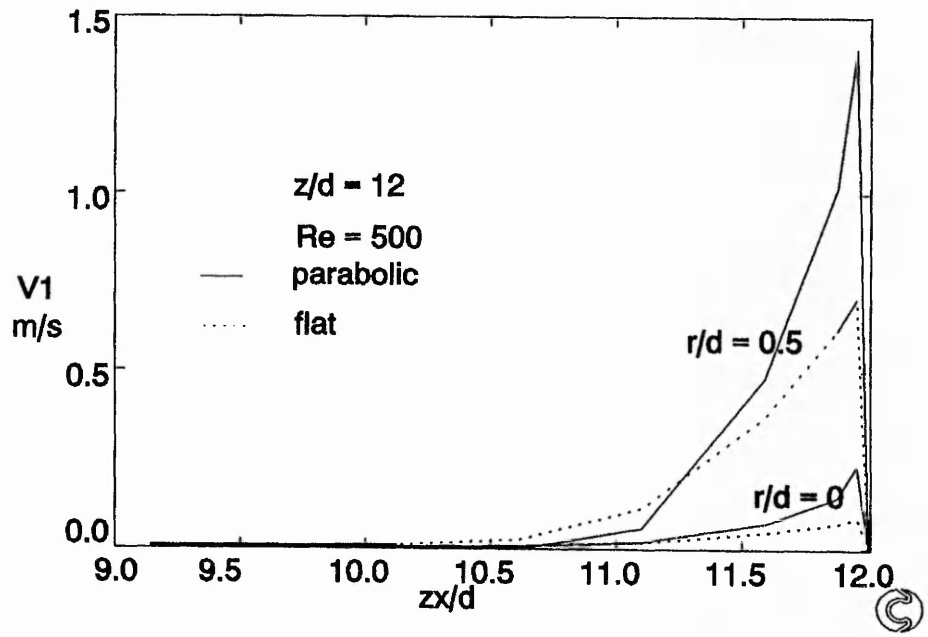

Figure 5.3.4 V1 versus zx/d, r/d = 0.0 and 0.5, Re = 500, z/d = 12 and W_{jet} (flat and parabolic)

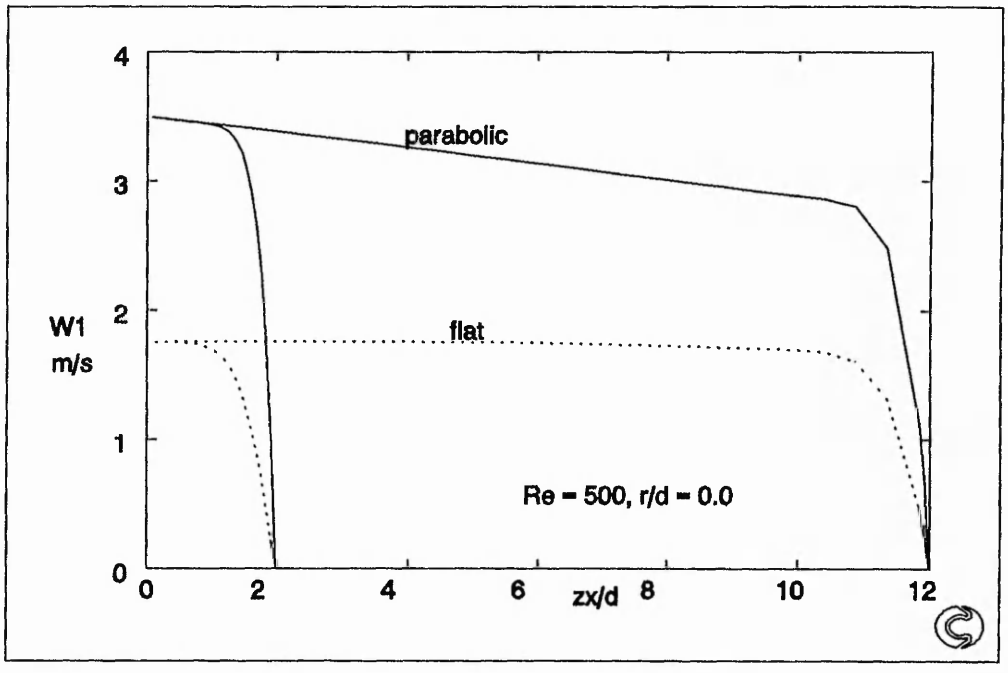

Figure 5.3.5 W1 versus zx/d, $r/d = 0.0$, $Re = 500$, $z/d = 2$ and 12 and W_{jet} (flat and parabolic)

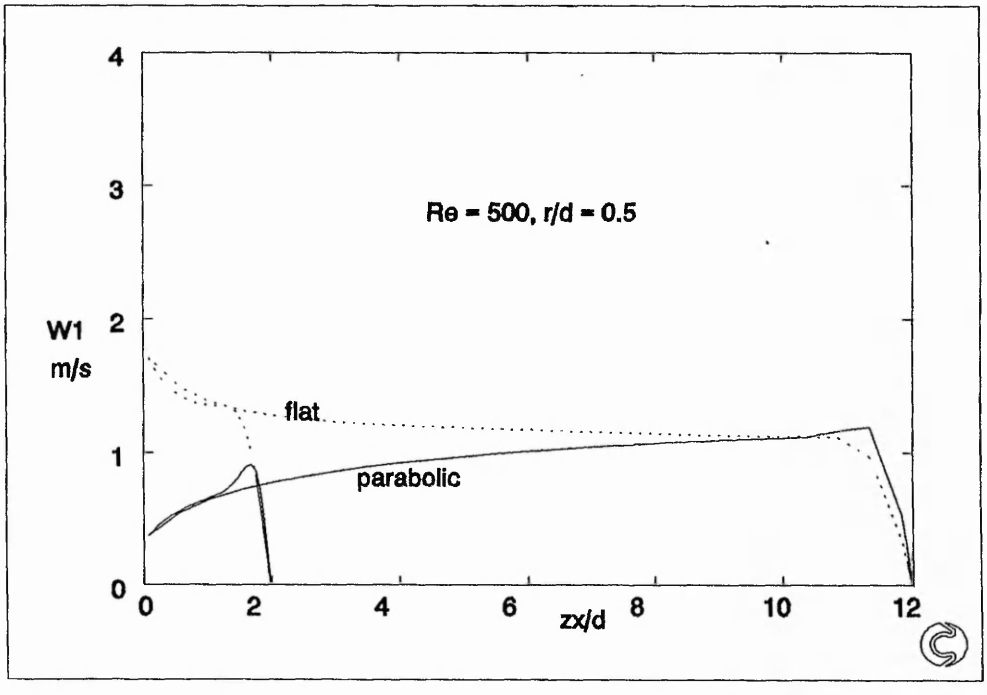

Figure 5.3.6 W1 versus zx/d, $r/d = 0.5$, $Re = 500$, $z/d = 2$ and 12 and W_{jet} (flat and parabolic)

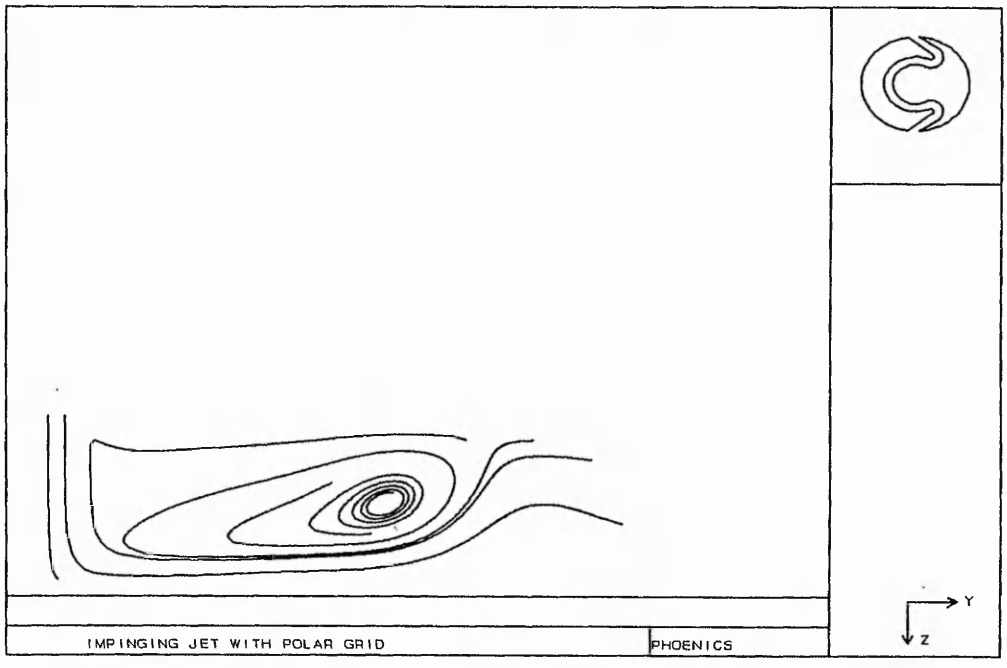

Figure 5.3.7 Streamlines for $Re = 500$, $z/d = 2$

5.3.2 The effect of flat jet velocity profile, on impingement heat transfer

Impingement heat transfer, due to the flat velocity profile jets are shown in Figure 5.3.8 to Figure 5.3.13. Predictions for $z/d = 2$, 4, 8, 10 and 12 have been obtained and for clarity only selected z/d are shown in the figures.

The effect of z/d for $Re = 100$ is shown in Figure 5.3.8. The maximum Nu decreases as the z/d is increased with in the impingement region $r/d < 1$. For low Re substantial diffusion of the jet occurs and the momentum of the jet is reduced, affecting the heat transfer. Maximum Nu for $z/d = 2$ is approximately twice of $z/d = 12$. The wall jet Nu distribution for $z/d = 2$ and 4 is lower than that found for $z/d > 4$. It shows that the confined region and the increased heat transfer at the stagnation point have saturated the boundary layer and consequently this has the effect of reducing the heat transfer in the wall jet. For $z/d > 4$, the wall jet Nu reaches an asymptotic value at around $r/d > 1.5$. This means, that the boundary layers for $z/d > 4$ become similar.

Figure 5.3.9 shows the maximum *Nu* is unaffected by changes in *z/d* for *Re* = 500. For *z/d* > 2, (4 and 10 not shown), the maximum *Nu* occurs on the centre line but for z/d = 2 it occurs at r/d ≈ 0.5. This means for *z/d* = 2 the jet is under developed at the centre line and the confined space at r/d = 0.5 causes accelerated flow at this point and therefore enhances the heat transfer. The maximum *Nu* for the range of *z/d* is the same. The wall jet is identified to exist beyond *r/d* > 4.5. For *z/d* > 2 the wall jet *Nu* is higher than for *z/d* = 2, this suggests that the confined region and the higher heat transfer at the stagnation point has saturated the boundary layer and caused a much reduced heat transfer at the wall.

Figure 5.3.10 shows *Nu* is unchanged in the region *r/d* < 0.5 for *z/d* = 2 to 12 and *Re* = 1000. For this *Re* and *z/d* = 2 to 12, the jet reaching the impingement surface is under developed and therefore a minimum *Nu* is obtained at the stagnation point. For *z/d* = 2 the wall jet *Nu* is low which suggests boundary layer saturation and therefore reduced heat transfer. The wall jet begins at around *r/d* ≈ 5 to 6.

Figure 5.3.11 shows a typical *Nu* distributions for *z/d* = 2, 4 (8, 10 and 12 not shown for clarity) at *Re* = 1500. Minimums at the stagnation point and maximum at *r/d* ≈ 0.5 are obtained for the same reasons as discussed earlier. The wall jet exists from *r/d* ≈ 6 to 7, which shows an expansion of the impingement region due to the higher momentum of the jet. The boundary layer does not get saturated and therefore enhanced *Nu* are obtained up to *r/d* ≈ 4.

Figure 5.3.12 show *Nu* distributions for *z/d* = 2, 12 (4, 8 and 10 not shown) at *Re* = 2000. Similar *Nu* distributions are shown as obtained for the previous case, a minimum at the stagnation point and maximum at *r/d* ≈ 0.5. The difference between the minimum and maximum *Nu* is greater at this *Re*. Results show that the momentum change within this region is much greater due to the significantly higher pressure gradients. A small difference in *Nu* distribution for *r/d* > 0.5 exists and it is thought that this is due to the proximity of the confinement wall at *z/d* = 2 and a positive pressure gradient which causes accelerated flow through this region. The wall jet starts at *r/d* > 7 due to the developing flow and the boundary

layer does not saturate due to the increased momentum of the flow.

The *Nu* distributions for a range of *Re* at $z/d = 2$ are compared in Figure 5.3.13. The increase in the *Nu* is not linearly proportional to the *Re*, this suggests that the boundary layer is the controlling mechanism. The heat transfer difference is small for the high *Re*, this means that the boundary layer becomes saturated and no enhancement is obtained. For $Re > 500$ an increased impingement area is observed with higher *Nu* and the wall jet shifts radially away from the stagnation point. It is thought that the accelerated flow in this region is still developing and therefore enhanced heat transfers are obtained. Location of the maximum *Nu* at $r/d \approx 0.5$ for $Re = 500$ is shifted radially with an increase in *Re,* caused by the higher momentum. This maximum is due to the pressure gradient at the stagnation point and this affects the acceleration of the flow and therefore the heat transfer.

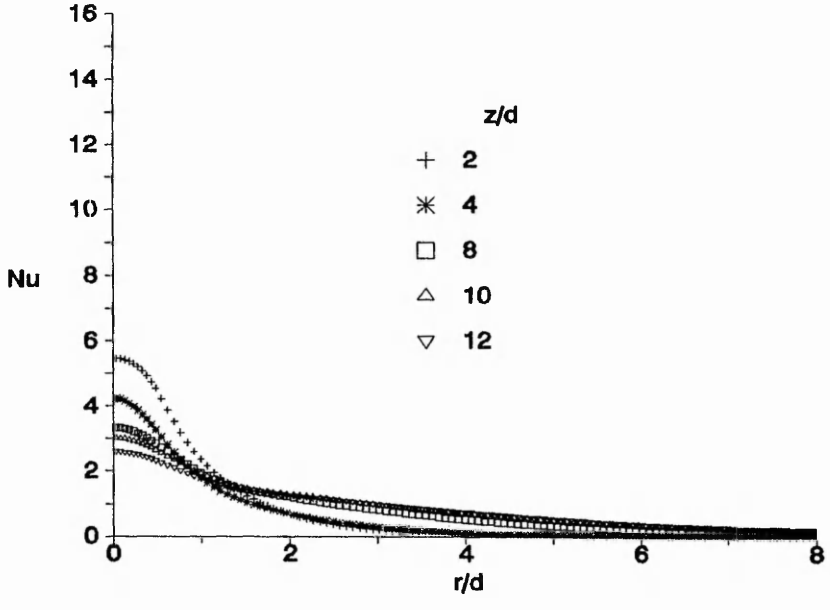

Figure 5.3.8 *Nu* versus r/d, $Re = 100$, $2 \leq z/d \leq 12$, and W_{jet} (flat)

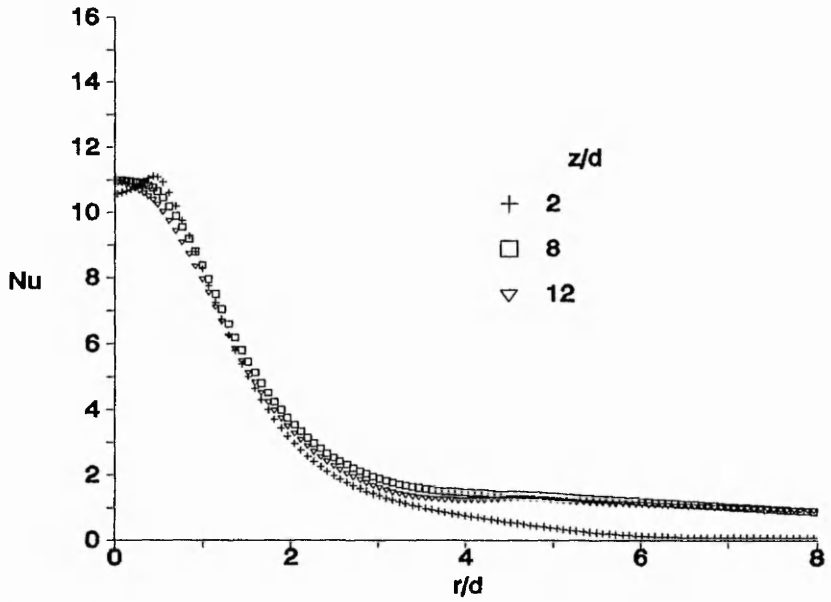

Figure 5.3.9 *Nu* versus *r/d*, $Re = 500$, $2 \leq z/d \leq 12$ and W_{jet} (flat)

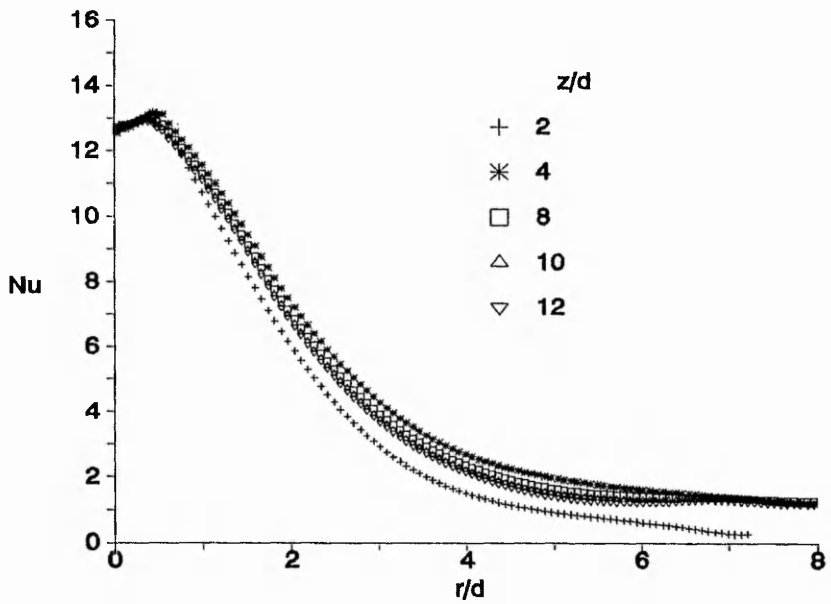

Figure 5.3.10 *Nu* versus *r/d*, $Re = 1000$, $2 \leq z/d \leq 12$, and W_{jet} (flat)

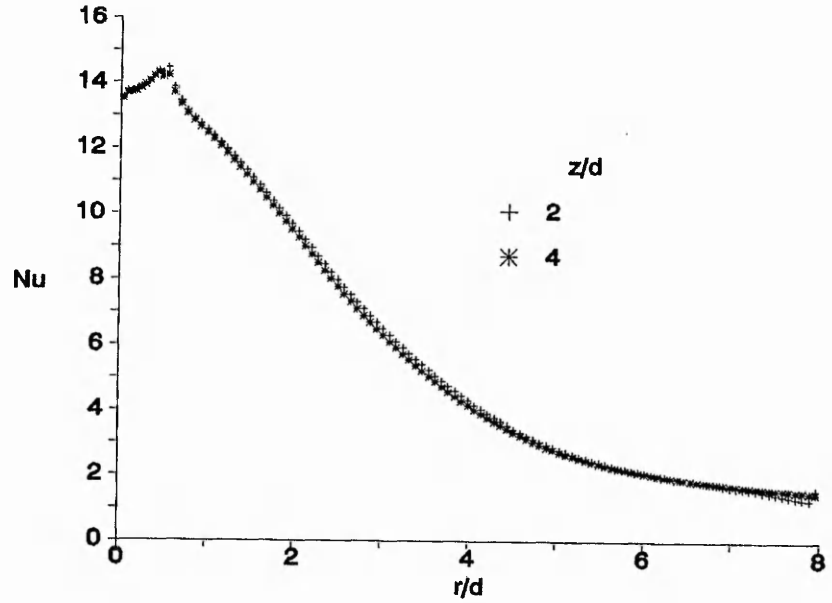

Figure 5.3.11 *Nu* versus *r/d*, *Re* = 1500, 2 ≤ *z/d* 12 and W_{jet} (flat)

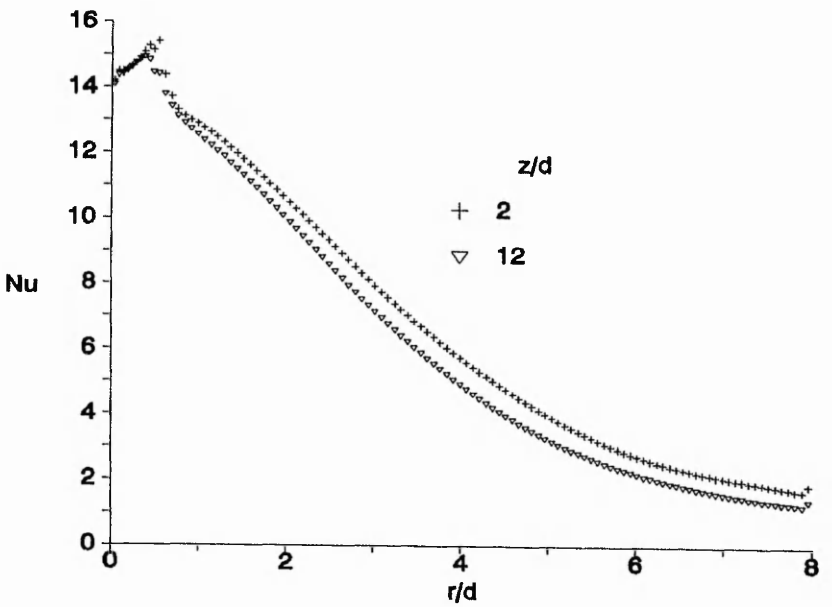

Figure 5.3.12 *Nu* versus *r/d*, *Re* = 2000, 2 ≤ *z/d* ≤ 12, and W_{jet} (flat)

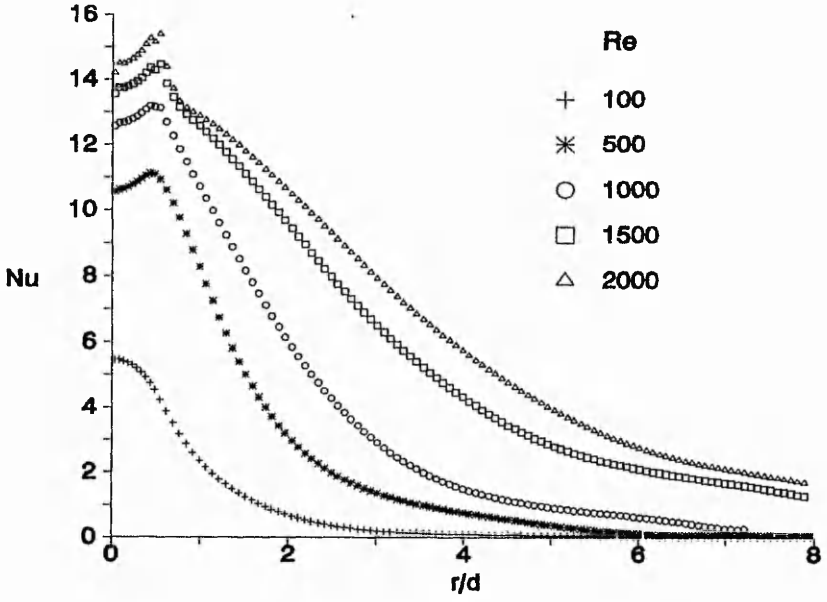

Figure 5.3.13 *Nu* versus *r/d*, 500 ≤ Re ≤ 2000, *z/d* = 2 and W_{jet} (flat)

5.3.3 The effect of parabolic jet velocity profile, on impingement heat transfer

Predictions for *Re* = 100, 500, 1000, 1500 and 2000 and *z/d* = 2, 4, 8, 10 and 12 are carried out except in this section the jet has a parabolic velocity profile.
Figure 5.3.14 shows *Nu* distributions for *Re* = 100 with *z/d* = 2 and 12 (4, 8 and 10 not shown). The maximum *Nu* at the centre line changes significantly between *z/d* = 2 to 12. The jet for *z/d* = 12 suggests significant diffusion on approach to the impingement surface and therefore a substantial decrease in heat transfer. Wall jet *Nu* distribution for *z/d* = 2 has decreased substantially because the boundary layer is saturated by the increased stagnation point heat transfer.

Nu predictions for *Re* = 500, with *z/d* = 2 and 12 (4, 8 and 10 omitted) are shown in Figure 5.3.15. Maximum *Nu* are different but not as great as seen for *Re* = 100, which shows that jet diffusion is insignificant at *Re* = 500. A difference in the wall jet *Nu* is shown between *z/d* = 2 and 12 which begins at *r/d* ≈ 3. It is thought that the confined region suppresses the heat transfer in the boundary layer because its growth is restricted.

Figure 5.3.16 shows *Nu* distribution for $Re = 1000$ with $z/d = 2$ and 12 (4, 8 and 10 omitted). The maximum *Nu* shows little difference between $z/d = 2$ and 12, again showing insignificant jet diffusion and similar momentum on impact. Wall jet *Nu* shows a significant difference between the two z/d, with the confinement having the same effect on the boundary layer as discussed earlier.

Figure 5.3.17 shows *Nu* distributions for $Re = 1500$ with $z/d = 2$ and 4 are not significantly different from one other. The abrupt change in the *Nu* distribution at $r/d = 0.5$ at the periphery of the nozzle suggests penetration of the boundary layer. Maximum *Nu* is marginally affected by z/d *and* jet diffusion is negligible. The momentum and boundary layer in the wall jet region must be similar because the *Nu* distributions are similar.

Figure 5.3.18 shows the *Nu* distribution for $Re = 2000$ with $z/d = 2$ and 12. A change in the slope of the *Nu* distribution is seen again at $r/d = 0.5$ due to jet penetration. The wall jet *Nu* distribution has the expected monotonic behaviour seen previously. The maximum *Nu* shows some dependence on z/d.

Figure 5.3.19 show *Nu* distributions for the $Re = 100$, 500, 1000, 1500 and 2000 with $z/d = 2$. The *Nu* distribution changes with the flow and the transition becomes apparent between $Re = 1000$ and 1500. This suggests that jet diffusion is insignificant and the momentum is unaffected by the z/d. The arrival velocity of the jet on the impingement wall is the main cause of the abrupt change in the *Nu* distribution at $r/d = 0.5$.

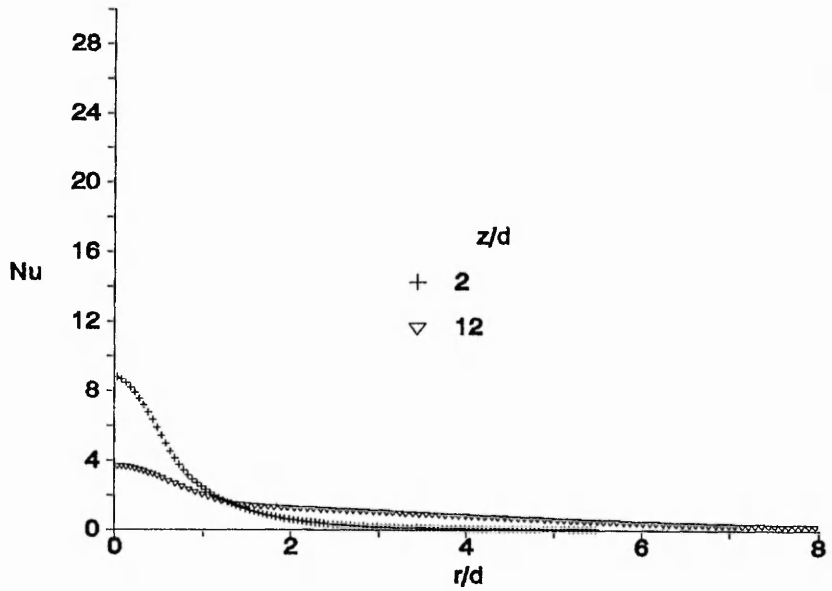

Figure 5.3.14 *Nu* versus *r/d*, *Re* = 100, $2 \leq z/d \leq 12$ and W_{jet} (parabolic)

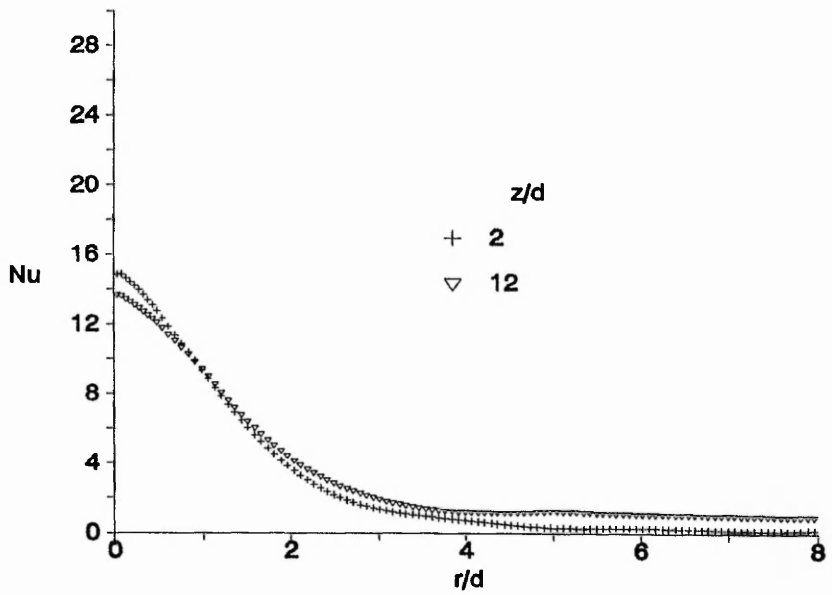

Figure 5.3.15 *Nu* versus *r/d*, *Re* = 500, $2 \leq z/d \leq 12$ and W_{jet} (parabolic)

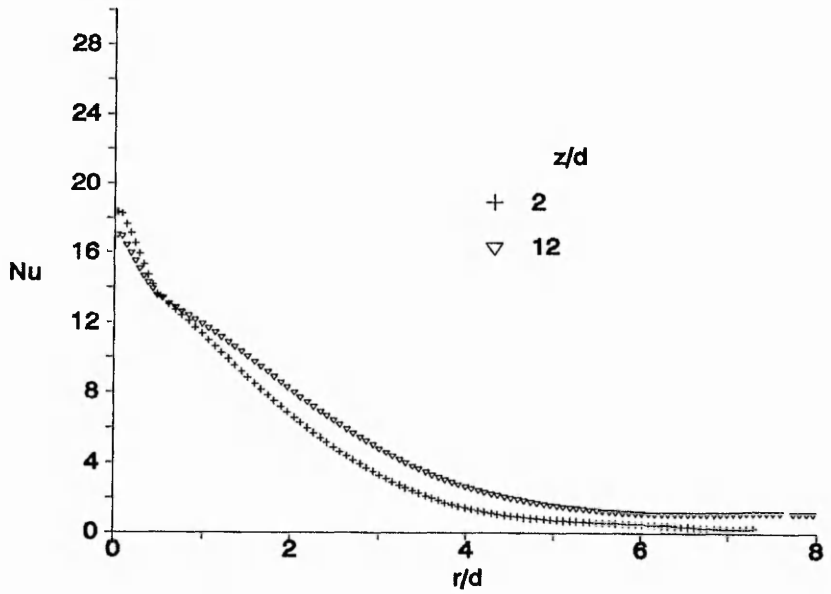

Figure 5.3.16 *Nu* versus *r/d*, *Re* = 1000, $2 \leq z/d \leq 12$ and W_{jet} (parabolic)

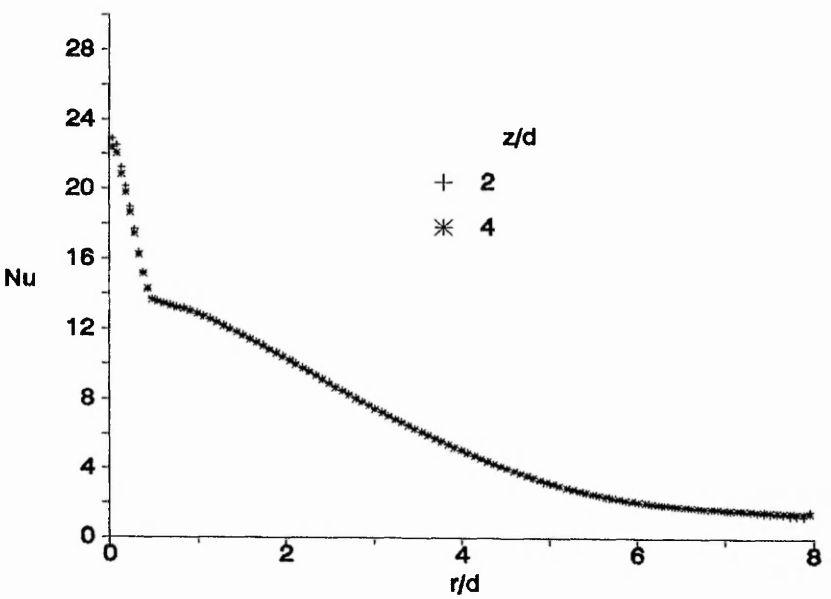

Figure 5.3.17 *Nu* versus *r/d*, *Re* = 1500, $2 \leq z/d \leq 12$ and W_{jet} (parabolic)

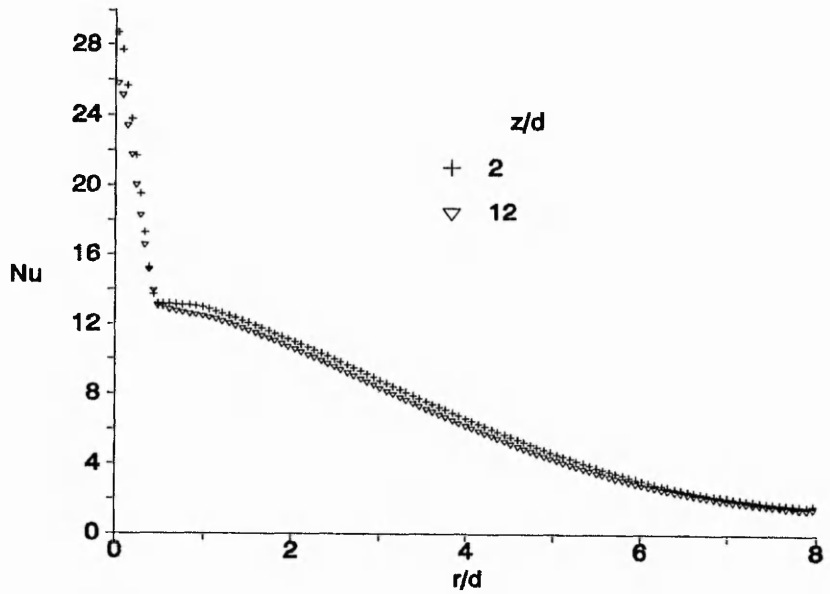

Figure 5.3.18 *Nu* versus *r/d*, $Re = 2000$, $2 \leq z/d \leq 12$ and W_{jet} (parabolic)

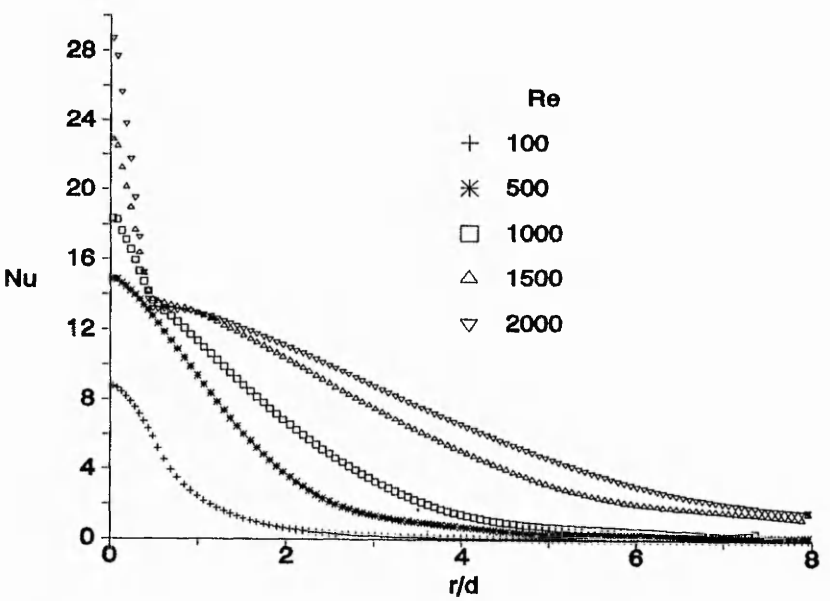

Figure 5.3.19 *Nu* versus *r/d*, $100 \leq Re \leq 2000$, $z/d = 2$ and W*jet* (parabolic)

5.4 Discussion of results

5.4.1 Experimental mass transfer

The experimental mass transfer technique is validated by making experiments of an unconfined jet impingement geometry and comparing the results with theoretical solutions of Scholtz and Trass. Repeatability of the experimental technique is also demonstrated by two replicate sets of tests of the semi-confined jet impingement geometry for various test times were in good agreement.

Experimental *Sh* for laminar semi-confined jet impingement geometry are obtained. The wall jet *Sh* are shown to be dependent on *z/d* spacing. A physical understanding gleaned from the experimental results are, for increased *z/d* causes a reduction in the momentum arriving at the impingement surface and therefore an associated lowering of the wall jet *Sh*. The maximum *Sh* is obtained at *z/d* spacing of 2, which suggests that high jet momentum and the semi-confined region through which the wall jet flow has a beneficial effect on the *Sh*. This confined region maintains a high momentum flow near the wall region and therefore an associated elevation of the *Sh* is observed compared to the data for the larger *z/d* spacings.

A regression equation for the laminar experimental *Sh* for the wall jet of semi-confined impingement jet is

$$Nu = 0.254\ (Re)^{0.734} \left(\frac{r}{d}\right)^{-1.42} \left(\frac{z}{d}\right)^{-0.139} \qquad \textbf{(5.4.1)}$$

for the range

$500 < Re < 2000$

$r/d > 2.5$

$2 < z/d < 12$

A regression equation for the laminar experimental Sh for the transition region of the semi-confined impingement jet is

$$Nu = 0.156\ Re^{0.714} \left(\frac{r}{d}\right)^{-0.811} \left(\frac{z}{d}\right)^{-0.121} \quad \textbf{(5.4.2)}$$

for the range

$500 < Re < 2000$

$r/d < 2.5$

$2 < z/d < 12$

The Monte-Carlo uncertainty simulation technique is used to estimate the confidence limits in the correlation equation. An estimated 95 per cent confidence interval in the correlation is evaluated to ± 53 per cent dependant on the radial location.

5.4.2 Numerical flow field and heat transfer

The presence of the wall is observed on axial velocity *(W1)* at a distance of $zx/d \approx 1$ above the wall. The maximum radial velocity *(V1)* for the parabolic jet is significantly higher because of the higher jet momentum. Predictions allow qualitative comparisons of *Nu* due to a flat and parabolic jet profile. Following geometric and flow constraints were modelled; z/d = 2, 4, 8, 10 and 12 with *Re* = 100, 500, 1000, 1500 and 2000. Parabolic jet produces about double the stagnation point *Nu* compared to the flat jet. The *Nu* distribution for the flat jet shows a minimum at r/d = 0.0 and maximum at r/d = 0.5. This is thought to be the consequence of the pressure gradient within the impingement zone being almost constant which generates low momentum changes near the stagnation point. This *Nu* minimum is not observed for the low *Re*. The area enclosed within the stagnation zone is increased from $r/d \approx$ 2 to 6 with the increasing *Re*. The predicted stagnation point *Nu* are significantly lower than analytical values for unconfined flow. However, the predicted wall jet *Nu* tend towards the experimental values, but only for the higher *Re*. Numerical predictions allow a convenient approach for studying the qualitative trends that may be attributed to subtle changes in various geometric and flow parameters in a particular application.

5.4.3 Comparison of predicted heat transfer with experimental results

This section reports the comparison of the predicted and experimental *Nu* versus *r/d* due to a parabolic jet for $z/d = 2$ and $Re = 500$, 1000, 1500 and 2000. The experimental *Sh* are transformed into *Nu* using the Chilton/Colburn analogy. Analytical solutions for unconfined jet impingement by Scholtz and Trass (1970) are shown in the figures. Comparisons of the data for $z/d = 2$ are shown because this separation is the most significant on the heat transfer. Figure 5.4.1 to Figure 5.4.4 show the plots of the data for the above range of conditions. The predicted *Nu* are lower than those obtained with the current mass transfer method. The predictions compare well to the experimentally determined wall jet *Nu* for the higher *Re*. Stagnation point *Nu* determined from the predictions is significantly lower than its corresponding analytical value. The predicted results suggest that numerical inadequacy and reduced momentum in low *Re* flow leads to under estimation of the *Nu* at the stagnation point and wall jet. Alternatively, it is thought that the experimental flow has some unexpected turbulence in the boundary layer and therefore enhancement in the heat transfer is obtained. However, this is not supported with the laminar analytical solution, which agrees closely with experimental results. It therefore suggests that the numerical inadequacy may be the cause of the deficiency in the prediction.

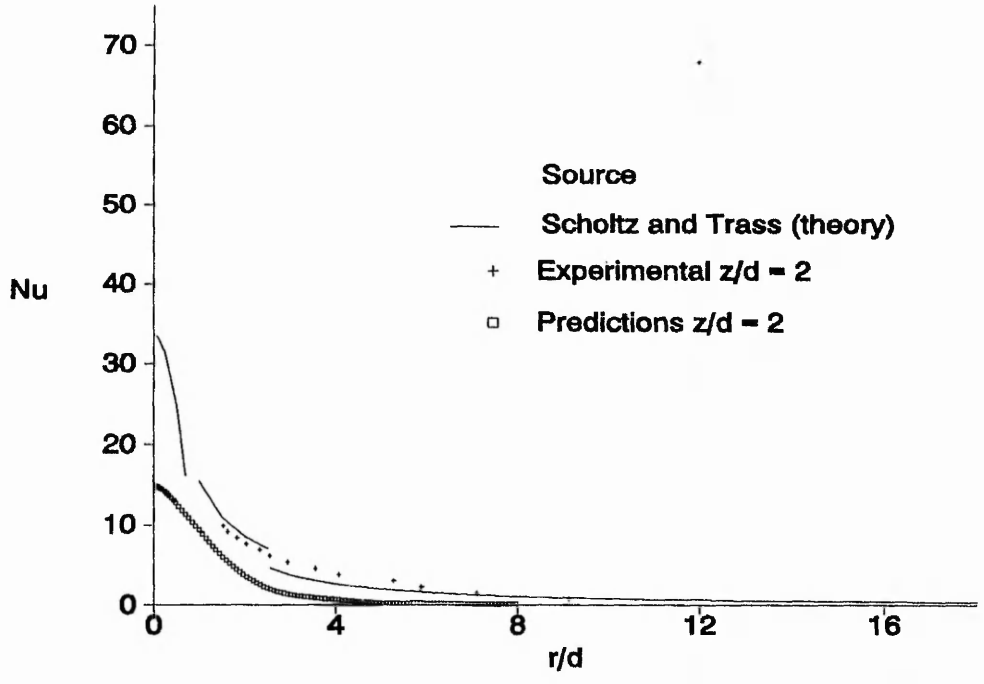

Figure 5.4.1 Comparison of *Nu* versus *r/d*, *Re* = 500, *z/d* = 2 and W_{jet} (parabolic)

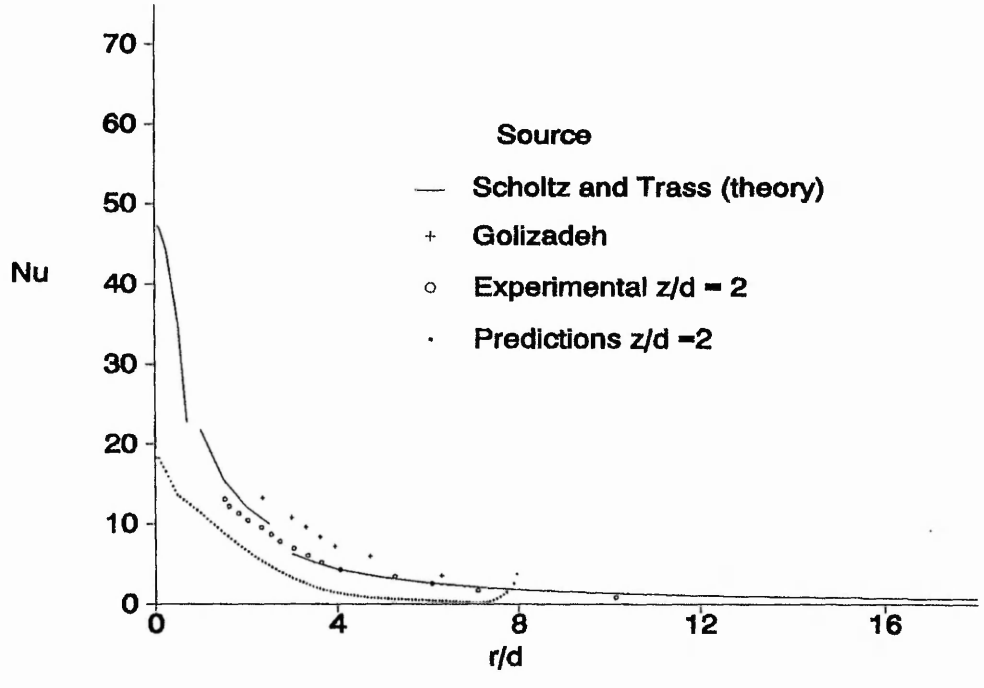

Figure 5.4.2 Comparison of *Nu* versus *r/d*, *Re* = 1000, *z/d* = 2 and W_{jet} (parabolic)

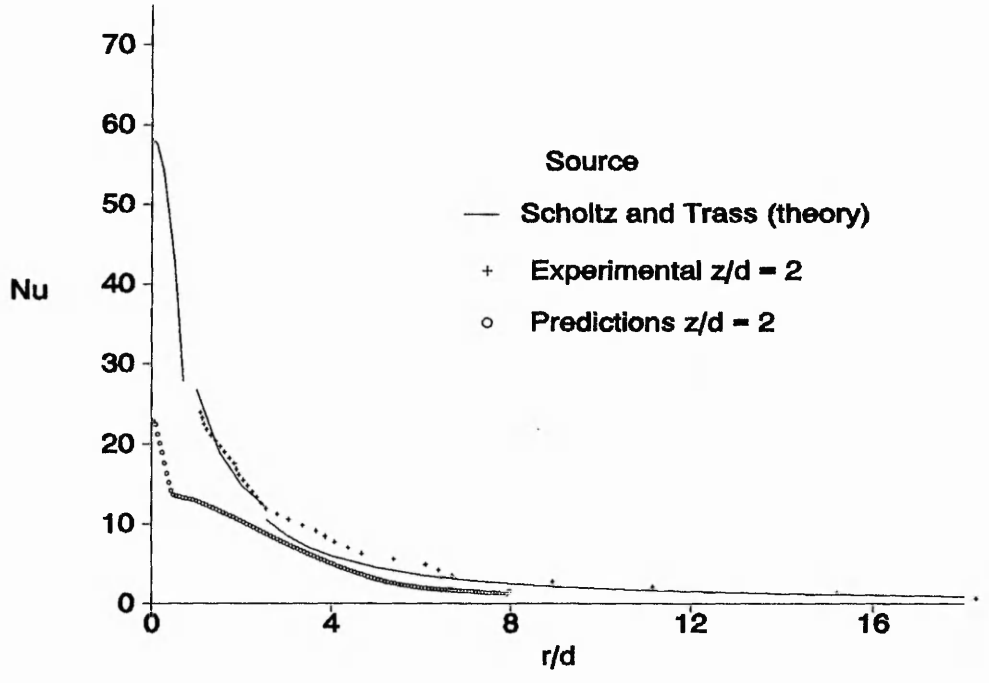

Figure 5.4.3 Comparison of *Nu* versus *r/d*, *Re* = 1500, *z/d* = 2 and W_{jet} (parabolic)

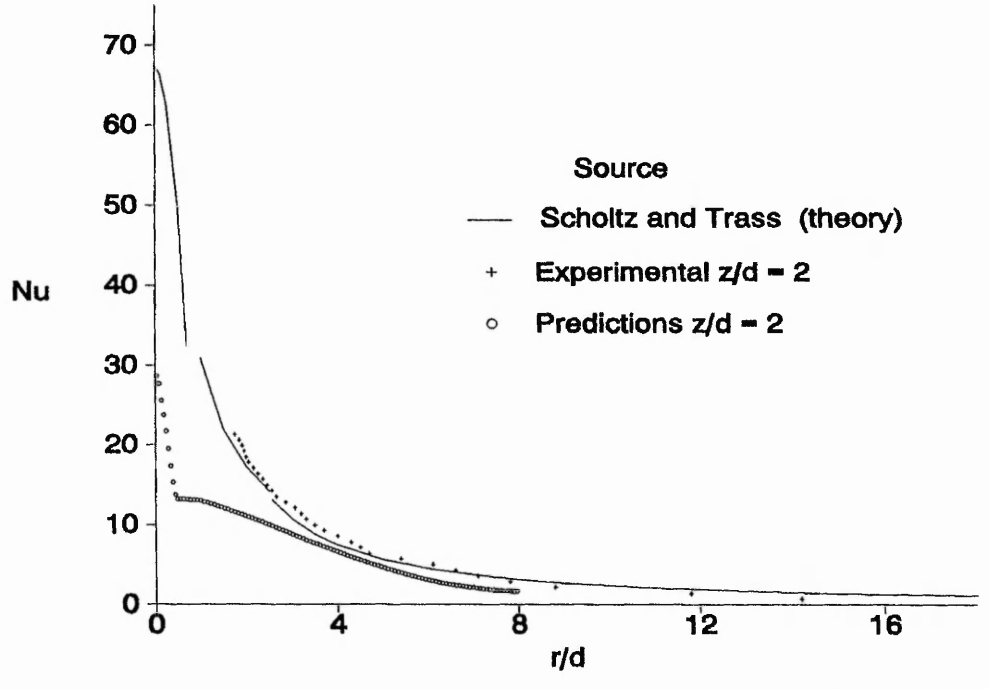

Figure 5.4.4 Comparison of *Nu* versus *r/d*, *Re* = 2000, *z/d* = 2 and W_{jet} (parabolic)

CHAPTER 6
EXPERIMENTAL AND NUMERICAL RESULTS FOR TURBULENT FLOW

6.1 Background to the mass transfer for turbulent flow

The following section reports the outcome of the mass transfer experiments for a turbulent semi-confined impingement jet. The experimental mass transfer technique used, is the same as that used for the laminar flow investigation. Mass transfer data are plotted and where possible compared with available data of similar conditions from literature. The experimentally obtained transfer rates are regressed into correlating equations that take the most appropriate form of a boundary layer equation. Uncertainty analysis of the experimental and correlation equations is undertaken to determine the confidence limits. The following test conditions were studied,

- Re = 3000 to 60000
- z/d = 2, 4, 6, 8, 12

The range of Re investigated is such that the Mach number is kept below 0.5, which avoids problems due to compressibility effects. Current experimental results are compared to the wall jet mass transfer solutions proposed by Dawson and Trass (1966) using classical boundary layer theory. The reported theoretical wall jet mass transfer correlations are 20 per cent lower than their own experimental results. They suggested a weakness in their original assumptions and therefore an empirical correction factor of 1.2 was used in the theoretical solution. The theoretical correlations can be modified to suit different values of Schmidt's numbers (Sc) from a graph providing the necessary data, which allows the exponent for the Re to be identified. The proportionality constant can also be found from the same graph for specific physical conditions.

6.1.1 Mass transfer distribution

The experimental mass transfer results for semi-confined jet impingement are presented in Figure 6.1.1 to Figure 6.1.11. Present experimental results are shown for various z/d and comparisons are made with the analytical correlation for a

turbulent radial wall jet obtained by Dawson and Trass (1966).

Results of the lowest tested turbulent Re = 3000, are shown in Figure 6.1.1. The plot of the obtained Sherwood numbers (Sh) against radial distance shows the wall jet distribution to be similar in trend to that obtained for the theoretical predictions. The Sh for the small z/d are tending towards the theoretical results particularly when $r/d > 5$. Deviation of the experimental Sh from the theoretical curve becomes significant in the region $r/d < 2$ as expected because the wall jet theory is only valid for the region where $r/d > 2.5$. The Sh has an error of 50 per cent from the theory for the large $z/d > 6$ and this over estimation increases to 56 per cent when the $z/d < 4$.

For Re = 5000, the Sh distributions presented in Figure 6.1.2 shows a significant dependence on the various z/d tested. The Sh distribution for $z/d = 6$ agrees to within 10 per cent of the wall jet theory. The Sh distributions are significantly dependant on z/d and the Sh reduces as z/d is increased. The difference in Sh when $r/d > 2.5$ is about 50 per cent, but this also depends on the z/d. For $z/d < 4$ the theoretical Sh are about 20 per cent less compared to the experimental Sh and when $z/d > 4$ the theoretical Sh are about 50 per cent higher.

Similar, Sh characteristics as above are observed for Re = 6000 with z/d as shown in Figure 6.1.3. The theoretical Sh distribution for the region $r/d > 5$ is asymptotic to all experimental z/d results. A change in the slope of the Sh distribution is shown for $z/d = 2$ at $r/d \approx 2$. This feature has been observed in both heat and mass transfer measurements by numerous workers investigating jet impingement flows. It is identified as a local maximum in the Sh. With the present experimental technique of double exposure holography, it is not possible to show this feature precisely because the fringe numbers have to be assigned monotonically. This monotonic behaviour does not occur for particular conditions of geometry and Re.

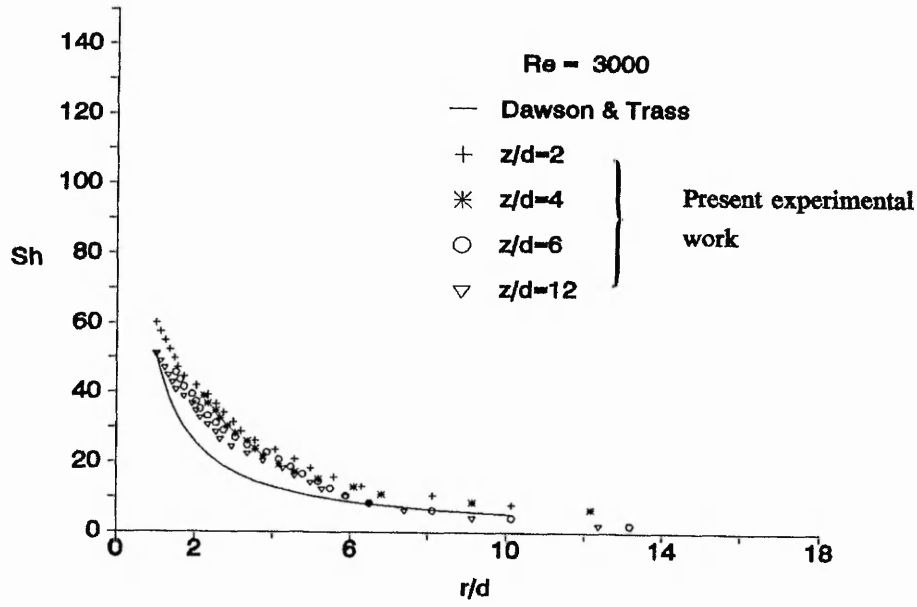

Figure 6.1.1 *Sh* versus *r/d*, *Re* = 3000, *z/d* = 2, 4, 6, and 12 in semi-confined jet impingement

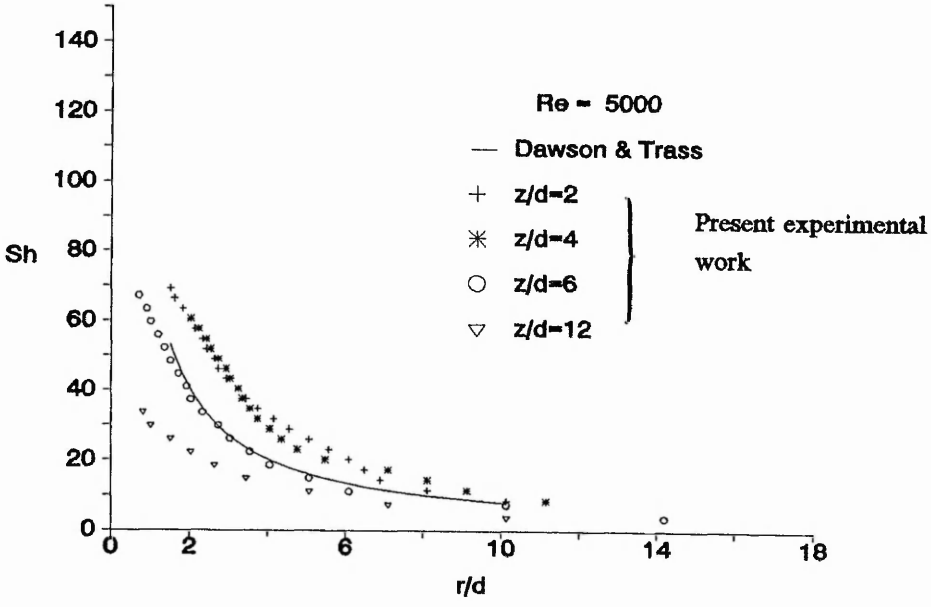

Figure 6.1.2 *Sh* versus *r/d*, *Re* = 5000, *z/d* = 2, 4, 6, and 12 in semi-confined jet impingement

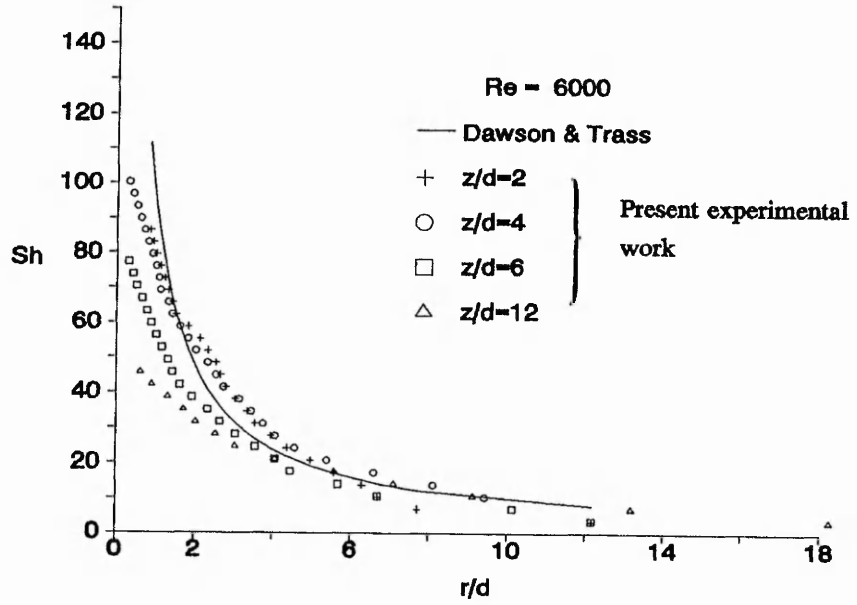

Figure 6.1.3 *Sh* versus *r/d*, *Re* = 6000, *z/d* = 2, 4, 6 and 12 in semi-confined jet impingement

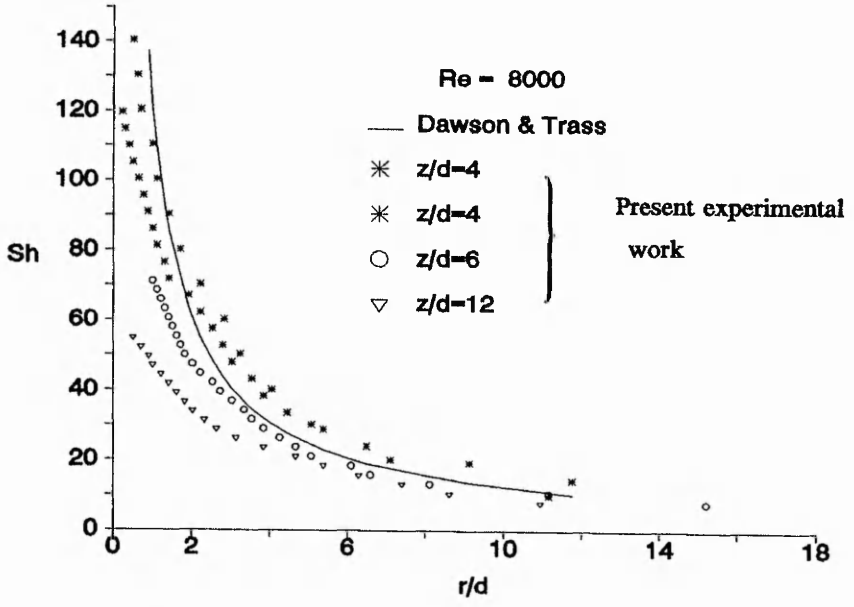

Figure 6.1.4 *Sh* versus *r/d*, *Re* = 8000, *z/d* = 4, 6, and 12 in semi-confined jet impingement

In Figure 6.1.4 the *Sh* obtained for the *Re* = 8000 are compared with the theoretical wall jet distribution. The correlation of Dawson and Trass falls within the range of experimental data and the distribution for $z/d = 6$ is 20 per cent below the theoretical correlation. *Sh* distribution for $r/d < 2$ moves away from the theoretical wall jet distribution as expected. Two repeat tests for $z/d = 4$ are presented showing good repeatability of the experiments.

Figure 6.1.5 shows *Sh* distributions for *Re* = 10000 and the comments are the same as made for the previous cases. The experimental wall jet data for $z/d > 6$ is approximately 30 per cent below the Dawson & Trass correlation. An inflexion zone in the *Sh* distribution is seen for the $z/d = 2$ at $r/d \approx 2$. The observable trend for the experimental wall jet *Sh* is a reduction in value for an increase in z/d.

Sh distributions for *Re* = 12000 and various z/d are shown in Figure 6.1.6. An inflexion region at $r/d \approx 2$ is seen when $z/d = 2$. The experimental *Sh* for the various z/d are closely bunched together compared to the results for the low *Re* cases. The wall jet *Sh* are lower than the theoretical values. Higher wall jet *Sh* are obtained for $z/d < 2$.

Figure 6.1.7 shows the *Sh* distributions for *Re* = 21000 and various z/d with Dawson & Trass's (1966) theoretical wall jet correlation. The current experimental *Sh* for $z/d = 2$ and 4, show a clear inflexion zone at $r/d \approx 2$. Heat transfer for similar *Re* and z/d condition has been investigated and documented by Gardon & Cobonpue (1962) and they identified local maximum at this r/d, which they attributed to the laminar to turbulent boundary layer transition near the wall. The current *Sh* distributions for $z/d > 6$ is substantially lower than *Sh* obtained for $z/d < 6$.

The *Sh* for *Re* = 35000 are shown in Figure 6.1.8. The data obtained for $r/d > 6$, seems to converge to the theoretical wall jet curve, but closer to the impingement region $r/d < 2$ the deviation is large as is expected. *Sh* distributions for $z/d = 2$ has no inflexion point as is observed in the lower *Re* and therefore suggests an already

turbulent boundary layer exist and therefore no transition takes place to generate the local enhancement.

For Re = 42000, the Sh are shown in Figure 6.1.9, the theoretical Sh are higher than the experimental Sh in the wall jet region. The experimental and theoretical data do not agree in the $r/d < 2$ region as would be expected. The experimental Sh in the region $2 < r/d < 6$ are higher by 20 per cent than the theory and beyond $r/d > 6$ the experimental Sh are under estimated by 40 per cent.

Main features of the experimental Sh for Re = 52000 are shown in Figure 6.1.10. The Sh distribution beyond $r/d > 4$ is 20 per cent below the theory of Dawson and Trass (1966). For the $r/d < 2$ region, the Sh shows significant deviation from the wall jet theory by up to 60 per cent.

The experimental Sh for Re = 60000 are shown in Figure 6.1.11. Sh in the region, $2.5 < r/d < 7.0$ for z/d = 2 and 4 are 20 per cent higher than the theory. The deviation from theory becomes greater as $z/d > 6$ and the Sh are 30 per cent below the theoretical value.

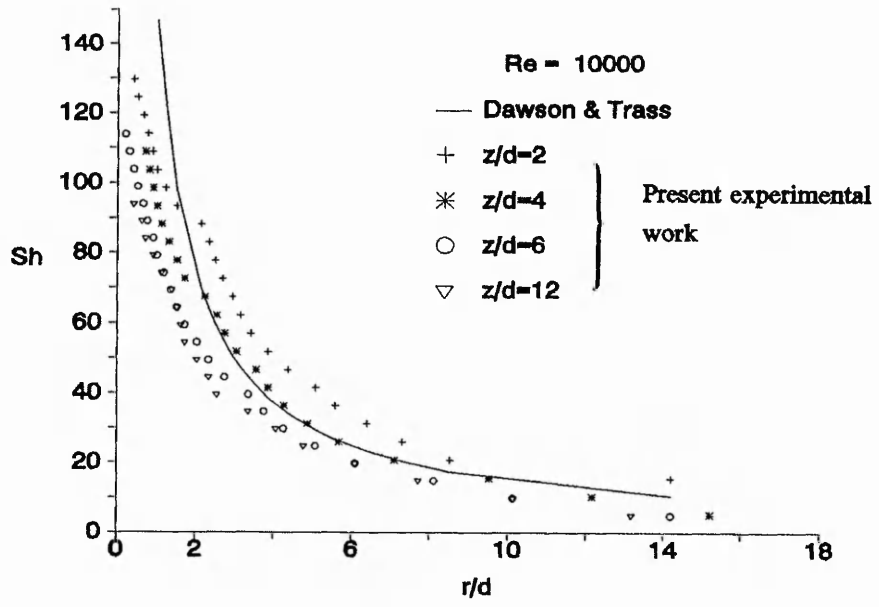

Figure 6.1.5 *Sh* versus *r/d*, *Re* = 10000, *z/d* = 2, 4, 6 and 12 in semi-confined jet impingement

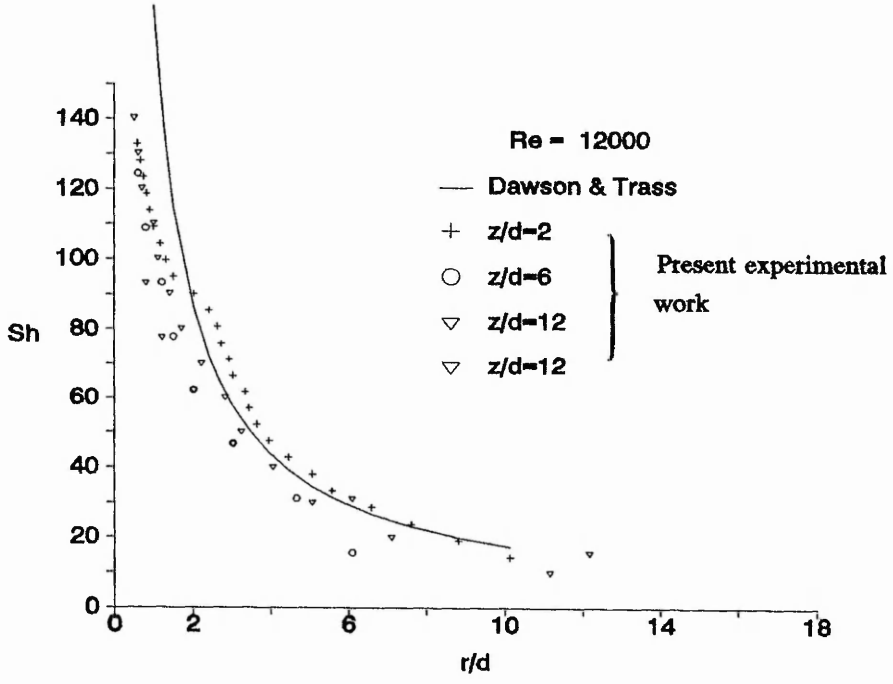

Figure 6.1.6 *Sh* versus *r/d*, *Re* = 12000, *z/d* = 2, 6 and 12 in semi-confined jet impingement

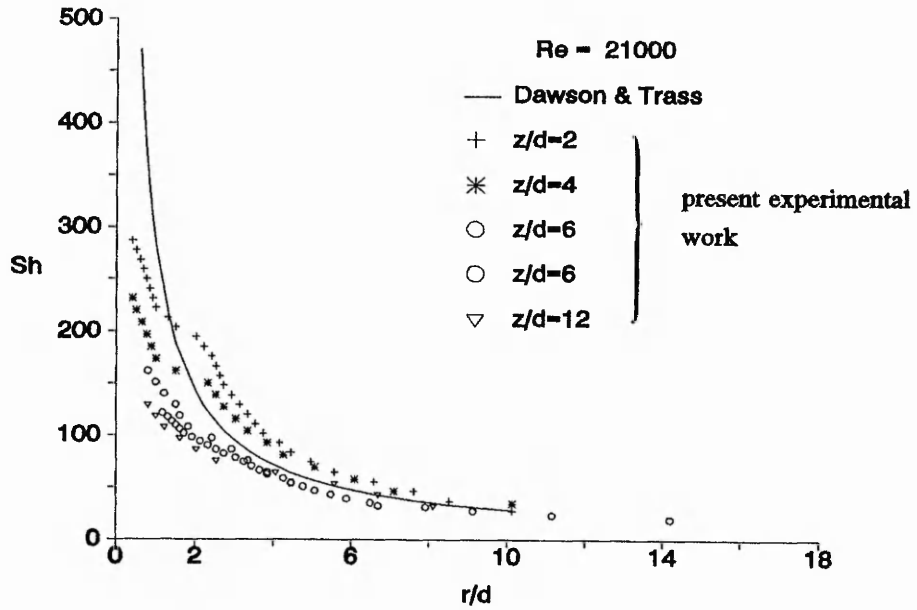

Figure 6.1.7 *Sh* versus *r/d*, *Re* = 21000, *z/d* = 2, 4, 6, and 12 in semi-confined jet impingement

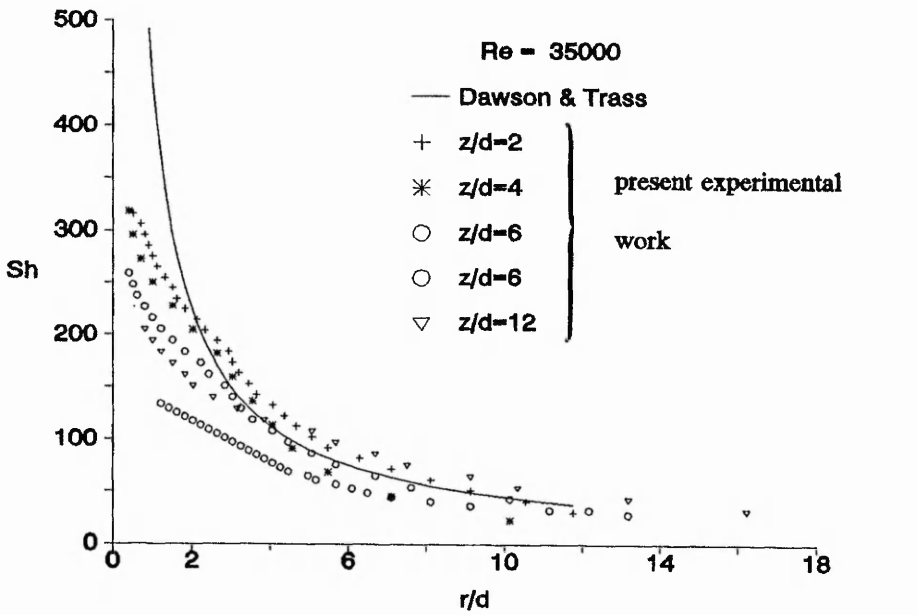

Figure 6.1.8 *Sh* versus *r/d*, *Re* = 35000, *z/d* = 2, 4, 6, and 12 in semi-confined jet impingement

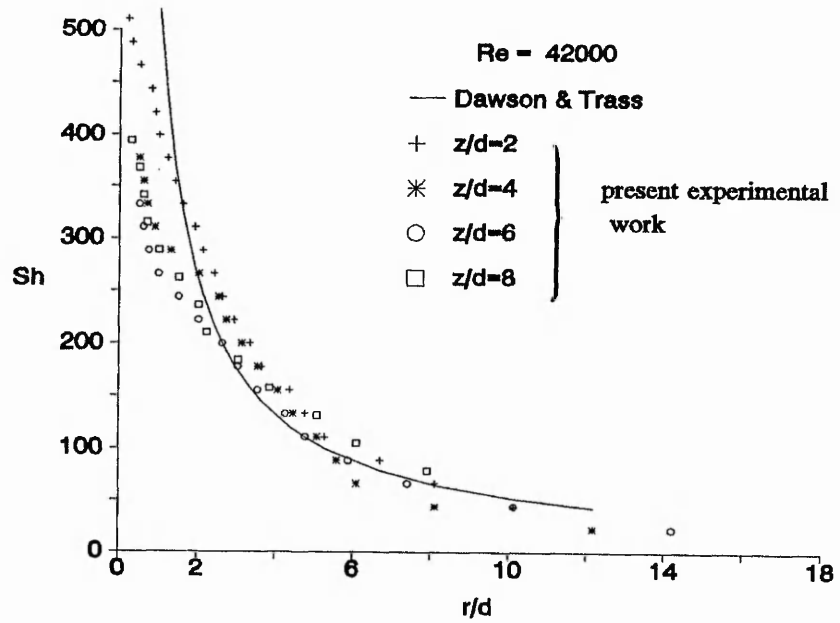

Figure 6.1.9 *Sh* versus *r/d*, *Re* = 42000, *z/d* = 2, 4, 6 and 8 in semi-confined jet impingement

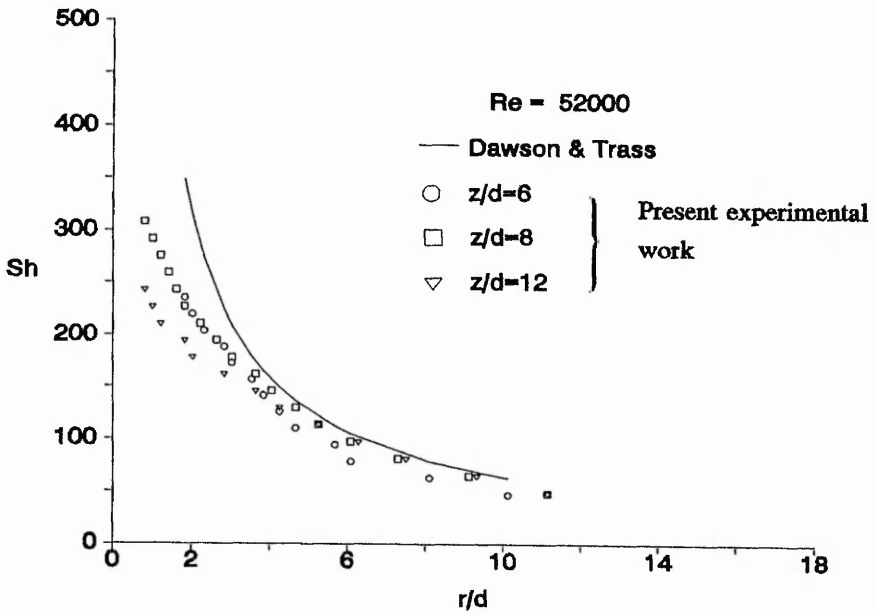

Figure 6.1.10 *Sh* versus *r/d*, *Re* = 52000, *z/d* = 6, 8 and 12 in semi-confined jet impingement

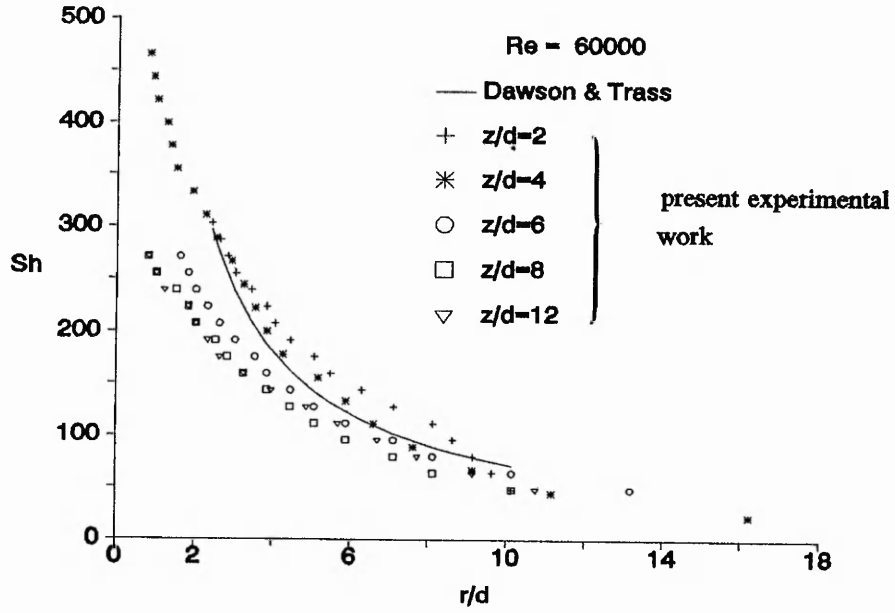

Figure 6.1.11 *Sh* versus *r/d*, *Re* = 60000, *z/d* = 2, 4, 6, 8 and 12 in semi-confined jet impingement

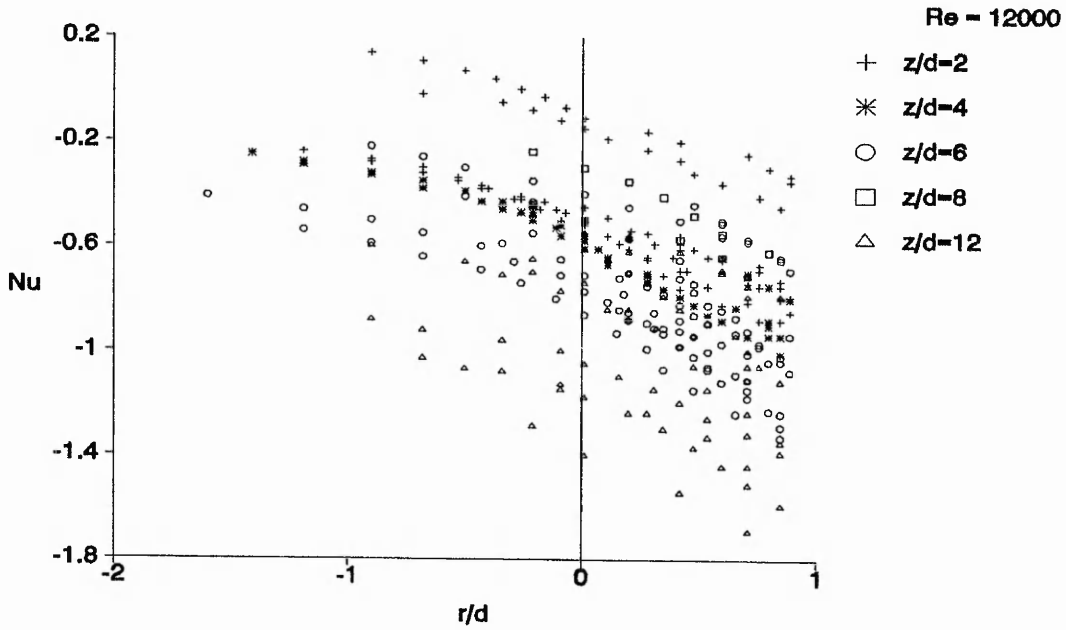

Figure 6.1.12 *Nu* versus *r/d*, *r/d* < 2.5, *Re* = 12000, *z/d* = 2, 4, 6, 8 and 12 for turbulent semi-confined jet impingement

6.1.2 Correlation equation from experimental data

The obtained experimental mass transfer *Sh* are transformed into heat transfer *Nu* using the Chilton/Colburn analogy $Nu = (Pr/Sc)^{0.4}\ Sh$. *Nu* are then entered into a statistical computer package called MINITAB, where a multiple regression technique is used to produce correlations of the *Nu* with the following predictors of *Re*, *r/d* and *z/d*. The data is also selectively regionalised into three categories such that the correlations reflected whether radial location is in the wall jet $r/d > 2.5$ or the transition region $0.7 < r/d < 2.5$ or both. The following general form of the correlation (6.1) is produced.

$$Nu = a\ Re^{\,b} \left(\frac{r}{d}\right)^{c} \left(\frac{z}{d}\right)^{d} \qquad \textbf{(6.1)}$$

The many variations of the correlation equations extracted from the experimental results are summarised in Table 6.1. The main radial categories are the wall jet $r/d > 2.5$, the transition region, $0.7 < r/d < 2.5$, and whole field, $0 < r/d < \infty$. Other permutations chosen for subsequent correlations are listed in Table 6.1. Most of the practical and useful correlations produced from the experimental data are for the wall jet region and the transition region.

The following plots in Figure 6.1.12 to Figure 6.1.15 are presented to illustrate the dependence of one chosen parameter with experimental *Nu* correlation. The *Sh* data converted to *Nu* for $Re = 12000$ and for $r/d < 2.5$ for the different *z/d* are plotted on a log - log scale in Figure 6.1.12, which shows clearly dependence on *z/d*. Data are separated from each in a sequential order showing the lower *z/d* having the higher transfer rates compared to the larger *z/d*.

The experimental transfer data for $Re = 12000$ in the wall jet $r/d > 2.5$ are plotted on a log - log scale in Figure 6.1.13, where the abscissa on the plot is Ln (Nu / ($0.115 * Re^{0.775} * z/d^{-0.202}$)) and the mantissa is Ln ($r/d^{-1.1}$). The correlation equation curve is shown on the plot as a solid line and the experimental data are seen to be scattered about this line. Data scatter around the correlation line shows the uncertainty in the regression of the data into the equation.

The experimental transfer data obtained for the full range of *Re* investigated for one fixed *z/d* spacing of 2 are plotted on log - log scales in Figure 6.1.14. This figure is included, to illustrate the trends of the investigated *Re* and show the *Sh* distributions in the radial direction. The almost parallel distributions show the same transport mechanism exists in radial direction for the investigated *Re*. *Sh* are significantly dependent on the *Re*, the exponent for this dependency is determined for various conditions and is tabulated in the following Table 6.1.

Figure 6.1.15 shows the transfer data obtained for *Re* of 12000 plotted on a log - log scale the abscissa and mantissa are functions of the experimental wall jet correlation equation. The *z/d* term of the correlation equation is not included in the abscissa, this helps to make clear the effect of *z/d* on the transfer correlation.

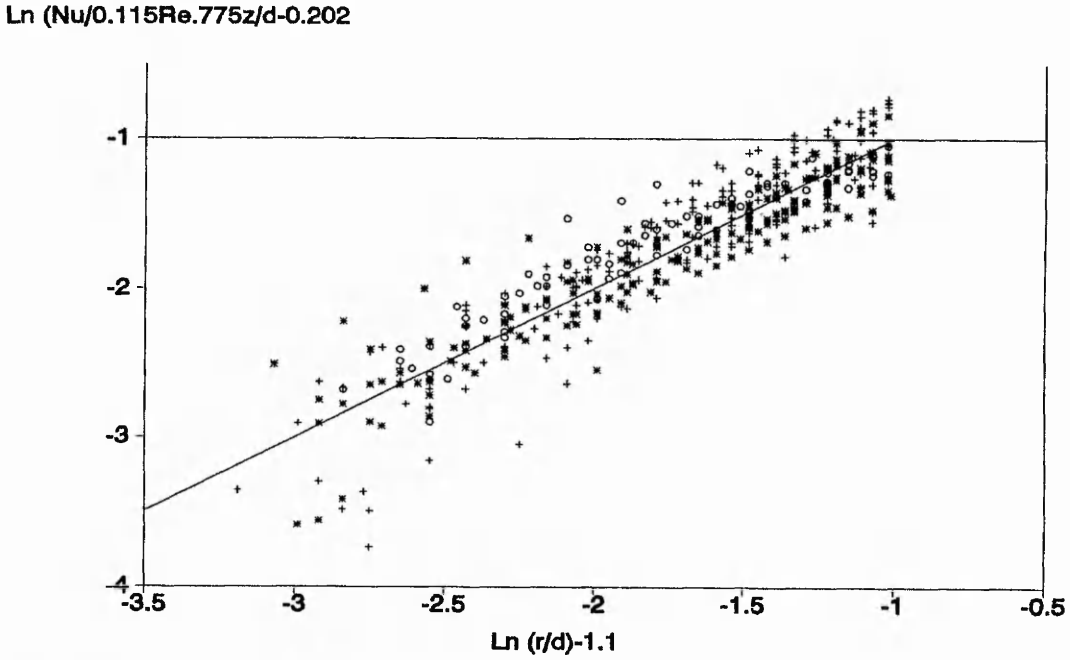

Figure 6.1.13 *Nu* versus *r/d*, *r/d* > 2.5, *Re* = 12000, *z/d* = 2, 4, 6, 8, and 12 and the regression equation for turbulent semi-confined jet impingement

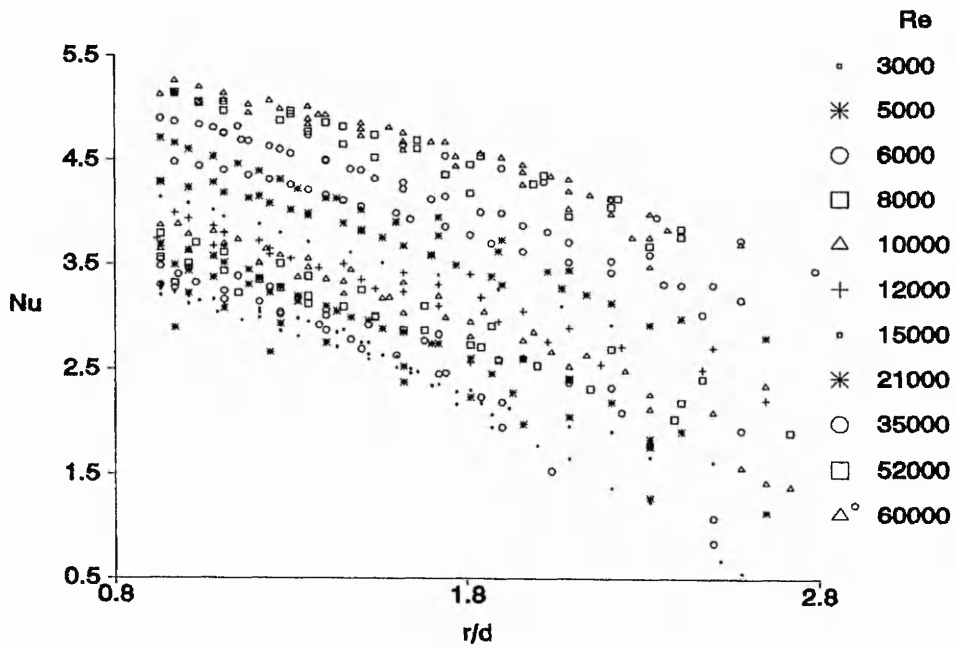

Figure 6.1.14 *Nu* versus *r/d*, *r/d* > 2.5, *z/d* = 2 and *Re* = 3000 to 60000 and the regression equation for turbulent semi-confined jet impingement

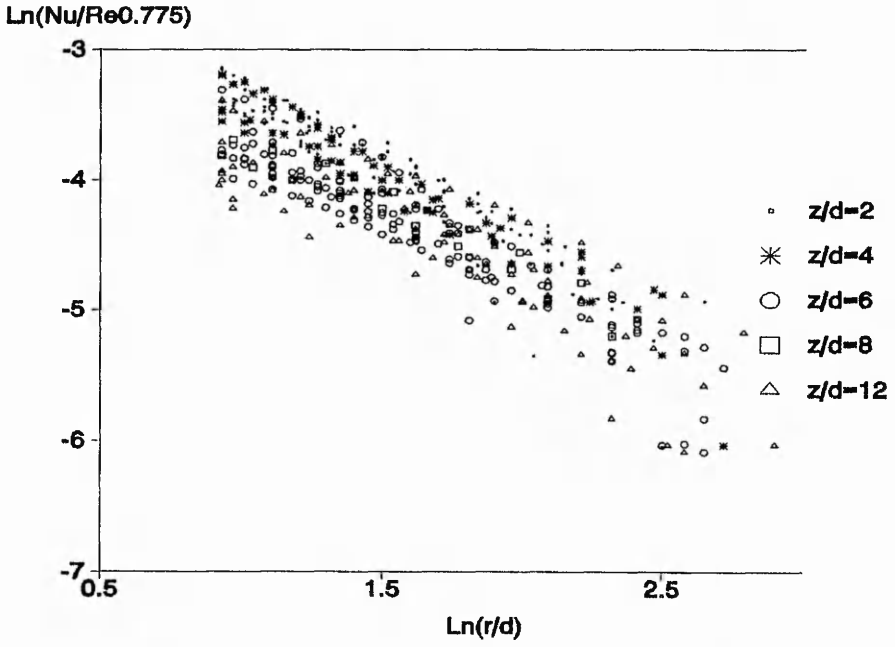

Figure 6.1.15 *Nu* versus *r/d*, *r/d* > 2.5, *Re* = 12000, *z/d* = 2, 4, 6, 8, and 12 and the regression equation for turbulent semi-confined jet impingement

6.1.3 Uncertainty analysis of the correlation equation

The experimental transfer data are subjected to the Monte-Carlo uncertainty analysis technique. The *Sh* is calculated from the measured quantities using a specified functional relationship. Measured quantities lacked precise discrimination and have errors that are uniformly distributed about their fixed means. Simulations use the functional reduction equation and randomly vary with the measured quantity by its discrimination error, which produces a simulated transfer population about the fixed mean. This population can then be used to find 2.5th and 97.5th percentile from the simulated distribution, which can then be quoted as the 95 per cent uncertainty interval. The experimental *Sh* are subjected to this uncertainty simulation technique and the 95 per cent confidence intervals are ± 22 per cent. The program written to carry out the simulations is presented in Appendix I.

Correlation equations shown in Table 6.1 for the turbulent conditions are subjected

Reynolds	r/d	z/d	a	b	c	d
3000-60000	0 - ∞	2 - 12	0.098	0.737	-0.697	-0.246
3000-60000	< 2.5	2 - 12	0.172	0.666	-0.307	-0.276
3000-60000	> 2.5	2 - 12	0.115	0.775	-1.1	-0.202
3000-60000	0 - ∞	2	0.0889	0.725	-0.75	-
3000-60000	> 2.5	2	0.099	0.79	-1.18	-
3000-60000	< 2.5	2	0.1086	0.694	-0.27	-
8000-60000	0 - ∞	2 - 12	0.0299	0.846	-0.669	-0.248
8000-60000	< 2.5	2 - 12	0.0578	0.779	-0.350	-0.290
8000-60000	< 2.5	2 - 4	0.028	0.835	-0.303	-0.0661
8000-60000	> 2.5	2 - 12	0.0437	0.856	-1.0	-0.207
8000-60000	> 2.5	2 - 4	0.0141	0.904	-0.941	0.0465
8000-60000	< 2.5	2	0.0255	0.84	-0.286	-
8000-60000	> 2.5	2	0.0584	0.834	-1.11	-

Table 6.1 Table of heat transfer correlations for the various regions and parametric limits

to error analysis using the Monte-Carlo technique so that confidence limits can be quoted in the experimental *Sh* correlation. The program used to carry out the uncertainty analysis on the correlation equation is shown in Appendix H. If the exponents of the correlation are kept constant during the simulation or 95 per cent uncertainty limits of the exponents are incorporated into the error simulations for the confidence limits the uncertainty is estimated at ± 30 per cent maximum. In the worst scenario, the *Sh* correlations can be used to an uncertainty of ± 30 per cent with 95 per cent confidence. Uncertainty limits in the correlations can be reduced by generating more experimental data for the regression and there by reducing the uncertainty in the correlation. A further method to reduce the uncertainty in the correlation is to improve the analysis procedure of the interferograms. The current approach used, is to manually interrogate the fringe patterns by hand, the uncertainty in the fringe location adds to the uncertainty in the results. Developments in image processing technology and computer

processing power could be used to automate this process that could eliminate the random variations introduced into the manual processing of data.

6.1.4 Comparison of the mass transfer data with other published works

Comparisons of the current experimental mass transfer data are made with experimental mass transfer data obtained by Golizadeh (1992). Golizadeh used a swollen polymer technique and holographic interferometry technique to investigate mass transfer in laminar / turbulent unconfined impingement jet. Although the comparisons are not for identical conditions, they are the best that are available in the literature. Figure 6.1.16 shows the experimental data for Re = 5000. The data obtained by Golizadeh is higher than the current data but the two sets of results converged in the far wall jet region. The difference in the results can be attributed to the semi-confinement used in the current work. The reduction in the transfer rate due to confinement is also observed by Obot et al (1982). Dawson and Trass's correlation is well below the experimental Sh.

Re = 10000 is investigated by Golizadeh, the data shown in Figure 6.1.17 with current experimental data for a comparable Re. Golizadeh's data is again consistently higher than the current experimental data and the data extracted from Gardon & Cobonpue's (1962) paper. The current data for z/d = 2 is nearer Dawson & Trass's correlation and Gardon and Cobonpue's data.

Comparison of the mass transfer data is made with Gardon & Cobonpue's (1962) data for Re = 8000 and 60000 shown respectively in Figure 6.1.18 and Figure 6.1.19. The data for Re = 8000 compares well with Gardon and Cobonpue's and Dawson & Trass's data. The current data for z/d = 12 is also shown in the figure and shows substantial reduction in the transfer rate when the nozzle is moved away from the impingement surface. The data for Re = 60000 shows Gardon and Cobonpue's data is significantly lower than the current data but compares favourably with the Dawson and Trass's correlation.

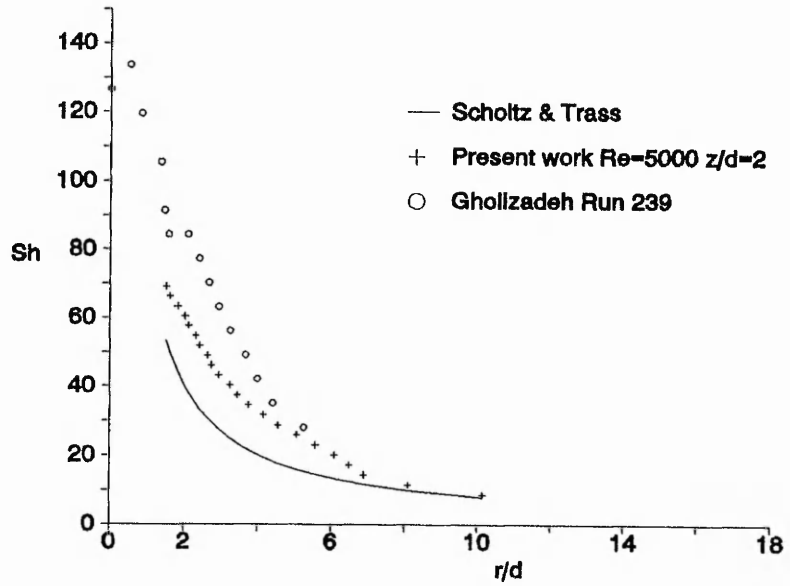

Figure 6.1.16 Comparison of *Sh* versus *r/d*, *Re* = 5000 and *z/d* = 2 with other available data

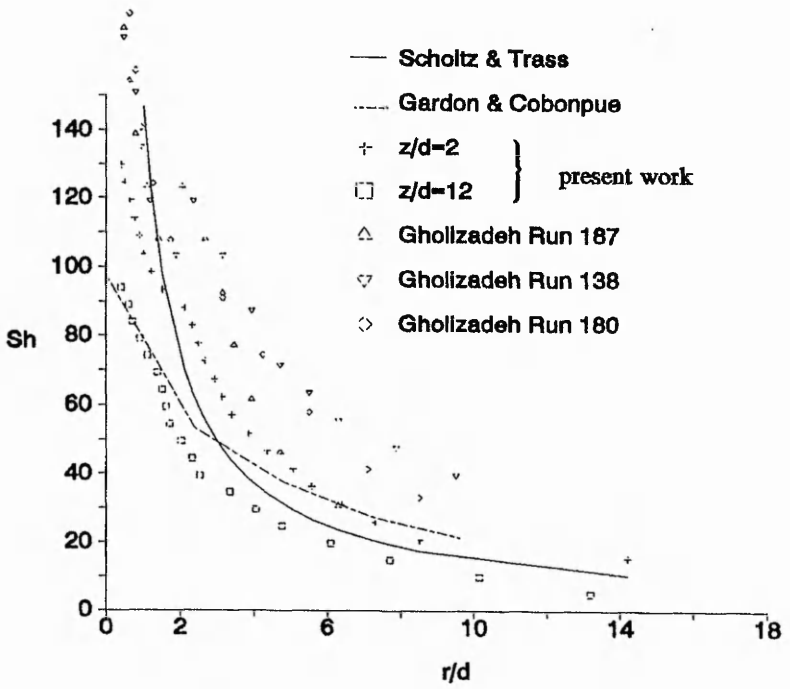

Figure 6.1.17 Comparison of *Sh* versus *r/d*, *Re* = 10000 and *z/d* = 2 with other available data

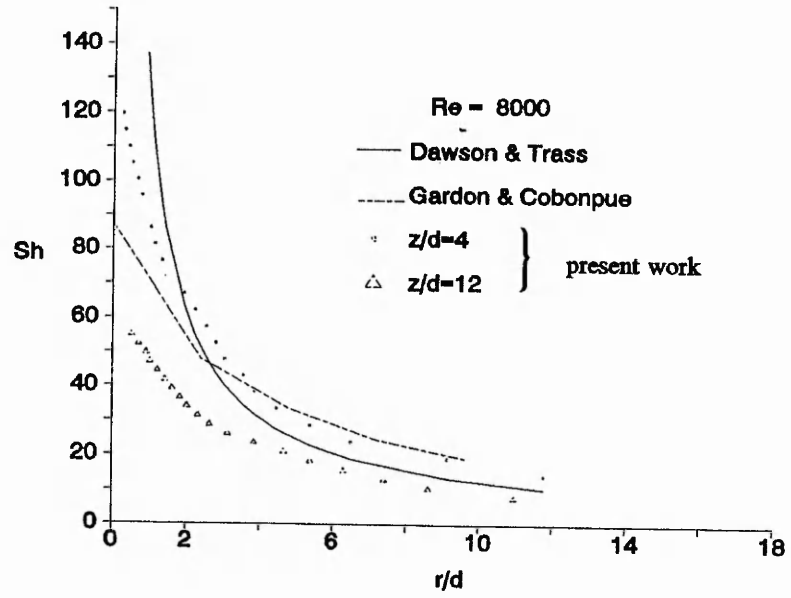

Figure 6.1.18 Comparison of *Sh* versus *r/d*, *Re* = 8000 with data from Gardon & Cobonpue (1962)

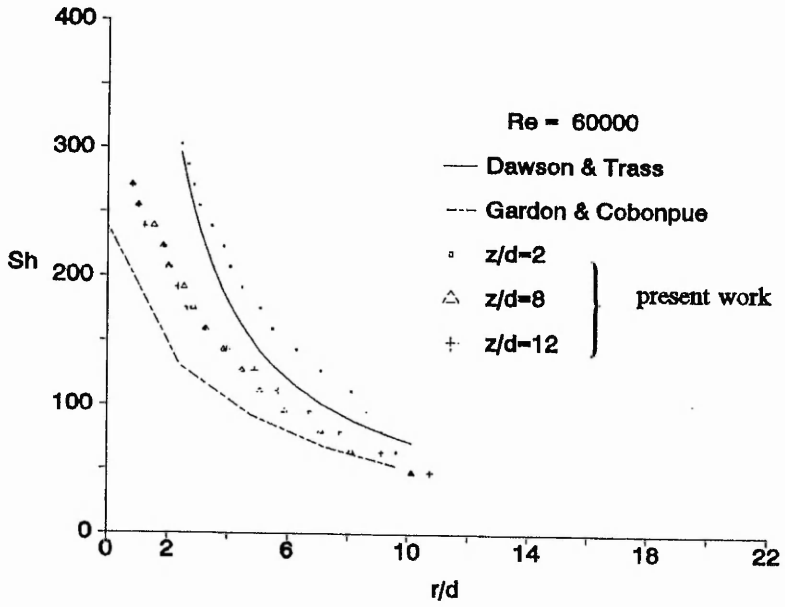

Figure 6.1.19 Comparison of *Sh* versus *r/d*, *Re* = 60000 with data from Gardon & Cobonpue (1962)

6.2 Numerical predictions for turbulent flow

This section reports the flow and heat transfer results obtained from the numerical predictions for a turbulent semi-confined jet impingement. The boundary conditions imposed on the model were summarised in chapter four and a sample of the PHOENICS Q1 input file for the turbulent case is given Appendix D. The results from these predictions are analysed to get an understanding of the trends that exist in the heat transfer distributions for the various boundary conditions investigated.

Fluid flow and heat transfer characteristics are predicted for turbulent jets with Re = 10000, 20000, and 60000 with z/d = 2, 6, and 12. The local Nu on the impingement surface are calculated from the predicted data for jets with flat and fully developed velocity profiles at exit from the nozzle. Comparisons have onnly been made between the current experimental and predicted data since no similar semi-confined investigations are available in the literature.

6.2.1 Predicted flow field

This section reports the predicted flow behaviour of the turbulent semi-confined impingement flow for Re = 20000. This Re is chosen because it is typically representative of the range of conditions studied in literature. The pressure ($P1$) distributions on the impingement surface are shown in Figure 6.2.1 for Re = 20000, z/d = 2 for both fully developed and flat profiled jet exit. Negative $P1$ gradient for the fully developed jet in the region r/d < 0.5 is significantly steeper than the corresponding flat jet. $P1$ gradient causes the characteristics of the boundary layer development to be changed and hence the Nu distribution within the stagnation region. Away from the jet centre line the $P1$ gradient decreases and the velocity and turbulence increase causing the boundary layer to go through a transition from laminar to turbulent flow.

Figure 6.2.2 shows the effect of the z/d on the $P1$ gradient for a fully developed jet. $P1$ for z/d = 2 is four times greater compared to the $P1$ values for z/d = 12, which

suggests significant jet diffusion and therefore substantial reduction in its momentum. The *P1* distribution for $z/d = 12$ is virtually flat showing that a well-mixed jet with a uniform velocity profile enters the impingement zone near the wall. The area over which this increased pressure exists extends radially out enclosing $r/d \approx 0.8$, showing that the jet width has expanded while traversing through this z/d gap. The boundary layer at the jet centre line is likely to be turbulent because the jet on exit from the nozzle is fully turbulent and well developed.

Figure 6.2.3 shows the *V1* distribution for $Re = 20000$, $z/d = 2$, at $r/d = 0.0$ and 0.5 for both the flat and developed jet. The maximum *V1* at $r/d = 0.5$ for the developed jet is 30 per cent greater than the corresponding flat jet. The maximum *V1* velocities at $r/d = 0.0$ are significantly less than the velocities at $r/d = 0.5$. Although the developed jet produces a significantly higher maximum *V1* compared to the flat jet at $r/d = 0.0$, which is reflected in the *Nu*. The boundary layer thickness is very thin in the impingement region and therefore the increased *V1* produce significantly higher heat transfer rates.

Figure 6.2.4 shows the *W1* distribution above the impingement wall at $r/d = 0.0$ for $Re = 20000$, $z/d = 2$ for both developed and flat jets. Deflection of *W1* commences at $z/d \approx 1$ above the impingement plate due to the presence of the wall boundary. Before this point, the *W1* is virtually unaffected and is thought to have similar characteristics to a free submerged jet flow. *W1* for the developed jet at $r/d = 0.5$ is also shown in this figure. It has a much reduced axial velocity, which decreases gradually until about $z/d \approx 0.7$ above the wall. At this point the rate of decrease becomes much greater due to the wall. *W1* for the flat jet at $r/d = 0.5$ shows substantial mixing as it emerges from the nozzle. This is because of the much higher shear flow produced between the free surface of the jet and the surrounding fluid. When $z/d \approx 0.7$ above the wall, shear mixing reduces W1 significantly. The decay rate of *W1* increases rapidly because of the presence of the wall.

Figure 6.2.5 shows the *KE* at $r/d = 0.5$, $Re = 20000$, $z/d = 2$ for both developed

and flat jets. The maximum *KE* is 4.0 per cent for the developed jet and 3.0 per cent for the flat jet. *KE* is a minimum at the wall surface and maximum within the boundary layer. There is a rapid increase in turbulence in the free shear layers of both jets. This could produce turbulence enhancement at this radial location on the wall and would have an associated increase in heat transfer at the same position.

Figure 6.2.6 shows stream line plots for $Re = 20000$, $z/d = 2$ for a flat profile jet. The flow structure is typical for all the investigated conditions. The bulk of the jet flow impinges on the wall and is deflected radially along the impingement plate while remaining attached to the surface until the outflow of the domain is reached. Space between the two confining boundaries is filled by the circulation bubble generated by the shear layer mixing. The circulation induced by the shear layer causes part of the outflow boundary to change to inflow into the domain. Although, there is some inflow, this does not greatly affect the heat transfer rate on the impingement wall.

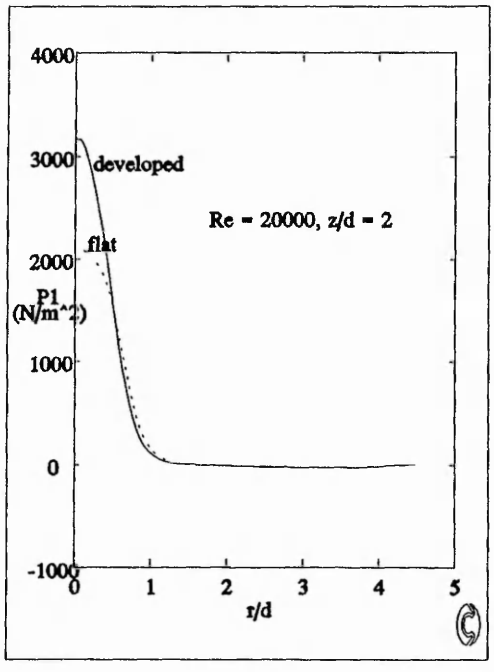

Figure 6.2.1 P1 versus *r/d*, *Re* = 20000, *z/d* = 2 and W_{jet} (flat and developed profiled)

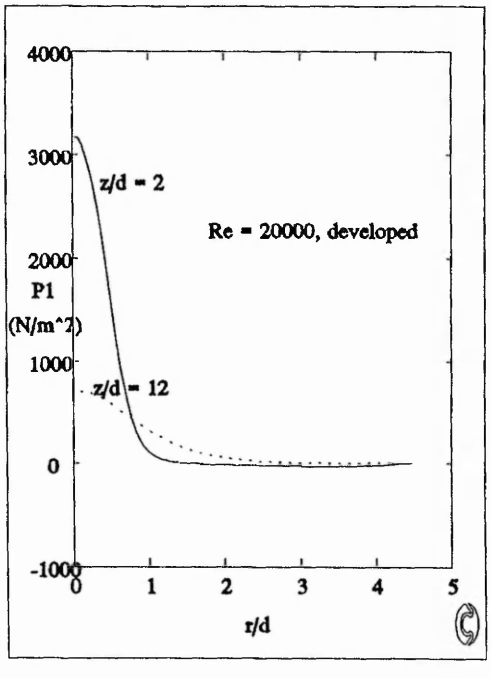

Figure 6.2.2 P1 versus *r/d*, *Re* = 20000, *z/d* = 12 and W_{jet} (flat and developed profiled)

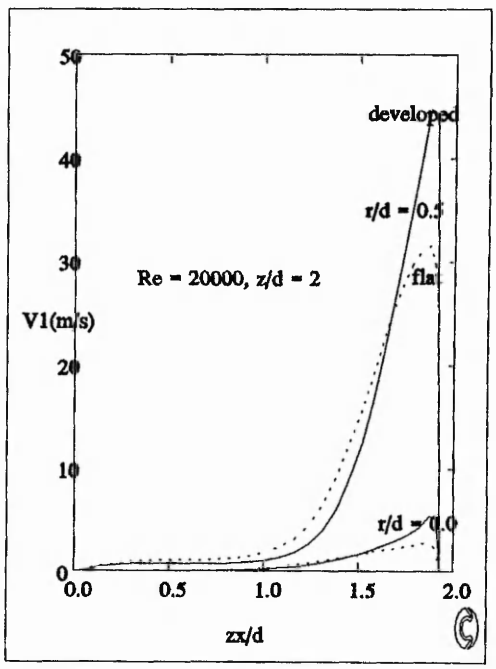

Figure 6.2.3 V1 versus zx/d, $r/d = 0.0$ and 0.5 $Re = 20000$, $z/d = 2$ and W_{jet} (flat and developed profiled)

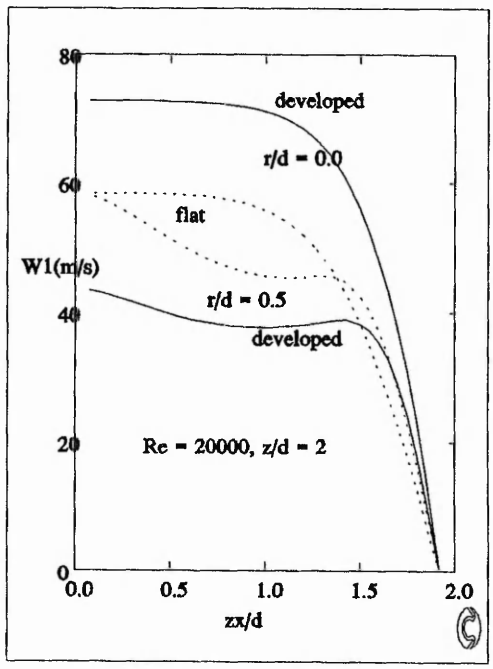

Figure 6.2.4 W1 versus zx/d, $r/d = 0.0$ and 0.5, $Re = 20000$, $z/d = 2$ and W_{jet} (flat and developed profiled)

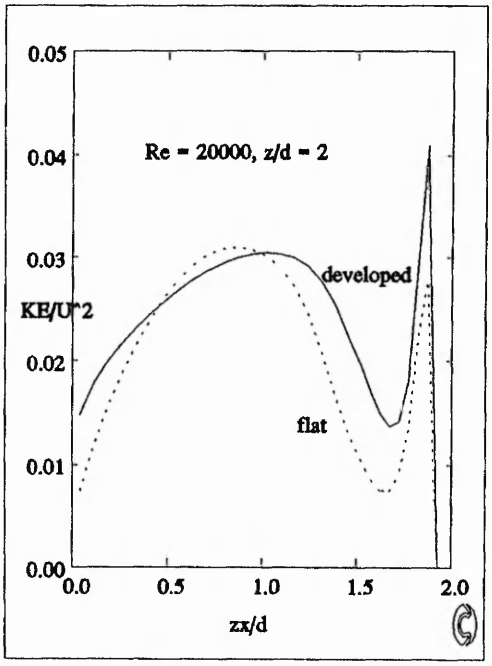

Figure 6.2.5 KE versus zx/d, r/d = of 0.5, Re = 20000, z/d = 2 and W_{jet} (flat and developed profiled)

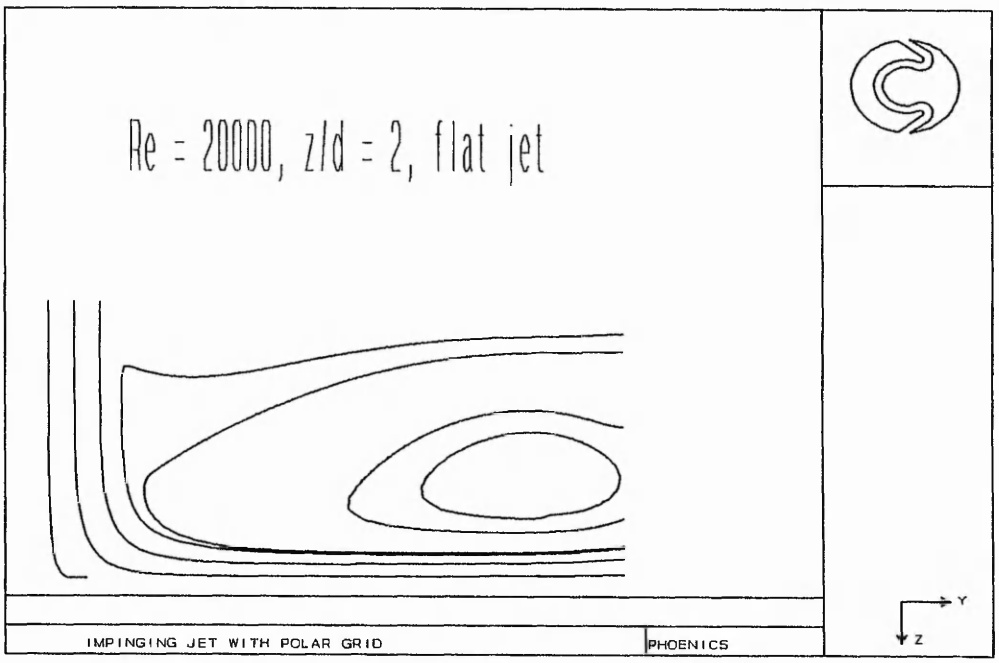

Figure 6.2.6 Whole field streamlines at Re = 20000, z/d = 2 and W_{jet} (flat profiled)

6.2.2 The effect of Re on impingement heat transfer

This section describes the heat transfer predictions for a semi-confined impingement from a fully developed turbulent jet. The effect of *Re* on the impingement wall jet *Nu* is considered. Figure 6.2.7 to Figure 6.2.9 show the *Nu* distributions for $z/d = 2$, 6 and 12, respectively. Figure 6.2.7 shows *Nu* has similar radial trends to each for the investigated range of *Re* with $z/d = 2$. In Figure 6.2.7 a local maximum in the *Nu* distribution occurs at $r/d \approx 0.8$, this is due to a combination of the numerical model grid size and an increase in turbulent kinetic energy. An important condition has to be met by the numerical grid size at the wall. This condition is that the grid *Re* has to be above a critical value of 132 for the turbulent log-wall function to be valid. But, this condition cannot be maintained and therefore the *Nu* is likely to be incorrect for this region. Further the *Nu* obtained from the jet centre line to $r/d = 1$ is likely to be incorrect because of the known shortcomings of the turbulence model in these regions. *Nu* calculated at the wall is inherently grid dependant and therefore the Y+ values have to be monitored so that the turbulent wall function is simulated. Trends observed in the wall jet region are as expected namely that the wall jet *Nu* shows significant *Re* and r/d dependence and the distributions are found to have a monotonic behaviour for the whole range of *Re* studied.

Figure 6.2.8 shows the predicted impingement *Nu* for the fully developed jet when $z/d = 6$. The trends for the *Nu* distribution are identical to those observed in the previous case and the valid range of *Nu* is again from $r/d > 1$. The *Nu* distribution for $z/d = 6$ is marginally higher than that for $z/d = 2$, which is probably due to the turbulent mixing in the jet that causes an increase in the *KE*. *Nu* distributions for low *Re* generate less steep *Nu* gradients in the wall jet region. This suggests turbulent mixing and entrainment flow into jet has significantly affected the *Nu*. The secondary peak is much reduced which indicates that jet development and turbulence is more effective when the *Re* is low.

Figure 6.2.9 shows the *Nu* distribution for $z/d = 12$ and a fully developed jet. The data for the low *Re* shows the wall jet *Nu* distributions are monotonic and

significantly reduced with the increased z/d. This suggests that the jet momentum and KE decay is rapid for separations greater than the potential core causing entrainment and turbulent mixing resulting in the amounts reaching the wall to be significantly different. It also has a dramatic effect on the local grid Re and therefore the validity of the turbulent log-wall function. Loss of validity of this wall function can be overcome by the wall grid size being increased, so that critical Re condition is reestablished. The Nu distribution for $z/d = 12$ is flat compared to that for the other values of z/d, a consequence of increasing z/d beyond its potential core length where the jet width is increased and the jet affected area is significantly wider.

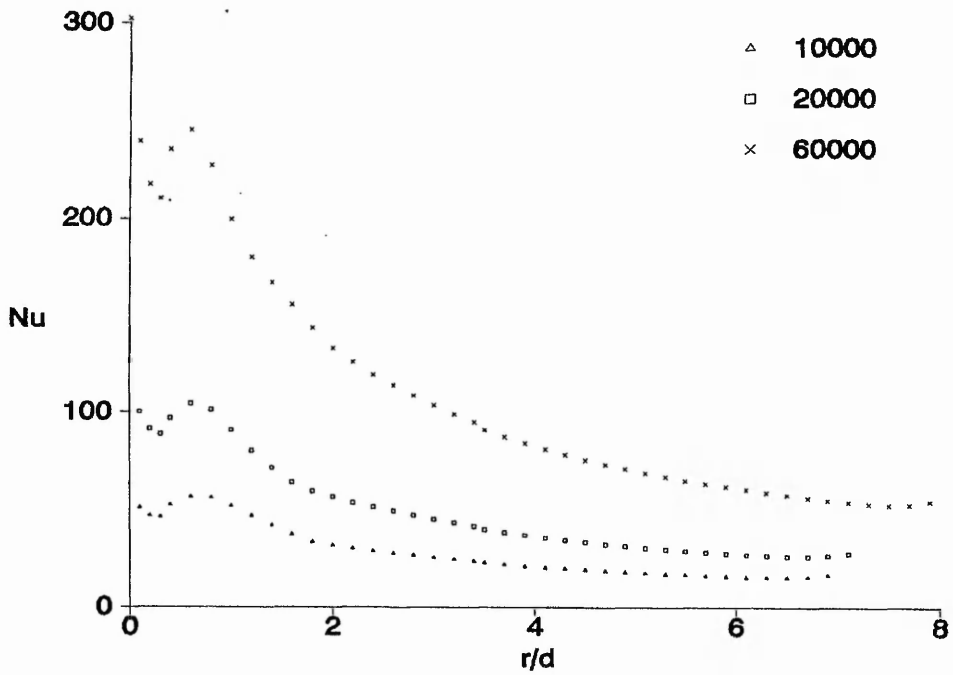

Figure 6.2.7 Predicted Nu versus r/d, $10000 \leq Re \leq 60000$, $z/d = 2$ and W_{jet} (fully developed)

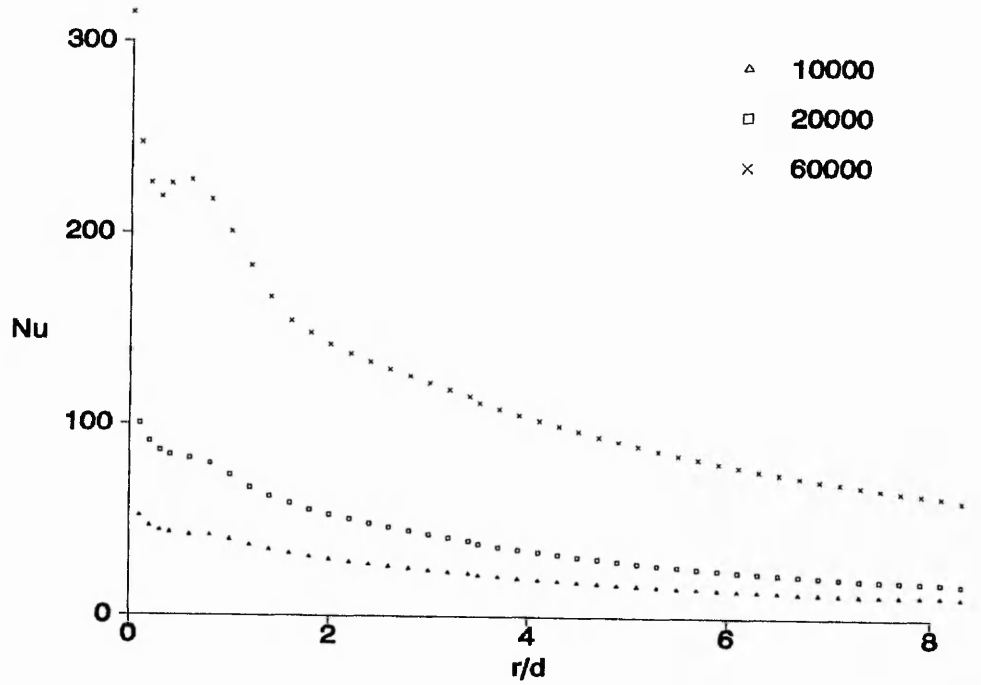

Figure 6.2.8 Predicted *Nu* versus *r/d*, $10000 \leq Re \leq 60000$, $z/d = 6$ and W_{jet} (fully developed)

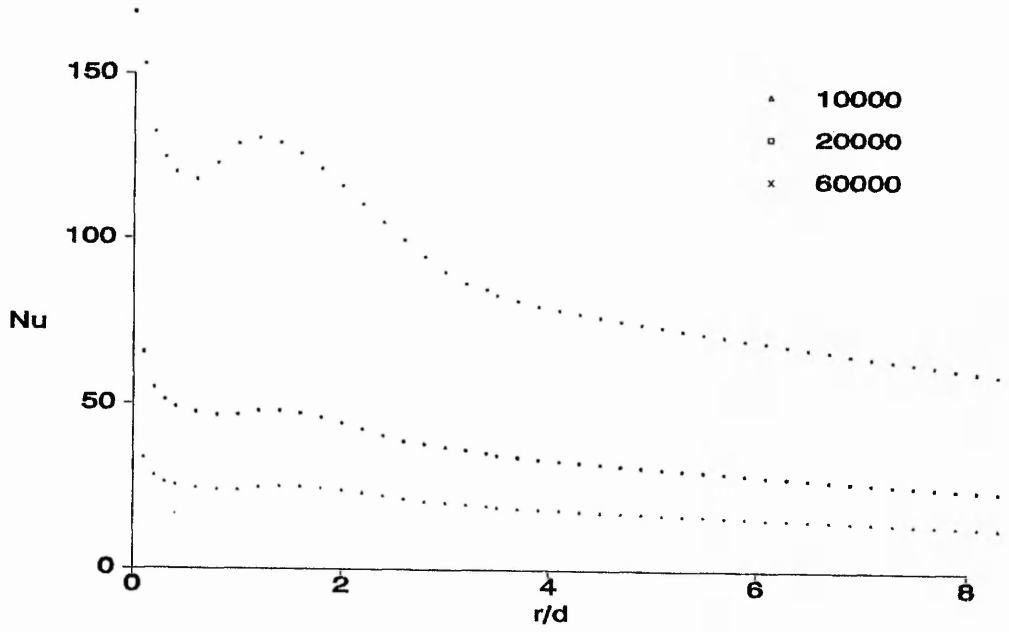

Figure 6.2.9 Predicted *Nu* versus *r/d*, $10000 \leq Re \leq 60000$, $z/d = 12$ and W_{jet} (fully developed)

6.2.3 The effect of jet velocity profile on impingement heat transfer

This section reports the comparison of the predicted *Nu* distributions due to the fully developed and flat turbulent jets impinging on a flat heated surface. Figure 6.2.10 to Figure 6.2.12 shows the *Nu* distributions for the three cases z/d = 2, 6 and 12 respectively. Each figure shows the *Nu* distribution for the two jet profiles with Re = 20000. This *Re* is chosen because it is representative of the range of *Re*. Figure 6.2.10 shows the *Nu* for z/d = 2 with this *Re* and the developed jet shows a local maximum *Nu* within the stagnation region, but the flat jet does not. The fully developed jet produces higher stagnation point *Nu* because its jet has an associated higher momentum at the centre line. The wall jet *Nu* distributions beyond $r/d > 2$ are identical for both jet profiles.

The *Nu* distribution for Re = 20000 when z/d = 6 is shown in Figure 6.2.11 Differences in the *Nu* distributions for the two jets are negligible and suggest both jet flows have attained the same flow characteristics before they reach the impingement region near the surface. The wall jet *Nu* distributions are identical and therefore the jet exit profiles do not affect these distributions. This is thought to be due to the turbulent mixing of the jet and for this z/d it has made the two jet flows have similar structure before impact.

Figure 6.2.12 shows the *Nu* distribution for z/d = 12 and Re = 20000. The flat jet has a significantly lower *Nu* distribution over the whole radial region when compared to the other jet, suggesting the momentum of the flat jet has decayed faster than for the developing jet. Ultimately, the wall jet *Nu* distributions tend towards different final values for each condition.

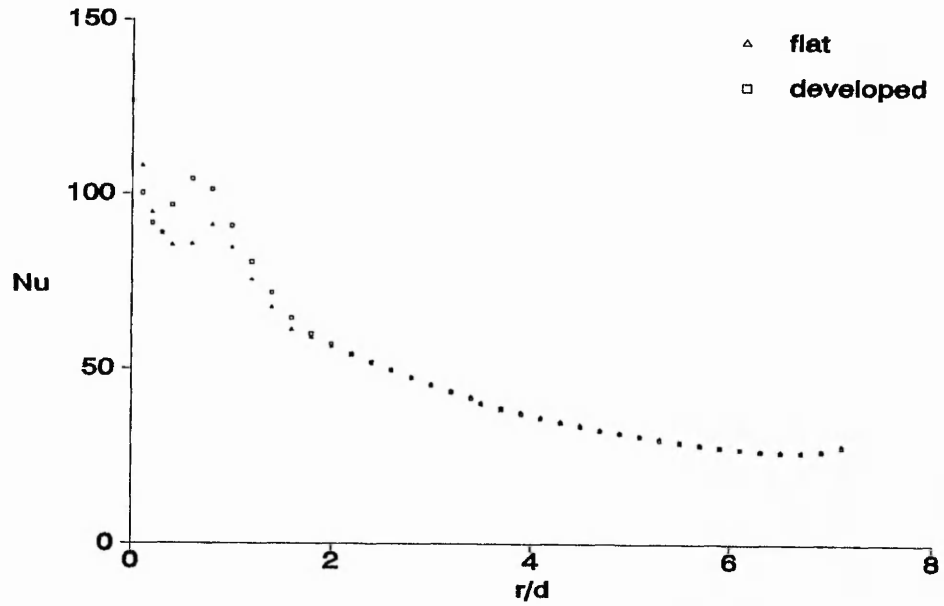

Figure 6.2.10 Predicted *Nu* versus *r/d*, *z/d* = 2, *Re* = 20000 and W_{jet} (flat and fully developed)

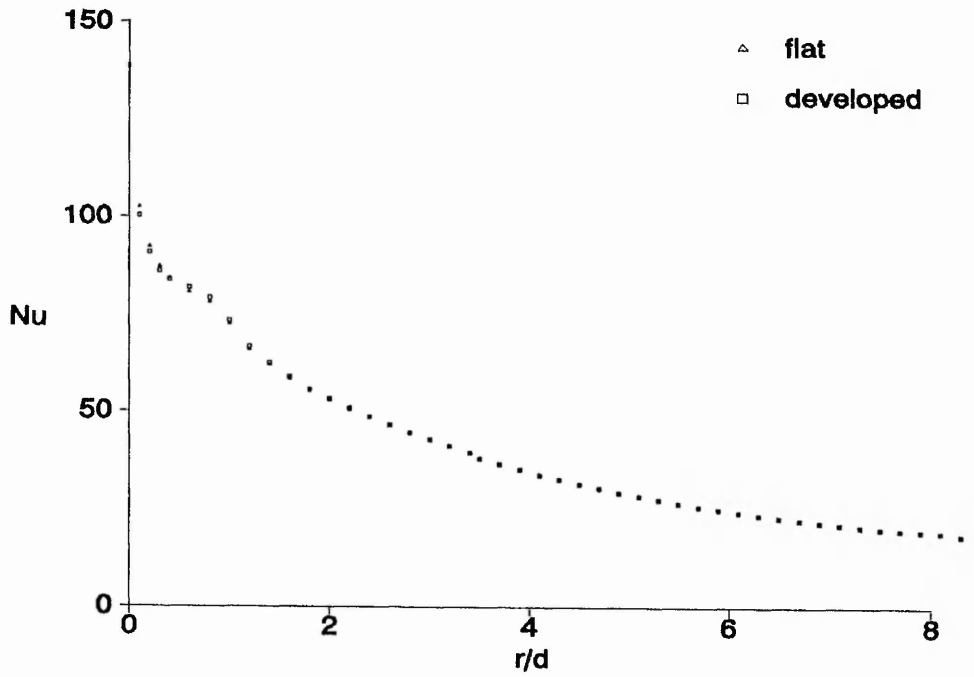

Figure 6.2.11 Predicted *Nu* versus *r/d*, *z/d* = 6, *Re* = 20000 and W_{jet} (flat and fully developed)

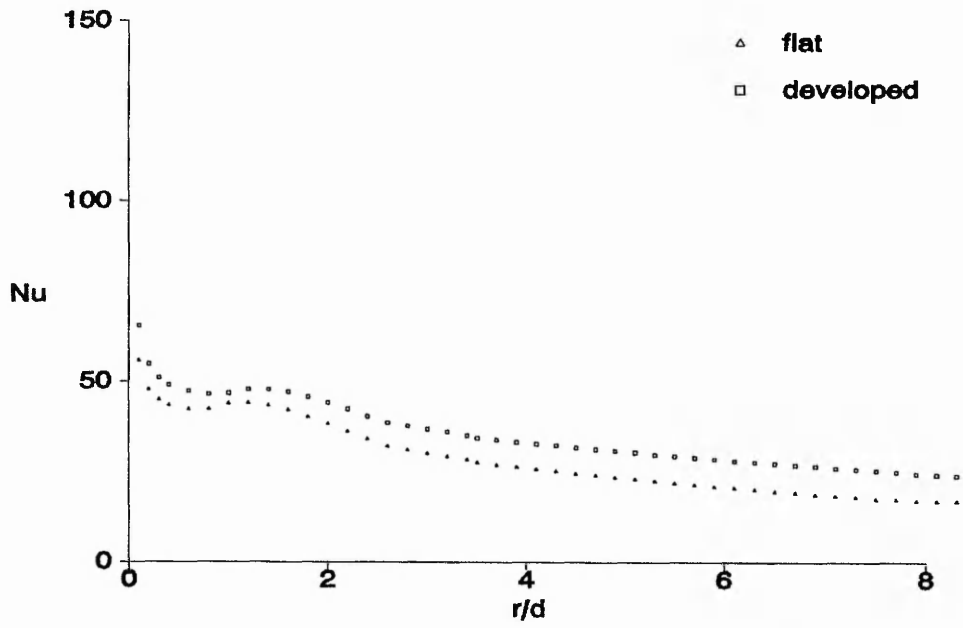

Figure 6.2.12 Predicted *Nu* versus *r/d*, *z/d* = 12, *Re* = 20000 and W_{jet} (flat and fully developed)

6.2.4 The effect of nozzle to plate spacing on impingement heat transfer

This section reports the effect of the *z/d* on the *Nu* distribution of impinging turbulent jets with flat or developed velocity profiles. Figure 6.2.13 to Figure 6.2.14 show the *Nu* distributions obtained for a flat jet with *Re* = 20000 and 60000, respectively. Figure 6.2.15 to Figure 6.2.16 show *Nu* for a fully developed jet, with Re = 20000 and 60000, respectively and all these figures contain data for *z/d* = 2, 6 and 12.

Figure 6.2.13 shows *Nu* distribution for a flat jet of *Re* = 20000, the data for *r/d* > 1 a significant dependence on *z/d* is seen, with the wall jet *Nu* for all the *z/d* converging to a single distribution. The data suggests that the optimum jet development length should be somewhere between *z/d* = 2 and 6. Trends of the *Nu* distributions are as expected, i.e. the further the jet is from the wall, the lower the *Nu* and the wall jet is not affected.

The *Nu* distributions for $Re = 60000$ with a flat jet are shown in Figure 6.2.14, it shows the same trends as those for the low *Re*. However, the magnitude of the *Nu* near the stagnation region decreases significantly when the separation $z/d = 12$, but the difference in the wall jet *Nu* becomes small. The *Nu* distribution for $z/d = 12$ has a local maximum at $r/d \approx 1.5$, which is further away to the jet centre line than the cases of $z/d = 2$ and 6. The wall jet *Nu* for $z/d = 2$ shows a rapid decline in value, because the temperature next to the wall attains the same temperature as the wall. Heat flux from the wall is suppressed, which in turn lowers the *Nu* and therefore data beyond this point is omitted for clarity.

Figure 6.2.15 shows the *Nu* distribution for a fully developed jet with $Re = 20000$ and $z/d = 2$, 6 and 12. The range of *Nu* for the three z/d shows similar trends to those of the flat jet in Figure 6.2.13. The small z/d produces high *Nu* shown in Figure 6.2.15. Valid data is for $r/d > 1$, the *Nu* distributions in the wall jet region for the $z/d = 2$ and 12 merge. However, for $z/d = 6$, the *Nu* distribution is low for $r/d > 4.0$ compared to the other z/d. This is suspected to be due to the heat flux at the wall being suppressed because of temperature saturation at the wall and adjacent grid points.

For the fully developed jet with $Re = 60000$ the *Nu* distributions are shown in Figure 6.2.16. The wall jet *Nu* for large z/d converge to a single value. The distribution for $z/d = 2$ shows a significant drop in *Nu* and is again due to the same effect as discussed in above case. The fluid temperature between the plates is higher due mainly to the circulation mixing in the flow. This increases the boundary layer temperature on the wall and therefore suppresses the heat transfer.

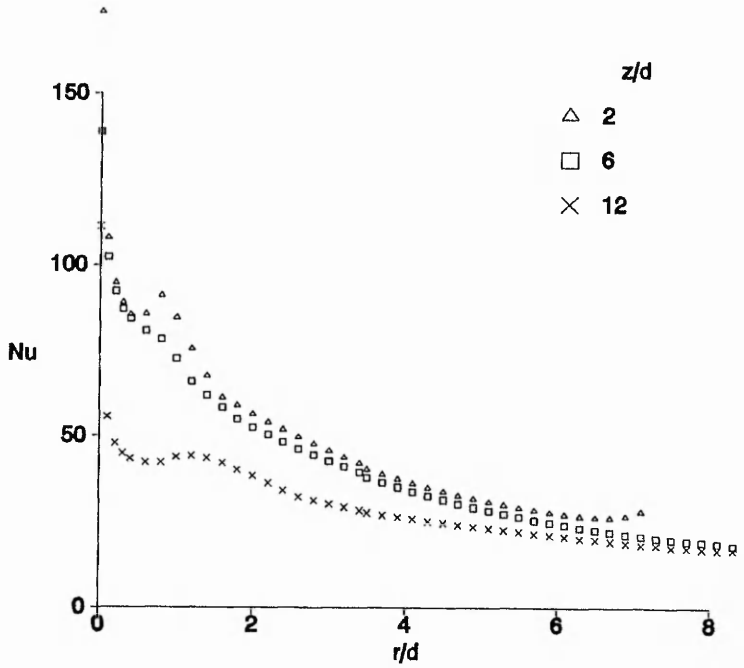

Figure 6.2.13 Predicted *Nu* versus *r/d*, *Re* = 20000, $2 \leq z/d \leq 12$ and Wjet (flat)

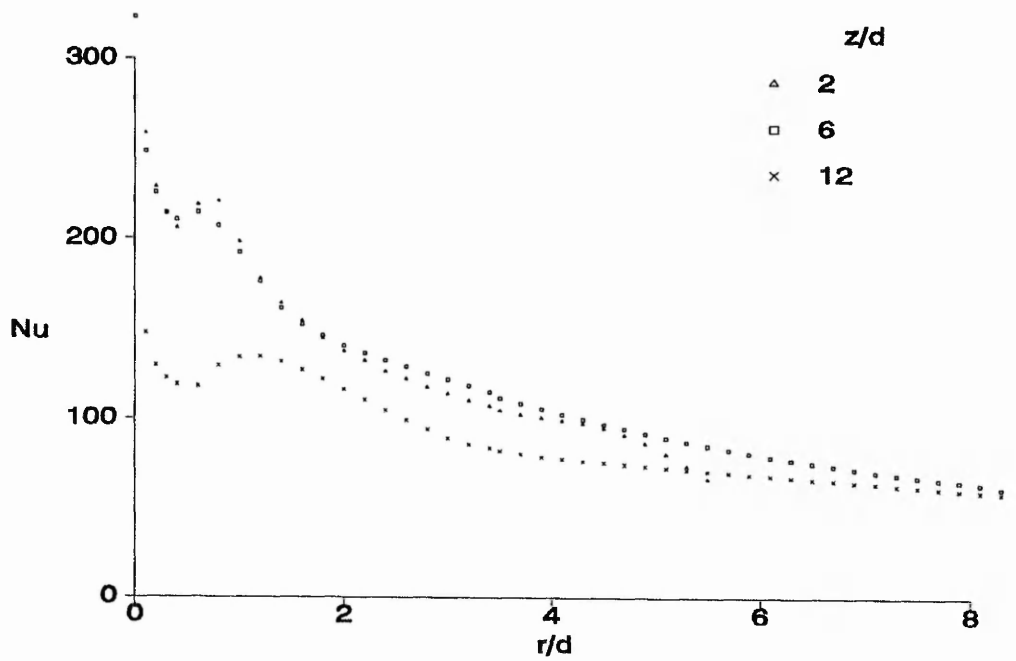

Figure 6.2.14 Predicted *Nu* versus *r/d*, *Re* = 60000, $2 \leq z/d \leq 12$ and W_{jet} (flat)

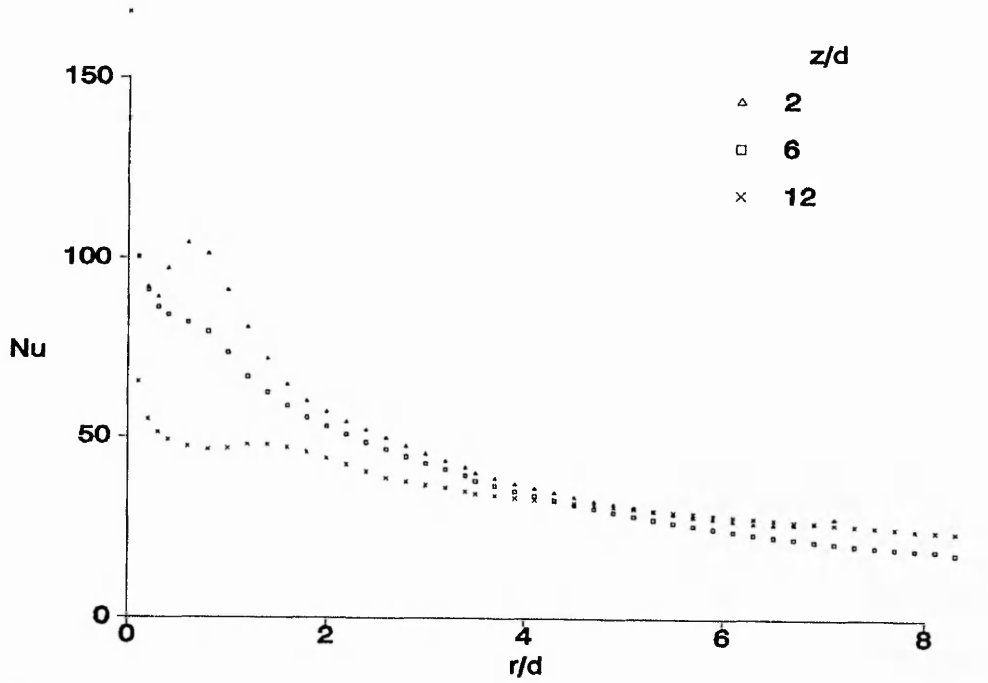

Figure 6.2.15 Predicted *Nu* versus *r/d*, *Re* = 20000, $2 \leq z/d \leq 12$ and W_{jet} (fully developed)

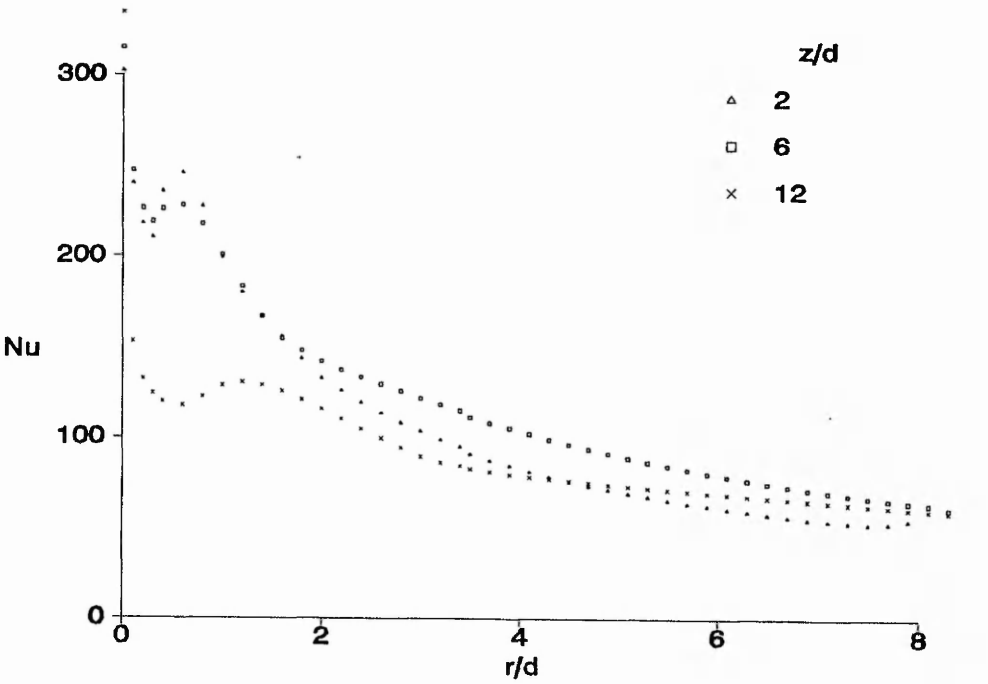

Figure 6.2.16 Predicted *Nu* versus *r/d*, *Re* = 60000, $2 \leq z/d \leq 12$ and W_{jet} (fully developed)

6.2.5 Comparison of predicted heat transfer with experimental results

This section reports on the comparison of the predicted wall jet *Nu* with the current experimental data and available analytical solution of Dawson and Trass (1966). Figure 6.2.17 to Figure 6.2.19 show *Nu* distributions for the fully developed jet with Re = 10000, 20000 and 60000 respectively and z/d = 2. The wall jet *Nu* for Re = 10000, Figure 6.2.17 is similar to the analytical data when $r/d > 4$. Stagnation region *Nu* are considered erroneous because of the limitations of the numerical modelling of the wall boundary near stagnation regions. Experimental wall jet *Nu* are higher than those obtained either by analysis or prediction. This discrepancy is associated with the failing of the initial assumptions made while constructing the predictive models. The wall jet *Nu* for Re = 20000 and 60000 are shown in Figure 6.2.18 to Figure 6.2.19 respectively, which shows the error between the predicted and analytical data reducing when $r/d > 4$. But, the experimental wall jet *Nu* is significantly higher in value compared to either the predicted or analytical data for the same reasons as discussed before.

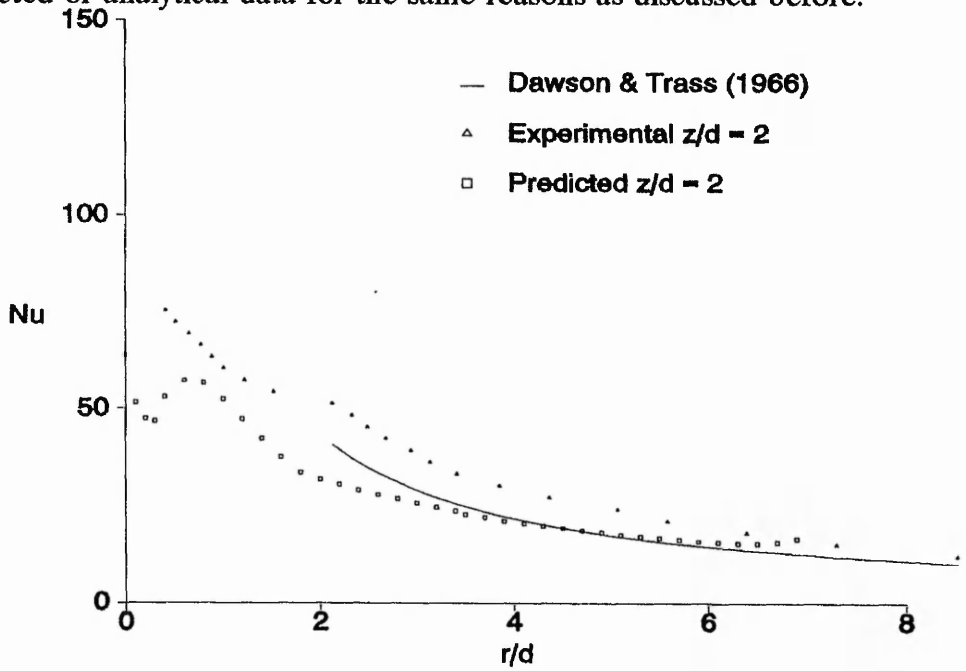

Figure 6.2.17 *Nu* versus r/d, Re = 10000, z/d = 2 and W_{jet} (fully developed)

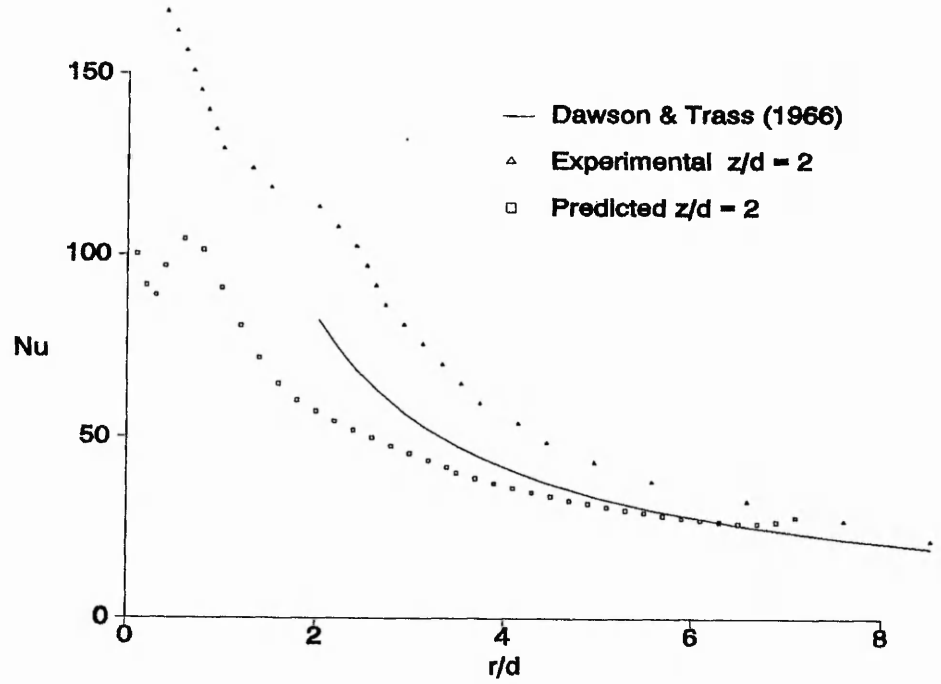

Figure 6.2.18 *Nu* versus *r/d*, *Re* = 20000, *z/d* = 2 and W_{jet} (fully developed)

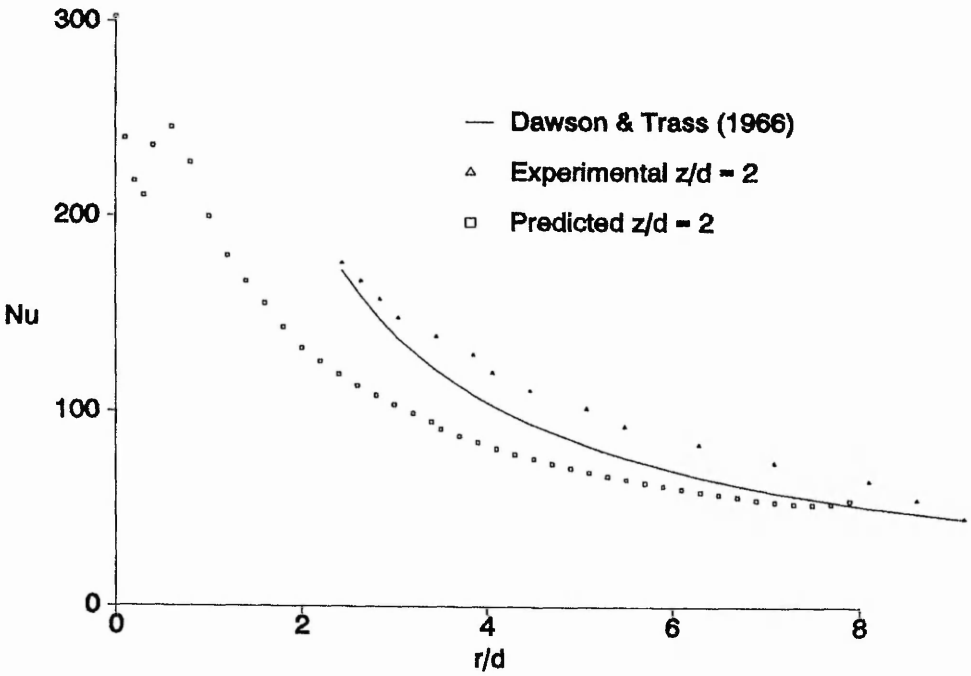

Figure 6.2.19 *Nu* versus *r/d*, *Re* = 60000, *z/d* = 2 and W_{jet} (fully developed)

6.3 Conclusions

A swollen polymer and holographic double exposure holographic technique is used to obtain mass transfer data in a semi-confined turbulent impingement jet flow. The experimental *Sh* shows a significant dependence on *z/d*. Flow and turbulence measurements for the current geometry have been studied by Ashforth-Frost (1994) who has explained some causes of the significant transport phenomena observed in the semi-confined geometry. *Sh* obtained for the wall jet region shows that higher values occur for lower *z/d*, which also is shown in the *Nu* distributions of Gardon and Akfirat (1965). Turbulence in the flow for $Re = 3000$ is considered negligibly small and the wall jet *Sh* are seen to be closer to each other for the various *z/d*. For $Re = 5000$, the *Sh* are significantly dependent on the *z/d*. The jet for $z/d > 8$ is considered completely mixed and therefore the wall jet flow is expected to have a lower momentum implying a lower *Sh*. The lower *z/d* has the effect of increasing the momentum passing through the restricted space between the semi-confinement plates and this has the desired effect of increasing the wall jet *Sh*.

The experimental *Sh* distribution for $z/d = 2$ and $Re = 10000$ to 35000 show a change in the distribution at around $r/d = 2$. This is also observed and discussed by Gardon and Cobonpue (1962) as the laminar to turbulent boundary layer transition zone. This effect is not observed in the higher *z/d*, as the jet and therefore the boundary layer would be turbulent at the outset.

The stagnation point *Sh* cannot be obtained with the current experimental technique and hence the effect of the jet potential core cannot be addressed. The length of the nozzle used, is greater than 40 *d* and according to Obot et al (1979), the shape of the nozzle does not affect the flow characteristics from the nozzle exit, but the *Sh* on the impingement surface is affected only when $z/d < 6$.

The turbulent experimental wall jet Sherwood data are regressed into the following equation

$$Nu = 0.115\ (Re)^{0.775} \left(\frac{r}{d}\right)^{-1.1} \left(\frac{z}{d}\right)^{-0.202} \quad \textbf{(6.2)}$$

within the range

$3000 < Re < 60000$

$r/d > 2.5$

$2 < z/d < 12$

and in the turbulent transition region the results are regressed into the equation

$$Nu = 0.172\ (Re)^{0.666} \left(\frac{r}{d}\right)^{-0.307} \left(\frac{z}{d}\right)^{-0.276} \quad \textbf{(6.3)}$$

within the range

$3000 < Re < 60000$

$r/d < 2.5$

$2 < z/d < 12$

The above correlation equations were subjected to the Monte-Carlo uncertainty error simulation technique and the confidence intervals were obtained. The 95 per cent confidence interval determined for the equations have a maximum error of ± 30 per cent. The same uncertainty analysis method was used on the experimental data transformed into Nusselt numbers *Nu* and 95 per cent confidence level was found to have an error band of ± 22 per cent.

A study of the flow characteristics has enabled physical interpretations of the heat transfer in the semi-confined jet impingement configuration. The predicted pressure (*P1*) distributions and gradients are significantly different between the two jet profiles investigated and when *z/d* changes from 2 to 12. The negative pressure gradient in the stagnation region maintains a stable laminar boundary layer. The radial and axial velocities (*V1*, *W1*) show significant differences existing in the flow for the two jet profiles and consequently its effect on heat transfer. The turbulent kinetic energy levels predicted above the impingement zone are erroneous because of the weakness of the κ - ϵ turbulence model at the wall and this is a major difficulty with the prediction of *Nu*.

The predicted *Nu* distribution for a fully developed jet with $z/d = 2$ is higher compared to the other z/d values. A local maximum in the *Nu* distribution is observed at $r/d \approx 0.8$. This local phenomena have been observed experimentally by Gardon and Cobonpue (1962) and Obot et al (1982), they explained its existence as the effect of the transition of the laminar boundary layer into a turbulent one. More recently it has been shown by Ashforth-Frost (1994) that this enhancement is the effect of increased turbulence energy levels in this region, which causes local enhancement in the *Nu*.

The two jet velocity profiles do not greatly affect the wall jet *Nu* distributions. However, when $z/d = 12$ a difference is noticed, but this becomes negligible for $z/d < 6$. This suggests an optimum $z/d \approx 6$ for the highest wall jet *Nu* for the fully developed jet with its potential core.

Numerical prediction of flow and heat transfer show possible trends that are present for the various flow conditions simulated. However, the results should be treated with caution, in that they do not give accurate answers for a particular flow situation being simulated. Serious difficultly with the current method of modelling turbulence quantities is that erroneous results are predicted in stagnation and separated flows. The current predictions help to illustrate the broad range of heat transfer values that can be generated for the various boundary conditions.

CHAPTER 7
CONCLUDING REMARKS

A study of a recently compiled database of 1167 jet impingement articles show that only 7 per cent of these references referred to some form of confinement in the jet impingement flow. It is concluded from this review that a substantial gap in our knowledge exists in relation to the energy and mass transport process in semi-confined jet impingement flows. The current work has supplied some of the data but a lot more needs to be done to get a fuller understanding. From this database of references, some 41 per cent are publications from within the last ten years. 55 per cent of the total number of papers include the study of heat transfer and 14 per cent are on the study of mass transfer with 20 per cent on numerical predictions. Studies of the flow field in the impingement geometry are contained in 27 per cent of the references. Creation of a database of jet impingement references was one of the first objectives of this research project that has now been made available commercially on a personal computer.

Mass transfer in a submerged semi-confined axisymmetric air jet impingement flow has been investigated experimentally using the swollen polymer technique. A plain nozzle tube of d = 4.9 mm is used and provides an axisymmetric fully developed jet flow for the experimental investigation. The physical and geometric conditions chosen for the current experimental work are based on similar works in literature. The confinement is designed to extend radially out to r/d = 17 and the nozzle length of 70 d is used to ensure a fully developed jet in the laminar flow range. Experimental conditions investigated are z/d = 2 to 12 and nozzle Re = 500 to 60000.

The swollen polymer and holographic interferometry techniques have been selected for measuring mass transfer. The method is verified with calibration tests of a laminar unconfined jet impingement. The wide range of quality experimental data has been obtained with estimates of uncertainties of ± 22 per cent with a 95 per cent confidence level using a statistical Monte-Carlo method. The largest single contributor to the overall uncertainty in the data is the vapour pressure data of the

swelling agent.

The semi-confined jet impingement is generated with a rig designed and developed from the extensive review of conditions used in literature and the ease of reproducibility of the experimental conditions. The literature shows that a detailed definition of the actual geometry used should be given because the flow is highly dependent on the geometry. The rig is placed on a vibration free optical table for stability during the experiment. The following boundary conditions are imposed on the experimental arrangement; an iso-concentration mass transfer surfaces, analogous to an isothermal surface, an isothermal jet passing through a settling plenum chamber impinging on the transfer surface.

The experimental tests are planned and conducted in random order to eliminate systematic errors within the experimental procedure. Initial replicate tests are done for specific conditions, which showed good repeatability of the method. A statistical Monte-Carlo technique is used to estimate the confidence intervals of the experimental measurements, utilising the instrument measuring resolutions and sensitivities for the analysis.

The refractive indices of the swollen polymer with ethyl salicylate and n-tetradecane is measured independently in the current work. The refractive indices for polymer/ethyl salicylate mix are correlated in the following equation for the temperature range of 5 - 30°C.

$$R_f = 1.48 - 0.00017\ T$$

where T is the environment temperature in degrees Kelvin

The saturated mass swelling percentage of the swollen polymer with ethyl salicylate is correlated by the following equation

$$M_s = 0.190\ T - 38.4$$

The 95 per cent confidence interval is estimated to be ± 5 per cent.

The refractive index of the swollen polymer with n-tetradecane for the same temperature range of 5 - 30°C is correlated by the following equation

$$R_f = 1.51 - 0.000288\ T$$

and the mass swelling percentage with n-tetradecane is correlated by

$$M_s = 0.705\ T - 120$$

Vapour pressure of ethyl salicylate in air with a 95 per cent confidence interval of ± 15 per cent has been measured by Zangeneh (1990). His results corroborate Paterson et al's (1987) data that are the most recently accepted values.

The air diffusion coefficients for ethyl salicylate has been measured in the temperature range of $297 < T < 318$ Kelvin with ± 50 per cent uncertainty in the data at a confidence level of 95 per cent. A correlation for the diffusion coefficient for ethyl salicylate is produced as,

$$D_f\ (\mathrm{cm^2/s}) = 6.08\mathrm{x}10^{-7}\ T^{1.98}$$

PHOENICS a commercial finite volume code is used to simulate numerically the fluid flow and heat transfer in a semi-confined jet impingement geometry. The software is easy to operate and has a well-developed user interface with its own input language. It is singled out as the best available research tool, without having to resort to a single purpose written code, which is beyond the scope of the current research objectives.

A grid independency study of a semi-confined laminar jet impingement geometry is carried out and an optimised arrangement of the grid is found to be a 32 x 90 mesh with cell size at the wall as small as 0.025 mm.

The predicted laminar flow field is qualitatively assessed to give a better understanding of its effect on the *Nu* distributions. The radial velocity due to a parabolic jet is a maximum near the impingement wall. Axial velocity at the jet centre is affected by the presence of the impingement wall at $z/d \approx 1$ above the wall. The stream line plot, shows the circulation bubble, jet and wall jet regions and none of them show any extraordinary flow characteristics. The outflow region is caused to have entrained inflow due to the presence of the semi-confinement boundary.

From the numerical study of the laminar semi-confined jet impingement geometry, it is shown that the impingement *Nu* distribution is not significantly dependent on the *z/d* unless $Re < 100$.

Stagnation point *Nu* for the laminar parabolic jet is twice that of the flat jet exiting with the same nozzle *Re*.

The *Nu* for a laminar flat jet has a minimum at the stagnation point and a maximum *Nu* at $r/d = 0.5$. This is the effect of the reduced pressure gradient from the flat jet, which greatly affects the velocity in this region.

Turbulent *Nu* are predicted for flow rates ranging between $3000 < Re < 60000$. The near wall turbulent energies and dissipation rates at the stagnation point are incorrectly predicted by the k - ϵ turbulence model, which in turn causes the prediction of the *Nu* to be in error.

A local peak in the predicted *Nu* distribution is seen at $1 < r/d < 2$ and this is also observed in the mass transfer experimental measurements.

The jet velocity profile from the nozzle exit for turbulent flows does not affect the wall jet *Nu* distribution for $2 < z/d < 6$. Confinement reduces jet entrainment but seems to not affect *Nu* distribution.

The experimental wall jet *Sh* corroborates the predicted *Nu* in the semi-confined jet impingement geometry. The effect of *z/d* on the wall jet *Nu* distribution is insignificant, but closer to the stagnation point, *Nu* decreases with increasing *z/d*.

Wall jet *Sh* for laminar semi-confined impinging jet are experimentally obtained for flow rates ranging from $500 < Re < 2000$ and separations of $2 < z/d < 12$. Comparisons of the semi-confined *Sh* with analytical solutions for the unconfined jet impingement geometry are presented. The difference in the data is less than the confidence interval of the experimental work and the effect of confinement on the wall jet transfer rate cannot be ascertained.

Wall jet *Sh* for the turbulent semi-confined impinging jet are experimentally obtained for flow rates ranging between $3000 < Re < 60000$ and separations between $2 < z/d < 12$. A 95 per cent confidence interval estimated in the *Sh* is approximately ± 22 per cent. The experimental semi-confined wall jet *Sh* are compared to available unconfined jet impingement data and it is shown that agreement in the results is obtained.

The experimental laminar wall jet *Nu* are regressed as

$$Nu = 0.254\ (Re)^{0.734} \left(\frac{r}{d}\right)^{-1.42} \left(\frac{z}{d}\right)^{-0.139} \qquad \textbf{(6.4)}$$

for the following range of

$500 < Re < 2000$

$r/d > 2.5$

$2 < z/d < 12$

The laminar transition region *Nu* equation is

$$Nu = 0.156\ Re^{0.714} \left(\frac{r}{d}\right)^{-0.811} \left(\frac{z}{d}\right)^{-0.121} \qquad \textbf{(6.5)}$$

for the following range of

$500 < Re < 2000$

$r/d < 2.5$

$2 < z/d < 12$

More correlation equation power indices for other selected ranges of conditions are tabulated in Chapter 5.

Confidence interval to a level of 95 per cent in the laminar correlation equations are estimated with the Monte-Carlo simulation technique to be less than ± 53 per cent with the precision estimates of the indices included in the analysis.

Comparison of the experimental laminar wall jet *Sh* with the analytical equation of

Scholtz and Trass (1966), shows good agreement in this region. It is concluded from the laminar flow results that the semi-confinement boundary does not have a significant effect on the wall jet *Sh*.

The experimental turbulent wall jet *Nu* are regressed as

$$Nu = 0.115\ (Re)^{0.775} \left(\frac{r}{d}\right)^{-1.1} \left(\frac{z}{d}\right)^{-0.202} \qquad \textbf{(6.6)}$$

for the range

$3000 < Re < 60000$

$r/d > 2.5$

$2 < z/d < 12$

The turbulent transition region *Nu* is regressed as

$$Nu = 0.172\ (Re)^{0.666} \left(\frac{r}{d}\right)^{-0.307} \left(\frac{z}{d}\right)^{-0.276} \qquad \textbf{(6.7)}$$

for the range

$3000 < Re < 60000$

$r/d < 2.5$

$2 < z/d < 12$

The *Re* power index shows agreement with available correlations equations for unconfined jet impingement found in literature. Further equation indices for turbulent jet impingement flow are is tabulated in Chapter 6. Confidence interval to a level of 95 per cent in the turbulent correlation equations are determined using the Monte-Carlo technique and found to be less than ± 30 per cent.

Comparison of the experimental and numerical wall jet heat transfer results for the lower laminar Reynolds numbers shows that the predicted results are significantly reduced by diffusion mixing when compared to the experimental data. This underprediction within the wall jet *Nu* is reduced when the Reynolds numbers is increased.

The turbulent wall jet heat transfer predictions are compared to the experimental and analytical data and good agreement in the distant wall jet region is obtained.

The contribution made to the mass transfer technique has been to investigate by appropriate selection of the experimental conditions and obtain full images of the deformed test area so that fringe number identification is simplified. The effect of semi-confinement has been to reduce mass transfer in the wall jet region but this is not conclusive because the uncertainties of the material properties needed for the experimental technique were high and therefore the overall experimental uncertainty was large and the effect of the confinement could not be isolated. Refractive indices of the swollen polymer have been obtained independently and diffusion coefficients of the swelling agent in air have been experimentally found at the low temperatures encountered in the experimental programme. An extensive study over a wide range of wall jet mass transfer has been completed and the resulting data has been correlated into suitable equations and these have been subjected to statistical methods to provide their uncertainty limits.

The contribution made to the numerical technique is a detailed grid independency study for a numerical model of the semi-confined jet impingement geometry and appropriate grids meshes found. Heat transfer coefficients from the impingement surface have been determined from the numerical model by a specially developed code that interfaces with the simulation software.

CHAPTER 8
FURTHER WORK AND RECOMMENDATIONS

This chapter reports on the recommendations for further work from the experience and knowledge gained from the current research work.

The experimental method used permits measurements of *Sh* covering the radial range starting from $r/d = 0.5$ and extending well into the wall jet region. Further work is recommended to obtain measurements of *Sh* at the stagnation point of the semi-confined jet impingement by using the real time holographic technique.

The scope of the current experimental work did not encompass measurements of flow and turbulence quantities in the semi-confined region. These measurements are being done by Ashforth-Frost (1994) to assist with a better physical understanding of the transport process on the impingement surface. It is recommended that more detailed flow measurements be made which may be used to validate new turbulence models. The semi-confined jet impingement configuration has been chosen by the UK computational fluid dynamics community as one of their future bench-mark test case for comparing new turbulence models.

The current experimental programme uses a plain nozzle with a fully developed jet exit velocity profile. It is recommended that further investigation of a flat jet be undertaken as many industrial applications use flat jets because of the ease with which they can be generated with a short nozzle. A study of the nozzle geometry is also suggested, because the effects of this geometry become significant on the transport process for lower values of z/d.

Manual post-processing of the holographic experimental data is a slow and laborious process. Semi-automation can be an improvement to this procedure and should make the technique more attractive to many other laboratories. Image processing technology has advanced significantly in recent years and this technology can quite easily be used to semi-automate the processing of the holographic interferograms.

Measurement resolution of the current holographic technique is excellent, provided the data is needed only at discrete points, i.e. the maximum or minimum locations of the resulting interference fringes. The measurement resolution of this technique can be increased by incorporating a phase shifting method with the holography, which will improve the resolution by an order of magnitude, Wang et al (1994). The resulting interferograms can be analysed using an image processing system because of the vast amount of data gathered makes it impossible to handle manually.

The holography technique requires the use of a conventional photography for recording the images. However, Electronic Speckle Pattern Interferometry (ESPI) has been used for studying jet impingement be it only to a limited extent, it is recommended that all future work be done with ESPI. The resulting specklegrams obtained from this technique can be directly read into an image processing system using a standard CCD video camera without the intermediate photographic process required for the conventional approach. The ESPI technique helps increased data acquisition speeds and subsequent processing as the acquired images are in digital format, which can be read directly to a computer to be analysed. The quality of the fringe pattern from the ESPI technique is poor compared to that of the holographic technique, the numbers of fringes generated by the ESPI and holography are the same. A most important advantage of ESPI however over the other techniques is the significant reduction in elapsed time of the manual data processing. An additional advantage is the need for a skilled technician to operate the experimental technique is eliminated.

A further recommendation for the ESPI technique is to incorporate phase shifting with it, because the resolution of the data is again increased as shown in Wang et al (1994). The combination of the higher resolution and semi-automated processing of the resulting data makes this technique ideal for non skilled personnel and probably would make this technique attractive to many research laboratories.

A study of temperature field within the jet impingement region has been undertaken as a related topic to the current research, Dobbins et al (1991) and Button et al (1991). Holography and ESPI are both used and the observations made about the real time characteristics of the flow are discussed. Unfortunately, limitation on time only allowed a few results to be obtained and therefore further investigation is recommended into this work. It does provide valuable insight into the transient nature of the flow and its resulting effects on the transport process.

The current numerical simulations of turbulent jet impingement flow produced inaccurate modelling of turbulent quantities around the stagnation point. This discrepancy is a main research topic for many well-known groups and their work is aimed at making modifications to the turbulence equations to fit the empirical data. A user interface within the PHOENICS package allows access to the coefficients of the turbulence equations that can be modified if it is so desired. This could be a further topic that can be pursued.

Numerical predictions of flow and convection are significantly dependant on the grid as shown by Jambunathan et al (1989). A study of grid dependency is essential before undertaking any numerical analysis. The turbulence modelling of the jet impingement geometry shows the transport quantity has a significant dependency on the near wall grid node location. This is another topic that needs many investigations to understand the interaction of the wall boundary to the main flow.

Numerical predictions by Huang et al (1978) with suction applied to the impingement wall showed increased heat transfer because of the reduction of the boundary layer thickness. Further investigations of these phenomena with suction at the impingement wall with the semi-confined geometry will be valuable.

CHAPTER 9
REFERENCES

Agarwal, R.K. and Bower, W.W., 1982. Navier-Stokes computations of turbulent compressible two-dimensional impinging jet flow fields. **AIAA J.**, 20(5), pp. 577-584

Amano, R.S., 1983. Turbulence effect on the impinging jet on a flat plate. **Bulletin of J.S.M.E.,** 26(221), November, pp. 1891-99.

Amano, R.S. and Brandt, H., 1984. Numerical study of turbulent axisymmetric jets impinging on a flat plate and flowing into an axisymmetric cavity. **Journal of Fluids Engineering, Transactions of the A.S.M.E.,** 106, December, pp. 410-417.

Amano, R.S. and Jensen, M.K., 1982. A numerical and experimental investigation of turbulent heat transport of an axisymmetric jet impinging on a flat plate. **A.S.M.E. paper 82-WA/HT-55.**

Amano, R.S. and Sugiyama, S., 1985. Investigation of turbulent heat transfer of an axisymmetric jet impinging on a flat plate. **Bulletin of J.S.M.E.,** 28(235), January, pp. 74-79.

Arganbright, D.M. and Resch, H., 1971. A review of basic aspects of heat trasnefr under impinging jets. **Wood Sci. Tech.**, 3, 73-94.

Ashforth-Frost, S., 1994. Flow visualisation of semi-confined jet impingement. **PhD Thesis, The Nottingham Trent University**, Nottingham, England.

Becko, Y., 1976. Impingement cooling - a review. **von Karman Inst. Fluid Dyn.,** Lecture Ser. 83.

Brdlik, P.M. and Savin, V.K., 1965. Heat transfer between an axisymmetric jet and a plate normal to the flow. **Journal of Engineering Physics,** 8(2), pp. 91-98.

References

Button, B.L. and Jambunathan, K., 1989. Jet-impingement heat transfer: a bibliography 1976-1985, **Previews Heat Mass Transfer**, 15(2), pp. 149-178

Button, B.L. and Wilcock, D., 1978. Impingement heat transfer - a bibliography 1890-1975. **Previews Heat Mass Transfer**, 4(3), 83-89.

Button, B.L. and Wilcock, D., 1982. Effect of nozzle geometry on single circular jet impingement heat transfer. **2nd Polytechnic Symposium on Thermodynamics and Heat Transfer,** November, Leicester.

Button, B.L., Dobbins, B.N., Jambunathan, K. Kapasi, S., He, S.P., and Wang, L.S., 1991. The measurement of temperature distribution in semi-confined jet impingement using ESPI and Holography. **112th ASME WAM**, Atlanta, Georgia, USA, 1-6 December.

Cadek, F.F and Zerkle, R.D., 1974. Local heat transfer characteristics of two-dimensional impinging air jets - theory and experiment. **Heat Transfer, 2, paper FC1.4,** pp. 15-19.

Carper Jr., H.J., Saavedra, J.J. and Suwanprateep, T., 1986. Liquid jet impingement cooling of a rotating disk. **Journal of Heat Transfer, Transactions of the A.S.M.E.,** 108, pp. 540-546.

Chia, C.-J., Giralt, F. and Trass, O., 1977. Mass transfer in axisymmetric turbulent impinging jets. **Industrial and Engineering Chemistry, Fundamentals,** 16(1), pp. 28-35.

Chin, D.-T. and Hsueh, K.-L., 1986. An analysis using the Chilton-Colburn analogy for mass transfer to a flat surface from an unsubmerged impinging jet. **Electrochimica Acta,** 31(5), pp. 561-564.

Dawson, D.A. and Trass, O., 1966. Mass transfer in a turbulent radial wall jet. **The Canadian Journal of Chemical Engineering,** June, pp. 121-129.

References

Deshpande, M.D., Vaishnav, R.N. and Vaishnav, M.P., 1988. A toroidal vortex around a submerged impinging jet. **Experiments in Fluids,** 6, pp. 355-356.

Deshpande, M.D., Vaishnav, R.N, 1982. Submerged laminar jet impingement on a plane. **J. Fluid Mech,**. 114(1), pp. 213-236.

Dobbins, B.N., He, S.P., Jambunathan, K., Kapasi, S., Wang, L.S. and Button, B.L., 1991. Measurement of temperature field in confined jet impingement using phase-stepping video holography. **SPIE International Symposium on OPtical Applied Science and Engineering**, San Diego, California, USA, 21-26 July.

Downs, S.J. and James, E.H., 1987. Jet impingement heat transfer - A literature survey. **National Heat Transfer Conference,** Pittsburgh, Pennsylvania, 9-12 August, Paper 87-HT-35.

Ero, M.I.O., 1978. Heat and mass transfer in close proximity impinging two-dimensional laminar jets. **A.I.A.A Journal,** 16(6), pp. 611-613.

Gardon, R. and Cobonpue, J., 1962. Heat transfer between a flat plate and jets of air impinging on it. **International Development in Heat Transfer, Proceedings 2nd International Heat Transfer Conference, A.S.M.E.,** New York, pp. 454-460.

Gardon, R. and Akfirat J.C., 1966. Heat transfer characteristics of impinging two-dimensional air jets. **Journal of Heat Transfer, Transactions of the A.S.M.E.,** pp. 101-107.

Gardon, R. and Akfirat, J.C., 1965. The role of turbulence in determining the heat-transfer characteristics of impinging jets. **International Journal of Heat and Mass Transfer,** 8, pp. 1261-1272.

Gaunter J.M. Livingood, J.N.B. and Hrycak, P., 1970. Survey of literature on the flow characteristics of a single turbulent jet impinging on a flat plate. **NASA TN D-5652**. NTIS N70-18963.

Gholizadeh, N., 1992. Interferometric measurement of local mass transfer rates to an impinging jet by non-photographic holography. **PhD Thesis, Edinburgh University.**

Giralt, F., Chia, C.-J. and Trass, O., 1977. Characteristics of the impingement region in an axisymmetric turbulent jet. **Ind. Eng. Chem. Fundam.**, 16(1), pp. 21-28.

Glauert, M.B., 1956. The wall jet. **J. Fluid Mech.**, 1, pp. 625-643.

Goldstein, R.J. and Behbahani, A.I., 1982. Impingement of a circular jet with and without cross flow. **International Journal of Heat and Mass Transfer,** 25(9), pp. 1377-1382.

Goldstein, R.J. and Franchett, M.E., 1988. Heat transfer from a flat surface to an oblique impinging jet. **Journal of Heat Transfer, Transactions of the A.S.M.E.,** 110, pp. 84-90.

Guo, C.Y. and Maxwell, W.H.C., 1984. Numerical modelling of normal turbulent plane jet impingement on solid wall. **Journal of Engineering Mechanics,** 110(10), pp. 1498-1509.

Harper, A.J. and Macleod N., 1978. Hot spots in heat transfer. **Physics Bulletin,** January. pp 13-14.

van Heiningen, A.R.P., Mujumdar, A.S. and Douglas, W.J.M., 1976. numerical prediction of the flow field and impingement heat transfer caused by a laminar slot jet. **Journal of Heat Transfer, Transactions of the A.S.M.E.,** November, pp. 654-658.

Hildebrand, B.P. and Haines, K.A., 1966. Interferometric measurement using the wavefront reconstruction technique. **Applied Optics,** 5(1), January, pp. 172-173.

Hollworth, B.R. and Gero, L.R., 1985. Entrainment effects on impingement heat

transfer: part ii - local heat transfer measurements. **Journal of Heat Transfer, Transactions of the A.S.M.E.,** 107, pp. 910-915.

Hrucak, P., Lee, D.T., Gaunter, W.J., and Livingood, J.N.B., 1970. Experimental flow characteristics of a single turbulent jet impinging on a flat plate. **NASA-TN-D-5690**. NTIS N70-20567.

Hrycak, P., 1983. Heat transfer from round impinging jets to a flat plate. **International Journal of Heat and Mass Transfer,** 26(12), pp. 1857-1865.

Hrycak, P., 1980. Heat transfer from impinging jets : a literature review. New Jersey Institute of Technology, Newark, **AFWAL-TR-81-3054, NTIS AD-A 106725.** pp. 1-50.

Huang, B., 1977. Predictions of flow and heat transfer under a laminar swirling impinging jet, **M.Eng. Thesis, McGill University,** Montreal, Canada

Huang, B., Mujumdar, A.S. and Douglas, W.J.M., 1981. Flow characteristics of a laminar swirling impinging jet: A numerical study. **The Canadian Journal of Chemical Engineering,** 59, August, pp. 423-429.

Huang, B., Douglas, W.J.M. and Mujumdar, A.S., 1978. Heat transfer under a laminar swirling impinging jet - A numerical study. **6th International Heat Transfer Conference,** paper# FC(b)-23, pp. 311-316.

Hyne, N.G. and Macleod, N., 1984. The use of electronic speckle-pattern interferometry for convective mass-transfer measurement : studies of transfer to a turbulent air jet impinging on a plane surface. **Institute of Chemical Engineers Annual Research Meeting 11th,** pp. 147-151.

Jambunathan, K., Kapasi, S., Button, B.L. and Bland, J.A., 1989. Numerical study of flow field for confined laminar jet impingement. **Third International PHOENICS User Conference**, Dubrovnik, Yugoslavia, 28 August - 1 September.

References

Jambunathan, K., Lai, E., Moss, M.A. and Button, B.L., 1992. A review of heat transfer data for single circular jet impingement. **Int. J. Heat and Fluid Flow,** 13, 2, June. pp.106-115

Jassaud, J.-P., Douglas, W.J.M. and Majumdar, A.S., 1984. Evaporation under an obliquely impinging laminar ducted slot jet - A numerical model. **International Communication in Heat and Mass Transfer,** 11, pp. 335-344.

Kapur, D.N., 1973. The profilometric determination of mass transfer coefficients by holographic interferometry. **PhD Thesis,** University of Edinburgh.

Kapur, D.N. and Macleod, N., 1975. Holographic determination of local mass transfer coefficients at a solid-liquid boundary. **A.I.Ch.E. Journal,** 21(1), January, pp. 101-187.

Kapur, D.N. and Macleod, N., 1974. The determination of local mass-transfer coefficients by holographic interferometry - I. **International Journal of Mass Transfer,** 17, pp. 1151-1162.

Kapur, D.N.and Macleod, N., 1972, Determination of local mass transfer coefficients by holography. **Nature Physical Science**, 237, May 22, pp. 57-59.

Kapur, D.N. and Macleod, N., 1976. Vapour pressure determination for certain high-boiling liquids by holography. **Ind. Eng. Chem. Prod. Res. Dev.**, 15(1), pp. 50-54.

Kataoka, K., 1985. Optimal nozzle-to-plate spacing for convective heat transfer in nonisothermal, variable-density impinging jets. **Drying Technology,** 3(2), pp. 235-254.

Kataoka, K., Kamiyama, Y., Hasimoto, S. and Komai, T., 1982. Mass transfer between a plane surface and an impinging turbulent jet: the influence of surface-pressure fluctuations. **Journal of Fluid Mechanics,** 119, pp. 91-105.

Law, H-S., 1982. **Mass transfer due to a confined laminar impinging two-dimensional jet.** Ph.D. Thesis, University of Alberta.

Law, H-S., 1984. Mass transfer due to a confined laminar impinging two-dimensional jet. **International Journal of Heat and Mass Transfer,** 27(4), pp. 529-539.

Law, H.-S. and Masliyah, J.H., 1984. Numerical predictions of the flow field due to a confined laminar two-dimensional submerged jet. **Computers and Fluids,** 12(3), pp. 199-215.

Li, Y.-K., 1977. Heat and mass transfer under laminar impinging jets. **MEng. Thesis.** McGill Univ., Montreal.

Lipsett, A.W. and Gilpin, R.R., 1978. Laminar jet impingement heat transfer including the effects of melting. **International Journal of Heat and Mass Transfer,** 21, pp. 25-33.

Livingood, J.N.B. and Hrycak, P., 1973. Impingement heat transfer form turbulent air jets to flat plates - a literature survey. **NASA TM X-2778.** NTIS N73-24927.

Macleod, N. and Todd, R.B., 1973. The experimental determination of wall-fluid mass transfer coefficients using plasticized polymer surface coating. **Int. J. Heat Mass Transfer,** 16, pp. 485-504.

Marple, V.A., Lui, B.V., Whitby, K.T., 1974. On the flow field of inertial impactors. **Transaction of ASME, J. of Fluid Eng.,** 96, 394.

Masliyah, J.H. and Nguyen, T.T., 1976. Holographic determination of mass transfer due to impinging square jet. **The Canadian Journal of Chemical Engineering,** 54, August, pp. 299-304.

Masliyah, J.H. and Nguyen, T.T., 1977. Experimental study of mass transfer due to

an impinging rectangular jet. **The Canadian Journal of Chemical Engineering,** 55, April, pp. 156-160.

Masliyah, J.H. and Nguyen, T.T., 1979. Mass transfer due to an impinging slot jet. **International Journal of Heat and Mass Transfer,** 22, pp. 237-244.

Miyazaki, H. and Silberman, E., 1972. Flow and heat transfer on a flat plate normal to a two-dimensional laminar jet issuing from a nozzle of finite height. **Journal Heat and Mass Transfer,** 15, pp. 2097-2107.

Moss, M.A., 1993. A knowledge based database system for jet impingement heat transfer correlations. **PhD Thesis, The Nottingham Trent University,** Nottingham, England.

Mujumdar, A.S. and Douglas W.J.M., 1972. Impingement heat transfer: a literature survey. **TAPPI meeting, New Orleans,** 3 Oct., 107-136.

Mujumdar, A.S., Li, Y.-K. and Douglas, W.J.M., 1980. Evaporation under an impinging jet: A numerical model. **The Canadian Journal of Chemical Engineering,** 58(4), August, pp. 448-453.

Obot, N.T., Majumdar, A.S. and Douglas, W.J.M., 1979. The effect of nozzle geometry on impingement heat transfer under a round turbulent jet. **Winter Annual meeting of the A.S.M.E.,** New York, 2-7 December, A.S.M.E. paper 79-WA/HT-53.

Obot, N.T., Douglas, W.J.M. and Majumdar, A.S., 1982. Effect of semi-confinement on impingement heat transfer. **Proceeding 7th International Heat Transfer Conference,** Munchen, 6-10 Sept, 3, pp. 395-400.

Pamadi, B.N. and Belov, I.A., 1980. A note on the heat transfer characteristics of circular impinging jet. **International Journal of Heat and Mass Transfer,** pp. 783-787.

Paterson, W.R., Colledge, R.A., Macnab, J.I. and Joy, J.A., 1987. Solid-gas mass transfer measurement by the swollen polymer method: proving of swelling agents. **Int. J. Heat Mass Transfer,** 30(2), pp.279-287.

Paullay, A.J., Melnik, R.E., Rubel, A., Rudman, S. and Siclari, M.J., 1985. Similarity solutions for plane and radial jets using a K-ϵ turbulence model. **Journal of Fluids Engineering, Transactions of the A.S.M.E.,** 107, March, pp. 79-85.

Polat, B., Huang, B., Mujumdar, A.S. and Douglas, W.J.M., 1989. Numerical flow and heat trasnefr under impinging jets: a review. **Ann. Rev. Numer. Fluid Mech. Heat Transfer,** 2, pp. 157-197.

Polat, S., Mujumdar, A.S. and Douglas, W.J.M., 1985. Heat transfer distribution under a turbulent impinging jet - A numerical study. **Drying Technology,** 3(1), pp. 15-38.

Pokusaev, B.G. and Volkov, N.V., 1980, Mass transfer from a wall to the stream of an axisymmetric fluid jet. **Journal of Engineering Physics,** 38(35), pp. 490-495.

Popiel, Cz. O., Van der Meer, Th. H. and Hoogendoorn, C.J., 1980. Convective heat transfer on a plate in an impinging round hot gas jet of low Reynolds number. **International Heat and Mass Transfer,** 23, pp. 1055-1068.

Popiel, Cz.O. and Boguslawski, L., 1986. Mass or Heat Transfer in impinging single, round jets emitted by a bell-shaped nozzle and sharp-ended orifice. **Proceeding of the Eighth International Heat Transfer Conference,** San Francisco, C.A., August, pp. 1187-1192.

Poreh, M., Tsuei, Y.G. and Cermak, J.E., 1967. Investigation of a turbulent radial wall jet. **Journal of Applied Mechanics, Transactions of the A.S.M.E.,** June, pp. 457-463.

Raj, S.A., 1987. A complete analytical solution to laminar heat transfer in

axisymmetric stagnation point flow. **International Journal of Heat and Mass Transfer,** 30(11), pp. 2441-2444.

Rakadjiev, R., Ennoji, H. and Asanuma, T., 1987. Numerical simulation of a viscous axisymmetric jet impinging normally on a flat wall. **Proceedings of the Faculty of Engineering, TOKAI University,** XIII, pp. 69-82.

Ravuri, R. and Tabakoff, W., 1975. A numerical solution for the heat transfer between an axi-symmetric air jet and a heated plate. **A.S.M.E. paper 75-WA/HT-106.**

Ramaprian, B.R. and Chandrasekhara, M.S., 1985. LDA measurements in plane turbulent jets. **Journal of Fluids Engineering, Transactions of the A.S.M.E.,** 107, June, pp. 264-271

Rao, V.K., 1980. A note on mass transfer in turbulent wall jets. International **Journal of Heat Mass Transfer,** 23, pp. 1690-1693.

Rao, V.V. and Trass, O., 1964. Mass transfer from a flat surface to an impinging turbulent jet. **The Canadian Journal of Chemical Engineering,** June, pp. 95-99.

Ravi, R. and Deshpande, M.D., 1986. Computation of plane jet impingement on a plate. **National Aeronautical Laboratory, India,** TM FM 8602.

Rubel, A., 1980, Computations of jet impingement on a flat surface. **A.I.A.A Journal,** 18(2), pp. 168-175.

Saad, N.R., 1975. **Simulation of flow and heat transfer under an impinging jet.** M.Eng. Thesis, McGill University, Canada.

Saad, N.R., Douglas, W.J.M. and Mujumdar, A.S., 1977. Prediction of heat transfer under an axisymmetric laminar impinging jet. Ind. Eng. Chem. Fundam., 16(1), 148-154

References

Schlichting, H. 1968, Boundary Layer Theory. McGraw-Hill, sixth edition.

Schwarz, W.H. and Caswell, B., 1961. Some heat transfer characteristics of the two-dimensional laminar incompressible wall jet. **Chem. Engng. Sc.**, 16, 338-351.

Schneider, W., Zauner, E. and Bohm, H., 1987. The recirculatory flow induced by a laminar axisymmetric jet issuing from a wall. **J. of Fluids Eng.**, 109, pp. 237-241.

Scholtz, M.T. and Trass, O., 1963. Mass transfer in a laminar radial wall jet. **A.I.Ch.E. Journal,** 9(4), pp. 548-554.

Scholtz, M.T. and Trass, O., 1970. Mass transfer in a nonuniform impinging jet. **A.I.Ch.E. Journal,** 16(1), January, pp. 82-96.

Smirnov, V.A., Verevochkin, G.E. and Brdlik, P.M., 1961. Heat transfer between a jet and a held plate normal to flow. **International Journal of Heat and Mass Transfer,** 2, pp. 1-7.

Sonin, A.A., 1983. Jet impingement systems for electroplating applications: Mass transfer coefficients. **Journal of Electrochemical Society,** 130(7), July, pp. 1501-1505.

Sparrow, E.M. and Lee, L. 1975. Analysis of flow field and impingement heat/mass transfer due to a nonuniform slot jet. **Journal of Heat Transfer, Transactions of the A.S.M.E.,** May, pp. 191-197.

Sparrow, E.M. and Wong, T.C., 1975. Impingement transfer coefficient due to initially laminar slot jets. **International Journal of Heat and Mass Transfer,** 18, pp. 597-605.

Sparrow, E.M., Xu, Z.X. and Azevedo, L.F.A., 1987. Heat(mass) transfer for circular jet impingement on a confined disk with annular collection of spent air. **Journal of Heat Transfer, Transactions of the A.S.M.E.,** 109, May, pp. 329-335.

References

Tani, I. and Komatsu, Y., 1966. Impingement of a round jet on a flat surface. **Proceeding 11th International congress of Applied Mechanics,** pp. 672-676.

Vallis, E.A., Patrick, M.A. and Wragg, A.A., 1978. Radial distribution of a convective heat transfer coefficient between an axisymmetric turbulent jet and a flat plate held normal to the flow. **6th International Heat Transfer Conference,** Toronto, Canada, 5, pp. 297-303.

Vallis, E.A., Bacon, D.H. and Patrick, M.A., 1979. The application of a two equation model of turbulence to the prediction of flows in regions of recirculation and impingment. **Polytechnic Symposium on Thermodynamics and Heat Transfer,** Leicester, 13-14 November, pp 27-35.

Vickers, J.M.F., 1959. Heat transfer coefficients between fluid jets and normal surfaces. **Industrial and Engineering Chemistry,** 51(8), August, pp.967-972.

Vlachopoulos, J. and Tomich, J.F., 1971. Heat transfer from a turbulent hot air jet impinging normally on a flat plate. **The Canadian Journal of Chemical Engineering,** 49, August, pp. 462-466.

Wang, L.S., Kapasi, S., Jambunathan, K., and Dobbins, B.N., 1994. Application of phase stepping speckle interferometry and swollen polymer technique to mass transfer measurements. **Optical Methods and Data Processing in Heat and Fluid FLow,** 14-15 April, City University, London.

Ward, J., Ideriah, F.J.K., Probert, S.D. and Duggan, A., 1972. Mass transfer technique for investigation of heat transfer by jet-impingement systems. **Journal of Mechanical Engineering Science,** 14(6), pp. 389-392.

Witze, P.O. and Dwyer, H.A., 1977. impinging axisymmetric turbulent flows: The wall jet, the radial jet and opposing free jets. **Symposium on Turbulent Shear Flows,** Penn State University, April 18-20, pp. 2.33-2.39.

Wolfshtein, M., 1966. **Empirical correlation for evaluation of Stanton Number in impinging jets.** Aeronautical Research Council, 27 613, H.M.T. 92.

Wolfshtein, M. and Stotter, A., 1964. Heat transfer between an impinging jet and a flat surface. **Israel Journal of Technology,** 2(1), pp. 131-134.

Zangeneh, S., 1990. Vapour pressure measurement. **MPhil Thesis, Trent Polytechnic,** Nottingham, England.

BIBLIOGRAPHY

Baitup, M.J.E. and Wright, C.C., 1982. **Calculation of diffusion coefficient for Ethyl Salicylate in air,** Memorandum SO3, Dept of statistics and operational research, Coventry (Lanchester) Polytechnic.

Bennett, C.O. and Myers, J.E., 1974. **Momentum; Heat and Mass transfer,** 2nd Edition, pp. 499-502.

Bird, R.B., Stewart, W.E. and Lightfoot, E.N., 1960. **Transport phenomena,** Wiley (1960), pp. 508-512.

CAHN 32 Instruction manual. European Instruments, The trading estate, old road, Headington, Oxford OX3 8TA.

Colledge, R.A., 1985. Heat and mass transfer at the wall of a packed bed at high Reynolds numbers, **PhD dissertation, University of Cambridge.** St John's College, Cambridge.

Laboratory Thermal Equipment. Operating Instruction Cold/warm temperature cabinet. LTE, Greenbridge lane, Greenfield nr. Oldham, Lancs, OL3 7EN.

TR100, The PHOENICS beginner's guide, CHAM Ltd, Bakery House 40 High

Street, Wimbledon, London, SW19 5AU.

TR200, The PHOENICS reference manual, CHAM Ltd, Bakery House 40 High Street, Wimbledon, London, SW19 5AU.

TR141, The AUTOPLOT user guide, CHAM Ltd, Bakery House 40 High Street, Wimbledon, London, SW19 5AU.

TR140, The PHOTON reference manual, CHAM Ltd, Bakery House 40 High Street, Wimbledon, London, SW19 5AU.

Patankar, S.V., 1980. **Numerical Heat Transfer and Fluid Flow**, Hemisphere (McGraw-Hill), New York.

Reid, M., 1989. Mass transfer measurement between a turbulent air jet and a flat plate by laser holography. **BEng Thesis, Trent Polytechnic**, Nottingham, England.

Galaud, A., 1988. Application of holographic interferometry to air jet impingement for mass transfer measurement. **BEng Thesis, Trent Polytechnic**, Nottingham, England.

Appendix A

MEASUREMENT OF DIFFUSIVITY OF ETHYL SALICYLATE N-TETRADECANE,METHYL SALICYLATE AND METHYL NAPHTHALENE

A.1 Experimental technique

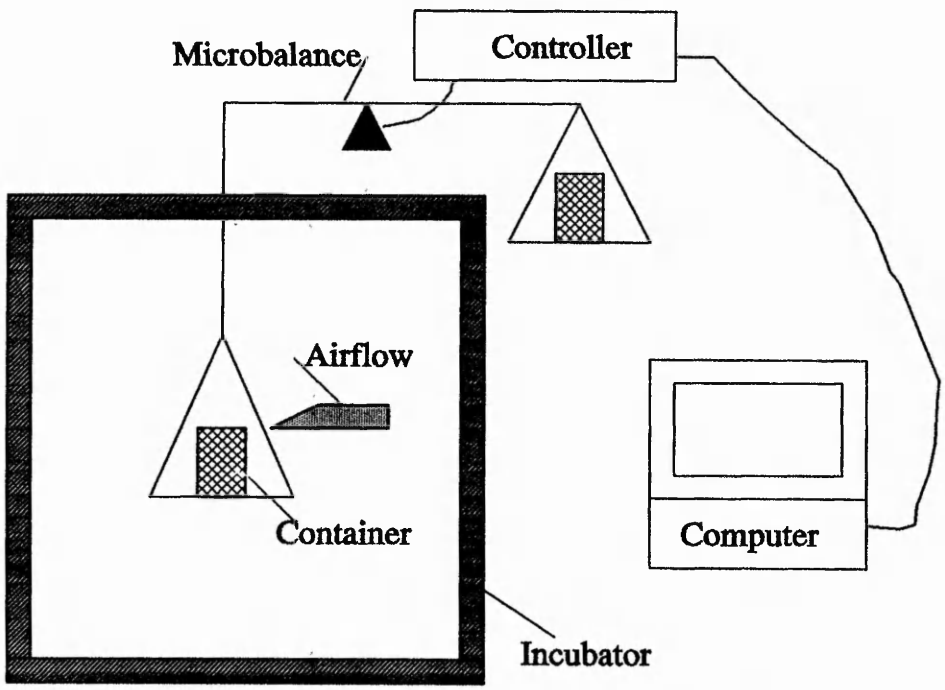

Figure A.1 Diagram showing the experimental arrangement for measurement of the air diffusion coefficient

This appendix reports measurement of the air diffusion coefficients of some commonly used esters with the swollen polymer technique. A constant temperature incubator provides a fixed temperature environment for the experiment. The incubator has an opening at the top of the incubator from which a weighing pan of the microbalance is introduced into the enclosure shown in Figure A.1. On this pan, a small container is placed with a sample quantity of the ester. The open surface area to air of the container is measured accurately and the depth of the ester is calculated from the mass of the ester put into the container. A method of ensuring a constant concentration at the free surface of the container is required.

A nozzle with rectangular cross-section placed parallel to the open surface of the container with a low air flow rate passing over the free surface of the container. This ensured a zero concentration plane and therefore set up a concentration gradient from the ester free surface to the top opening of the container. The loss of mass of the ester from the container is measured using the microbalance. Accuracy of the balance is 10 micrograms on the B scale of the balance. Steady state conditions are allowed to be set up before the test measurement is taken. The duration time for making the measurements ranged from six to eight hours. The diffusion measurements are made with two different depths of the ester in the container, 2 mm and 4 mm. The two sets of results are combined to eliminate any effects due to uncontrolled factors, i.e. convection present in the environment.

A.2 Mathematical Concept

For steady state conditions prevailing, the mass transfer equation (A.1) is used.

$$M = D_f A \frac{\delta C}{\delta h} = D_f A \frac{C_s - C_o}{\delta h} \qquad \textbf{(A.1)}$$

One container is used twice with two different depths of ester, which is be represented by the following two equations (A.2)

$$\delta h_1 = D_f A \frac{\delta C}{\delta M_1} \qquad \delta h_2 = D_f A \frac{\delta C}{\delta M_2} \qquad \textbf{(A.2)}$$

Subtracting the equations (A.2) from each other, the following equation (A.3) is derived and any common but unknown effects are eliminated from the results.

$$\delta h_1 - \delta h_2 = D_f A \, \delta C \left[\frac{1}{M_1} - \frac{1}{M_2}\right] \qquad \textbf{(A.3)}$$

therefore

$$\delta_f = \frac{\delta h_1 - \delta h_2}{A \, \delta C \left[\frac{1}{M_1} - \frac{1}{M_2}\right]} \qquad \textbf{(A.4)}$$

where δh_1 and δh_2 are the depths of ester from surface, M_1 and M_2 are the mass losses during test, A is the area of the vessel open to the free air, δC is the concentration gradient between ester surface and top of the container

$C_s = 0.002662 \times P_s / T$

$Ln(P_s) = 25.9 - 7072 / T$ (Pa)

T = Temperature in Kelvin

A.3 Experimental procedure

The first experimental concept considered was to measure the initial rate of mass loss from the container when the ester was introduced into the container. This method proved to be unsatisfactory because the arrangement did not work as expected and the mass loss measurements were very unstable. This transient method was abandoned in favour of a steady state method. With the steady state method the initial tests for the four esters measured gave scattered diffusion coefficients values for the measured temperature range. It was observed subsequently that the initial temperature and concentration conditions of the measurements are important and must be allowed to reach steady state before any readings can be taken. The ester is taken from a source at ambient temperature and therefore the ester and measuring vessel are not in equilibrium with each other. Settling time of the experiment is as long as the experimental test period. The diffusion coefficients are dependant on the small changes in temperature during the test. The experimental procedure is again modified so that the ester is introduced into the measuring vessel from a source that was stored in the same temperature environment. A steady reading of the mass loss is obtained consequently and the uncertainty in the diffusion coefficient is reduced. The greatest difficulty is that of ensuring a zero concentration at the open surface of the container. This is probably the main source of error as the flow of air over the surface may have set up convective currents in the container. Convective loss of mass may contribute to the diffusive loss and therefore produce great uncertainty in the value. One solution to this problem may be to increase the height of the vessel. This should lessen the open surface proximity from the free surface of the ester in the container and this should reduce the convective losses.

A.4 Discussion of results

A.4.1 Range of experimental tests

Table A.1 Range of diffusion coefficient experiments for the four different swelling agents

temperature	ethyl salicylate	n-tetra decane	methyl naphthalene	methyl salicylate
10	●	●	●	●
15	●	●	●	●
20	●	●	●	●
25	●	●	●	●
30	●	●	●	●
35	●	-	-	-
40	●	-	-	-
50	●	-	-	-
62	●	-	-	-

The diffusion coefficients are calculated from all the experimental conditions listed inTable A.1 and the data are plotted in graphical form. For comparison a binary mixture value obtained from Lennards - Jones equation is also shown. The uncertainty analysis carried out for the ethyl salicylate experiments required measurement of the following three quantities; mass loss, depth and temperature. These have resolution errors of, i.e. 10 micro grams in 15 minutes, 0.05 mm estimated and 0.5 °C, respectively. Using these quantities, the Monte Carlo simulation is undertaken for the diffusion coefficient and the results are presented in graphical form. The percentage uncertainty in each test is about 50 per cent. A correlation equation of the data for ethyl salicylate is statistically determined as

$$D_f = 6.08 \times 10^{-7} \; T^{1.98}$$

Results for ethyl salicylate are plotted in Figure A.2 with confidence intervals. It is clear the correlated line is a good approximation to the theoretically calculated line but the individual experimental data points are scattered around this line. The

results for the other three esters are shown in Figure A.3, Figure A.4 and Figure A.5, it can be seen that the correlation lines do not represent the theoretically calculated values. Experimental data is given little confidence, since the uncertainty is very high. The results for n-tetradecane for temperatures below ambient show some freezing of the compound and therefore the results are seen to have totally deviated from the expected value.

A.5 Future work and recommendations

Following modifications to the technique are suggested for future work. The range of tested temperatures should be broadened to higher values and this will give greater confidence in the results. The container height needs to be increased to minimise the effect of air movement on the diffusion coefficient within the incubator. Zero vapour concentration at the open end of the container should be maintained and therefore, there is scope for improvement to the current technique used.

A.6 Conclusions

The experimental procedure used, is refined and the results are in approximate agreement to the expected values from theory. The apparatus has the sensitivity range to measure the diffusion coefficients for the esters. The correlation of the diffusion coefficient for ethyl salicylate is close to the theoretically calculated values but for the other esters the results are regarded as highly inaccurate because the procedure used, is shown to have a large uncertainties associated with them.

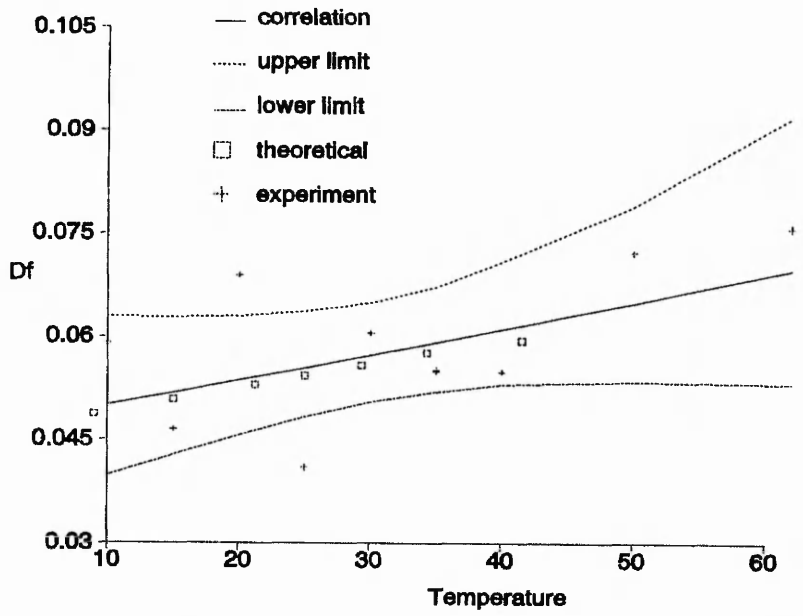

Figure A.2 Diffusion coefficient of ethyl salicylate in air for a temperature range of 10 to 60°C

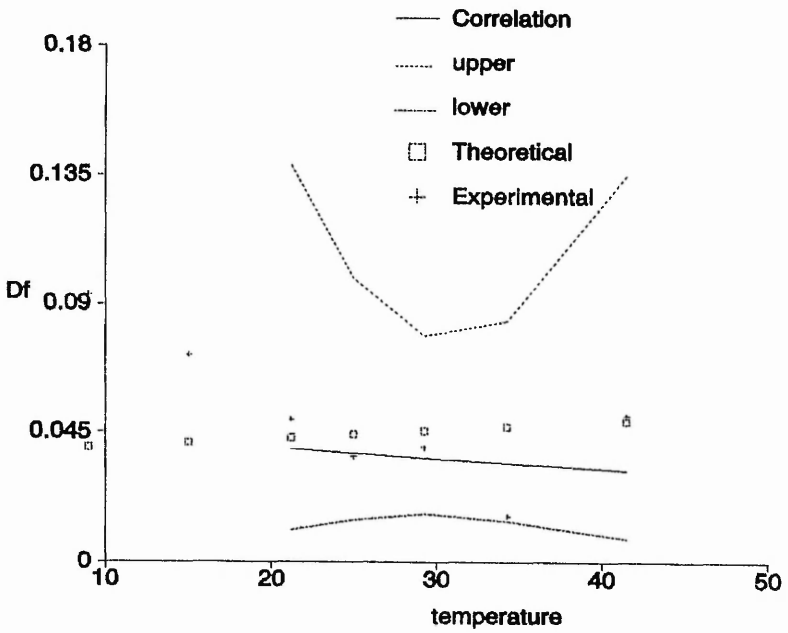

Figure A.3 Diffusion coefficient of n-tetradecane in air for a temperature range of 10 to 60°C

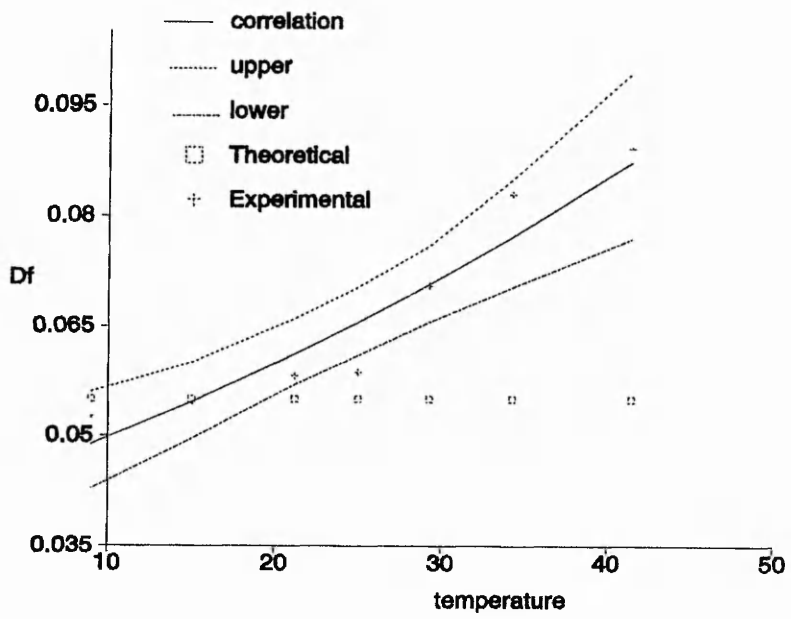

Figure A.4 Diffusion coefficient of methyl salicylate in air for a temperature range of 10 to 60°C

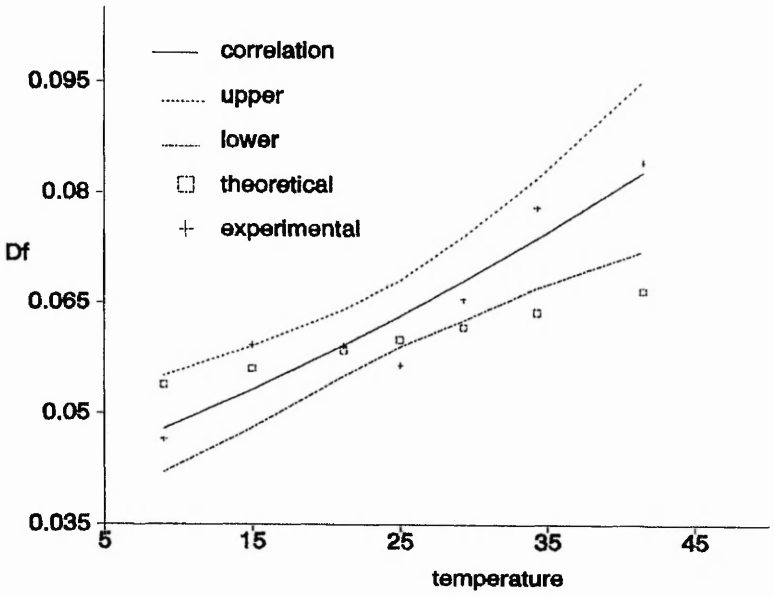

Figure A.5 Diffusion coefficient of methyl naphthalene in air for a temperature range of 10 to 60°C

Appendix B
MEASUREMENT OF THE REFRACTIVE INDEX OF POLYMER SWOLLEN BY ESTER

B.1 Introduction

This appendix reports measurements of physical properties of a swollen polymer required to analyse the mass transfer from a swollen polymer surface subjected to air jet impingement. This mass transfer technique is discussed in detail in chapter 3. Preliminary identification and investigation of the most appropriate swelling agents for the swollen polymer technique have been carried out by Paterson et al (1987). Their studies were directed towards obtaining saturated vapour pressures in air of these swelling agents. The conclusion from their study is that ethyl salicylate and n-tetradecane are considered the most appropriate to be used with the swollen polymer technique.

The current experimental work to obtain, refractive index and mass swelling in the silicon rubber RTV 615 and four suitable swelling agents identified in literature. These measurements are necessary because the published data in the literature is limited and requires independant corroboration. The experimental parameters are determined with respect to time so that the swelling process can be observed and the time required to reach saturation estimated. The measured quantities are for a temperature range of 5 to 30 °C. The swelling agents studied are; n-tetradecane, ethyl salicylate, methyl salicylate and methyl naphthalene.

B.2 Experimental procedure

The environmental temperature is controlled during the experiment by a TECHNE constant temperature water bath that also supplies constant temperature water to the Abbe refractometer. The swelling agent and polymer are kept in this constant temperature environment. The temperature is controlled accurately by a refrigeration unit and heater working together, it is possible to keep the temperature accurately under control to with in 0.1 °C. For the low temperature

experiments the difference in temperature between the water bath and refractometer is about 2 to 3 °C as the ambient is around 20 °C therefore the circulating water warms up rather rapidly. Condensation on the prisms faces of the refractometer was a problem at the lower temperature range, the water film had to be wiped clear at regular intervals. A Satorious digital balance was used to weight the swollen polymer sample, the balance was initialised at zero before every reading because the set zero setting had slight drift. The accuracy and resolution of the balance were to one tenth of a milligram. The Abbe refractometer was designed for measuring refractive indices of liquids placed between the two prisms. The physical principle was described in Nelkon & Parker and was based on the total internal reflection principle. Although the Abbe refractometer was designed for thin liquid films, a thin polymer sheet could be used and still produce valid and satisfactory results. An approximately 1mm thick, flat sheet of polymer was cast so that specimen samples of the polymer could be cut into appropriate sizes. The size of the sample was 20 mm by 10 mm, which was approximately the size of the faces of the prisms in the refractometer. The polymer specimens were weighted dry and refractive indices taken, then each was immersed in the swelling agent for intervals of 15 minutes. After the end of this time the sample was removed from the swelling agent and dryed throughly with lint free tissue. The sample was weighed and without delay was placed in the refractometer for measurement of the refractive index. The eye piece telescope was focused and prism adjusted so that a light and dark region of light was in the field of view and the crosswires were placed at the interface of this region. The other eyepiece was focused on the graduated scale and where the calibration line crossed the scale, the value of the refractive index could be read.

B.3 Discussion of results

Three sets of tests were carried out, the first set with polymer that had been cast several months before the experiment, so had time to completely cure. The second and third sets of tests were done with the polymer that had been cast just a few weeks before the test. The ester was not changed during each set of tests because any effect caused by the fresh ester would have added another variable in the

experiment.

B.3.1 Ethyl salicylate

The results of swelling against time for an old and newly cast polymer for a temperature range of 5 to 30°C showed that 1.5 hours was insufficient for complete saturation of the silicon with the ester. The percentage difference after 1.5 hours immersion in the swelling agent for two differently aged polymers were within 1.5 percent of each other. However, the older polymer sample had swollen a little more than the newly cast polymer. Since the total mass being measured was in dry air after swelling had taken place, small amounts of polymer could have leeched out of polymer and therefore reduced the weight that was measured. The refractive index was unchanged after 1.5 hours of swelling in ethyl salicylate, the age of the polymer did not effect the refractive index. The refractive index against temperature showed no dependence due to the age of the polymer shown in Figure B.1.

B.3.2 N-tetradecane

Mass swelling against time was used as an indicator for liquid saturation with the polymer having been achieved. The difference in mass increase due to swelling between the old and new polymers was significant. For the temperature range 10 to 20°C and after 1.5 hours swelling, the percentage difference in mass swelling was about 13 - 23 percent. Tests to check repeatability of the new polymer from a separately mixed batch sample were done and from this data it was found that exact repeatability was not possible. But, similar trends were obtained, these were thought to be due to the cured state of the polymer. The refractive index results for the old polymer sample and new polymer samples were presented, which showed a small difference in the refractive index of about 0.001 after 1.5 hours immersion. The repeated test with a new polymer from a different batch showed similar trends to the other the refractive index curves. Mass swelling with temperature had a clear dependence between the old and new polymer batches. Repeat tests with the new polymer samples showed that refractive indices were

within 5 per cent of each other. Swelling was greater for the newly cast polymer than for the older cured polymer. Figure B.2 showed the refractive indices against temperature for n-tetradecane and the older polymer was marginally different when compared to the newer polymer. Linear correlation equation for the refractive index against temperature was obtained for all the polymer samples.

B.4 Conclusions

The refractive and mass swelling properties of swollen polymers with differently aged polymers had been investigated for the temperature range of 10 to 30°C that would be encountered during their use. The following correlation equations were obtained for the new polymer with the ethyl salicylate Figure B.3

$$Ms = 0.190\ T - 38.4$$

$$Rf = 1.48 - 0.00017\ T$$

For n-tetradecane

$$Ms = 0.705\ T - 120$$

$$Rf = 1.51 - 0.000288\ T$$

The volume fraction could be estimated crudely from the mass swelling data by assuming an additive process between the polymer and swelling agent.

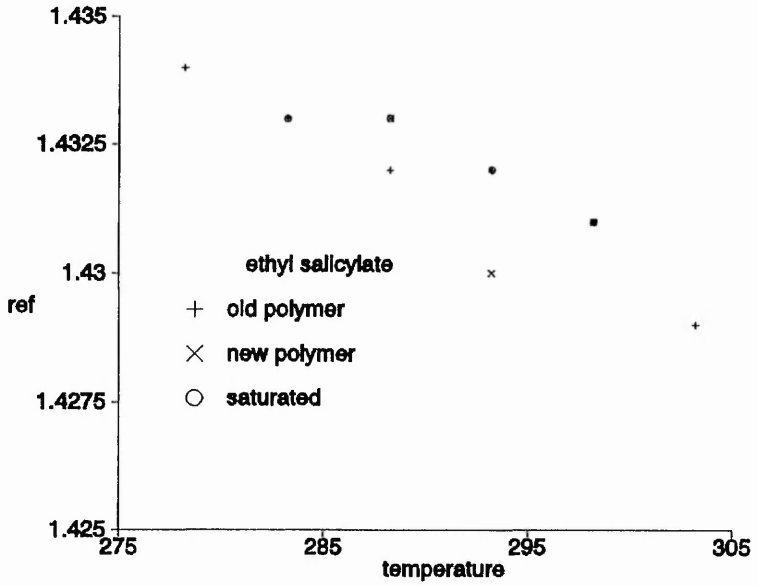

Figure B.1 Refractive index of the swollen polymer with ethyl salicylate for a temperature range of 5 to 30°C

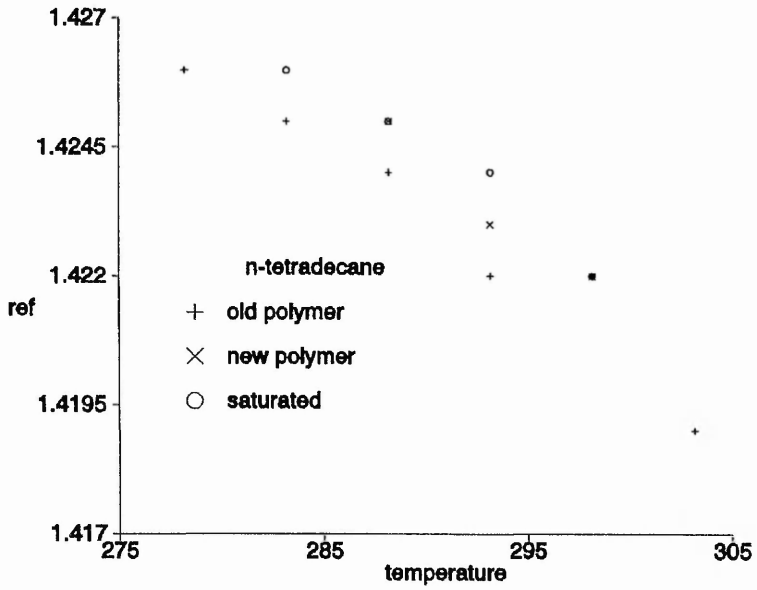

Figure B.2 Refractive index of the swollen polymer with n-tetradecane for a temperature range of 5 to 30°C

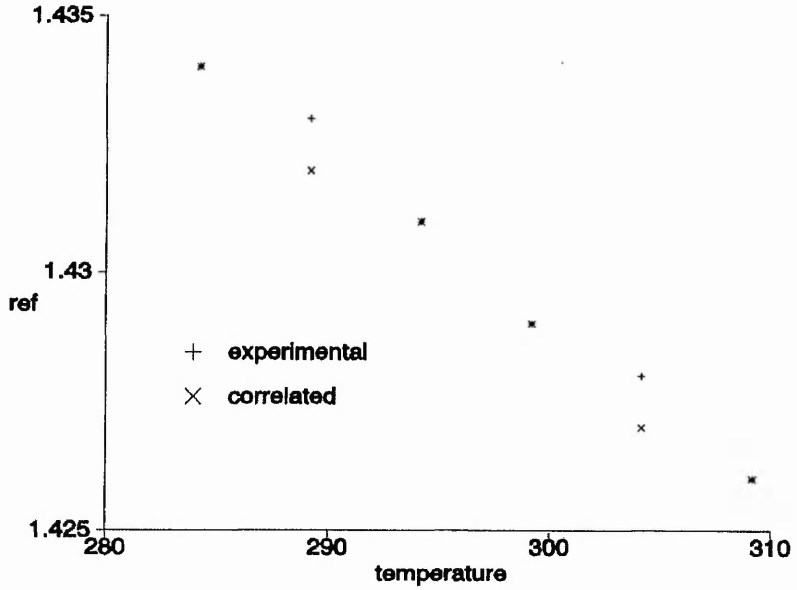

Figure B.3 Refractive index of the swollen polymer with ethyl salicylate and the correlated equation for the temperature range of 5 to 30°C

Appendix C

PHOENICS Q1 input file for laminar semi-confined jet impingement

```
TALK=F;RUN( 1, 1);VDU= 3
   GROUP 1. Run title and other preliminaries
TEXT(IMPINGING JET WITH POLAR GRID
REAL(WIN,DIA,GK,TIN,CP)
TIN=20.0;DIA=0.004;GK=0.02624;CP=1004.9;WIN=3.5
   GROUP 2. Transience; time-step specification
   GROUP 3. X-direction grid specification
CARTES=F
   GROUP 4. Y-direction grid specification
NY=110;YVLAST=1.0
YFRAC(1)=-10.0;YFRAC(2)=0.0002
YFRAC(3)=100.0;YFRAC(4)=0.0003
   GROUP 5. Z-direction grid specification
NZ=29;ZWLAST=1.0
ZFRAC(1)=-1.0;ZFRAC(2)=0.0003
ZFRAC(3)=12.0;ZFRAC(4)=0.000292
ZFRAC(5)=12.0;ZFRAC(6)=0.000292
ZFRAC(7)=2.0;ZFRAC(8)=0.0003
ZFRAC(9)=2.0;ZFRAC(10)=0.00003
   GROUP 6. Body-fitted coordinates or grid distortion
   GROUP 7. Variables stored, solved & named
SOLUTN(P1,Y,Y,Y,N,N,N)
SOLUTN(V1,Y,Y,N,N,N,N)
SOLUTN(W1,Y,Y,N,N,N,N)
SOLUTN(H1,Y,Y,N,N,N,N)
   GROUP 8. Terms (in differential equations) & devices
DIFCUT=0
   GROUP 9. Properties of the medium (or media)
   The medium is air
ENUL=1.4E-5
RHO1=1.2928
PRNDTL(H1)=0.7
   GROUP 10. Inter-phase-transfer processes and properties
   GROUP 11.
  NAMFI=
FIINIT(P1)=READFI
FIINIT(W1)=READFI
FIINIT(V1)=READFI
FIINIT(H1)=20
   GROUP 12. Convection and diffusion adjustments
   GROUP 13. Boundary conditions and special sources
    ** JET VELOCITY DEFINITION fully developed
PATCH(JET1,LOW,1,1,1,10,1,1,1,1)
COVAL(JET1,W1,ONLYMS,3.5)
```

```
COVAL(JET1,H1,ONLYMS,20.0)
COVAL(JET1,P1,FIXFLU,3.5*RHO1)
    ** TO FIX VALUES AT BOUNDARIES
    ** BLOCKAGE FOR IMPINGING PLATE
PATCH(SET2,CELL,1,1,1,NY,NZ,NZ,1,1)
COVAL(SET2,W1,FIXVAL,0.0)
COVAL(SET2,V1,FIXVAL,0.0)
COVAL(SET2,H1,FIXVAL,100.0)
    ** BLOCKAGE FOR CONFINEMENT PLATE
PATCH(SET1,CELL,1,1,11,NY,1,1,1,1)
COVAL(SET1,W1,FIXVAL,0.0)
COVAL(SET1,V1,FIXVAL,0.0)
    ** OUTFLOW REGION
PATCH(OUTREG,CELL,1,1,NY,NY,1,NZ,1,1)
COVAL(OUTREG,P1,FIXP,0.0)
    ** LAMINAR WALL FUNCTIONS OF THE BLOCKAGES
PATCH(IMPING,HWALL,1,1,1,NY,NZ-1,NZ-1,1,1)
COVAL(IMPING,W1,FIXVAL,0.0)
COVAL(IMPING,V1,1.0,0.0)
COVAL(IMPING,H1,1.0/PRNDTL(H1),100.0)
PATCH(CONFINE,LWALL,1,1,11,NY,2,2,1,1)
COVAL(CONFINE,V1,1.0,0.0)
   GROUP 14. Downstream pressure for PARAB=.TRUE.
   GROUP 15. Termination of sweeps
LSWEEP=100
RESREF(P1)=1.0E-10
RESREF(W1)=1.0E-10
RESREF(V1)=1.0E-10
RESREF(H1)=1.0E-7
   GROUP 16. Termination of iterations
   GROUP 17. Under-relaxation devices
RELAX(P1,LINRLX,0.5)
RELAX(V1,FALSDT,0.1)
RELAX(W1,FALSDT,0.1)
RELAX(H1,FALSDT,1.0)
   GROUP 18. Limits on variables or increments to them
VARMIN(H1)=20.0
   GROUP 19. Data communicated by satellite to GROUND
USEGRX=T
RG(1)=1.4E-5
RG(2)=1.2928
RG(3)=WIN
RG(4)=DIA
RG(5)=GK
RG(6)=TIN
RG(7)=CP
   GROUP 20. Preliminary print-out
ECHO=T
   GROUP 21. Print-out of variables
```

```
OUTPUT(W1,Y,Y,Y,Y,Y,Y)
OUTPUT(V1,Y,Y,Y,Y,Y,Y)
OUTPUT(P1,Y,Y,Y,Y,Y,Y)
OUTPUT(H1,Y,Y,Y,Y,Y,Y)
   GROUP 22. Spot-value print-out
NPRMON=5,IXMON=1,IYMON=10,IZMON=10
NPLT=1
IZPRF=1;IZPRL=32
   GROUP 23. Field print-out and plot control
NUMCLS=6
NYPRIN=1
NZPRIN=1
   GROUP 24. Dumps for restarts
  NSAVE=
SAVE=T;AUTOPS=F
RESTRT(V1);RESTRT(W1);RESTRT(P1);RESTRT(H1)
                  STOP
```

Appendix D

PHOENICS Q1 input file for turbulent semi-confined jet impingement

```
TALK=F;RUN( 1, 1);VDU= 3
   GROUP 1. Run title and other preliminaries
TEXT(IMPINGING JET WITH POLAR GRID
REAL (WIN,TIN,TW,EPIN,TKEIN,DIA,REYNO,GMIXL)
REAL (NOZEND)
TIN=20.0; REYNO=60000;ENUL=1.46E-5;DIA=0.005
WIN=REYNO*ENUL/DIA
   GROUP 2. Transience; time-step specification
   GROUP 3. X-direction grid specification
CARTES=F
   GROUP 4. Y-direction grid specification
NY=90;YVLAST=1.0
YFRAC(1)=-10.0;YFRAC(2)=0.00025;YFRAC(3)=20.0;YFRAC(4)=0.00025
YFRAC(5)=60.0;YFRAC(6)=0.00025
   GROUP 5. Z-direction grid specification
NZ=30;ZWLAST=1.00
ZFRAC(1)=-20;ZFRAC(2)=0.000375;ZFRAC(3)=8;ZFRAC(4)=0.00025
ZFRAC(5)=2;ZFRAC(6)=0.000025
   GROUP 6. Body-fitted coordinates or grid distortion
   GROUP 7. Variables stored, solved & named
SOLUTN(P1,Y,Y,Y,N,N,N)
SOLUTN(V1,Y,Y,N,N,N,N)
SOLUTN(W1,Y,Y,N,N,N,N)
NAME(14)=TEMP
SOLUTN(TEMP,Y,Y,N,N,N,N)
TURMOD(KEMODL)
STORE(ENUT);VIST=50;NAME(50)=ENUT
   GROUP 8. Terms (in differential equations) & devices
DIFCUT=0.5
TERMS(TEMP,N,Y,Y,N,Y,N)
   GROUP 9. Properties of the medium (or media)
   *** The medium is air
ENUL=1.46E-5;RHO1=1.225;PRNDTL(TEMP)=0.7;PRT(TEMP)=0.86
   GROUP 10. Inter-phase-transfer processes and properties
   GROUP 11.
FIINIT(P1)=readfi;FIINIT(W1)=readfi;FIINIT(V1)=readfi
FIINIT(TEMP)=readfi;FIINIT(ENUT)=readfi
TKEIN=0.25*WIN**2*0.01
FIINIT(KE)=readfi
GMIXL=DIA/2*0.09
EPIN=(TKEIN**1.5)*0.1643/GMIXL
FIINIT(EP)=readfi
INIADD=F
   GROUP 12. Convection and diffusion adjustments
```

```
   GROUP 13. Boundary conditions and special sources
    ** JET VELOCITY DEFINITION flat inlet
PATCH(JET1,LOW,1,1,1,10,1,1,1,1)
COVAL(JET1,W1,ONLYMS,win)
COVAL(JET1,TEMP,ONLYMS,TIN)
COVAL(JET1,KE,ONLYMS,tkein)
COVAL(JET1,EP,ONLYMS,epin)
COVAL(JET1,P1,FIXFLU,win*RHO1)
  ** OUT FLOW REGION
PATCH(OUT,NORTH,1,1,NY,NY,1,NZ,1,1)
COVAL(OUT,P1,FIXP,0.0)
  **SET VELOCITY AT IMPINGEMENT WALL V1,W1=0
PATCH(IMPWALL,HIGH,1,1,1,NY,NZ,NZ,1,1)
COVAL(IMPWALL,V1,FIXVAL,0.0)
COVAL(IMPWALL,W1,FIXVAL,0.0)
PATCH(IMP1,HIGH,1,1,1,NY,NZ,NZ,1,1)
COVAL(IMP1,TEMP,FIXVAL,100.00)
    ** TURBULENT WALL FUNCTIONS ON WALL
PATCH(IMPING,HWALL,1,1,1,NY,NZ-1,NZ-1,1,1)
COVAL(IMPING,V1,GRND2,0.0)
COVAL(IMPING,TEMP,GRND2,100.0)
   COVAL(IMPING,W1,FIXVAL,0.0)
COVAL(IMPING,KE,GRND2,GRND2)
COVAL(IMPING,EP,GRND2,GRND2)
  **SET VELOCITY AT CONFINEMENT WALL V1,W1=0
PATCH(conf,HIGH,1,1,11,NY,1,1,1,1)
COVAL(conf,V1,FIXVAL,0.0)
COVAL(conf,W1,FIXVAL,0.0)
    ** TURBULENT WALL FUNCTIONS ON WALL
PATCH(confun,LWALL,1,1,11,NY,2,2,1,1)
COVAL(confun,V1,GRND2,0.0)
COVAL(confun,KE,GRND2,GRND2)
COVAL(confun,EP,GRND2,GRND2)
   GROUP 14. Downstream pressure for PARAB=.TRUE.
   GROUP 15. Termination of sweeps
LSWEEP=100
ISWC1=1
RESREF(P1)=1.0e-6
RESREF(W1)=1.0e-6
RESREF(V1)=1.0e-6
RESREF(TEMP)=1.0e-6
RESREF(KE)=1.0e-6
RESREF(EP)=1.0e-6
   GROUP 16. Termination of iterations
   GROUP 17. Under-relaxation devices
RELAX(P1,LINRLX,0.4)
RELAX(V1,FALSDT,0.1)
RELAX(W1,FALSDT,0.1)
RELAX(TEMP,FALSDT,1.0)
```

```
RELAX(EP,FALSDT,0.1)
RELAX(KE,FALSDT,0.1)
   GROUP 18. Limits on variables or increments to them
VARMAX(TEMP)=100.0
   GROUP 19. Data communicated by satellite to GROUND
RG(1)=ENUL;RG(2)=RHO1;RG(3)=WIN;RG(4)=DIA;RG(5)=2.428E-2;RG(6)
=20;RG(7)=1004
   GROUP 20. Preliminary print-out
   GROUP 21. Print-out of variables
OUTPUT(W1,Y,Y,Y,Y,Y,Y);OUTPUT(V1,Y,Y,Y,Y,Y,Y)
OUTPUT(P1,Y,Y,Y,Y,Y,Y);OUTPUT(TEMP,Y,Y,Y,Y,Y,Y)
   GROUP 22. Spot-value print-out
NPRMON=1;IXMON=1;IYMON=10;IZMON=29;NPLT=1
   GROUP 23. Field print-out and plot control
NUMCLS=6
   GROUP 24. Dumps for restarts
SAVE=T;AUTOPS=F
restrt(P1);restrt(V1);restrt(W1);restrt(KE);restrt(EP);restrt(TEMP)
STOP
```

Appendix E

PHOENICS ground code for the calculation of heat transfer from the temperature field - user interface

```
CXXXXXXXXXXXXXXXXXXXXXXXXXXXXXXXXXXXXXXXX USER
SECTION STARTS:
C
C 1   Set dimensions of data-for-GROUND arrays here. WARNING: the
C corresponding arrays in the MAIN program of the satellite
C and EARTH must have the same dimensions.
  PARAMETER (NLG=20, NIG=20, NRG=100, NCG=10)
C

COMMON/LGRND/LG(NLG)/IGRND/IG(NIG)/RGRND/RG(NRG)/CGRND/C
G(NCG)
  LOGICAL LG
  CHARACTER*4 CG
C
C 2   User dimensions own arrays here, for example:
C DIMENSION GUH(10,10),GUC(10,10),GUX(10,10),GUZ(10)
C
C 3   User places his data statements here, for example:
C DATA NXDIM,NYDIM/10,10/
C
C 4   Insert own coding below as desired, guided by GREX examples.
C Note that the satellite-to-GREX special data in the labelled
C COMMONs /RSG/, /ISG/, /LSG/ and /CSG/ can be included and
C used below but the user must check GREX for any conflicting
C uses. The same comment applies to the EARTH-spare working
C arrays EASP1, EASP2,....EASP20. In addition to the EASPs,
C there are 10 GRound-earth SPare arrays, GRSP1,...,GRSP10,
C supplied solely for the user, which are not used by GREX. If
C the call to GREX has been deactivated then all of the arrays
C may be used without reservation.
C
EQUIVALENCE (IZ,IZSTEP)
C##########################################################
################
C####      This section allows definition of variables to be used
C####      in the users coding
C####
C##########################################################
################
      REAL GMU,GRHO1,GWIN,GDIA,GK,GTIN,TGW
      INTEGER NUMNY
```

```
      DIMENSION GSTAN1(160,1),GSKIN(160,1),GRELVEL(160,1)
      DIMENSION GYDIS(160,1),GH1(160,1),GHH1(160,1)
      DIMENSION GZDIS(30),GZHI(30),GHT(160),GNU(160),GST(160)
      PARAMETER(MY=90,MX=1,MZ=30)
      EQUIVALENCE(GMU,RG(1))
      EQUIVALENCE(GRHO1,RG(2))
      EQUIVALENCE(GWIN,RG(3))
      EQUIVALENCE(GDIA,RG(4))
      EQUIVALENCE(GK,RG(5))
      EQUIVALENCE(GTIN,RG(6))
      EQUIVALENCE(GCP,RG(7))
C##################################################
################
C#### User definitions end
C##################################################
################

  IXL=IABS(IXL)
  IF(IGR.EQ.13) GO TO 13
  IF(IGR.EQ.19) GO TO 19
  GO TO (1,2,3,4,5,6,25,8,9,10,11,12,13,14,25,25,25,25,19,20,25,
 125,23,24),IGR
   25 CONTINUE
  RETURN
C*****************************************************************
C
C--- GROUP 1. Run title and other preliminaries
C
1 GO TO (1001,1002),ISC
1001   CONTINUE
C##################################################
################
C#### Creates geometric data in system variables, these can be
C#### accessed by the user
C##################################################
################
   CALL MAKE(YG2D)
   CALL MAKE(ZGNZ)
   CALL MAKE(ZWNZ)
C##################################################
################
C#### End of this section
C##################################################
################
C
C User may here change message transmitted to the VDU screen or
C batch-run log file.
  IF(IGR.EQ.1.AND.ISC.EQ.1) THEN
CALL WRYT40('GROUND file is GROUND.FTN of:110191 ')
```

```
CALL WRYT40('PHOENICS version number is  :1.6')
CALL WRYT40('October 1992 heat transfer code S Kapasi')
  ENDIF
C
  RETURN
1002  CONTINUE
  RETURN

C
C--- GROUP 13. Boundary conditions and special sources
C   Index for Coefficient - CO
C   Index for Value   - VAL
   13 CONTINUE
  GO TO (130,131,132,133,134,135,136,137,138,139,1310,
 11311,1312,1313,1314,1315,1316,1317,1318,1319,1320,1321),ISC
  130 CONTINUE
C------------------- SECTION  1 ------------ coefficient = GRND
  RETURN
  131 CONTINUE
C------------------- SECTION  2 ------------ coefficient = GRND1
  RETURN
  132 CONTINUE
C##############################################################
##################
C##  This section of the code retrieves the F-Array and finds
C##  the turbulent Stanton number for the wall patch.
C##  The Nusselt number is deduced from this value
C##############################################################
##################

        IF ((INDVAR .EQ. 14) .and. (IZ .EQ. (NZ-1))) THEN
        CALL GETYX(C1,GSTAN1,NY,MX)
        CALL GETYX(C2,GSKIN,NY,MX)
        CALL GETYX(C3,GRELVEL,NY,MX)
        CALL GETYX(H1,GH1,NY,MX)
        CALL GETYX(HIGH(H1),GHH1,NY,MX)
        LOCO=L0F(CO)
        LOSK=L0PVAR(PVSKIN,IREG,0)
        LORLVL=L0PVAR(PVRLVL,IREG,0)
        LOMUDD=L0F(LD11)
        IPLUS=(IXF-2)*NY
        J=0
c       DO 13211 IX=IXF,IXL
              IPLUS=IPLUS+NY
              DO 13211 IY=IYF,IYL
              I=IY+IPLUS
              J=J+1
C             heat transfer coefficient
        TGW=(GHH1(IY,1)-GH1(IY,1))/(GHH1(IY,1)-20.0)
```

```
                GSTAN1(IY,1)=F(LOCO+I)*1005*1.202*TGW
c               yplus
CC
GSKIN(IY,1)=((F(LOSK+J))**0.5)*F(LORLVL+J)/(F(LOMUDD+I+TINY))
c               skin friction s
                GSKIN(IY,1)=F(LOSK+J)
c               Reynolds number
                GRELVEL(IY,1)=F(LORLVL+J)/(F(LOMUDD+I)+TINY)
CC      WRITE(6,*)IY,IZ,INDVAR,GSTAN1(IY,1),GHH1(IY,1),GH1(IY,1)
13211   CONTINUE


        OPEN(UNIT=30,STATUS='UNKNOWN',FILE='HTRANS.DAT')
        OPEN(UNIT=31,STATUS='UNKNOWN',FILE='HTnuss.DAT')

        IF(ISWEEP.EQ.LSWEEP-1) then
        CALL GETYX(YG2D,GYDIS,NY,MX)
        IF (IZ.EQ.(NZ-1)) THEN
        DO 13212 IY=1,90,2
        WRITE(30,13213)GYDIS(IY,1)/GDIA,GSTAN1(IY,1)
        write(31,13213)GYDIS(IY,1)/GDIA,GSTAN1(IY,1)*GDIA/GK
13212   CONTINUE
13213   FORMAT(1X,F6.1,2x,f8.1)
        ENDIF

        WRITE(6,*)IY,IZ,INDVAR,GSTAN1(1,1),GSKIN(1,1),GRELVEL(1,1)


        ENDIF
        endif
        CALL SETYX(C1,GSTAN1,NY,MX)
        CALL SETYX(C2,GSKIN,NY,MX)
        CALL SETYX(C3,GRELVEL,NY,MX)

C##############################################################
#########################
C##  end of section of coding to determine the turbulent Nusselt number
C##############################################################
#########################
C------------------ SECTION  3 ------------ coefficient = GRND2
  RETURN


  195 CONTINUE
C   * ------------------ SECTION 5 ---- Finish of iteration.
  RETURN
C##############################################################
#########################
C#### This section allows access to the coding after completion of the
```

```
C####     last slab the impingement wall. The temperature and velocity
C####     data for the previous slab can be accessed. The laminar Nusselt
C####     number is calculated.
C##########################################################
##########################

  196 CONTINUE
C   * ------------------ SECTION 6 ---- Finish of iz slab.
1999   FORMAT(1X,'ISWEEP= ',I5)
C#### Check sweep number is one before the last
       IF(ISWEEP.EQ.LSWEEP-1) GOTO 1961
       GOTO 1969
C#### Check the slab is one before the last in the z-direction
1961   IZLAST=NZ-1
       IF(IZ.EQ.IZLAST) GOTO 1962
       GOTO 1969
C#### Accessing the solved variables temperature, cell distances
C#### in both y and z directions
1962   CALL GETYX(H1,GH1,NY,MX)
       CALL GETYX(HIGH(H1),GHH1,NY,MX)
       CALL GETYX(YG2D,GYDIS,NY,MX)
       CALL GETZ(ZGNZ,GZDIS,NZ)
       CALL GETZ(ZWNZ,GZHI,NZ)
C#### Derivation of the heat transfer begins in this part
       GDX=GZHI(NZ-1)-GZDIS(NZ-1)
C      OPEN(UNIT=32,STATUS='UNKNOWN',FILE='HTstan.DAT')
       DO 1963 IY=1,NY
       GHT(IY)=GK*(GHH1(IY,1)-GH1(IY,1))/((GHH1(IY,1)-GTIN)*GDX)
       GNU(IY)=GHT(IY)*GDIA/GK
C      write(32,19631)GK,Ghh1(iy,1),GH1(IY,1),GTIN,GDX
19631  format(' ',5f10.5)
CC     GST(IY)=GHT(IY)/(GRHO1*GCP*GWIN)
1963   CONTINUE
1969   CONTINUE
RETURN
C#### Output of derived information to a graphics format file
  197   CONTINUE
C   * ------------------ SECTION 7 ---- FINISH OF SWEEP.
       IF(ISWEEP.NE.LSWEEP-1) GOTO 1979
CC     OPEN(UNIT=30,STATUS='UNKNOWN',FILE='HTRANS.DAT')
CC     OPEN(UNIT=31,STATUS='UNKNOWN',FILE='HTnuss.DAT')
CC     OPEN(UNIT=32,STATUS='UNKNOWN',FILE='HTstan.DAT')
CC     OPEN(UNIT=33,STATUS='UNKNOWN',FILE='WJNUSS.DAT')
CC     NUMNY=40+1+INT((NY-40)/4.0)
       NUMNY=90
       GREY=GWIN*GDIA/GMU
       DELZ=(GZHI(NZ-1)-GZDIS(1))/GDIA
cc     WRITE(30,19711)GREY,DELZ,NUMNY
CC     WRITE(31,19711)izlast,GREY,DELZ,NUMNY
```

```
CC     WRITE(32,19711)GREY,DELZ,NUMNY
19711  FORMAT(' ',I3,F6.0,'H=',F4.1,/,'X 1 0',/,I3)
       DO 1971 IY=1,90,2
CC     WRITE(30,1967)GYDIS(IY,1)/GDIA,GHT(IY)
CC     write(31,1967)GYDIS(IY,1)/GDIA,GNU(IY)
CC     WRITE(32,1967)GYDIS(IY,1)/GDIA,GST(IY)
1971CONTINUE
1967   FORMAT(1X,F10.5,F10.5)
1979   CONTINUE
C#### End of the output section

C   * ------------------- SECTION 7 ---- Finish of sweep.
  RETURN
  198 CONTINUE
C   * ------------------- SECTION 8 ---- Finish of time step.
C
  RETURN
```

Appendix F

Program for the calculation of jet Reynolds number from pressure drop across orifice

```
REM ORIFICE PLATE AND NOZZLE FLOW RATE CALCULATOR


CLS
PRINT" Flow rate calculations for orfice plate/ nozzle combination"
PRINT" Orifice and it's pipework should be to BS 1042"
PRINT
CALL INIT
INPUT "AGAIN?",F$
IF F$="Y" THEN CALL INIT
END



SUB INIT
CLS
INPUT "Enter orifice tube diameter ( m ) ",D
INPUT "Enter orifice diameter (m )",OD
INPUT "Enter Nozzle diameter ( m ) ",DN
INPUT "Air denisity will be calculated from temp, please enter IN KELVIN",T
RHO=1.284-.00428*(T-275)
V=1.725E-5+.00484E-5*(T-275)
PRINT

B=OD/D
A=3.15159*OD^2/4
INPUT "DO YOU REQUIRE SINGLE REYNOLDS NO. OR RANGE OF
PRESSURES 1/0",Y
IF Y=0 THEN CALL PRESS(RHO,B,DN,V,A,OD,D) ELSE CALL
REN(RHO,B,DN,V,A)
END  SUB

SUB PRESS(RHO,B,DN,V,A,OD,D)
CLS
PRINT"WHAT RANGE AND STEP OF Re DO YOU WISH THE PRESSURE
DROP CALCULATING?"
INPUT"Enter lower value for Re ",R1
INPUT"Enter upper value for Re ",R2
INPUT"Enter Step",S
LPRINT"ORIFICE DIA=";OD;" NOZZLE DIA=";DN;" TUBE DIA=";D
PRINT"RESULTS IN MM WATER"

LPRINT"RESULTS IN MM WATER"
```

```
PRINT
FOR RE=R1 TO R2 STEP S
REM NEED TO CALCULATE FLOW COEFICIENTT Co
CO=0.5959+.0312*B^2.1-0.184*B^8+.0029*B^2.5*(10^6/RE)^0.75+0.039*B
^4*(1-B^4)^-1-0.0337*.5*B^3
REM NOW CALC PRESSURE DROP
DP=RHO*(1-B^4)*0.5*(RE*V*3.14159*DN/(4*RHO*A*CO))^2
DP=DP/9.810



LPRINT "RE= ";RE;"  PRESSURE DROP= ";DP
PRINT "RE= ";RE;"   PRESSURE DROP= ";DP;"  C= ";CO
NEXT

END SUB

SUB REN(RHO,B,DN,V,A)
CLS
INPUT"ENTER OBSERVERED PRESSURE DROP ( M ) ",DP1
DP=DP1*9810
IT=0:C=0:CO=0.6
DO
U=0
RE=(2*DP/(RHO*(1-B^4)))^0.5*(4*RHO*A*CO/(V*3.14159*DN))
CO1=0.5959+.0312*B^2.1-0.1840*B^8+0.0029*B^2.5*(10^6/RE)^0.75+0.039
*B^4*(1-B^4)^-1-0.0337*0.5*B^3
C=ABS((CO-CO1)/CO1):IF C<0.000000001 THEN U=1
CO=CO1
IT=IT+1
PRINT "NO ITERATIONS=";IT
LOOP UNTIL U=1
LPRINT "REYNOLDS NUMBER =";RE;" FOR PRESSURE DROP OF ";DP1;"
M"
END SUB
```

Appendix G

Analysis program for calculation of mass transfer from experimental data

```
100 REM This program calculates the
101 REM mass transfer coefficient against radial distance
102 REM outputs fringe order number against radial distance
103 REM and Sherwood number against radial distance
104 REM Output files are in the format of PA4 files

    INPUTS::
    TST$  == output filename for mass transfer coefficient
    CAGE$      == output filename for fringe order number
    SHR$ == output filename for Sherwood number
    DIA   == nozzle diameter (cm)
    T     == temperature of room (C)
    RE    == Reynolds number of jet
    VVPS       == vapour pressure 27.8 - 7650/T (N/m^2)
    DIFF  == diffusion coefficient  -0.0516+0.000367xT (cm^2/s)
    RHO   == density of the swollen polymer 1.01 (gm/cm^3)
    ETA   == refractive index 1.48 - 0.00017xT
    x     == radial position of last fringe (cm)
    TIM   == experimental time period (s)
    NF    == first fringe order number
    LF    == last fringe order number


110 LPRINT
"=========================================
====="
120 LPRINT DATE$, TIME$
130 PRINT "Input test photo number filename"
140 INPUT TST$
150 LPRINT "The test number is "; TST$
161 PRINT "1) Fringe out file 2) Sherwood out"
162 PRINT "example          P36                S36     "
166 INPUT CAGE$
168 INPUT SHR$
180 DIM XDIS(40), HMT(40), HMX(40), CENT(40), SHER(40), NFRIN(40)
200 PRINT "Nozzle diameter in cm"
210 INPUT DIA
215 PRINT "Temperature of test"
217 INPUT T
220 T = T + 273
230 LPRINT "Temperature= "; T; " K  DIAMETER= ", DIA; " CM"
235 REM diffusion correlation for 18-22 degrees centigrade
```

```
237 DIFF = -.0516 + .000367 * T
240 RHO = 1.01
254 PRINT "Reynolds"
255 INPUT RE
260 LPRINT "Diffusion= ";DIFF;" cm^2/s Density= ";RHO;" gm/cm^3 Re= ";
RE
300 PRINT " Refractive index neta"
305 REM Vapour pressure using S. Zangeneh(1990) correlation
310 VVPS = 27.8 - 7650 / T
320 VPS = (1 / 133.4) * EXP(VVPS)
340 REM refractive index correlation obtained experimentally
350 ETA = 1.48 - .00017 * T
360 LPRINT "Vapour pressure= "; VPS; " (mmHg) Neta= "; ETA
400 REM GC is the gamma function
450 GC = .495
455 PRINT "input the x distance of the last fringe"
460 INPUT x
461 x = x
470 LPRINT "Gamma= "; GC, " distance= "; x; " cm"
490 REM TIM is the experimental time and YLAMDA the wavelength
495 PRINT "Input Mass transfer test time"
500 INPUT TIM
600 YLAMDA = .0000633
700 LPRINT "Time = "; TIM; " s  Lamda= "; YLAMDA; " cm"
1100 REM AI1,AI2 are incident and reflection angles
1200 AI1 = 17
1205 AI2 = 15.5
1210 AI1 = AI1 * (3.1415 / 180)
1220 AI2 = AI2 * (3.1415 / 180)
1250 AAI1 = SIN(AI1) / ETA
1260 AAI2 = SIN(AI2) / ETA
1270 REM Inverse Sine these  AAI1,AAI2
1300 ALPHA = AAI1 + (AAI1 ^ 3) / 6 + .075 * AAI1 ^ 5
1310 BETA = AAI2 + (AAI2 ^ 3) / 6 + .075 * AAI2 ^ 5
1450 LPRINT "Alpha(rad)= "; ALPHA; " Beta(rad)= "; BETA
1500 CON1 = 1 / COS(ALPHA) * (ETA - (COS(AI1 - ALPHA)))
1600 CON2 = 1 / COS(BETA) * (ETA - (COS(AI2 - BETA)))
1700 CONS = CON1 + CON2
1750 REM LPRINT "CONST"; CONST
1800 SI = (1 + .002337 * RE * ((DIA / x) ^ 3)) ^ -.75
1900 HM = .426 * DIFF * (RE ^ .75) * GC * ((DIA / x ^ 5) ^ .25) * SI
2000 CS = .002662 * VPS / T
2080 NF = HM * CS * CONS * TIM * 2 / (RHO * YLAMDA)
2100 PRINT "fringe No "; NF
2150 NF = INT(NF + .5)
3000 LPRINT "Fringe order number deduced from theory at X="; x; " is  "; NF
3100 PRINT "Do you want to change this fringe number answer YES or NO"
3200 INPUT Y$
3300 IF Y$ = "YES" THEN GOTO 3500
```

```
3400 IF Y$ = "NO" THEN GOTO 4000
3450 GOTO 3100
3500 PRINT "The new fringe number"
3600 INPUT NF
4000 PRINT "Input last fringe numbers on photo"
4500 INPUT LF
5000 PRINT "Input X distance for fringe "; NF + 1; " to "; LF
5400 XDIS(NF) = x
5500 FOR J = NF + 1 TO LF
6000 PRINT "Fringe "; J
6050 INPUT XDIS(J)
6025 XDIS(J) = XDIS(J) * DIA
6500 NEXT J
6501 REM ************************************************************
6502 REM output of mass transfer data
6503 REM ************************************************************
6505 OPEN "O", #3, TST$
6510 PRINT #3, "M"
6511 PRINT #3, "0"
6512 PRINT #3, "0 4.0 8.0 12.0 16.0 20.0 24.0"
6513 PRINT #3, "0"
6514 PRINT #3, "0 1.5 3.0 4.5 6.0 7.5 9.0"
6517 PRINT #3, "1 0"
6518 PRINT #3, "Mass Transfer Coefficient for Re="; RE; " Test = "; TST$; "*"
6520 PRINT #3, "Temperature = "; T - 273; " Nozzle diameter = "; DIA; "*"
6525 PRINT #3, "Non Dimensional Distance from Stagnation pt*"
6530 PRINT #3, "*"
6535 PRINT #3, "Mass transfer coefficient*"
6536 PRINT #3, "cm/s*"
6537 PRINT #3, "KEY*"
6538 PRINT #3, "2"
6540 PRINT #3, "Experimental*"
6545 PRINT #3, "X 1 1"
6550 PRINT #3, LF - NF + 1
6800 REM LPRINT "Mass transfer from experiment"
6810 REM LPRINT "----------------------------"
7000 FOR J = NF TO LF
7500 HMT(J) = RHO * J * YLAMDA / (2 * CONS * CS * TIM)
8000 PRINT #3, XDIS(J) / DIA, HMT(J)
8500 NEXT J
8510 PRINT #3, "Theoretical*"
8520 PRINT #3, "X 1 1"
8550 PRINT #3, LF - NF + 1
8800 LPRINT " Fringe   Non-dimensional   Experimental      Theoretical"
8805 LPRINT " Order    Distance          Coefficient       Coefficient"
8810 LPRINT "-------------------------------------------------------"
9000 FOR J = NF TO LF
9100 SI = (1 + .002337 * RE * ((DIA / XDIS(J)) ^ 3)) ^ -.75
9200 HMX(J) = .426 * DIFF * (RE ^ .75) * GC * ((DIA / (XDIS(J)) ^ 5) ^
```

```
.25) * SI
9300 LPRINT J; "      "; XDIS(J) / DIA; "      "; HMT(J); " cm/s      "; HMX(J);
" cm/s"
9350 PRINT #3, XDIS(J) / DIA, HMX(J)
9400 NEXT J
9450 CLOSE #3
9500 LPRINT
"=============================================
====="
9501 REM ************************************************************
9502 REM output fringe data against radial distance
9503 REM ************************************************************
9505 OPEN "O", #1, CAGE$
9550 PRINT #1, LF - NF + 1
9555 FOR J = NF TO LF
9556 SI = (1 + .002337 * RE * ((DIA / XDIS(J)) ^ 3)) ^ -.75
9557 HM = .426 * DIFF * (RE ^ .75) * GC * ((DIA / XDIS(J) ^ 5) ^ .25) * SI
9558 CS = .002662 * VPS / T
9559 NFRIN(J) = HM * CS * CONS * TIM * 2 / (RHO * YLAMDA)
9560 REM LPRINT "fringe No ";NFRIN(J)
9561 REM NFRIN(J)=INT(NFRIN(J)+.5)
9562 LX = XDIS(J) / DIA
9563 LFN = LOG(NFRIN(J)): LX = LOG(LX)
9564 PRINT #1, LX, LFN
9565 REM PRINT XDIS(J),NFRIN(J)
9570 NEXT J
9575 PRINT #1, "Experimental*"
9576 PRINT #1, "X 1 1"
9577 PRINT #1, LF - NF + 1
9580 FOR J = NF TO LF
9582 LX = LOG(XDIS(J) / DIA)
9583 LFN = LOG(J)
9585 PRINT #1, LX, LFN
9586 PRINT XDIS(J), J
9590 NEXT J
9591 REM ************************************************************
9592 REM output sherwood number against radial distance
9593 REM ************************************************************
10005 OPEN "O", #3, SHR$
10010 PRINT #3, "M"
10011 PRINT #3, "0"
10012 PRINT #3, "0 4.0 8.0 12.0 16.0 20.0 24.0"
10013 PRINT #3, "0"
10014 PRINT #3, "0 5.0 10.0 15.0 20.0 25.0 30.0"
10017 PRINT #3, "1 0"
10018 PRINT #3, "Mass Transfer Coefficient for Re="; RE; " Test = "; TST$; "*"
10020 PRINT #3, "Temperature = "; T - 273; " Nozzle diameter = "; DIA; "*"
10025 PRINT #3, "Non Dimensional Distance from Stagnation pt*"
10030 PRINT #3, "*"
```

```
10035 PRINT #3, "Sherwood number Sh*"
10036 PRINT #3, "*"
10037 PRINT #3, "KEY*"
10038 PRINT #3, "2"
10040 PRINT #3, "Experimental*"
10045 PRINT #3, "X 1 1"
10050 PRINT #3, LF - NF + 1
10055 FOR J = NF TO LF
10056 SHER(J) = (HMT(J) * DIA) / DIFF
10060 PRINT #3, XDIS(J) / DIA, SHER(J)
10070 REM LPRINT XDIS(J)/DIA,SHER(J)
10080 NEXT J
10100 PRINT #3, "S&T's correl"
10110 PRINT #3, "X 1 1"
10120 PRINT #3, "LF-NF+1"
10200 FOR J = NF TO LF
10220 SHER(J) = (HMX(J) * DIA) / DIFF
10240 PRINT #3, XDIS(J) / DIA, SHER(J)
10260 NEXT J
20000 STOP
50000 END
```

Appendix H

Fortran program for estimating the uncertainty in the correlation equations

```
C     Program for determining the uncertainty in the correlation for
C     Nusselt number from the different experimental techniques
C
C     INPUT::
C     ref,rel,res == first,last,step for Reynolds number
C     rdf,rdl,rds == first,last,step for radial distance
C     Zd ==  Jet to plate spacing
C     FN == Filename for output
C     a,b,c,d == Coefficients of the correlation
C     aerr,berr,cerr,derr == Error in the coefficients
C     Reye == Error in the Reynolds number
C     rde == Error in the radial distance
C     zde == Error in the spacing
C     J == seed value for the random number generator
C
C     OUTPUT::
C     rd == radial distance
C     DMEAN == Mean Nusselt number
C     RPLUS == upper uncertainty limit of Nusselt number
C     RMINUS == lower uncertainty limit of Nusselt number

      REAL MIN
      INTEGER IN
      CHARACTER*50 FN
      DIMENSION  RE(11000),RX(11000),ZX(11000)
      DIMENSION  RNU(11000),R(11000),RPLUS(10),RMINUS(10)
      OPEN(UNIT=26,FILE='INP.DAT',STATUS='UNKNOWN')
      IN=1
111   READ(26,*) ref,rel,res
      READ(26,*) rdf,rdl,rds
      READ(26,*) ZD
      READ(26,*) FN
      OPEN(UNIT=25,FILE=FN ,STATUS='UNKNOWN')
      n=1000
      m=int(0.025*n)
      read(26,*) a,b,c,d
      read(26,*) aerr,berr,cerr,derr
      READ (26,*) Reye
      READ(26,*) rde
      READ(26,*) zde
      READ(26,*) J
      DO 500 REY=ref,rel,res
      WRITE(25,*) rey,fn
      WRITE(25,*)'x 1 1'
```

```
      WRITE(25,*) int((rdl-rdf)/rds)+1
      DO 200 RD=rdf,rdl,rds
      Reyn=Rey-Reye
      rdis=rd-rde
      zdis=ZD-zde
      DSUM=0
      DFT=0
      DO 10 I=1,N
      aX=a-(aerr)+2*RAN(J)*(aerr)
      bX=b-(berr)+2*RAN(J)*(berr)
      cX=c-(cerr)+2*RAN(J)*(cerr)
      dX=d-(derr)+2*RAN(J)*(derr)
      ReN=Reyn+RAN(J)*2*Reye
      rxN=rdis+RAN(J)*2*rde
      zxN=zdis+RAN(J)*2*zde
      RNU(I)=dX*(ReN**aX)*(rxN**bX)*(zxN**cX)
      DSUM=DSUM+RNU(I)
      DFS=(RNU(I)**2)
      DFT=DFT+DFS
10    CONTINUE
      DMEAN=DSUM/N
      D1=(DFT-(N*DMEAN**2))/N
      D2=(D1)**0.5
      K=1
40    MIN=1E+35
      DO 50 I=K,N
      IF(RNU(I).GT.MIN) GOTO 50
      MIN=RNU(I)
      IL=I
50    CONTINUE
      DUMMY=RNU(K)
      RNU(K)=RNU(IL)
      RNU(IL)=DUMMY
      K=K+1
      IF(K.EQ.N-1) GOTO 60
      GOTO 40
60    CONTINUE
      L=INT((RD-rdf)/rds)+1
      RPLUS(L)=RNU(N-M)
      RMINUS(L)=RNU(M)
11    format('RD=',F4.1,' Nu=',F5.1,' Nu-=',F5.1,' Nu+=',F5.1,' STD=',F5.2)
      WRITE(25,12) RD,DMEAN
12    FORMAT(1x,F4.1,1X,F5.1)
200   CONTINUE
      WRITE(25,*)'Upper'
      WRITE(25,*)'x 1 1'
      WRITE(25,*) int((rdl-rdf)/rds)+1
      DO 300 RD=rdf,rdl,rds
      L=INT((RD-rdf)/rds)+1
```

```
      WRITE(25,13) RD,RPLUS(L)
13    FORMAT(1x,F4.1,1X,F6.1)
300   CONTINUE
      WRITE(25,*)'Lower'
      WRITE(25,*)'x 1 1'
      WRITE(25,*) int((rdl-rdf)/rds)+1
      DO 400 RD=rdf,rdl,rds
      L=INT((RD-rdf)/rds)+1
      WRITE(25,14) RD,RMINUS(L)
14    FORMAT(1x,F4.1,1X,F6.1)
400   CONTINUE
500   CONTINUE
      IN=IN+1
      IF(IN.LT.7) GOTO 111
      END
```

Appendix I

Program to calculate the uncertainty limit of the experimental mass transfer coefficients

INPUT::
FL1$ == input data filename
TMP == temperature in Kelvin
TE == uncertainty in temperature
VPS == vapour pressure of ester
PE == uncertainty in vapour pressure
TIMA == time in seconds
TME == uncertainty in time
NTA == refractive index
NTE == uncertainty in refractive index
AI1 == incidence angle of beam
I1E == uncertainty in angle
AI2 == reflection angle of beam
I2E == uncertainty in angle

OUTPUT::
KMEAN== mean mass transfer coefficient
S2 == standard deviation of KMEAN

```
100 REM The mass transfer coefficient with uncertainties
150 DIM T(1100),PS(1100),TIM(1100),NT(1100),I1(1100),I2(1100)
155 DIM R(1100),K(1100)
200 RANDOMIZE
300 LET R=623
330 PRINT "Output filename for initial data and mean calculation"
340 INPUT FL1$
350 OPEN FL1$ FOR OUTPUT AS #2
400 PRINT "Input Temperature/K and error in temperature"
450 INPUT TMP,TE
460 PRINT #2,"Input Temperature/K";TMP;" and error in temperature";TE
500 PRINT "Input Vapour pressure/mm hg and error"
550 INPUT VPS,PE
560 PRINT #2,"Input Vapour pressure/mm hg";VPS;" and error";PE
600 PRINT "Input Time/sec and error"
650 INPUT TIMA,TME
660 PRINT #2,"Input Time/sec";TIMA;" and error";TME
700 PRINT "Input Refractive index and error"
750 INPUT NTA,NTE
760 PRINT #2,"Input Refractive index";NTA;" and error";NTE
800 PRINT "Input Incidence angle/deg and error"
850 INPUT AI1,I1E
```

```
851 PRINT #2,"Input Incidence angle/deg";AI1;" and error";I1E
855 LET AI1=AI1*8.726639E-03
856 LET I1E=I1E*8.726639E-03
900 PRINT "Input reflection angle/deg and error"
950 INPUT AI2,I2E
951 PRINT #2,"Input reflection angle/deg";AI2;" and error";I2E
955 LET AI2=AI2*8.726639E-03
956 LET I2E=I2E*8.726639E-03
1000 LET DIF1=TMP-TE
1010 LET DIF2=VPS-PE
1020 LET DIF3=TIMA-TME
1030 LET DIF4=NTA-NTE
1040 LET DIF5=AI1-I1E
1050 LET DIF6=AI2-I2E
1060 LET TE=2*TE
1070 LET PE=2*PE
1080 LET TME=2*TME
1090 LET NTE=2*NTE
1100 LET I1E=2*I1E
1110 LET I2E=2*I2E
1200 FOR I=1 TO 1000
1210 LET R(I)=RND
1220 LET T(I)=RND*TE+DIF1
1230 LET PS(I)=RND*PE+DIF2
1240 LET TIM(I)=RND*TME+DIF3
1250 LET NT(I)=RND*NTE+DIF4
1260 LET I1(I)=RND*I1E+DIF5
1270 LET I2(I)=RND*I2E+DIF6
1300 NEXT I
1400 KSUM=0
1500 PRINT "Output filename is "
1510 INPUT FL$
1520 OPEN FL$ FOR OUTPUT AS #3
1800 FOR I=1 TO 1000
1850 LET X1=SIN(I1(I)/NT(I))
1860 LET X2=SIN(I2(I)/NT(I))
1900 LET ALPHA=X1+(X1^3)/6+.075*X1^5
2000 LET BETA=X2+(X2^3)/6+.075*X2^5
2100 LET C1=(NT(I)-COS(I1(I)-ALPHA))/COS(ALPHA)
2200 LET C2=(NT(I)-COS(I2(I)-BETA))/COS(BETA)
2300 LET C3=1/(C1+C2)
2400 LET K(I)=.012*T(I)/(PS(I)*TIM(I))*C3
2450 REM   PRINT REM "K= ";K(I);" R= ";R(I)
2460 PRINT #3,K(I),R(I)
2490 LET KSUM=KSUM+K(I)
2500 NEXT I
2700 FOR I=1 TO 1000
2800 LET S=(K(I)^2)
2900 LET S1=S1+S
```

```
3000 NEXT I
3100 LET KMEAN=KSUM/1000
3200 LET S=(S1-(1000*KMEAN^2))/1000
3300 LET S2=SQR(S)
3400 PRINT "The mean coefficient =";KMEAN;" cm/s";" The std deviation=";S2
3410 PRINT #2,"The mean coefficient =";KMEAN;" cm/s";" The std
deviation=";S2
3500 END
```

Appendix J

Tabulation of mass transfer data for laminar jet impingement

Test 150 Re = 500 t = 360 s z/d = 2 d = 4.93 mm T = 26.3°C		Test 151 Re = 500 t = 360 s z/d = 4 d = 4.93 mm T = 26.3°C	
r/d	*Sh*	*r/d*	*Sh*
9.13	1.32	5.07	3.95
7.10	2.63	4.26	5.27
5.88	3.95	3.55	6.59
5.27	5.27	3.04	7.90
4.06	6.59	2.64	9.22
3.55	7.90	2.33	10.54
2.94	9.22	2.13	11.85
2.54	10.54	1.93	13.17
2.33	11.85	1.72	14.49
2.03	13.17	1.52	15.81
1.83	14.49	1.42	17.12
1.62	15.81	1.32	18.44
1.52	17.12	1.22	19.76

Test 146 Re = 1000 t = 360 s z/d = 2 d = 4.93 mm T = 25.4°C		Test 147 Re = 1000 t = 360 s z/d = 4 d = 4.93 mm T = 25.4°C	
r/d	*Sh*	*r/d*	*Sh*
10.14	1.42	10.65	1.42
7.10	2.84	8.11	2.84
6.09	4.25	6.09	4.25
5.27	5.67	5.07	5.67
4.06	7.09	4.46	7.09
3.65	8.51	4.06	8.51
3.35	9.92	3.55	9.92
3.04	11.34	3.25	11.34
2.74	12.76	2.84	12.76
2.54	14.18	2.54	14.18
2.33	15.60	2.43	15.60
2.03	17.01	2.23	17.01
1.83	18.43	2.13	18.43
1.62	19.85		

Test 148 Re = 1000 t = 360 s z/d = 6 d = 4.93 mm T = 26.2°C		Test 149 Re = 1000 t = 360 s z/d = 12 d = 4.93 mm T = 26.2°C	
r/d	*Sh*	*r/d*	*Sh*
14.20	1.33	7.10	3.98
8.11	2.66	6.09	5.31
6.09	3.98	4.56	6.64
5.07	5.31	3.85	7.97
4.36	6.64	3.31	9.30
3.65	7.97	3.04	10.62
3.25	9.30	2.78	11.95
3.04	10.62	2.54	13.28
2.74	11.95	2.23	14.61
2.54	13.28	2.03	15.94
2.33	14.61	1.83	17.26
2.03	15.94	1.62	18.59
1.83	17.26		
1.62	18.59		
1.52	19.92		

Test 35 Re = 1500 t = 600 s z/d = 2 d = 4.93 mm T = 21.8 °C		Test 62 Re = 1500 t = 600 s z/d = 4 d = 4.93 mm T = 18.0 °C	
r/d	*Sh*	*r/d*	*Sh*
18.26	1.15		
15.21	2.29		
11.16	3.44	18.26	1.59
8.92	4.59	13.18	3.17
6.69	5.74	8.11	4.76
6.39	6.88	6.69	6.34
6.09	8.03	5.27	7.93
5.38	9.18	4.67	9.51
4.67	10.32	4.06	11.10
4.36	11.47	3.55	12.68
4.06	12.62	3.04	14.27
3.85	13.76	2.78	15.86
3.65	14.91	2.54	17.44
3.35	16.06	2.37	19.03
3.04	17.21	2.23	20.61
2.78	18.35	2.13	22.20
2.54	19.50	2.03	23.78
2.43	20.65	1.87	25.37
2.33	21.79	1.72	26.95
2.23	22.94	1.67	28.54
2.13	24.09	1.62	30.13
2.03	25.23	1.58	31.71
1.93	26.38	1.52	33.30
1.88	27.53	1.36	34.88
1.83	28.68	1.22	36.47
1.72	29.82	1.18	38.05
1.62	30.97		
1.52	32.12		
1.42	33.26		
1.32	34.41		
1.22	35.56		
1.16	36.71		
1.12	37.85		

Test 37 Re = 1500 t = 600 s z/d = 6 d = 4.93 mm T = 22.3 °C		Test 39 Re = 1500 t = 600 s z/d = 8 d = 4.93 mm T = 21.3 °C	
r/d	*Sh*	*r/d*	*Sh*
13.18	1.10		
11.22	2.20		
9.18	3.30	11.16	1.20
7.76	4.40	9.23	2.39
6.33	5.50	7.14	3.59
5.51	6.60	6.12	4.79
4.69	7.70	5.10	5.98
4.39	8.80	4.74	7.18
4.08	9.90	4.39	8.37
3.82	11.00	4.02	9.57
3.57	12.10	3.67	10.77
3.31	13.20	3.47	11.96
3.06	14.30	3.27	13.16
2.86	15.40	3.06	14.36
2.65	16.50	2.86	15.55
2.55	17.60	2.76	16.75
2.45	18.70	2.65	17.95
2.35	19.80	2.49	19.14
2.25	20.90	2.35	20.34
2.14	22.00	2.18	21.53
2.04	23.10	2.04	22.73
1.94	24.20	1.94	23.93
1.84	25.30	1.84	25.12
1.74	26.40	1.78	26.32
1.63	27.50	1.74	27.52
1.53	28.60	1.69	28.71
1.43	29.70		
1.33	30.80		

Test 36 Re = 2000 t = 600 s z/d = 2 d = 4.93 mm T = 21.7°C		Test 63 Re = 2000 t = 600 s z/d = 4 d = 4.93 mm T = 17.8°C	
r/d	*Sh*	*r/d*	*Sh*
14.20	1.16	20.28	1.61
11.80	2.31	14.20	3.23
8.80	3.47	10.14	4.84
7.80	4.63	8.11	6.45
7.10	5.78	6.09	8.07
6.60	6.94	5.58	9.68
6.10	8.10	5.07	11.29
5.40	9.25	4.67	12.91
4.70	10.41	4.26	14.52
4.50	11.57	3.96	16.13
4.30	12.72	3.65	17.75
4.00	13.88	3.35	19.36
3.70	15.04	3.04	20.97
3.50	16.19	2.78	22.58
3.30	17.35	2.54	24.20
3.20	18.51	2.37	25.81
3.06	19.66	2.23	27.42
2.86	20.82	2.13	29.04
2.65	21.98	2.03	30.65
2.55	23.13	1.93	32.26
2.45	24.29	1.83	33.88
2.35	25.45	1.72	35.49
2.25	26.60	1.62	37.10
2.15	27.76	1.52	38.72
2.04	28.92	1.42	40.33
1.98	30.07	1.36	41.94
1.94	31.23		
1.90	32.39		
1.84	33.55		
1.74	34.70		

Test 38 Re = 2000 t = 600 s z/d = 6 d = 4.93 mm T = 21.7°C		Test 40 Re = 2000 t = 600 s z/d = 8 d = 4.93 mm T = 21.2°C	
r/d	*Sh*	*r/d*	*Sh*
9.74	3.47	12.17	1.21
7.91	4.63	9.59	2.41
6.09	5.78	7.14	3.62
5.38	6.94	6.33	4.83
4.67	8.10	5.51	6.03
4.36	9.25	5.00	7.24
4.06	10.41	4.49	8.45
3.85	11.57	4.18	9.65
3.65	12.72	3.88	10.86
3.35	13.88	3.71	12.07
3.04	15.04	3.57	13.27
2.84	16.19	3.31	14.48
2.64	17.35	3.06	15.68
2.47	18.51	2.76	16.89
2.33	19.66	2.45	18.10
2.17	20.82	2.35	19.30
2.03	21.98	2.24	20.51
1.97	23.13	2.14	21.72
1.93	24.29	2.04	22.92
1.83	25.45	1.94	24.13
1.72	26.60	1.84	25.34
1.68	27.76	1.74	26.54
1.62	28.92	1.63	27.75
1.52	30.07	1.53	28.96
1.42	31.23	1.43	30.16
1.38	32.39	1.33	31.37
		1.23	32.58
		1.12	33.78

Appendix K

Tabulation of mass transfer data for turbulent jet impingement

Test 180 Re = 3000 t = 240 s z/d = 2 d = 4.93 mm T = 22.9°C		Test 153 Re = 3000 t = 240 s z/d = 4 d = 4.93 mm T = 25.2°C	
r/d	*Sh*	*r/d*	*Sh*
10.14	7.85	12.17	6.49
8.11	10.46	9.13	8.65
6.29	13.08	6.80	10.81
5.58	15.69	6.09	12.97
4.97	18.31	5.17	15.13
4.56	20.92	4.56	17.29
4.06	23.54	4.16	19.46
3.55	26.15	3.75	21.62
3.18	28.77	3.55	23.78
2.98	31.38	3.35	25.94
2.74	34.00	3.04	28.10
2.54	36.61	2.84	30.27
2.33	39.23	2.64	32.43
2.03	41.84	2.54	34.59
1.72	44.46	2.33	36.75
1.56	47.07	2.23	38.91
1.48	49.69		
1.36	52.30		
1.24	54.92		
1.12	57.53		
1.01	60.15		

Test 181 Re = 3000 t = 300 s z/d = 6 d = 4.93 mm T = 23.0°C		Test 184 Re = 3000 t = 300 s z/d = 12 d = 4.93 mm T = 23.2°C	
r/d	*Sh*	*r/d*	*Sh*
13.18	2.07	12.37	2.04
10.14	4.15	9.13	4.08
8.11	6.22	7.40	6.12
6.49	8.30	6.49	8.16
5.88	10.37	5.88	10.20
5.48	12.45	5.27	12.24
5.17	14.52	4.97	14.28
4.77	16.60	4.56	16.32
4.46	18.67	4.26	18.36
4.16	20.75	3.75	20.41
3.85	22.82	3.35	22.45
3.35	24.90	2.94	24.49
3.04	26.97	2.64	26.53
2.74	29.05	2.54	28.57
2.54	31.12	2.33	30.61
2.33	33.20	2.13	32.65
2.13	35.27	2.03	34.69
2.03	37.35	1.93	36.73
1.93	39.42	1.72	38.77
1.72	41.50	1.52	40.81
1.62	43.57	1.42	42.85
1.52	45.65	1.32	44.89
		1.22	46.93
		1.12	48.97
		1.01	51.01

Test 154 Re = 5000 t = 180 s z/d = 2 d = 4.93 mm T = 25.2°C		Test 155 Re = 500 t = 180 s z/d = 4 d = 4.93 mm T = 25.2°C	
r/d	*Sh*	*r/d*	*Sh*
10.14	8.65	11.16	8.65
8.11	11.53	9.13	11.53
6.90	14.41	8.11	14.41
6.49	17.29	7.10	17.29
6.09	20.18	5.48	20.18
5.58	23.06	4.77	23.06
5.07	25.94	4.36	25.94
4.56	28.82	4.06	28.82
4.16	31.71	3.75	31.71
3.75	34.59	3.55	34.59
3.45	37.47	3.35	37.47
3.25	40.35	3.25	40.35
2.94	43.24	3.04	43.24
2.74	46.12	2.94	46.12
2.64	49.00	2.74	49.00
2.43	51.88	2.54	51.88
2.33	54.77	2.43	54.77
2.13	57.65	2.23	57.65
2.03	60.53	2.03	60.53
1.83	63.41		
1.62	66.30		
1.52	69.18		

Test 174 Re = 5000 t = 180 s z/d = 6 d = 4.93 mm T = 22.1°C		Test 175 Re = 5000 t = 180 s z/d = 12 d = 4.93 mm T = 22.1°C	
r/d	*Sh*	*r/d*	*Sh*
14.20	3.73	10.14	3.73
10.14	7.46	7.10	7.46
6.09	11.19	5.07	11.19
5.07	14.91	3.45	14.91
4.06	18.64	2.64	18.64
3.55	22.37	2.03	22.37
3.04	26.10	1.52	26.10
2.74	29.83	1.01	29.83
2.33	33.56	0.81	33.56
2.03	37.28		
1.93	41.01		
1.72	44.74		
1.52	48.47		
1.36	52.20		
1.20	55.93		
1.01	59.65		
0.91	63.38		
0.71	67.11		

Test 171 Re = 6000 t = 180 s z/d = 2 d = 4.93 mm T = 23.0°C		Test 172 Re = 6000 t = 180 s z/d = 4 d = 4.93 mm T = 23.0°C	
r/d	*Sh*	*r/d*	*Sh*
12.17	3.46	9.43	10.37
7.71	6.92	8.11	13.83
6.69	10.37	6.59	17.29
6.29	13.83	5.38	20.75
5.58	17.29	4.56	24.21
4.97	20.75	4.06	27.66
4.36	24.21	3.75	31.12
3.96	27.66	3.45	34.58
3.55	31.12	3.14	38.04
3.35	34.58	2.74	41.50
3.04	38.04	2.54	44.95
2.80	41.50	2.33	48.41
2.66	44.95	2.03	51.87
2.54	48.41	1.83	55.33
2.33	51.87	1.62	58.79
2.13	55.33	1.42	62.24
1.83	58.79	1.32	65.70
1.52	62.24	1.12	69.16
1.42	65.70	1.08	72.62
1.32	69.16	1.01	76.08
1.22	72.62	0.91	79.53
1.12	76.08	0.81	82.99
1.01	79.53	0.71	86.45
0.93	82.99	0.61	89.91
0.85	86.45	0.51	93.37
		0.41	96.82
		0.30	100.28

Test 177 Re = 6000 t = 180 s z/d = 6 d = 4.93 mm T = 22.8°C		Test 178 Re = 6000 t = 180 s z/d = 12 d = 4.93 mm T = 22.8°C	
r/d	*Sh*	*r/d*	*Sh*
12.17	3.52	18.26	3.52
10.14	7.03	13.18	7.03
6.69	10.55	9.13	10.55
5.68	14.06	7.10	14.06
4.46	17.58	5.58	17.58
4.06	21.10	4.06	21.10
3.55	24.61	3.04	24.61
3.04	28.13	2.54	28.13
2.64	31.65	2.03	31.65
2.33	35.16	1.72	35.16
1.93	38.68	1.32	38.68
1.62	42.19	0.91	42.19
1.42	45.71	0.61	45.71
1.32	49.23		
1.16	52.74		
1.01	56.26		
0.89	59.78		
0.77	63.29		
0.65	66.81		
0.51	70.32		
0.41	73.84		
0.30	77.36		

Test 188 Re = 8000 t = 150 s z/d = 2 d = 4.93 mm T = 21.3°C		Test 92 Re =8000 t = 60 s z/d = 4 d = 4.93 mm T = 23.8°C	
r/d	*Sh*	*r/d*	*Sh*
11.76	14.36	11.16	10.03
9.13	19.14	7.10	20.07
6.49	23.93	5.07	30.10
5.38	28.71	4.06	40.14
4.46	33.50	3.25	50.17
3.85	38.28	2.84	60.20
3.55	43.07	2.23	70.24
3.04	47.85	1.72	80.27
2.80	52.64	1.42	90.31
2.54	57.43	1.12	100.34
2.23	62.21	1.01	110.38
1.93	67.00	0.71	120.41
1.42	71.78	0.61	130.44
1.32	76.57	0.51	140.48
1.12	81.35		
1.01	86.14		
0.89	90.92		
0.77	95.71		
0.65	100.50		
0.51	105.28		
0.41	110.07		
0.30	114.85		
0.24	119.64		

Test 160 Re = 8000 t = 180 s z/d = 6 d = 4.93 mm T = 26.4°C		Test 161 Re = 8000 t = 180 s z/d = 12 d = 4.93 mm T = 26.4°C	
r/d	*Sh*	*r/d*	*Sh*
15.21	7.90	10.95	7.84
11.16	10.54	8.62	10.45
8.11	13.17	7.40	13.06
6.59	15.81	6.29	15.68
6.09	18.44	5.38	18.29
5.07	21.07	4.67	20.90
4.67	23.71	3.85	23.52
4.26	26.34	3.14	26.13
3.85	28.98	2.64	28.74
3.55	31.61	2.33	31.36
3.35	34.25	2.03	33.97
3.04	36.88	1.83	36.58
2.74	39.52	1.62	39.19
2.54	42.15	1.42	41.81
2.23	44.78	1.22	44.42
2.03	47.42	1.01	47.03
1.83	50.05	0.91	49.65
1.72	52.69	0.71	52.26
1.62	55.32	0.51	54.87
1.52	57.96		
1.42	60.59		
1.32	63.22		
1.22	65.86		
1.12	68.49		
1.01	71.13		

Test 168 Re = 10000 t = 120 s z/d = 2 d = 4.93 mm T = 23.0°C		Test 169 Re = 10000 t = 120 s z/d = 4 d = 4.93 mm T = 23.0°C	
r/d	*Sh*	*r/d*	*Sh*
14.20	15.56	15.21	5.19
8.52	20.75	12.17	10.37
7.30	25.93	9.53	15.56
6.39	31.12	7.10	20.75
5.58	36.31	5.68	25.93
5.07	41.50	4.87	31.12
4.36	46.68	4.26	36.31
3.85	51.87	3.85	41.50
3.41	57.06	3.55	46.68
3.14	62.24	3.04	51.87
2.94	67.43	2.74	57.06
2.68	72.62	2.54	62.24
2.49	77.80	2.23	67.43
2.33	82.99	1.72	72.62
2.13	88.18	1.52	77.80
1.52	93.37	1.32	82.99
1.22	98.55	1.12	88.18
1.01	103.74	1.01	93.37
0.89	108.93	0.91	98.55
0.77	114.11	0.81	103.74
0.65	119.30	0.71	108.93
0.51	124.49		
0.41	129.67		

Test 186 Re = 10000 t = 120 s z/d = 2 d = 4.93 mm T = 23.0°C		Test 187 Re = 10000 t = 120 s z/d = 2 d = 4.93 mm T = 23.0°C	
r/d	*Sh*	*r/d*	*Sh*
14.20	4.95	13.18	4.95
10.14	9.90	10.14	9.90
8.11	14.85	7.71	14.85
6.09	19.80	6.09	19.80
5.07	24.75	4.77	24.75
4.26	29.70	4.06	29.70
3.75	34.65	3.35	34.65
3.35	39.60	2.54	39.60
2.74	44.55	2.33	44.55
2.33	49.50	2.03	49.50
2.03	54.45	1.72	54.45
1.72	59.40	1.62	59.40
1.52	64.35	1.52	64.35
1.36	69.30	1.38	69.30
1.18	74.25	1.12	74.25
1.01	79.20	0.91	79.20
0.91	84.15	0.71	84.15
0.75	89.10	0.61	89.10
0.65	94.05	0.41	94.05
0.51	99.00		
0.41	103.95		
0.30	108.90		
0.20	113.85		

Test 189 Re = 12000 t = 150 s z/d = 2 d = 4.93 mm T = 21.4°C		Test 139 Re = 12000 t = 30 s z/d = 6 d = 4.93 mm T = 26.5°C	
r/d	*Sh*	*r/d*	*Sh*
10.14	14.24	6.09	15.55
8.82	18.98	4.67	31.10
7.61	23.73	3.04	46.65
6.59	28.47	2.03	62.20
5.58	33.22	1.52	77.75
5.07	37.96	1.22	93.30
4.46	42.71	0.81	108.85
3.96	47.45	0.61	124.40
3.65	52.20		
3.45	56.94		
3.35	61.69		
3.04	66.43		
2.94	71.18		
2.74	75.93		
2.64	80.67		
2.43	85.42		
2.03	90.16		
1.52	94.91		
1.32	99.65		
1.18	104.40		
1.01	109.14		
0.91	113.89		
0.83	118.63		
0.75	123.38		
0.67	128.12		
0.59	132.87		

Test 126 Re = 12000 t = 30 s z/d = 8 d = 4.93 mm T = 23.7°C		Test 140 Re = 12000 t = 30 s z/d = 12 d = 4.93 mm T = 26.5°C	
r/d	*Sh*	*r/d*	*Sh*
11.16	10.03	12.17	15.55
7.10	20.07	6.09	31.10
5.07	30.10	3.04	46.65
4.06	40.14	2.03	62.20
3.25	50.17	1.22	77.75
2.84	60.20	0.81	93.30
2.23	70.24		
1.72	80.27		
1.42	90.31		
1.12	100.34		
1.01	110.38		
0.71	120.41		
0.61	130.44		
0.51	140.48		

Test 191 Re = 21000 t = 75 s z/d = 2 d = 4.93 mm T = 21.7°C		Test 90 Re = 21000 t = 60 s z/d = 4 d = 4.93 mm T = 21.7°C	
r/d	*Sh*	*r/d*	*Sh*
10.14	27.76	10.14	34.70
8.52	37.02	7.10	46.27
7.61	46.27	6.09	57.84
6.59	55.52	5.07	69.40
5.58	64.78	4.26	80.97
4.97	74.03	3.85	92.54
4.46	83.28	3.35	104.11
4.16	92.54	3.04	115.67
3.75	101.79	2.74	127.24
3.55	111.05	2.54	138.81
3.35	120.30	2.33	150.37
3.14	129.55	1.52	161.94
2.94	138.81	1.01	173.51
2.74	148.06	0.89	185.08
2.64	157.31	0.77	196.64
2.54	166.57	0.65	208.21
2.43	175.82	0.51	219.78
2.23	185.08	0.41	231.35
2.03	194.33		
1.52	203.58		
1.32	212.84		
1.01	222.09		
0.93	231.35		
0.85	240.60		
0.77	249.85		
0.69	259.11		
0.61	268.36		
0.51	277.61		
0.41	286.87		

Test 141 Re = 21000 t = 75 s z/d = 6 d = 4.93 mm T = 26.0°C		Test 164 Re = 21000 t = 150 s z/d = 6 d = 4.93 mm T = 26.4°C	
r/d	*Sh*	*r/d*	*Sh*
6.69	32.40	14.20	19.60
5.48	43.19	11.16	23.52
4.46	53.99	9.13	27.44
3.85	64.79	7.91	31.36
3.35	75.59	6.49	35.27
2.94	86.39	5.88	39.19
2.43	97.19	5.48	43.11
1.83	107.98	5.07	47.03
1.62	118.78	4.77	50.95
1.52	129.58	4.46	54.87
1.22	140.38	4.26	58.79
1.01	151.18	3.85	62.71
0.81	161.98	3.65	66.63
		3.45	70.55
		3.25	74.47
		3.04	78.39
		2.74	82.31
		2.54	86.23
		2.33	90.15
		2.13	94.07
		1.93	97.99
		1.72	101.91
		1.62	105.82
		1.52	109.74
		1.42	113.66
		1.32	117.58
		1.18	121.50

Test 142 Re = 35000 t = 45 s z/d = 12 d = 4.93 mm T = 26.0°C	
r/d	*Sh*
8.11	32.40
6.69	43.19
5.58	53.99
4.06	64.79
2.54	75.59
2.03	86.39
1.62	97.19
1.22	107.98
1.01	118.78
0.81	129.58

Test 183 Re = 35000 t = 60 s z/d = 2 d = 4.93 mm T = 23.2°C		Test 93 Re = 35000 t = 30 s z/d = 4 d = 4.93 mm T = 21.4°C	
r/d	*Sh*	*r/d*	*Sh*
11.76	30.61	10.14	22.75
10.55	40.81	7.10	45.50
9.13	51.01	5.48	68.25
8.11	61.22	4.56	91.00
7.10	71.42	4.06	113.74
6.29	81.62	3.55	136.49
5.48	91.82	3.04	159.24
5.07	102.03	2.64	181.99
4.67	112.23	2.03	204.74
4.36	122.43	1.52	227.49
4.06	132.63	1.01	250.24
3.65	142.84	0.71	272.99
3.45	153.04	0.51	295.73
3.20	163.24	0.41	318.48
3.04	173.44		
2.94	183.65		
2.64	193.85		
2.33	204.05		
2.13	214.25		
1.83	224.46		
1.62	234.66		
1.52	244.86		
1.32	255.06		
1.12	265.27		
1.01	275.47		
0.91	285.67		
0.81	295.87		
0.71	306.08		
0.51	316.28		

Test 114 Re = 35000 t = 30 s z/d = 4 d = 4.93 mm T = 22.2°C		Test 143 Re = 35000 t = 45 s z/d = 6 d = 4.93 mm T = 26.0°C	
r/d	*Sh*	*r/d*	*Sh*
18.26	22.18	12.17	32.40
16.23	44.37	10.14	43.19
14.20	66.55	7.61	53.99
12.17	88.73	6.69	64.79
10.14	110.92	5.68	75.59
8.11	133.10	5.07	86.39
6.69	155.28	4.46	97.19
5.58	177.47	4.06	107.98
4.77	199.65	3.55	118.78
4.26	221.83	3.25	129.58
3.55	244.01	3.04	140.38
3.35	266.20	2.84	151.18
3.04	288.38	2.43	161.98
2.54	310.56	2.23	172.78
2.03	332.75	1.83	183.57
1.22	354.93	1.52	194.37
1.01	377.11	1.22	205.17
0.71	399.30	1.01	215.97
0.61	421.48	0.81	226.77
0.51	443.66	0.61	237.57
		0.51	248.36
		0.41	259.16

Test 145 *Re* 35000 *t* = 120 s *z/d* = 6 *d* = 4.93 mm *T* = 26.0°C		Test 144 *Re* = 35000 *t* = 45 s *z/d* = 12 *d* = 4.93 mm *T* = 26.0°C	
r/d	*Sh*	*r/d*	*Sh*
13.18	28.35	16.23	32.40
11.16	32.40	13.18	43.19
9.13	36.44	10.34	53.99
8.11	40.49	9.13	64.79
7.10	44.54	7.51	75.59
6.49	48.59	6.69	86.39
6.09	52.64	5.68	97.19
5.68	56.69	5.07	107.98
5.17	60.74	3.85	118.78
4.97	64.79	3.16	129.58
4.46	68.84	2.54	140.38
4.26	72.89	2.03	151.18
4.06	76.94	1.83	161.98
3.85	80.99	1.52	172.78
3.65	85.04	1.22	183.57
3.45	89.09	1.01	194.37
3.25	93.14	0.81	205.17
3.04	97.19		
2.84	101.24		
2.64	105.28		
2.43	109.33		
2.23	113.38		
2.03	117.43		
1.83	121.48		
1.62	125.53		
1.42	129.58		
1.22	133.63		

Test 107 *Re* 42000 *t* = 30 s *z/d* = 2 *d* = 4.93 mm *T* = 22.2°C		Test 108 *Re* = 42000 *t* = 30 s *z/d* = 4 *d* = 4.93 mm *T* = 22.2°C	
r/d	*Sh*	*r/d*	*Sh*
12.17	22.18	12.17	22.18
10.14	44.37	8.11	44.37
8.11	66.55	6.09	66.55
6.69	88.73	5.58	88.73
5.27	110.92	5.07	110.92
4.77	133.10	4.46	133.10
4.36	155.28	4.06	155.28
3.65	177.47	3.55	177.47
3.35	199.65	3.14	199.65
2.94	221.83	2.74	221.83
2.64	244.01	2.54	244.01
2.43	266.20	2.03	266.20
2.13	288.38	1.32	288.38
1.93	310.56	0.91	310.56
1.62	332.75	0.71	332.75
1.42	354.93	0.61	354.93
1.22	377.11	0.51	377.11
1.01	399.30		
0.91	421.48		
0.81	443.66		
0.51	465.85		
0.30	488.03		
0.20	510.21		

Test 109 Re = 42000 t = 30 s z/d = 6 d = 4.93 mm T = 20.2°C		Test 110 Re = 42000 t = 30 s z/d = 8 d = 4.93 mm T = 20.2°C	
r/d	*Sh*	*r/d*	*Sh*
14.20	22.18	7.91	78.79
10.14	44.37	6.09	105.05
7.40	66.55	5.07	131.32
5.88	88.73	3.85	157.58
4.77	110.92	3.04	183.85
4.26	133.10	2.23	210.11
3.55	155.28	2.03	236.37
3.04	177.47	1.52	262.64
2.64	199.65	1.01	288.90
2.03	221.83	0.71	315.16
1.52	244.01	0.61	341.43
1.01	266.20	0.51	367.69
0.75	288.38	0.30	393.96
0.61	310.56		
0.51	332.75		

Test 134 Re = 52000 t = 30 s z/d = 6 d = 4.93 mm T = 26.4°C		Test 111 Re = 52000 t = 30 s z/d = 4 d = 4.93 mm T = 22.2°C	
r/d	*Sh*	*r/d*	*Sh*
10.14	47.03	12.17	7.66
8.11	62.71	9.13	10.21
6.09	78.39	7.91	12.77
5.68	94.07	6.49	15.32
4.67	109.74	5.48	17.87
4.26	125.42	4.87	20.42
3.85	141.10	4.36	22.98
3.55	156.78	3.96	25.53
3.04	172.45	3.45	28.08
2.84	188.13	3.04	30.64
2.33	203.81	2.74	33.19
2.03	219.49	2.33	35.74
1.83	235.17	2.13	38.30
		1.83	40.85
		1.32	43.40
		1.01	45.95
		0.71	48.51
		0.61	51.06
		0.51	53.61

Test 135 Re = 52000 t = 30 s z/d = 8 d = 4.93 mm T = 26.0°C		Test 136 Re = 52000 t = 30 s z/d = 12 d = 4.93 mm T = 26.0°C	
r/d	*Sh*	*r/d*	*Sh*
11.16	48.59	11.16	48.59
9.13	64.79	9.33	64.79
7.30	80.99	7.51	80.99
6.09	97.19	6.29	97.19
5.27	113.38	5.27	113.38
4.67	129.58	4.26	129.58
4.06	145.78	3.65	145.78
3.65	161.98	2.84	161.98
3.04	178.17	2.03	178.17
2.64	194.37	1.83	194.37
2.23	210.57	1.22	210.57
1.83	226.77	1.01	226.77
1.62	242.97	0.81	242.97
1.42	259.16		
1.22	275.36		
1.01	291.56		
0.81	307.76		

Test 129 Re = 60000 t = 30 s z/d = 2 d = 4.93 mm T = 26.2°C		Test 112 Re = 60000 t = 30 s z/d = 4 d = 4.93 mm T = 22.2°C	
r/d	*Sh*	*r/d*	*Sh*
10.14	47.81	16.23	22.18
9.63	63.74	11.16	44.37
9.13	79.68	9.13	66.55
8.62	95.61	7.61	88.73
8.11	111.55	6.59	110.92
7.10	127.48	5.88	133.10
6.29	143.42	5.17	155.28
5.48	159.35	4.26	177.47
5.07	175.29	3.85	199.65
4.46	191.22	3.55	221.83
4.06	207.16	3.25	244.01
3.85	223.10	2.94	266.20
3.45	239.03	2.54	288.38
3.04	254.97	2.27	310.56
2.84	270.90	1.93	332.75
2.64	286.84	1.52	354.93
2.43	302.77	1.38	377.11
		1.26	399.30
		1.01	421.48
		0.91	443.66
		0.81	465.85

Test 130 Re = 60000 t = 30 s z/d = 6 d = 4.93 mm T = 26.2°C		Test 131 Re = 60000 t = 30 s z/d = 8 d = 4.93 mm T = 26.2°C	
r/d	*Sh*	*r/d*	*Sh*
13.18	47.81	10.14	47.81
10.14	63.74	8.11	63.74
8.11	79.68	7.10	79.68
7.10	95.61	5.88	95.61
5.88	111.55	5.07	111.55
5.07	127.48	4.46	127.48
4.46	143.42	3.85	143.42
3.85	159.35	3.25	159.35
3.55	175.29	2.84	175.29
3.04	191.22	2.54	191.22
2.64	207.16	2.03	207.16
2.33	223.10	1.83	223.10
2.03	239.03	1.52	239.03
1.83	254.97	1.01	254.97
1.62	270.90	0.81	270.90

Test 132 Re = 60000 t = 30 s z/d = 12 d = 4.93 mm T = 26.2°C	
r/d	*Sh*
10.75	47.81
9.13	63.74
7.71	79.68
6.69	95.61
5.68	111.55
4.87	127.48
3.96	143.42
3.25	159.35
2.64	175.29
2.33	191.22
2.03	207.16
1.83	223.10
1.22	239.03
1.01	254.97
0.81	270.90

Numerical study of flow field for confined laminar jet impingement

K Jambunathan, S Kapasi and B L Button
Faculty of Engineering
Department of Mechanical Engineering
and
J A Bland
Faculty of Science
Department of Mathematics, Statistics and Operational Research
Trent Polytechnic Nottingham
Burton Street, Nottingham, NG1 4BU
United Kingdom

Prepared for Third International PHOENICS User Conference,
Dubrovnik, Yugoslavia 28 August - 1 September 1989.

ABSTRACT

The flow field between two horizontal stationary surfaces arising from a laminar incompressible jet issuing from the upper surface and impinging normally on the lower surface have been numerically investigated using PHOENICS. The velocity pressure and shear stress distributions in the impingement region were predicted for a parabolic exit velocity profile over a Reynolds number range of 100 to 2000 and a surface to surface spacing of two jet diameters. A non-dimensional correlation for the maximum shear stress and the position where it occurs are given. Limited comparisons of the effect of nozzle exit velocity profile and with existing numerical data are presented.

PHOENICS version 1.3 issued on 1 April 1987 was used on VAX 785 computer, operating system VMS version 4.2.

CONTENTS

1 INTRODUCTION

1.1 Background

Impinging jets of various configurations are used in industrial equipment because of their excellent heat and mass transfer characteristics. Cooling of turbine blades, and electronic components, heat treatment of glass or metal sheets, drying of textiles and paper are among the many common practical applications of jet impingement. Laminar impinging jets in partially confined flow fields have not received much attention in the literature, due mainly to the fact that most industrial applications involve turbulent flows. This leaves considerable scope for a fuller investigation of laminar jet impingement. The work reported here is part of a comprehensive study that is being undertaken to compare full-field heat and mass transfer techniques by measurement and prediction of jet impingement phenomena supported by an SERC grant GR/D/98693 and is a precursor to a study of turbulent jets. The basic geometry chosen is a circular incompressible jet issuing normally from the flat surface and impinging perpendicularly onto a parallel surface a short distance away with the fluid exiting radially between the two stationary surfaces.

1.2 Aim of work

Numerical computer simulations provide a relatively inexpensive approach to understanding the transport phenomena associated with jet impingement. The aim of this work in therefore to perform a parametric study of a laminar impinging jet partially confined by parallel surfaces for various Reynolds numbers in the range 100 to 2000 for a non-dimensional spacing to jet-diameter ratio of two. Although the results reported here were essentially for a nozzle diameter of 4 mm with parabolic exit velocity, some comparisons with a 10 mm diameter nozzle and for a flat exit velocity profile are made. The results will help to minimise costly experimentation.

1.3 Summary of previous work

The most relevant publication which has studied a similiar physical arrangement to this work namely an axisymmetric jet in a confined region was by Saad et al (1977). The full Navier-Stokes and energy equations were numerically modelled and solved in terms of vorticity-stream functions. Although some fluid flow characteristics were included, their main interest was on the enhancement of the transport phenomena occuring at the impingement surface by the introduction of suction at the impingement wall. Comparisons of the effects of parabolic and flat inlet velocity profiles were reported. Earlier Marple et al (1974) utilised a flow visualisation technique in confined water-jet impingement with both circular and rectangular jets to show that the confined boundary has very little effect on the impingement zone, but affected the recirculation region between the plates. This was later confirmed by numerical simulation of the vorticity-stream formulations of the governing equations. The most novel application of laminar jet impingement has been in obtaining yield shear strength of the vascular endothelium linings in arteries, Despande and Vaishnav (1982). An axisymmetric laminar jet in an unconfined space was numerically modelled to obtain the shear stress distribution on the impingement wall which was then used to ascertain the strengths of the linings. Other works by Law and Masliyah (1984) and van Heiningen et al (1976) consider laminar impingement but with a rectangular nozzle in confined space. A comprehensive jet-impingement heat transfer bibliography has recently been carried out by Button and Jambunathan (1989) which include most studies in the period 1976-85.

2 COMPUTATIONAL ASPECTS

2.1 The model

The model consists of a circular nozzle of diameter d, the exit plane of which is flush with the confinement plate Figure 1. The jet issues from the nozzle with a mean velocity w_{jet} and impinges perpendicularly on to an impingement plate in parallel to the confinement plate and at a non-dimensional distance H from it. Both the confinement and impingement plates extend radially to 37.5 times the nozzle diameter where the outflow region is positioned. The whole system is symmetrical about the jet centreline.

The governing equations for steady axisymmetric laminar flow are Continuity :

$$\frac{1}{r}\frac{\partial}{\partial r}(rv) + \frac{\partial w}{\partial z} = 0$$

Momentum :

$$\rho\left(v\frac{\partial v}{\partial r} + w\frac{\partial v}{\partial z}\right) = -\frac{\partial p}{\partial r} + \mu\left(\frac{\partial^2 v}{\partial r^2} + \frac{1}{r}\frac{\partial v}{\partial r} + \frac{\partial^2 v}{\partial z^2} - \frac{v}{r^2}\right)$$

$$\rho\left(v\frac{\partial w}{\partial r} + w\frac{\partial w}{\partial z}\right) = -\frac{\partial p}{\partial z} + \mu\left(\frac{\partial^2 w}{\partial r^2} + \frac{1}{r}\frac{\partial w}{\partial r} + \frac{\partial^2 w}{\partial z^2}\right)$$

Boundary conditions :

Boundary I (impingement wall)

$$w = 0,\ v = 0 \qquad \text{at } z = z_{max}$$

Boundary II (parabolic or flat jet velocity profile at exit)

Parabolic $w = \frac{2Re\mu}{\rho d}\left(1-\frac{4r^2}{d^2}\right)$ at $z = 0$

or Flat $w = w_{jet}$ at $z = 0$

Boundary III (jet centreline)

$$v = 0 \qquad \text{at } r = 0$$

Boundary IV (confinement plate)

$$w = 0,\ v = 0 \qquad \text{at } z = 0$$

Boundary V (outflow region)

$$p = 0.0 \qquad \text{at } r = 37.5d$$

3 PHOENICS SETTINGS

3.1 SATELLITE

The PHOENICS commands which identify the boundary and activate the respective boundary conditions are:

Boundary I
PATCH(imping,HWALL,1,1,1,158,14,14,1,1)
COVAL(imping,V1,1.0,0.0) and COVAL(imping,W1,FIXVAL,0.0)

Boundary II
PATCH(jet,LOW,1,1,1,1,1,1,1,1)
COVAL(jet,P1,FIXFLU,w*rho1) and COVAL(jet,W1,ONLYMS,w)

Boundary III
Default setting at domain boundary

Boundary IV
PATCH(confine,LWALL,1,1,11,158,1,1,1,1)
COVAL(confine,V1,1.0,0.0)

Boundary V
PATCH(outreg,cell,1,1,158,158,1,15,1,1)
COVAL(outreg,P1,FIXVAL,0.0)
The governing equations are solved, by a variant of the SIMPLE algorithm. The details of the mathematical representation of the equations may be found in Hedberg et al (1986).

3.2 GROUND code calculation of shear stress

A post-processor was coded in GROUND specifically to obtain the shear stress values at the wall. In laminar flow shear stress is defined as $\tau=\mu(dv/dz)$, the velocity gradient dv/dz was obtained from the post processor coding rather than the standard GREX1 activated function FNDVDZ. This GREX1 function determines an averaged gradient around the cell faces, which gives an underestimate of the velocity gradient at the wall. The velocity control cells are staggered by half a cell due to the velocities being located at the cell faces see figure 2. To model the wall the velocity at the high node is set to zero and the velocity v on the north face of the control cell is solved. The velocity gradient at the wall is then determined by dividing v by half the cell height.

3.3 Covergence criteria

To monitor convergence, the residual sum of the pressure and the two components of velocity were used. The residual of the pressure has a physical significance, in the sense that it is the volumetric continuity error of each cell summed over the whole field. By observing the value of this residual reduce after every sweep and setting a maximum value of 10^{-4}, at which calculations are required to stop, continuity was taken to be satisfied. A similar approach to the velocity residual was adopted, with the same tolerance.

4 RESULTS AND DISCUSSION

All results were obtained with a non-uniform, 15 x 158 grid, 15 lines parallel to the plates, 158 lines parallel to the jet centreline. Use of a grid spacing which was non-uniform in both directions permitted a finer grid spacing in the regions of steeper gradients, i.e. near the impingement plate and adjacent to the jet centreline.

4.1 Grid dependency

The grid dependence of the flow parameters was ascertained and the smallest grid size in the optimal region was used in further work so that an increased value can be used if necessary without greatly affecting the predicted variable. The typical conditions chosen to assess grid independency were the following; the Reynolds number Re=1000, the nozzle to plate distance H=2, and outflow boundary distance from the jet centreline R=37.5. The grid size was altered at the wall as this was the main area of interest. The grid sizes chosen for the analysis were $\Delta z/d$= 0.00125 to 0.125 where d=4 mm. The smallest size was assessed to be 0.0075 which will give a maximum variation of 3 percent on the shear stress as shown in Figure 3.

4.2 Effect of parabolic and flat jet profile

To establish whether the impingement plate was sensitive to the initial velocity profile of the jet, an investigation of parabolic and flat jet profiles with similar boundary conditions to those used for the grid dependency analysis was undertaken. Figure 4 indicates a substantial reduction in the friction factor value for the flat velocity profile in

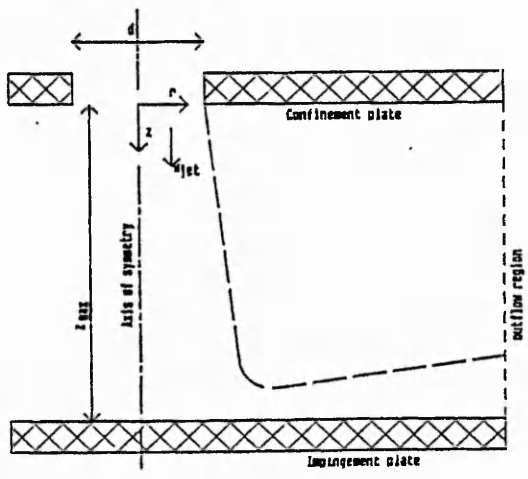

Figure 1. Jet impingement geometry

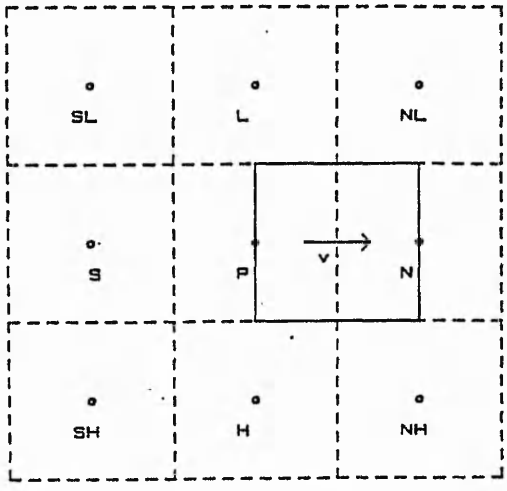

Figure 2. Staggered control cell for v

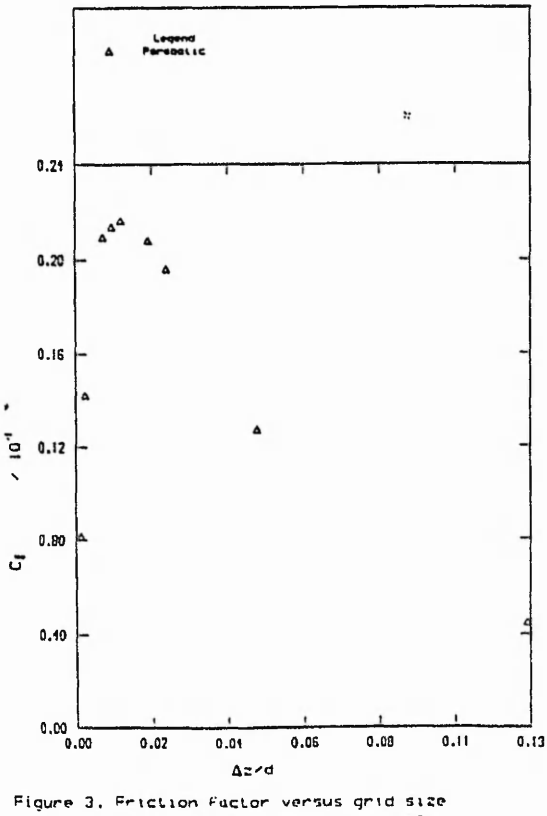

Figure 3. Friction factor versus grid size For z=zmax when H=2 and Re=1000

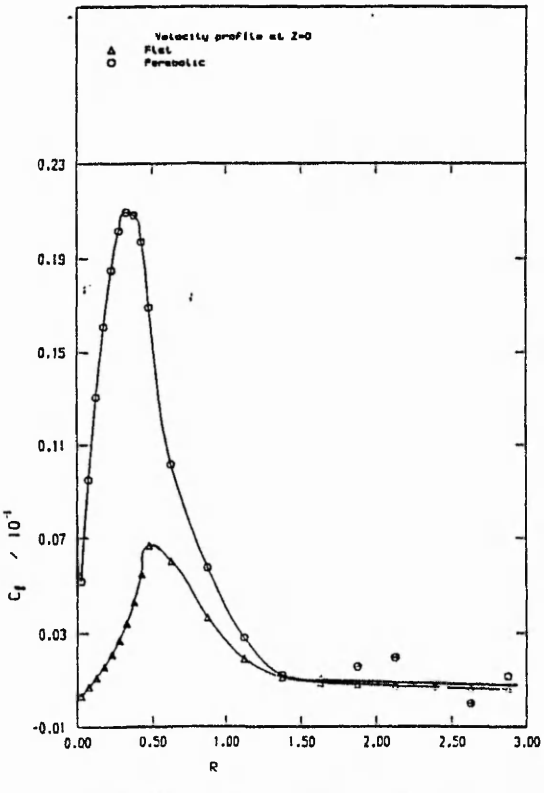

Figure 4. Friction factor at z=zmax when H=2 and Re=1000

comparison to the fully developed profile. Also the radial location at which the maximum friction factor occurs has been displaced to the perimeter of the jet. The radial velocity profile, as Figure 5 shows is such that the flat jet profile has much smaller gradients near the wall and the maximum velocity is a fraction of that for the parabolic case. From Figure 6 the presence of the wall in the axial velocity is evident at about 1.2 diameters above the wall. The pressure profiles along the wall, as shown in Figure 7, reflects the momentum of the jets; the flat profile value is approximately a third that of the parabolic jet.

The effect of maintaining the same number of grid cells on a larger diameter nozzle is shown in Figure 8. Significant lowering of the friction factor values is the result of flattening the exit velocity profile in the model due to using the same number of cells over a larger flow area.

4.3 Graphical output

A typical streamline plot from GRAFFIC for Reynolds number 1000. is presented in Figure 9. The figure shows a recirculatory region attached to the jet and further downstream the flow becomes similar to flow between parallel plates. With the increase in Reynolds number the large recirculation region is pushed further downstream by the higher momentum of the jet and the main flow remains attached to the impingement plate.

4.4 Effect of Reynolds number

A study of the effect of a range of Reynolds numbers, Re = 100, 500, 1000, 1500, 2000, on the non-dimensional wall shear stress C_f is shown in Figure 10. When the Reynolds number is increased C_f decreases in magnitude. However it has been shown and confirmed by the authors that for values of Reynold number less than 100 there is a decrease of skin friction factor Despande and Vaishnav (1982). The friction factor C_f is zero at R=0, the stagnation point, and approaches zero asymptotically for the larger radial values. The location of the peak value of wall friction factor C_f remains stationary at about R=0.4. The axial velocity profile for the above Reynolds numbers shows that the lower Reynolds number flows decelerate as soon as they emerge from the nozzle, as shown in Figure 11. This is not the case at higher Reynolds numbers due to strong axial momentum. The presence of the impinging wall causing the deceleration and deflection of the flow is evident at about 1.2 jet diameters above the wall. The radial velocity at R=0.5 from the jet axis for the above range of Reynolds numbers are shown in Figure 12. It is seen that steeper velocity gradients at the wall are obtained as the Reynolds number increases. The pressure on the impingement surface is related to momentum and mass flux hence higher Reynolds number flows give higher values of pressure, as indicated in Figure 13. The area over which the pressure is most significant is within 2 radii of the nozzle from the stagnation point.

4.5 Effect of nozzle to plate spacing

The results discussed so far has been for a spacing to diameter ratio H=2. Limited work was carried out to see the effect of spacing on the friction coefficient by changing the value of H to 4. This was done only for a Reynolds number of 1000. As can be seen in Figure 14 the effect of moving the plate further away from the jet is to decrease the wall friction relative to the smaller plate spacing results. The greater plate spacing has a decelerating and flattening influence on the velocity profile and hence a lower wall friction factor is observed.

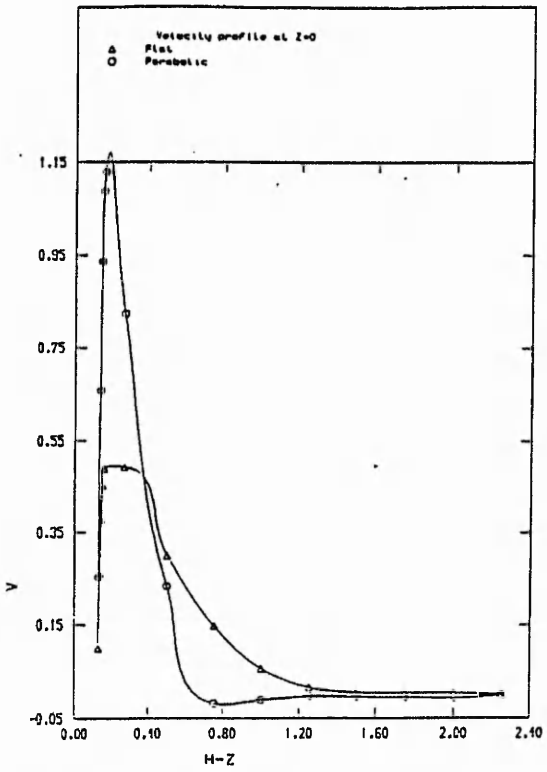

Figure 5. Radial velocity at R=0.5 when H=2 and Re=1000

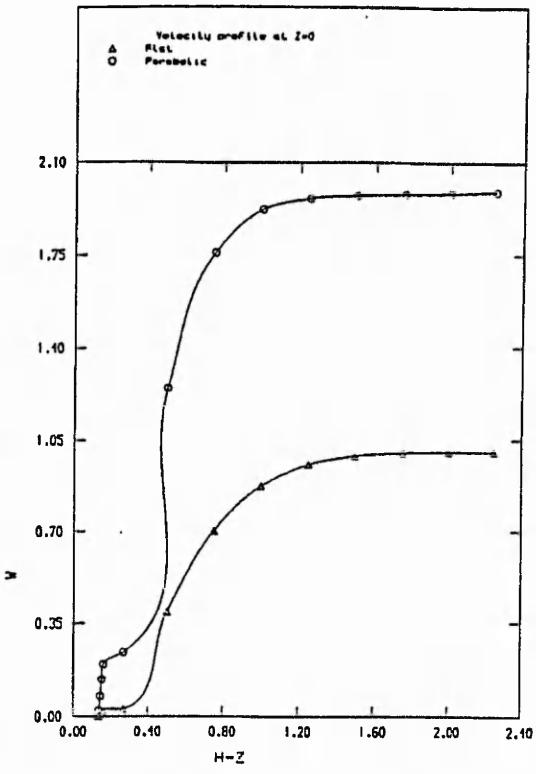

Figure 6. Axial velocity at R=0 when H=2 and Re=1000

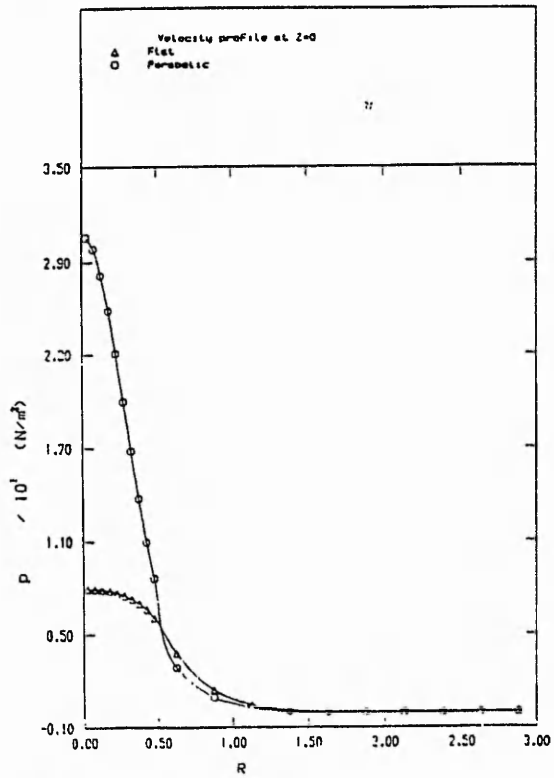

Figure 7. Pressure at z=zmax when H=2 and Re=1000

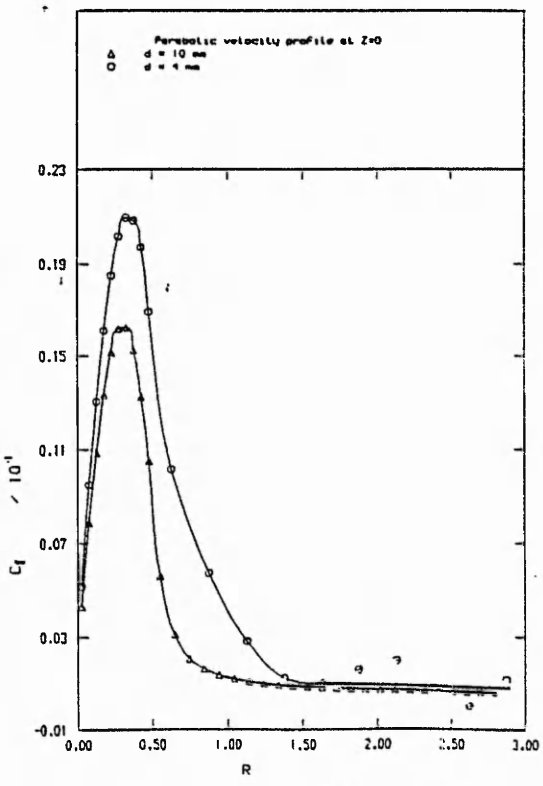

Figure 8. Friction factor at z=zmax when H=2 and Re=1000

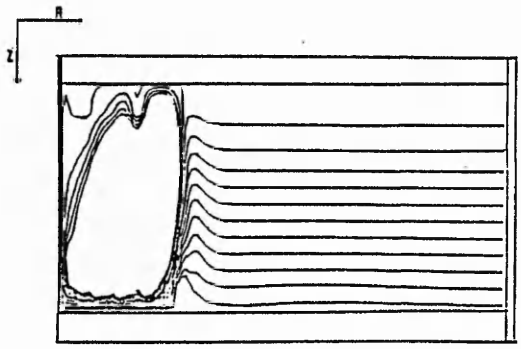

Figure 9. Streamline plot for Re=1000
When H=2

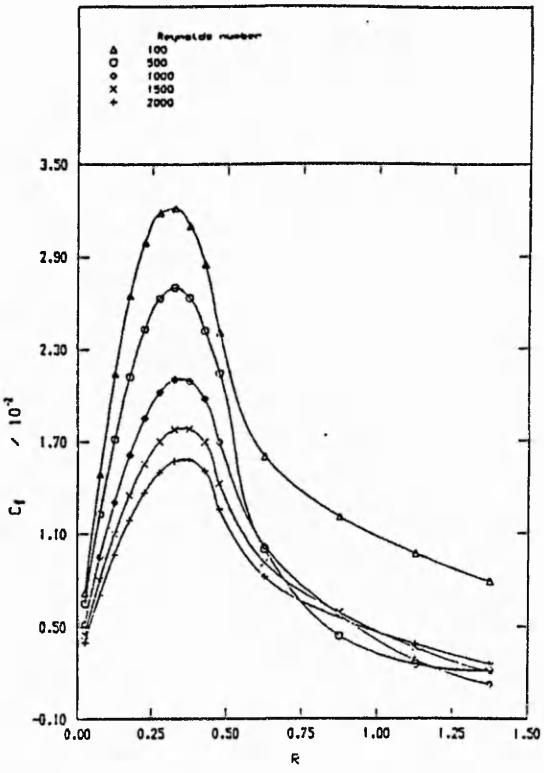

Figure 10. Friction factor at z=zmax when H=2

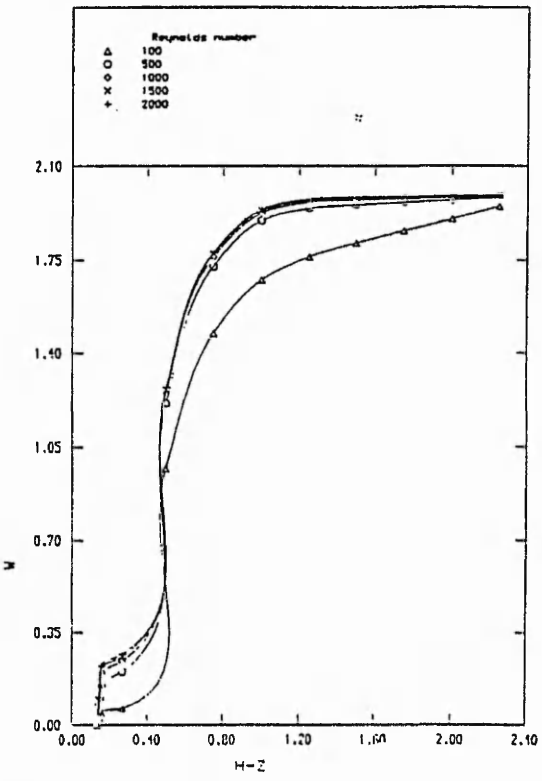

Figure 11. Axial velocity at R=0 when H=2

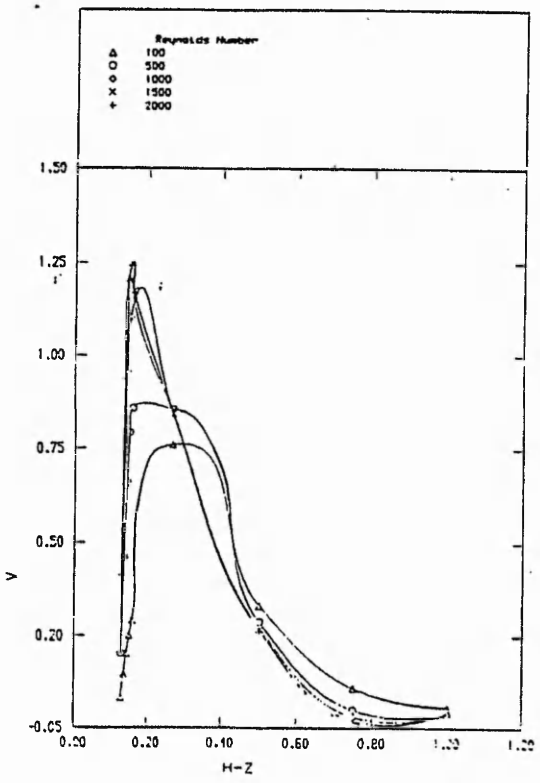

Figure 12. Radial velocity at R=0.5 when H=

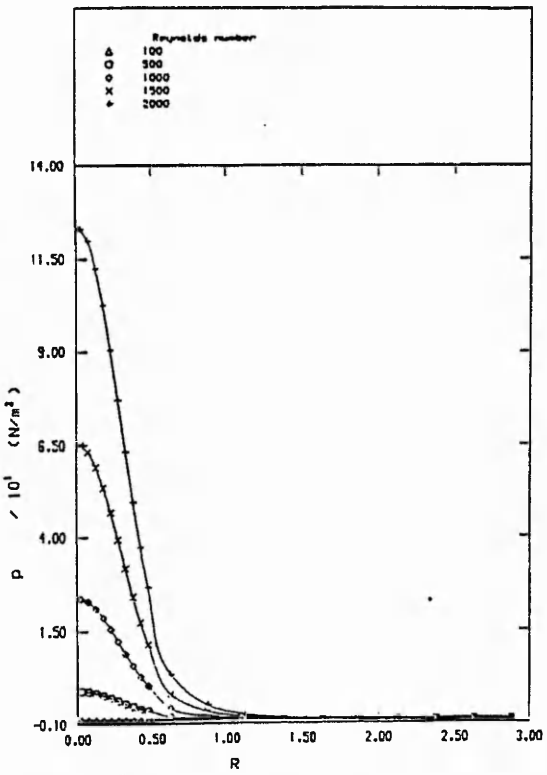

Figure 13. Pressure at z=zmax when H=2

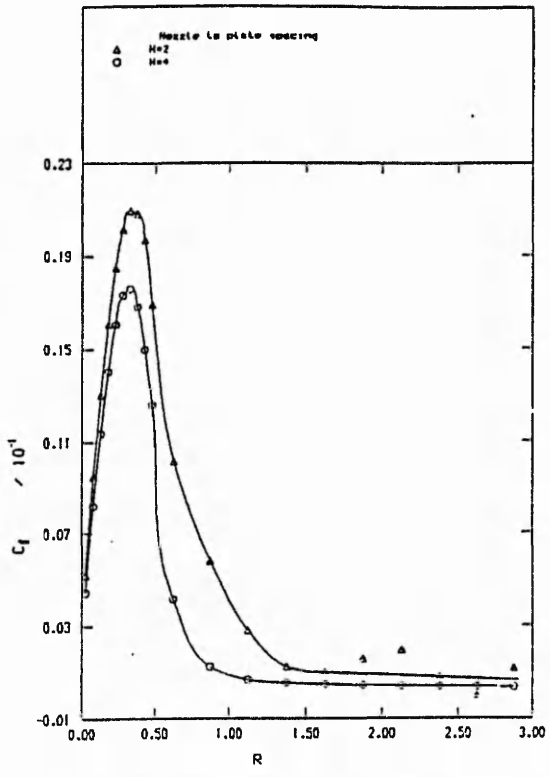

Figure 14. Friction Factor at z=zmax when d=4 mm and Re=1000

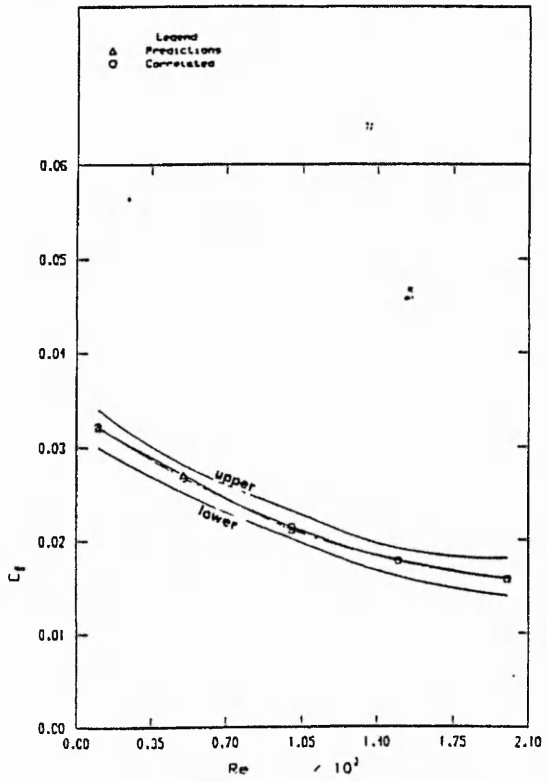

Figure 15. Correlated friction factor when H=2

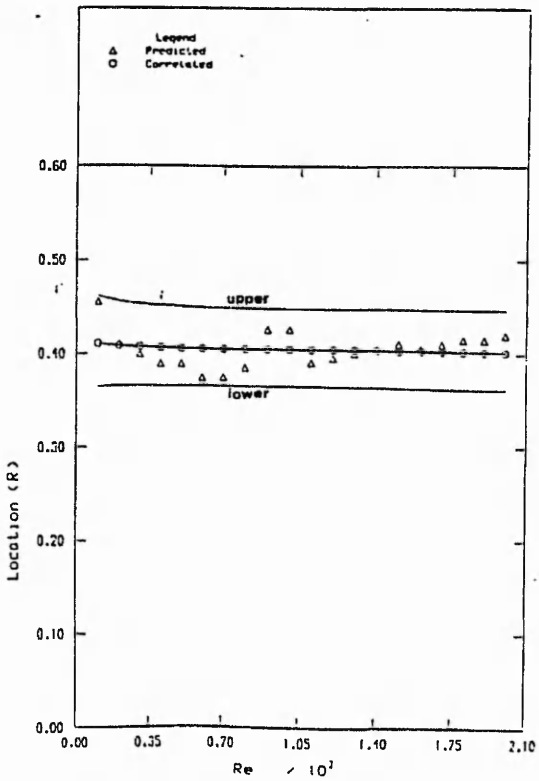

Figure 16. Correlation for location of maximum friction factor when H=2

4.6 Correlation

A statistical analysis was undertaken to correlate the maximum shear stress at the wall with Reynolds number. The correlated equation was found to be C_f=3.378E-2 - 1.605E-5Re + 3.528E-9Re^2 for the Reynolds number range of 100 to 2000. The technique of regression was applied using MINITAB (a statistical software package) see Ryan et al (1985). The prediction intervals with 95% confidence for the correlated equation were also produced. Figure 15 shows the observed numerical results with the correlated curve and prediction intervals. For further information on regression and prediction intervals see Chatfield (1983). The location of the maximum shear stress on the impingement surface was also regressed with Reynolds number and the equation obtained was a horizontal straight line R=0.4 and the prediction intervals were also obtained and are shown in Figure 16. This result is of the same order of magnitude as the one given by Despande and Vaishnav.

4.7 Comparison with other workers

Reynolds	Present circular H=2	Saad circular H=8	Despande circular H=2	Law slot H=2
400-500	0.027	0.026	0.034	0.017
950-1000	0.021	0.023	0.025	-
1960-2000	0.016	0.019	0.018	-

TABLE 1. Comparison of maximum values of C_f with other workers

It is clear from Table 1 that the comparisons of friction factor C_f are not for exactly identical geometries and boundary conditions. The friction factor C_f values for the current numerical simulation are only comparable with Despande and Vaishnav and Saad et al, this is despite the fact that Despande and Vaishnav's model is unconfined and Saad et al's uses a greater value of H. Considering Saad et al's results with the present model, the discrepancy is within 10 percent for the middle to lower Reynolds number range notwithstanding the geometrical differences.

5 CONCLUSIONS

The characteristics of an impinging circular jet in a confined region were found to be sensitive to the inlet jet velocity profile. Comparison of results with other workers shows similiar trends and are good at the lower Reynolds number range, particularly with Saad et al's data. From the literature review Button and Jambunathan (1989) it is clear that laminar jets have not been investigated extensively and it is not always possible to find corrobarating data, resulting in having to make non-unique comparisons.

6 FUTURE WORK

Extensive experimental studies are currently being undertaken in parallel with this numerical work which will help to validate the accuracy of the numerical model. Further work will involve extending the model to turbulent flow at the nozzle exit with heat transfer on the impingement plate.

7 ACKNOWLEDGEMENTS

The work was carried out in the Department of Mechanical Engineering using computer facilities provided by the Polytechnic's Computer services. One of the authors (S Kapasi) was supported by an SERC grant (GR/D/98693) which is gratefully acknowledged.

8 NOMENCLATURE

C_f	Skin friction $C_f = \tau/(4\rho w_{jet}^2)$
d	Diameter of jet
H	Non-dimensional plate spacing z_{max}/d
p	Pressure
r	Radial distance
R	Non-dimensional radial distance r/d
Re	Reynolds number $(w_{jet}d\rho/\mu)$
v	Radial velocity
V	Non-dimensional radial velocity (v/w_{jet})
w	Axial velocity
W	Non-dimensional axial velocity (w/w_{jet})
w_{jet}	Mean jet velocity at z=0
z_{max}	Maximum value of z
z	Axial distance
Z	Non-dimensional axial distance z/d
Greek	
$\Delta z/d$	Axial grid cell spacing
τ	Wall shear stress
μ	Laminar viscosity
ρ	Density

9 REFERENCES

Button B L and Jambunathan K, 1989. Jet-Impingement heat transfer, a bibliography 1976-85. Accepted for publication in Previews of Heat and Mass Transfer, March-April.

Chatfield C, 1983. Statistics for technology. 3rd ed., Chapman and Hall.

Deshpande M D and Vaishnav R M, 1982. Submerged laminar jet impingement on a plane. J. Fluid Mech. 114, 213-236.

Hedberg P K, Rosten H I and Spalding D B, 1986. The PHOENICS equations. CHAM TR/99. CHAM Ltd. 40 High Street, Wimbledon, London. SW19 5AU.

van Heiningen A R P, Mujumdar A S and Douglas W J M, 1976. Numerical prediction of the flow field and impingement heat transfer due to a laminar slot jet. Trans A.S.M.E., J. Heat Transfer 98, 654-658.

Law H-S and Masliyah J H, 1984. Numerical prediction of the flow field due to a confined laminar two-dimensional submerged jet. Computers and Fluids 12, 3, 199-215.

Marple V A, Liu B Y H and Whitby K T, 1974. On the flow fields of inertial impactors. Transactions of the ASME, Journal of Fluids Engineering, 394-400.

Ryan B F, Joiner B L and Ryan T A, 1985. Minitab Handbook, 2nd edition. Duckbury press.

Saad N R, Douglas W J M, and Mujumdar A S, 1977. Prediction of heat transfer under an axisymmetric laminar impinging jet. Ind. Engng Chem. Fundam. 16, 148-154.

Appendix I Q1 input file

```
 TALK=F;RUN( 1, 1);VDU= 3
    GROUP 1. Run title and other preliminaries
TEXT(IMPINGING JET WITH POLAR GRID
     Jet Reynolds number is 1500 and z/d=2
REAL(WIN,DIA,GK,TIN,CP)
TIN=20.0
DIA=0.004
GK=0.02624
CP=1004.9
WIN=5.25
    GROUP 2. Transience; time-step specification
    GROUP 3. X-direction grid specification
CARTES=F
    GROUP 4. Y-direction grid specification
NY=158;YVLAST=1.0
YFRAC(1)=-10.0;YFRAC(2)=0.0002
YFRAC(3)=50.0;YFRAC(4)=0.0002
YFRAC(5)=98.0;YFRAC(6)=0.001408
    GROUP 5. Z-direction grid specification
NZ=15;ZWLAST=1.0
ZFRAC(1)=-1.0;ZFRAC(2)=0.001
ZFRAC(3)=7.0;ZFRAC(4)=0.001
ZFRAC(5)=1.0;ZFRAC(6)=0.00085
ZFRAC(7)=5.0;ZFRAC(8)=0.00003
ZFRAC(9)=1.0;ZFRAC(10)=0.001
    GROUP 6. Body-fitted coordinates or grid distortion
    GROUP 7. Variables stored, solved & named
SOLUTN(P1,Y,Y,Y,N,N,N)
SOLUTN(V1,Y,Y,N,N,N,N)
SOLUTN(W1,Y,Y,N,N,N,N)
SOLUTN(H1,Y,Y,N,N,N,N)
    GROUP 8. Terms (in differential equations) & devices
DIFCUT=0
    GROUP 9. Properties of the medium (or media)
    The medium is air
ENUL=1.4E-5
RHO1=1.2928
PRNDTL(H1)=0.7
    GROUP 10. Inter-phase-transfer processes and properties
    GROUP 11.
FIINIT(P1)=READFI
FIINIT(W1)=READFI
FIINIT(V1)=READFI
FIINIT(H1)=READFI
    GROUP 12. Convection and diffusion adjustments
    GROUP 13. Boundary conditions and special sources
     ** Jet velocity definition fully developed
PATCH(JET1,LOW,1,1,1,1,1,1,1,1)
COVAL(JET1,W1,ONLYMS,10.47375)
COVAL(JET1,H1,ONLYMS,20.0)
COVAL(JET1,P1,FIXFLU,10.47375*RHO1)
PATCH(JET2,LOW,1,1,2,2,1,1,1,1)
COVAL(JET2,W1,ONLYMS,10.26375)
COVAL(JET2,H1,ONLYMS,20.0)
COVAL(JET2,P1,FIXFLU,10.26375*RHO1)
PATCH(JET3,LOW,1,1,3,3,1,1,1,1)
COVAL(JET3,W1,ONLYMS,9.843749)
COVAL(JET3,H1,ONLYMS,20.0)
COVAL(JET3,P1,FIXFLU,9.843749*RHO1)
PATCH(JET4,LOW,1,1,4,4,1,1,1,1)
COVAL(JET4,W1,ONLYMS,9.21375)
COVAL(JET4,H1,ONLYMS,20.0)
COVAL(JET4,P1,FIXFLU,9.21375*RHO1)
PATCH(JET5,LOW,1,1,5,5,1,1,1,1)
COVAL(JET5,W1,ONLYMS,8.37375)
COVAL(JET5,H1,ONLYMS,20.0)
COVAL(JET5,P1,FIXFLU,8.37375*RHO1)
```

```
PATCH(JET6,LOW,1,1,6,6,1,1,1,1)
COVAL(JET6,W1,ONLYMS,7.37375)
COVAL(JET6,H1,ONLYMS,20.0)
COVAL(JET6,P1,FIXFLU,7.37375*RHO1)
PATCH(JET7,LOW,1,1,7,7,1,1,1,1)
COVAL(JET7,W1,ONLYMS,6.06375)
COVAL(JET7,H1,ONLYMS,20.0)
COVAL(JET7,P1,FIXFLU,6.06375*RHO1)
PATCH(JET8,LOW,1,1,8,8,1,1,1,1)
COVAL(JET8,W1,ONLYMS,4.59375)
COVAL(JET8,H1,ONLYMS,20.0)
COVAL(JET8,P1,FIXFLU,4.59375*RHO1)
PATCH(JET9,LOW,1,1,9,9,1,1,1,1)
COVAL(JET9,W1,ONLYMS,2.91375)
COVAL(JET9,H1,ONLYMS,20.0)
COVAL(JET9,P1,FIXFLU,2.91375*RHO1)
PATCH(JET10,LOW,1,1,10,10,1,1,1,1)
COVAL(JET10,W1,ONLYMS,1.023751)
COVAL(JET10,H1,ONLYMS,20.0)
COVAL(JET10,P1,FIXFLU,1.023751*RHO1)
     ** To fix values at boundaries
     ** Blockage for impinging plate
PATCH(SET2,CELL,1,1,1,158,15,15,1,1)
COVAL(SET2,W1,FIXVAL,0.0)
COVAL(SET2,V1,FIXVAL,0.0)
COVAL(SET2,H1,FIXVAL,100.0)
     ** Blockage for confinement plate
PATCH(SET1,CELL,1,1,11,158,1,1,1,1)
COVAL(SET1,W1,FIXVAL,0.0)
COVAL(SET1,V1,FIXVAL,0.0)
     ** outflow region
PATCH(OUTREG,CELL,1,1,158,158,1,15,1,1)
COVAL(OUTREG,P1,FIXP,0.0)
     ** Laminar wall functions of the blockages
PATCH(IMPING,HWALL,1,1,1,158,14,14,1,1)
COVAL(IMPING,W1,FIXVAL,0.0)
COVAL(IMPING,V1,1.0,0.0)
COVAL(IMPING,H1,1.0/PRNDTL(H1),100.0)
PATCH(CONFINE,LWALL,1,1,11,158,2,2,1,1)
COVAL(CONFINE,V1,1.0,0.0)
    GROUP 14. Downstream pressure for PARAB=.TRUE.
    GROUP 15. Termination of sweeps
LSWEEP=3
RESREF(P1)=1.0E-7
RESREF(W1)=1.0E-7
RESREF(V1)=1.0E-7
RESREF(H1)=1.0E-7
    GROUP 16. Termination of iterations
    GROUP 17. Under-relaxation devices
RELAX(P1,LINRLX,0.5)
RELAX(V1,FALSDT,0.01)
RELAX(W1,FALSDT,0.01)
RELAX(H1,FALSDT,1.0)
    GROUP 18. Limits on variables or increments to them
VARMIN(H1)=20.0
VARMAX(H1)=100.0
    GROUP 19. Data communicated by satellite to GROUND
USEGRX=T
RG(1)=1.4E-5
RG(2)=1.2928
RG(3)=WIN
RG(4)=DIA
RG(5)=GK
RG(6)=TIN
RG(7)=CP
    GROUP 20. Preliminary print-out
ECHO=T
     GROUP 21. Print-out of variables
OUTPUT(W1,Y,Y,Y,Y,Y,Y)
```

```
OUTPUT(V1,Y,Y,Y,Y,Y,Y)
OUTPUT(P1,Y,Y,Y,Y,Y,Y)
OUTPUT(H1,Y,Y,Y,Y,Y,Y)
    GROUP 22. Spot-value print-out
NPRMON=5,IXMON=1,IYMON=10,IZMON=10
NPLT=1
IZPRF=1;IZPRL=15
    GROUP 23. Field print-out and plot control
NUMCLS=6
NYPRIN=1
NZPRIN=1
    GROUP 24. Dumps for restarts
    NSAVE=
SAVE=T;AUTOPS=F
RESTRT(V1)
RESTRT(W1)
RESTRT(P1)
RESTRT(H1)
STOP
```

Appendix II Ground code

```
C--- GROUP 1. Run title and other preliminaries
1001    CONTINUE
        CALL MAKE(EASP1)
        CALL MAKE(YG2D)
        CALL MAKE(ZGNZ)
        CALL MAKE(ZWNZ)
C--- GROUP 19. Special calls to GROUND from EARTH
194     CONTINUE
C       Get the gradient averaged over the cell
        CALL FNDVDZ(EASP1,V1)
C   * ------------------- SECTION 6 ---- FINISH OF IZ SLAB.
C       This if prints out on the last but one sweep
        IF(ISWEEP.EQ.LSWEEP-1) GOTO 1967
        GOTO 1969
C       This next section get earth arrays into local variables
1967    CALL GETYX(V1,GV1,MY,MX)
        CALL GETYX(EASP1,GDVDZ,MY,MX)
        CALL GETYX(YG2D,GYDIS,MY,MX)
        CALL GETZ(ZGNZ,GZDIS,NZ)
C       This if check whether it is on impingement surface
C       so that the surface variables can be printed
19617   IZLAST=NZ-1
        IF(IZ.EQ.IZLAST)GOTO 19613
        GOTO 1966
19613   GREY=GWIN*GDIA/GMU
        DO 1964 IY=1,NY
C       Shear stress calculated with PHOENICS gradient
        GTAUW(IY,1)=-GMU*GDVDZ(IY,1)/(4*GWIN*GWIN)
C       Shear stress calculated with approximated gradient
        APPDV=GV1(IY,1)/(GZDIS(NZ-1)-GZDIS(NZ-2))
C       Friction factor
        APPTAU=GMU*APPDV/(4*GWIN*GWIN)
        WRITE(50,1963)GYDIS(IY,1)/GDIA,APPTAU
1963    FORMAT(' ',E15.7,2X,E15.7)
1964    CONTINUE
1966    CONTINUE
```

Measurement of temperature field in confined jet impingement using phase-stepping video holography

B.N.Dobbins*,S.P.He+,K.Jambunathan*,S.Kapasi*,L.S.Wang*,B.L.Button*

* Nottingham Polytechnic, Department of Mechanical Engineering,
Burton Street, Nottingham NG1 4BU, UK.
+ University of Science and Technology of China, Department of Modern Mechanics,
Hefei, Anhui 230026, P. R. of China

ABSTRACT

Phase-stepping video holography has been applied to the measurement of the temperature distribution within a confined turbulent air jet impinging on a thermally conductive surface.

The optical arrangement, the apparatus and operating procedure are described. Sample temperature distribution was derived and the results were compared with thermocouple measurements. Advantages and limitations of the technique together with sources of error and measurement uncertainties were discussed.

1. INTRODUCTION

Measurement of the full-field temperature distribution in gases for engineering design is an important capability. Optical techniques are powerful tools in the measurements because they are non-intrusive and can provide full-field information. Of which, holographic interferometry has been widely used for the gas temperature field measurement[1,2,3].

Video holography and ESPI use a video camera instead of holographic plates as the recording medium and offers a fast, non-intrusive method for the measurement of gas temperature fields[4]. Video holography not only maintains the measuring accuracy and sensitivity of holographic interferometry but also avoids the delays involved in normal photographic processing and offers the advantage that interferometric patterns can be processed electronically or digitally.

Speckle noise, however, results in poor quality fringe patterns, this makes the techniques based on intensity analysis difficult to apply. The application of phase-stepping techniques[5,6,7] to video holography has the potential to solve the problem, it permits electronic or digital processing and automatic analyzing of the correlation fringe patterns and can produce results with better accuracy and with higher spatial resolution.

Phase-stepping video holography has been applied to the measurement of the temperature distribution within a confined turbulent impingement air jet. The air jet was heated and made to impinge on a thermally conductive surface. The purpose of this study was to contribute towards a fuller understanding the heat and mass transfer phenomena under an impinging jet.

2. EXPERIMENTAL SETUP

The arrangement of the experimental apparatus is shown in figure 1. The jet impingement structure consisted of a tube, a confinement plate and a impingement plate. The tube exit was flush with the confinement plate which is parallel to the impingement plate with a separation H. The plate spacing used corresponded to six jet diameters and the jet diameter, d, was 10.26 mm. The air jet was heated by an electrical heater after passing through a rotameter. The jet length after the rotameter was sufficient to allow the jet to achieve a fully developed velocity profile. The jet exit was normal to the impingement plate.

A conductive plate made of steel was used for the impingement surface. A row of thermocouples were arranged in the radial direction from the stagnation point of the jet. The thermocouples used were calibrated copper nickel thermocouples which had plugs fitted so that they could be used with a multiselector device attached to hand held temperature indicator.

586 / SPIE Vol 1554B Moiré Techniques, Holographic Interferometry, Optical NDT, and Applications to Fluid Mechanics (1991)
0-8194-0705-4/92/$4.00

3. OPTICAL ARRANGEMENT AND TECHNIQUES

Figure 2 shows the optical arrangement for phase-stepping video holography which was similar to that used in conventional holography, but a CCD camera was used rather than a holographic plate. The object beam was imaged onto a ground glass screen by using a lens system, and the reference beam was projected directly on to the screen. The reference path included a piezo-electric translator (PZT) to permit phase-stepping. The wavefront resulting from the interference of the object and reference beams was modulated by the ground glass to produce a speckle field. The speckle fields were imaged using the CCD camera and stored in the frame store of a PC based image processing system.

The experimental procedure is as follows:

a) An initial speckle pattern, denoted by 0SP, was stored when the jet was fully developed but with no heating;
b) Two more speckle patterns, 1SP and 2SP, were recorded and stored whilst the optical path length of the reference beam was changed by $\lambda/3$ and $2\lambda/3$, by driving the PZT;
c) Carrier fringes were imposed by translating the reference beam expander, this was done in order to enhance the visual interpretation of the data and to validate the stepped phases produced by the PZT. After applying the carrier fringes, a further pattern, CSP, was captured;
d) The air was then heated and the resulting deformed speckle pattern DSP was acquired;
e) From speckle patterns 0SP, 1SP, 2SP and CSP, three carrier fringe patterns were obtained by calculating the square of the differences between related speckle patterns before and after applying the carriers, then the phase distribution of the carrier fringe pattern was produced using conventional 3-step phase-stepping technique;
f) From speckle patterns 0SP, 1SP, 2SP and DSP, three phase-stepped temperature fringe patterns modulated by the carrier fringes and hence the wrapped phase distribution were produced using the same way as in step (e);
g) Finally, the phase distribution of the temperature fringe pattern was calculated by subtracting the phases of the carrier fringes from the combined phases of the temperature fringes with the carrier fringes.

The intensities of three phase-stepped fringe patterns can be written as

$$A = \langle I_o \rangle [1 - \gamma \cos\phi] \tag{1a}$$

$$B = \langle I_o \rangle [1 - \gamma \cos(\phi - 2\pi/3)] \tag{1b}$$

$$C = \langle I_o \rangle [1 - \gamma \cos(\phi + 4\pi/3)] \tag{1c}$$

where $\langle I_o \rangle$ the average intensity of the fringe pattern, Φ is its phase and γ is the modulation of fringes.

Before calculating the phase Φ, low-pass filtering is performed by five iterations of averaging over 3 by 3 sample region to reduce speckle noise of the fringe patterns. Then, the phase Φ at each detected point (x,y) can be calculated from

$$\phi = \arctan\left[\frac{\sqrt{3}\,(B - C)}{2A - B - C}\right] \tag{2}$$

The calculated phase, Φ, is the principal value of the arctangent function, which ranges from $-\pi$ to π rad. Five iterations of a median filter within a three by three pixel area are executed to reduce salt and pepper noise caused by speckles. Discontinuities of the phase distribution occur near $-\pi$ or π rad. To obtain the phase distribution on the whole surface, a correction procedure to the discontinuity of the calculated Φ is performed by the method used in the conventional phase-stepping technique.

4. BASIC EQUATIONS

Generation of correlation fringe patterns with video holography is caused by variation of the gas refractive index. From the phase distribution Φ measured above, the change of the gas refractive index can be determined by using the following equation:

$$\int \Delta n(x,y,z)\,dz = \frac{\phi(x,y)}{2\pi}\lambda \tag{3}$$

in which, $\Delta n(x,y,z)$ is the change of the gas refractive index between two states before and after the heating, λ is the wavelength of the laser.

For an axisymmetric case (as shown in figure 3), the above equation can be written as

$$2\int [\Delta n(r,y)\, r/\sqrt{r^2-x^2}]\,dr = \frac{\phi\lambda}{2\pi} \tag{4}$$

where

$$\Delta n(r,y) = \Delta n(x,y,z) \tag{4a}$$

$$r = \sqrt{z^2+x^2} \tag{4b}$$

y-axis of the coordinate system was chosen along the symmetric axis of the jet setup and z-axis the direction of the object beam.

Using the Abel-transformation[1], equation (4) can be written as

$$\Delta n(r,y) = -(\lambda/\pi) \int_r^\infty \left[\frac{d(\Phi/2\pi)}{dx}\right] / \sqrt{(x^2-r^2)}\,dx \tag{5}$$

After the change of the gas refractive index $\Delta n(r,y)$ was found from the above equation, the distribution of the gas density ρ can be further derived from the following equation:

$$\rho = \frac{\Delta n(r,y)}{K} + \rho_o \tag{6}$$

in which, K = 0.226E-3 $m^3\,kg^{-1}$, is the Gladstone-Dale constant of air, ρ_0 is the density of air during the first exposure.

Using the ideal gas equation, the gas temperature T can be shown to be

$$\frac{1}{T} = \frac{1}{T_o} + \frac{R\Delta n(r,y)}{K\mu P} \tag{7}$$

where

μ = 28.97 g mol^{-1}, is the molecular mass of air;
P = 0.10135 MPa, is the gas pressure;
R = 8.309E3 J $(mol\ K)^{-1}$, is the universal gas constant;
T_o is the gas temperature during the first exposure.

5. EXPERIMENTAL RESULTS

Phase-stepping video holography was applied to the measurement of the temperature distribution within a confined turbulent impingement air jet. A thermally conductive surface with a heated air jet was investigated.

Figures 4(a) and 4(b) show respectively the phase maps of the carrier fringe pattern and the temperature fringe pattern. The Reynolds number in the experiment was 5400 ± 200 when the heated air jet was at 102°C.

Figure 5 shows the temperature distribution profile on the impingement surface derived from the phase map 4(b). In which, the measured results are compared with the data obtained by thermocouples. The difference between the two measured results is less than 8.0 per cent for most investigated region. The sources of error come mainly from following aspects:

a) Speckle noise and phase measurement error resulting from uncertainties of step quantities which although were validated by the intensity method;
b) Curve-fitting and calculation errors resulting from numerical computation method;
c) The assumption that the beams propagated in straight line whereas they constrained to propagate in curved path through the heated flow field due to the variations of the refractive index[2];
d) The assumption in the calculation that the temperature field was axisymmetric which, in practice, however, might not be completely true;
e) The error in the measurement by thermocouples which was found to be ±1.5 per cent.

6. DISCUSSION AND CONCLUSION

From the fringe pattern obtained in real-time without the carrier fringes (infinite fringes), it was seen that the fringes oscillated rapidly due to the temperature fluctuations. The introduction of carrier fringes decreased the apparent fluctuations and facilitated the visual interpretation of the data.

It was found difficult to ensure repeatability of the two stepped phases, because a non feedback PZT had been employed. The carrier fringes were employed to validate the phase steps using the procedure below:

a) The coordinates of the fringe centres and their fringe numbers were determined according to the grey level distributions for each of the three phase-stepped carrier fringe patterns;
b) A polynomial curve was fitted to each set of data using the method of least squares;
c) The relative phases of the steps were obtained by comparing the three distribution curves of the fringe order numbers.

The method based on the intensity analysis does not offer results of very high accuracy, but using this method the confidence in the step size is better than that obtained from the low cost PZT calibration.

It is found from the experiment that phase-stepping video holography is useful and effective means of the measurement and visualisation of a gas temperature field and has a number of advantages:

a) The technique can provide non-intrusive and full field temperature distribution which will be valuable in understanding heat transfer and fluid flow phenomena;
b) The speckle interferometric patterns can be digitally processed;
c) The determination of the relative fringe order numbers and interpolation of the fractional fringe order numbers can be performed automatically;
d) The sign of the deformation is provided directly.

Because the speckle noise in the speckle fringe pattern cannot be completely eliminated, phase-stepping speckle interferometry cannot achieve the potential accuracy of phase-stepping holographic interferometry.

7. REFERENCES

1. C.M.Vest, Holographic Interferometry, John Wiley & Sons, New York, 1979.
2. D.L.Reuss,"Temperature measurement in a radially symmetric flame using holographic interferometry", Combustion and Flame, 49, 207-219, 1983.
3. S.P.He, X.P.Wu, "The application of holographic thermometry in engineering thermophysics", Int. Conf. on Experimental Mechanics, Beijing, 1985.
4. B.Lu, X.Yang, H.Abendroth, H.Eggers, E.Ziolkowski, "Measurement of a three dimensional temperature field applying ESPI and CT techniques", Optics Communications, 69, 1, 6-10, 1988.
5. S.Nakadate, H.Saito, "Fringe scanning speckle-pattern interferometry", Appl. Opt., 24, 2172-80, 1985.
6. K.Creath, "Phase-shifting speckle interferometry", Appl. Opt., 24, 3053-58, 1985.
7. D.W.Robinson, D.C.Williams, "Digital phase stepping speckle interferometry", Optics Communication, 57, 26-30, 198

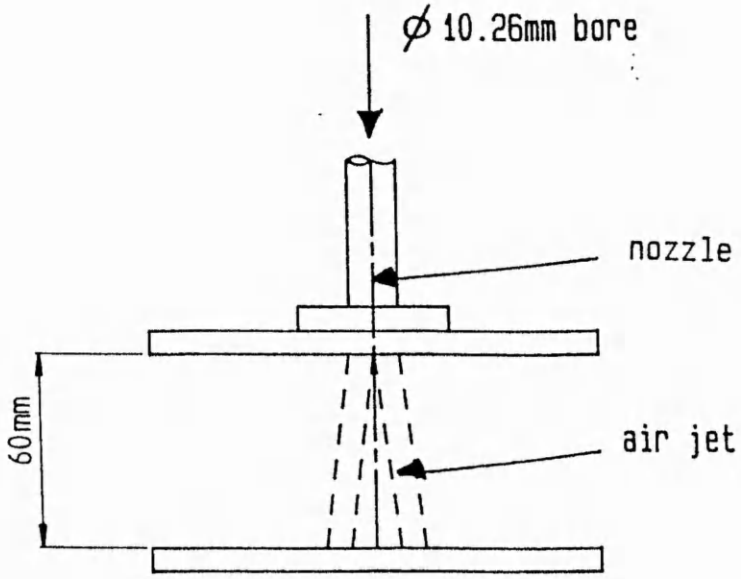

Figure 1 Jet impingement under investigation

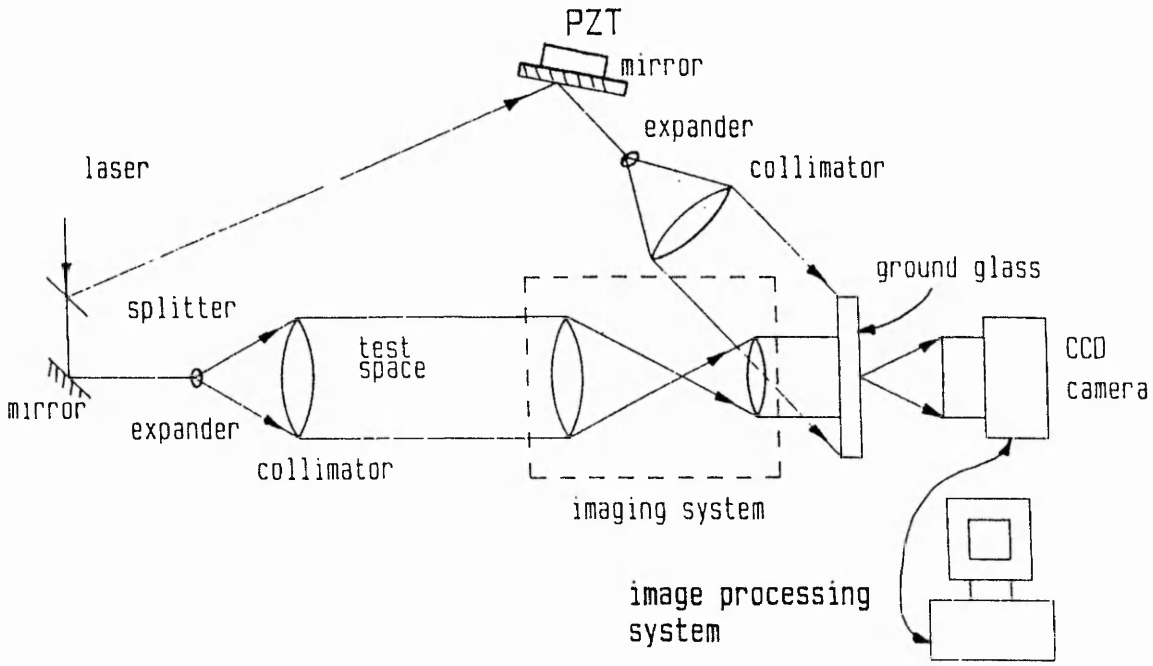

Figure 2 Optical arrangement of phase-stepping video holography

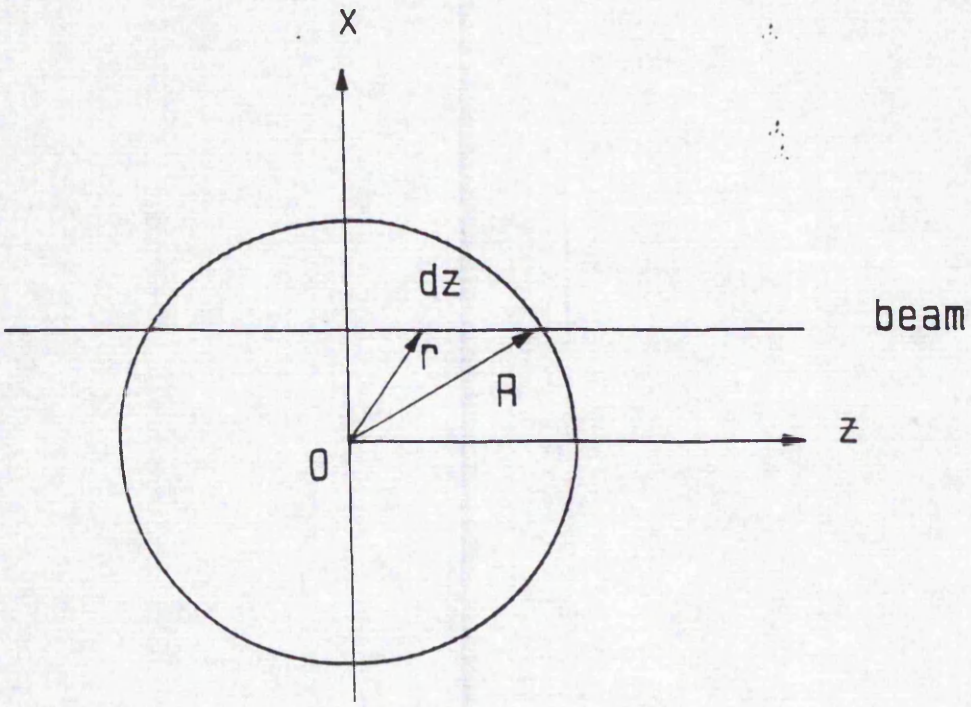

Figure 3 Analysis of axisymmetric temperature field

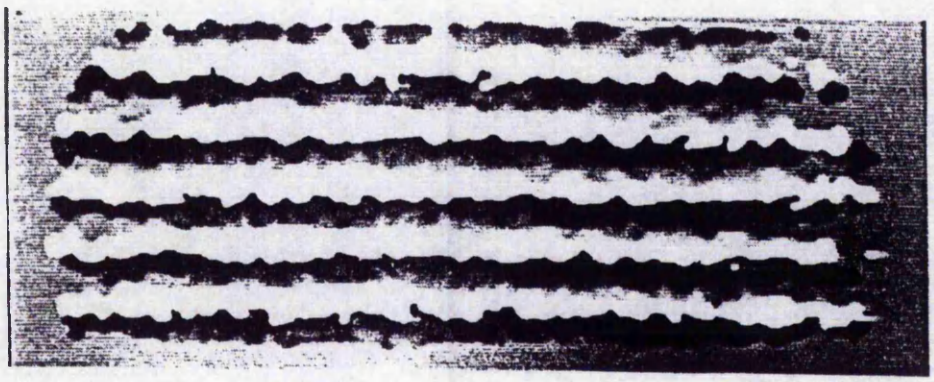

Figure 4(a) Phase map of carrier fringe patterns

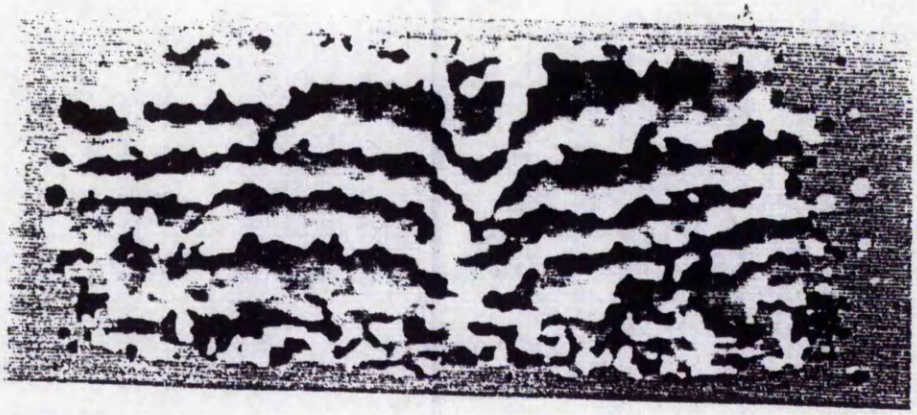

Figure 4(b) Phase map of combined temperature and carrier fringe patterns

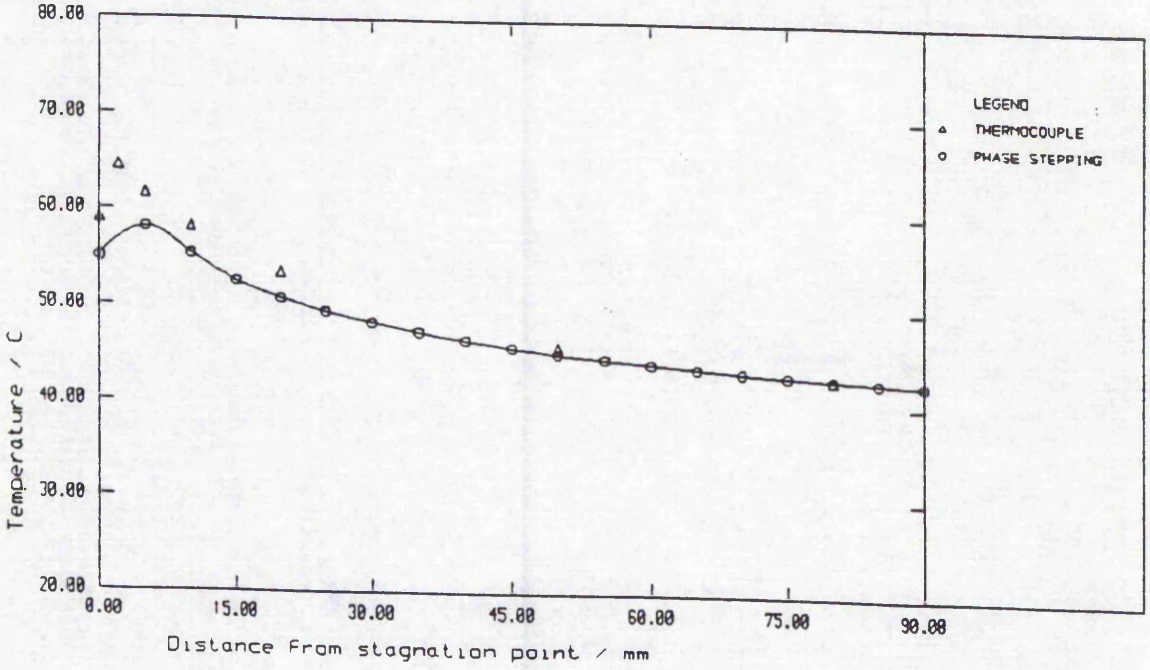

Figure 5 Temperature distribution along the impingement surface

FED-Vol. 128, Experimental and Numerical
Flow Visualization
ASME 1991

THE MEASUREMENT OF TEMPERATURE DISTRIBUTION IN SEMI-CONFINED JET IMPINGEMENT USING ESPI AND HOLOGRAPHY

B. L. Button, B. N. Dobbins, K. Jambunathan, and S. Kapasi
Department of Mechanical Engineering
Faculty of Engineering
Nottingham Polytechnic
Nottingham, United Kingdom

S. P. He and L. S. Wang
Department of Modern Mechanics
University of Science and Technology of China
Hefei, People's Republic of China

ABSTRACT

Electronic speckle pattern interferometry (ESPI), video holography and holography have been used to visualise and measure the temperature distribution of a semi-confined turbulent impinging air jet of diameter 10.26 mm with jet Reynolds numbers of 6400, 8000 and 8900. The temperature distributions have been visualised with isothermal, adiabatic and a conductive boundary conditions imposed on the impingement surface.

The arrangements of the optical and experimental apparatus are shown and the operating procedures are described. Typical fringe patterns acquired using ESPI, video holography and conventional photographic holography are presented. A temperature distribution derived from one holographic fringe pattern is compared with thermocouple measurements and with predictions from numerical simulations.

1. INTRODUCTION

A great deal of work has been done by numerous authors on heat and mass transfer processes within jet impingement environments. The hydrodynamic flow fields have been studied experimentally and simulated numerically by a number of authors, see Button and Jambunathan (1989). Heat transfer coefficients at the impingement wall have been obtained using direct measurement methods and analogous techniques such as the mass sublimation technique,(Macleod & Kapur 1974).

Optical techniques for the measurement of the hydrodynamic flow field have been used widely and offer many advantages, they are non-intrusive and yield full field information. Of these, holographic interferometry is perhaps the most widely used for measurements of gas temperature fields, (Vest 1979), (Reuss and Schutz 1987) and (He and Wu 1985). In general, high powered pulsed lasers are required for studying dynamic behavior of flows in order to capture instantaneous flow fields.

Video holography and Electronic Speckle Pattern Interferometry (ESPI) utilise the laser speckle effect with recording by video instead of wavefront interference photography, a full description of ESPI can be found in Jones and Wykes (1989).

ESPI and video holography differ from conventional holography in that the fringe pattern is generated electronically by analoque or digital subtraction of the video resolvable speckle pattern instead of by optical interference at the photographic recording medium. ESPI and video holography consequently offer the potential for rapid and relatively unskilled operation at the expense of reduced resolution. ESPI and video holography have been used extensively in vibration measurement (Tyrer 1988) and in deformation measurement (Saluja et al 1988). Lu et al (1988) have used an ESPI technique applied to the measurement of an axisymmetrical temperature field.

The present work utilises a combined arrangement of ESPI and holography, so the strengths of individual techniques can be exploited. ESPI gives results in real time which can be used to monitor the flow development, whereas the holographic system can give higher resolution results taken under conditions for which the full history is available from the ESPI recording.

In this paper, boundary conditions implemented on the impingement plate were varied so that effects of buoyancy and natural convection could be identified. The following four boundaries were investigated (1) a cold isothermal surface; (2) a hot isothermal surface; both the above impinged on by an ambient air jet; (3) a thermally conductive surface and (4) an adiabatic surface; both impinged on by a heated air jet.

A commercial finite volume package PHOENICS has been used to create a numerical model for the impingement geometry and incorporates a K-ε turbulence model. The K-ε turbulence model is presently the best and most widely used turbulence model. The output from the simulation can be easily manipulated to produce graphical representation of the individual variables.

2. EXPERIMENTAL SETUP

The arrangement of the experimental apparatus is shown in Figure 1. The jet consist of a circular tube, with boundaries made up of a round confinement plate and a round impingement plate. The tube exit was flush with the confinement plate and this plate was

positioned parallel to the impingement plate with a plate spacing distance, H, of 60 mm. The jet tube diameter, d, was 10.26 mm.

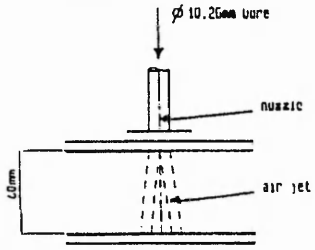

Figure 1 Jet Impingement

The air flow was metered using a rotameter after which the air was heated by an electrical heater. The jet length after the rotameter was sufficient to allow the jet to achieve a fully developed velocity profile. The nozzle exit was normal to the impingement plate.

The material used for the impingement plate for both the hot and cold surfaces was made of copper, 1 mm thick. This thickness was chosen so that there would be no significant temperature gradient across the plate and it would not flex under the impingement pressure of the jet. The plate was placed over a tank which was filled with either ice or hot water. The plate was mounted with fins so that immersion into the tank would keep the surface of the plate at constant temperature for the duration of the test. For the adiabatic surface a smooth polystyrene foam surface was constructed to fit over the tank and for the conductive surface a 1 mm thick steel plate was used.

All the impingement plates had thermocouples mounted in the radial direction from the centre of the plate. The thermocouple beads protruding 0.5 mm above the plate surface. The calibrated thermocouples used were of copper nickel type, which had plugs fitted so that they could be used with a multiselector device attached to a hand held temperature indicator. Accuracy of any thermocouple was better than 0.5°C

3. OPTICAL ARRANGEMENTS

Three different optical arrangements, a commercial ESPI, video holography and holography were used to obtain the temperature field in the confined jet impingement regime.

The optical arrangement of a commercial ESPI is shown in Figure 2. A collimating lens was introduced into the illuminating beam which passes through the jet impingement field. The beam was incident on a diffusely reflecting surface and passed back through the jet to a camera. This two pass arrangement resulted in twice the number of fringes as compared with the single pass holographic set up. In consequence sensitivity was doubled as compared with the holographic set up.

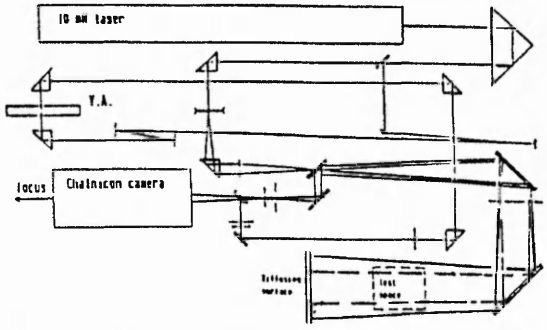

Figure 2 Optical arrangement of commecial ESPI

Figure 3 shows the optical arrangement for video holography. The system is similar to the physical arrangement of the holographic setup, which may be seen in Figure 4, but a CCD camera was substituted for the holographic recording medium. The centre of the jet impingement field was imaged onto a ground glass by an imaging lens system, and the ground glass created a speckle field. The ground glass was used to avoid the appearance of optical system in the holographic reconstruction. The interference of the speckle field from both the object and reference waves resulted in a new speckle field which was resolved by the CCD camera. The CCD camera signal was output to a subtraction unit or was recorded for subsequent manipulation by a PC based image processing system.

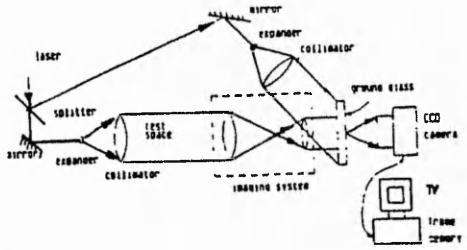

Figure 3 optical arrangement of Video Holography

Figure 4 shows the optical arrangement of the combined commercial ESPI and holographic interferometer. The collimated beams from the ESPI and holographic interferometer were arranged to be mutually perpendicular. This allowed simultaneous acquisition of measurement data. For the holographic interferometer, the impingement field was imaged onto a ground glass by an imaging system.

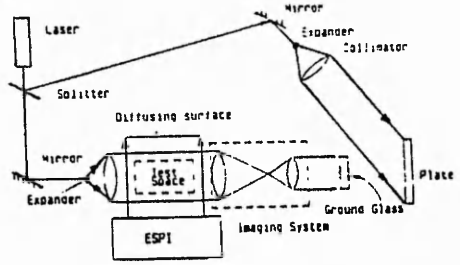

Figure 4 Optical arrangement of combined ESPI and Holography

The infinite fringe patterns produced by the above methods are patterns where the zeroth fringe initially extends over the entire image representing zero deformation. By moving the imaging system output lens a small vertical distance prependicular to the object path equally spaced horizontal carrier fringes were produced. Subsequently the fringes produced by the jet impingement were easier to analyse than those produced without the carrier fringes.

4. EXPERIMENTAL PROCEDURE

All the techniques rely on the generation of fringes by interference or correlation of two images taken at different times. The fringes correspond to contours of equal phase change between the two images. The first image was produced by initial exposure of the holographic plate and simultaneous acquisition of a reference frame on the ESPI. These were taken before the introduction of the impingement jet. For ESPI the second image was obtained in real time and the correlation fringes produced by a real time video subtraction unit. The fringes were displayed on a video monitor and were used to monitor real time temperature

fluctuations, the fringe patterns were recorded on video cassette. When the fringe patterns were observed to be steady, the holographic plate was exposed for the second time and a double-exposure holographic fringe pattern was obtained after reconstruction. The experimental procedure for the video holography was the same as that for the ESPI system.

5. ANALYSIS

The intensity distribution of the holographic fringe pattern is given by

$$I \propto I_o \cos^2\left[\frac{\phi}{2}\right] \qquad (1)$$

in which, I_o is the intensity of the object beam, ϕ is phase change of the object beam due to presence of the impinging jet.

The intensity distribution of the fringe pattern from ESPI or video holography is proportional to

$$I \propto I_o I_r \sin^2\left[\phi_{o,r} + \frac{\Delta\phi}{2}{}_{o,r}\right] \sin^2\left[\frac{\Delta\phi}{2}{}_{o,r}\right] \qquad (2)$$

where I_o and I_r are intensities of the object and reference beam respectively; $\phi_{o,r}$ is the phase difference between the object beam and reference beam; $\Delta\phi_{o,r}$ is change of the phase difference $\phi_{o,r}$ due to jet impingement.

It is found by comparing the intensity distribution that apart from the speckled noise due to the random phase fluctuations $\phi_{o,r}$ between the object and reference beams, the fringe patterns produced by of the ESPI are virtually the same as those from holography. Except that the dark and bright fringes are interchanged.

The ESPI has double the number of fringes because the object beam passes through the jet space twice, compared with the holographic arrangement.

Generation of the interferometric fringe patterns with the holographic interferometer or the correlation fringe patterns of the ESPI or video holographic setup are caused by changes of gas refractive index in the flow field. From the fringe patterns, the change of gas refractive index can be determined by the following equation

$$\int \Delta\eta_{(x,y,z)}\, dz = N_{(x,y)}\, \lambda \qquad (3)$$

in which, $\Delta\eta_{(x,y,z)}$ is the change of the gas refractive index between the two exposures; $N_{(x,y)}$ is fringe order number (note that these are doubled with the ESPI); λ is wavelength of the laser.

The y-axis of the coordinate system is along the symmetric axis of the flow field, and z-axis is along the direction of the object beam.

For an axisymmetric case, equation (3) can be rewritten as

$$2\int_x^{\infty} \Delta\eta_{(r,y)} \frac{r\, dr}{\sqrt{r^2-x^2}} = N_{(x,y)}\, \lambda \qquad (4)$$

where $\Delta\eta_{(r,y)} = \Delta\eta_{(x,y,z)}$ and $r = \sqrt{z^2+x^2}$

A digital calculation method was employed to find the change of the gas refractive index $\Delta\eta_{(r,y)}$ from equation (4). Then, the distribution of the gas density ρ was obtained using following equation

$$\frac{\rho}{K} = \frac{\Delta\eta_{(r,y)}}{K} + \frac{K_o \rho_o}{K} \qquad (5)$$

in which, $K_o = 0.226\times10^{-3}$ m^3/kg, is the Gladstone-Dale constant of air during the first exposure, K is the Gladstone-Dale constant of the air during the second exposure; ρ_o is the density of air in the first exposure.

Using the ideal gas state equation, the formula of the air temperature T can be described as

$$T = \frac{(K \mu P T_o)}{K_o \mu_o P + R_o T_o \Delta\eta_{(r,y)}} \qquad (6)$$

where μ is the molecular mass of the air during the second exposure;

μ_o = 28.97 kg/kmol is the molecular mass of air; P = 0.10135 MPa, is the air pressure; R_o = 8.314 kJ/kmol K, is the universal gas constant; T_o is the air temperature during the first exposure. There was no change of air constituents in the jet, so the values of K and μ were unchanged between the first the second exposure.

6. COMPUTER SIMULATION

The numerical model was created by using the Navier Stokes and energy equations, which were solved using a finite volume technique with the K-ε turbulence model. The following boundary conditions were used for the impingement surface, zero velocities at the wall with a wall function on the fluid side of the surface. The temperature boundaries at the impingement wall were either a fixed temperature surface or an adiabatic surface . The inlet jet was modelled by equating the velocities to a fully developed velocity profile with initial temperature and turbulence conditions. The outlet was modelled by setting the pressure at the extreme radial position of the domain to ambient pressure. Flow visualisation of the predictions were produced in the form of vector and streamline plots of the velocities. The thermal field was presented as a contour plot. The data was further manipulated to produce a pseudo infinite fringe pattern of the flow field so that a qualitative visual comparison of the experimental fringes and the numerical predictions could be made.

7. RESULTS

The temperature fields in a confined jet impingement regime were obtained using the three optical techniques outlined above. The four boundary conditions considered were

1. heated air jet, conductive surface
2. heated air jet, adiabatic surface
3. ambient air jet, heated isothermal surface
4. ambient air jet, cold isothermal surface

The experimental fringe patterns are presented in figures 5 to 10. Figures 5 to 7 are of infinite fringe patterns of the jet impingement temperature field. The experimental parameters and boundary conditions of the jet impingement are given in table 1.

The fringe pattern in figures 5a,b show large speckles which are due to the ground glass and the CCD camera. The jet is central on the upper surface and impinging on the lower surface. Four fringes are present and this corresponds with the holographic results.

The speckle size in figures 6a,b are finer due to the nature of the diffusing surface and the number of fringes are doubled because the object beam pass the through the object twice.

Table 1. Experimental conditions for infinite fringe pattern

Number of figure		Boundary conditions	Air jet	Reynolds number	Method used
Fig.5	a	Conductive	Heated (80°C)	8900 ± 400	Video Holography
	b	Adiabatic			
Fig.6	a	Conductive	Heated (66°C)	6400 ± 300	ESPI
	b	Adiabatic			
Fig.7	a	Conductive	Heated (66°C)	6400 ± 300	Holography
	b	Adiabatic			

The improved quality of the holographic fringe pattern may be seen in figure 7a,b. The presence of the ground glass screen and the use of the CCD camera to record the reconstructed fringe pattern. The pattern obtained corresponds to that obtained using ESPI and by comparison with figure 5a,b the fringes can be seen to be more widely spaced due to the smaller temperature gradient at the lower Reynolds number

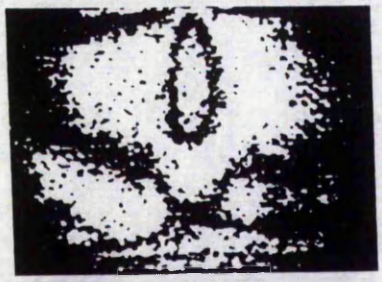

Figure 5a

Figure 5b

Figure 5a,b Infinite fringe pattern by Video Holography

Figure 6a

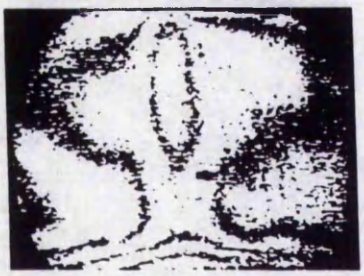

Figure 6b

Figure 6a,b Infinite fringe pattern by ESPI

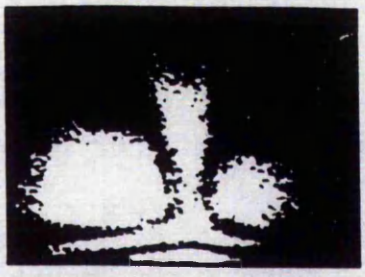

Figure 7a

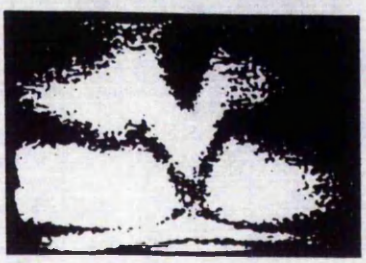

Figure 7b

Figure 7a,b Infinite fringe pattern by Holography

Figures 8 and 9 show finite fringe patterns of the jet impingement temperature field obtained using the ESPI. Figures 8(a) and 9(a) are the carrier fringe patterns. Figures 8(b) and 9(b) are fringe patterns of natural convection resulting from the heated impingement plate and due to natural air cooling from the cooled impingement plate respectively. Figures 8(c) and 9(c) show fringe patterns within the impingement field, for the experimental and boundary conditions given in table 2. The air jet is placed from the centre of the figure because of the need to see the entire region of the flow. The field of view was limited by the size of the collimating optics ϕ 150mm. The carrier fringes were found to substantially improve the apparent stability of the fringe pattern and to facilitate fringe counting and analysis.

Table 2. Experimental conditions for finite fringe patterns

Number of figure		Boundary Conditions	Air jet	Reynolds number
8	c	Heated isothermal surface 46°C	Ambient 23°C	8000 ± 350
9	c	cold isothermal surface 2°C	Ambient 23°C	8000 ± 350

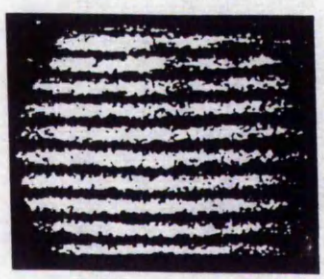

Figure 8a
Carrier Fringe

Figure 8b
Natural convection

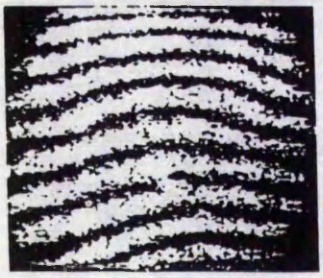

Figure 8c
Jet Impingement

Figure 8a,b,c Finite fringe pattern by ESPI

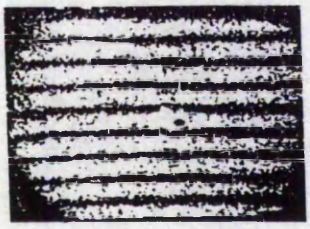

Figure 9a
Carrier fringe

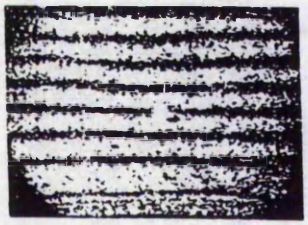

Figure 9b
Natural air cooling

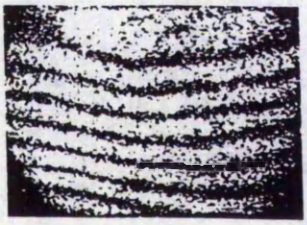

Figure 9c
Jet Impingement

Figure 9a,b,c Finite fringe patterns by ESPI

Figure 10a,b show fringe patterns obtained using real-time holography. In which, (a) is a carrier fringe pattern and (b) is a finite fringe pattern of the impingement temperature field. The impingement plate was a conductive surface, and Reynolds number of the heated air jet was 8330 ± 350. The calculation procedure using equation 4 was based on determining the fringe order number distribution along a horizontal across the symmetric field. The analysis was performed by analysing horizontal rasters and counting fringe numbers from the edge. The angled carrier fringe shown in figure 10a facilitates the computer based analysis of the fringe pattern compared with both the infinite and horizontal carrier fringe cases.

Figure 10a
Carrier fringe

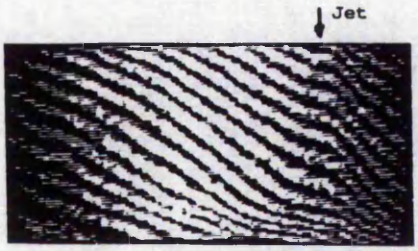

Figure 10b
Jet Impingemen

Figure 10a,b Finite fringe pattern by Holography
Re= 8330 ± 350 Heated air jet (68 °C)

Figure 11 shows a temperature distribution profile along the impingement plate surface derived from the fringe pattern of figure 10(b) at 0.5mm from the impingement surface and is compared with the results measured using thermocouples. The numerical predictions for a conductive boundary condition are plotted on the same figure. The difference between the two experimental results is less than 2 per cent except at the centre where the difference reaches 6 per cent. The difference in value between experimental and numerical results is of the order of 10 per cent.

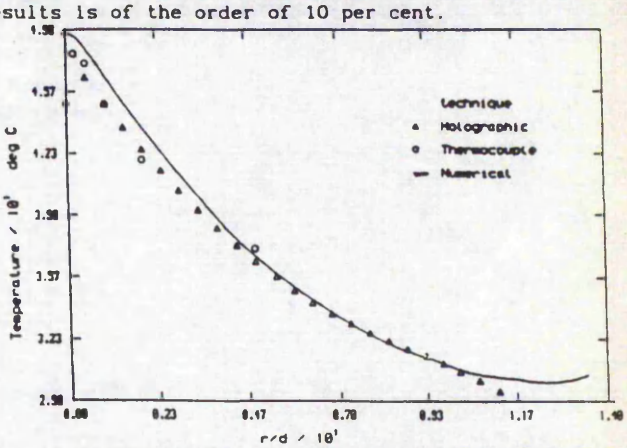

Figure 11 Temperature distribution for Re=8330 ± 350
T_{jet} = 68 °C

The pseudo fringe pattern in figure 12 generated from the numerical simulation shows a similar pattern to that obtained from the experimental results. Even though the experimental pattern was very unsteady and fluctuated rapidly. The accuracy of the numerical model depends on the specification of the boundary conditions. Inaccuracies within the K-ε turbulence model at the stagnation point and at the wall contribute to the error for the predicted results.

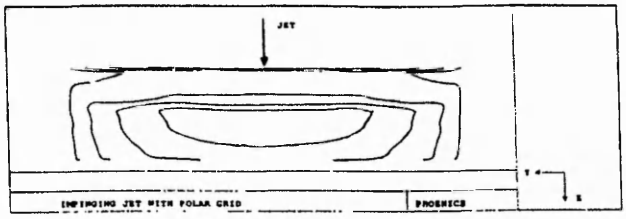

Figure 12 Pseudo infinite fringe from numerical simulation Re= 8330 T_{jet}= 68 °C

The main sources of experimental error;

1. The estimation error of the fringe order numbers.
2. The assumption that the beams propagated in straight line. The beams will exhibit a slight curvature through the impingement field due refractive index variations. Reuss (1985),has shown this error to be less than 0.5 per cent.
3. The error due to the assumption in the calculations that the temperature distribution is axisymmetric.

8. DISCUSSION AND CONCLUSIONS

In order to visualize qualitatively the temperature field within the jet impingement region, the infinite fringe pattern is very useful because of the ease with which visualisation of temperature fringes can be obtained. The infinite fringe pattern displayed in real-time can be used to investigate dynamic development of the temperature field within the flow regime, when the velocity or temperature of the air jet is changed, and can be used to compare the temperature and flow distributions for the various boundary conditions.

The infinite fringes were found to oscillate rapidly within the recirculation and mixing zone regions due to local temperature fluctuations. The introduction of carrier fringes facilitated analysis of the fringe patterns due to decrease of the fringe fluctuation and the identification of fringe number is made simpler.

The fringe patterns are acquired by double exposure, the information obtained is averaged over the exposure time. For the ESPI and video holography this is normally 1/25th of a second. For holography using a 10mW laser the exposure time was 3 seconds. Better temporal resolution required for dynamic flow visualisation can be obtained using higher powered lasers. The temporal resolution of ESPI and video holography could be improved by a combination of a higher powered laser and electronic shuttering of the CCD camera.

It is difficult to determine the fringe order number from the double-exposure holographic fringe pattern as the zeroth fringe moves from the field of view. Both the real-time and carrier fringe methods can be used to facilitate the determination of the absolute fringe order numbers by allowing real-time fringe counting

ESPI, video holography and holography are powerful tools for the measurement and visualisation of gas temperature fields, jet impingement, and natural convection. ESPI and video holography provide real time fringe patterns which have been used to provide insight into the dynamic behaviour of gas temperature fields. The commercial ESPI generates double the number of fringes because the object beam passes through a phase field twice, and this therefore doubles the measuring sensitivity. Holography provides good quality high resolution fringe patterns.For quantitative values of the temperature field a phase stepping technique is currently being investigated for higher resolution results. The temperature distributions obtained may ultimately be used to calculate the heat transfer coefficient on the surface of impingement and are being used to support the development of numerical models for jet impingement heat transfer.

9. ACKNOWLEDGEMENTS

The work was carried out in the Department of Mechanical Engineering at Nottingham Polytechnic. The facilities and financial support provided by Department is gratefully acknowledged.

REFERENCES

Button B L and Jambunathan K. 1989. Jet-impingement heat transfer: a bibliography 1976-85. Previews of Heat and Mass Transfer, 15 (2), 149-178.

He S P, Wu X P. 1985. The application of holographic thermometry in engineering thermophysics. International Conference on Experimental Mechanics, Beijing.

Jones and Wykes. 1989. Holographic and speckle interferometry, 2nd Edition, Cambridge, University Press.

Kapur D N and Macleod N. 1974. The determination of local mass transfer coefficients by holographic interferometry - I. International Journal Heat Mass Transfer, 17, 1151-1162.

Lu B, Yang X, Abendroth H, Eggers H and Ziolkowski E. 1988. Measurement of a three dimensional temperature field applying ESPI and CT techniques. Optics Communications 69, 1, 6-10.

Reuss D L. 1985. Interferometric probing of a cylindrical tube using holography. Applied Optics, 24, 14, 2197-2205.

Reuss D L and Schutz P H. 1987. Interferometric temperature measurement of a flame in cylindrical tube using holography. Applied Optics, 26, 9.

Saluja C L, Button B L and Dobbins B N. 1988. Full-field in situ measurement of local mass transfer coefficient using ESPI with the swollen polymer technique, Int. J. of Heat and Mass Transfer, 31, 7, 1375-1384.

Tyrer J R. 1988. The use of TV holography (ESPI) for loudspeaker chassis and cabinet modal analysis. J. Audio Eng. Soc., 36, 5, 342-9

Vest C M. 1979. Holographic interferometry. New York. John Wiley and Sons.

C485/031

Application of Phase Stepping Speckle Interferometry and Swollen Polymer Technique to Mass Transfer Measurement

by L S Wang, BSc, S Kapasi, BSc, K Jambunathan, PhD BSc CEng FIMechE and B N Dobbins, BSc MPhil AMIMechE, *The Nottingham Trent University, UK*

SYNOPSIS Phase shifting Digital Speckle Pattern Interferometer (DSPI) with the swollen polymer technique has been applied to the measurements of mass transfer under a semi-confined and unconfined laminar axisymmetric impinging jet. The optical arrangement of a dual beam DSPI is presented and the experimental procedure described. A semi-automatic method of analysis is presented and phase maps are extracted from the resultant fringe patterns obtained by a four-step phase-stepping technique. The mass transfer coefficients evaluated from the experiment are compared to available data.

NOTATION

A_i	Intensities of phase shifted fringe patterns (i=0,1,2,3)
d	Diameter of nozzle
H	Separation from the jet exit to impinging plate
h_m	Local mass transfer coefficient
$\langle I_o \rangle$	Average intensity of fringe pattern
i_1	Incidence angle of object beam along the centre line, measured from the normal direction
i_2	Viewing angle, measured from the normal
i_{xy}	Incidence angle of object beam, corresponding to coordinate (x,y)
M_a	Molecular mass of ester
N	Fringe order number
P^o	Vapour pressure of ester
R	Distance of object beam from the point source to test surface, along the beam centre
R_o	Universal gas constant
Re	Jet Reynolds number based on nozzle diameter d
r	Radial distance on polymer coating surface, measured from the jet stagnation point
T	Thermodynamic temperature
t	Time duration of mass transfer
x,y	Cartesian coordinates on polymer coating surface, $r=(x^2+y^2)^{1/2}$
α_1	Refraction angle of object beam
α_2	Refraction angle corresponding to i_2
γ	Fringe modulation (visibility)
δ	Normal direction recession of the polymer
ϕ	Phase of fringe pattern, $\phi=2N\pi$
θ_i	Phase shifts (i=0,1,2,3)
λ	Wavelength of laser
η_f	Refractive index of air
η_p	Refractive index of polymer
ρ	Density of ester/polymer

1 INTRODUCTION

Numerous full-field heat and mass transfer techniques are available for obtaining heat and mass transfer coefficients in varying flow situations. The swollen polymer technique has been used for about twenty years for mass transfer investigations. It has been applied in conjunction with optical profilometric techniques: holography, electronic speckle pattern interferometry (ESPI) and moiré methods.

Optical techniques have been recognised to be one of the most powerful tools since they are non-intrusive, highly sensitive and capable of providing full-field measurement data. Holographic interferometry (1) has been used extensively but with the increasing advancement of computer and electronic technology, ESPI (2, 3) and digital speckle pattern interferometry (DSPI) have become more common due to their ease of use and high speed of data processing.

The major limitation with ESPI/DSPI profilometers compared with holography is that the fringe quality obtained is worse. Conventional intensity-based fringe analysis techniques are in general difficult to apply. The application of phase stepping technique to ESPI/DSPI (4) facilitates the analysis and significantly increases the spatial resolution (5, 6). Phase stepping DSPI has been used extensively for displacement and strain measurements (7-10).

In this paper, an investigation of axisymmetric laminar air jet impingements using DSPI and the swollen polymer technique is reported. A conventional four-step phase stepping algorithm is employed to perform the reduction of the data obtained in DSPI. Experimental results for a semi-confined and unconfined impingement jet are presented and compared with an analytical solution of a wall jet.

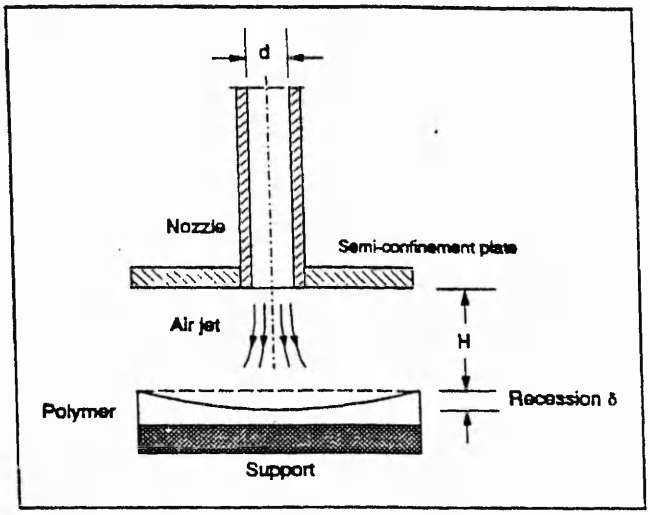

Figure 1 The arrangement of the semi-confined jet impingement configuration.

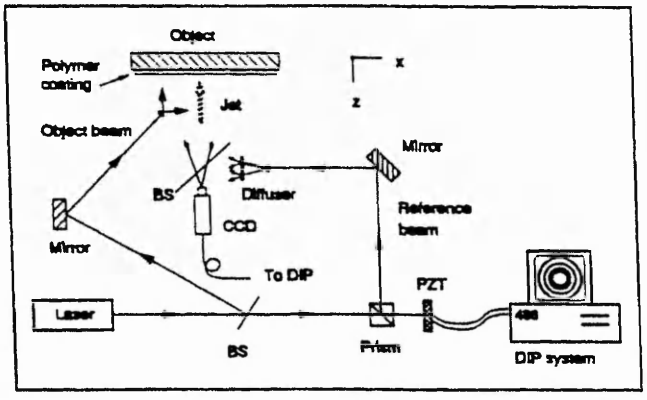

Figure 2 Schematic setup of the dual beam DSPI used in conjunction with swollen polymer technique to investigate the mass transfer

2 EXPERIMENTATION

The arrangement of the experimental apparatus is shown in Figure 1. The jet impingement rig consisted of a nozzle, a confinement plate and an impingement plate. The nozzle exit was flush with the confinement plate which was parallel to the impingement plate with a separation distance of H. The plate spacing was initially two nozzle diameters and the diameter d=10.26 mm. The air jet exiting from the nozzle had a fully developed velocity profile and was isothermal. A rotameter was used to obtain the rate of the flow from a compressed air supply. The nozzle was positioned normal to the impingement plate.

The impingement plate was manufactured from aluminium. A recess of 0.5 mm deep was machined in the plate in which the polymer was cast. Details of the preparation of the polymer and test plate can be found in (11).

The polymer coated test plate was immersed in a bath of swelling agent (ethyl salicylate) for a minimum of 24 hours prior to the commencement of the test. To perform the test, the plate was removed from the bath, dried by using a lint free paper and installed as shown in Figure 2. The swollen polymer test plate was then exposed to the air jet which convected the swelling agent from the polymer surface. This generated a recession on the surface which was measured using the DSPI technique as discussed in the following section.

3 OPTICAL SETUP AND OPERATING PROCEDURE

The digital speckle pattern interferometric arrangement is illustrated schematically in Figure 2. The object surface was illuminated by an expanded laser beam (object beam). The diffuse reflection from the object was collected by the CCD camera. The reference beam was directed to the camera with the help of a diffuser and beamsplitter BS. The interferometric speckle pattern formed on the sensor of the CCD camera was transferred by the CCD element array and stored as an intensity distribution in a PC-based digital image processing (DIP) system. The phase of the reference beam was changed by translating a mirror mounted on a piezoelectric transducer (PZT). The PZT movement was controlled by a D/A converter in the PC.

The experimental procedure used is summarised as follows:

1) An initial speckle pattern SP0 of the original test surface was acquired and stored in the DIP system;
2) Three other speckle patterns SP1, SP2 and SP3 were obtained with the phase of the reference beam shifted by $\pi/2$, π and $3\pi/2$ respectively by driving the piezoelectric transducer;
3) The polymer surface was exposed to the air jet for a preset time interval t;
4) A final speckle pattern SPL was grabbed and stored with the polymer surface recessed by the mass transfer;
5) A phase map was generated using speckle patterns SP0, SP1, SP2, SP3 and SPL. The phase was unwrapped using a conventional procedure (10) and surface deformation was determined from the phase value and the illumination geometry;
6) The deformation of the surface was used to determine the mass transfer coefficients.

Optimal time duration, t, of the experiment was determined prior to the actual test using real-time monitoring of DSPI fringe pattern. t was chosen in the case that the zero fringe was always in the imaging area and that sufficient number of fringes were present for later analysis.

Intensities of the four phase stepped fringe patterns can be represented mathematically as

$$A_i = <I_0>[1 - \gamma \cos(\phi + \theta_i)] \qquad (1)$$

where $\langle I_0 \rangle$ is the average intensity of the fringe pattern, ϕ is the phase of the fringe pattern and is related to the polymer recession, γ is the fringe modulation (visibility) and $\theta_i = i\pi/2$ (i=0,1,2,3) are the phase shifts for the four fringe patterns imposed by the movement of the PZT.

Before calculating the phase ϕ, low pass filtering was performed with four iterations of averaging the image within a 7x7 pixel window to reduce the speckle noise in the correlated fringe patterns. The principal value of phase ϕ at all valid points (x,y) was calculated from

$$\phi \text{ modulo } 2\pi = \arctan \frac{A_3 - A_1}{A_0 - A_2}. \qquad (2)$$

The phase value calculated using Eq.(2) was the principal value of the arctangent function, which ranges from $-\pi$ to π.

To remove the discontinuities of the phase distribution calculated using Eq.(2) a correction algorithm was performed based on a conventional row-to-row and column-to-column phase unwrapping procedure (10).

Phase stepping technique can only provide relative phase distributions. For a measurement where the absolute fringe order number (or absolute phase) is required, an additional method must be incorporated. In our work, preliminary real-time fringe monitoring method was used to determine the test duration time so that the zero fringe was present within the fringe pattern and hence the resultant phase map. Thus the overall absolute phase distribution can be obtained.

3 PHYSICAL EQUATIONS

The correlation fringes obtained from the DSPI technique are generated by the change in optical path difference (OPD) between the reference and object beams. For the swollen polymer technique, the change in OPD is generated by the recession of the polymer through which the object beam passes. The recession is determined from the phase distribution or the fringe number N, together with the optical geometry and the physical properties of the polymer, using the following equation:

$$\delta = \frac{N\lambda}{\dfrac{\eta_p - \eta_f \cos(i_1 - \alpha_1)}{\cos\alpha_1} + \dfrac{\eta_p - \eta_f \cos(i_2 - \alpha_2)}{\cos\alpha_2}} \qquad (3)$$

where i_1 is defined as the illumination angle of the object beam along the centre line (see Figure 3) and i_2 is the viewing angle (i_2=0 in our case as the camera was positioned normal to the test surface). For an arbitrary point (x,y) on the surface, the corresponding incident angle, i_1 varies according to the coordinates due to the divergence of the object beam. Such an angle is given by the following equation (assuming that the central line of the beam cone lies in the horizontal plane Oxz),

$$i_{xy} = 90° - \tan^{-1} \frac{R\cos i_1}{\sqrt{(x + R\sin i_1)^2 + y^2}} \qquad (4)$$

where R is the distance along the beam centre from the source (point B in Figure 3) to the surface.

The relationship between the incident and refraction angles is defined by Snell's law as follows

$$\frac{\sin i_{1,2}}{\sin \alpha_{1,2}} = \frac{\eta_p}{\eta_f} \qquad (5)$$

Finally from the polymer recession δ, local mass transfer coefficient h_m can be found from,

$$h_m = \frac{\rho \delta T R_0}{t P^0 M_w}. \qquad (6)$$

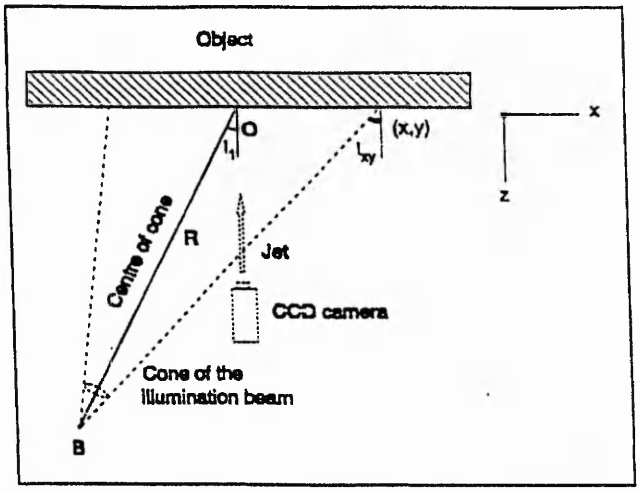

Figure 3 Calculation of the illumination angle i_{xy} at point (x,y). Assume the central line of the spherical illumination cone of the beam is in the horizontal plane Oxz

4 EXPERIMENT AND RESULTS

The swollen polymer mass transfer technique with phase stepping DSPI has been used to investigate mass transfer under an axisymmetric laminar semi-confined and unconfined jet impingement. Figure 4 shows a typical correlation fringe pattern obtained using the DSPI by subtracting a speckle pattern acquired before the mass transfer from that obtained after. Four phase-shifted correlation fringe patterns have been subsequently used to extract a phase map of the surface as shown in Figure 5. The phase map was unwrapped into continuous phase data which were translated into mass transfer coefficients on the

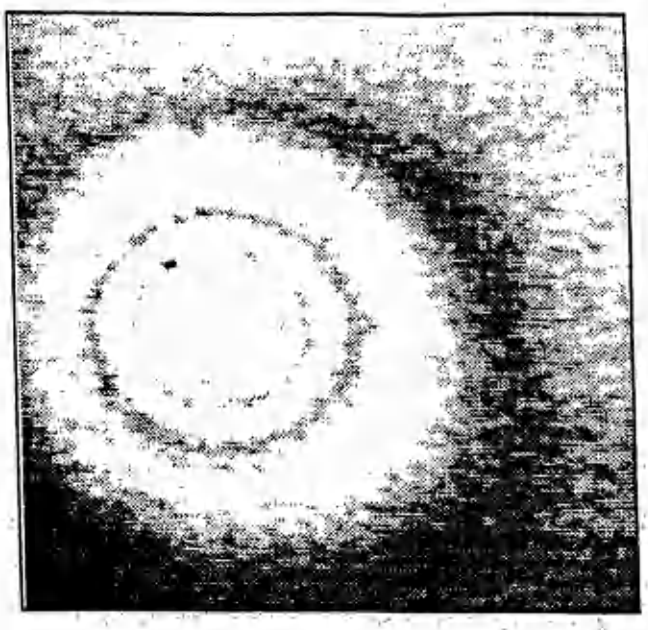

Figure 4 A typical speckle correlation fringe pattern obtained from the swollen polymer and DSPI technique (unconfined jet with Re=1000, d=10.26 mm and H/d=2).

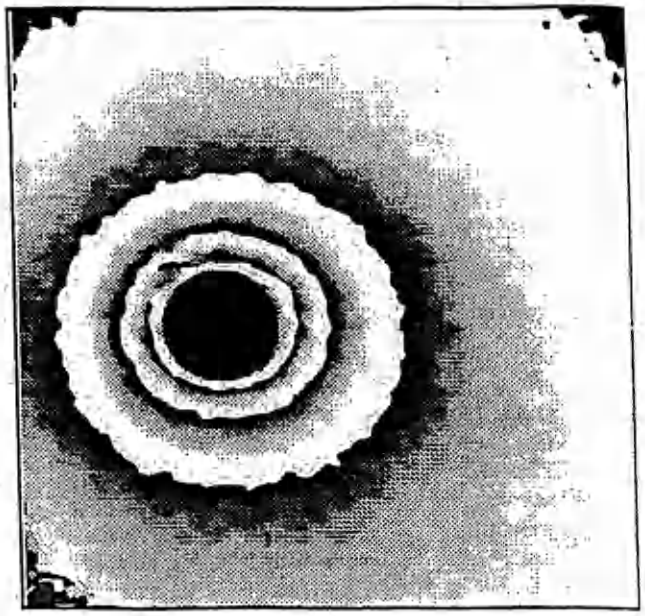

Figure 5 A typical phase map derived from four phase-shifted correlation fringe patterns when Re=1000, d=10.26 mm and H/d=2 (from an unconfined jet).

impingement surface.

Around the jet stagnation point, the fringe modulation was low and the derived phase values were found to be random. To prevent the conventional phase unwrapping procedure being performed incorrectly, this region in Figure 5 has been masked out. The low modulation was caused by two factors:

- the combination of speckle noise and high density of fringes in this area (the fringe spacing was less than 10 pixels);
- the low pass filtering procedure during the extraction of phase map.

The results reported here are for a jet Reynolds number of 1000 with spacing from the nozzle outlet to plate of 2d. Both unconfined and semi-confined cases were studied.

Figure 6 represents a calculated mass transfer distribution at a jet Reynolds number of 1000. Both unconfined and semi-confined results are shown. The experimental data have been plotted with the wall jet solution of Scholtz and Trass (**12**). The difference between the data of semi-confined jet and that of Scholtz and Trass was found to be less than 5 per cent in the region where r/d>6.0 and increased to 26 per cent at the limit of Scholtz and Trass's correlation (2.5d for the stagnation point). For unconfined impingement jet, the experimental data are about 32 per cent below that of Scholtz and Trass for the region 2.5<r/d<6.0.

5 DISCUSSION AND CONCLUSIONS

The DSPI phase stepping technique and swollen polymer method have been investigated to obtain full-field local mass transfer coefficients. The application of phase stepping has allowed the analysis of the experimental data to be performed using a semi-automatic procedure with high spatial resolution. However, phase stepping technique can only offer relative phase distribution. To determine the absolute fringe order number in the image, a real-time fringe monitoring method was used to trace the fringe development.

In the current investigation of jet impingement using the swollen polymer and DSPI technique, low modulation of the fringes around the stagnation point was observed and phase values derived from the shifted and low-pass filtered fringes were found to be random. Therefore no data was available within the region of about 1.5d from the stagnation point.

Main contributions to the experimental error have been identified as follows:

- Physical properties of the ester, P^0, η_p and ρ.
- Random speckle noise and phase measurement errors due to uncertainties in the phase shifting piezoelectric transducer.

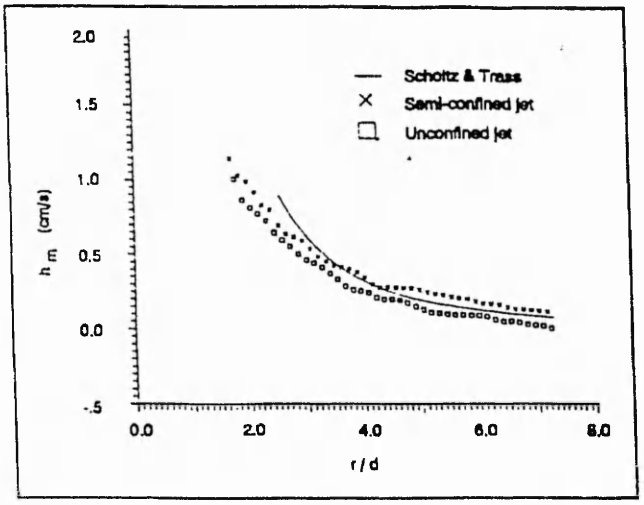

Figure 6 Radial distribution of mass transfer coefficients due to a semi-confined and unconfined laminar impingement jet (Re=1000, d=10.26 mm, H/d=2.0)

ACKNOWLEDGEMENTS

The financial support from HEFCE for this work is gratefully acknowledged. The authors would also like to thank Professor Shiping He of the University of Science and Technology of China for his technical advice.

REFERENCES

(1) VEST, C M, *Holographic Interferometry*, 1977, John Wiley & Sons, New york.

(2) ROBINSON, D W and WILLIAMS, D C, Digital phase stepping speckle interferometry, *Optics Communication*, 1986, **57**, 26-30.

(3) SALUJA, C L, BUTTON, B L and DOBBINS, B N, Fill-field in situ measurement of local mass transfer coefficient using ESPI with the swollen polymer technique, *Int. J. Heat Mass Transfer*, 1988, **31**, 1375-1384.

(4) CREATH, K, Phase-shifting speckle interferometry, *Applied Optics*, 1985, **24**, 3053-3058.

(5) DOBBINS, B N, HE, S P, JAMBUNATHAN, K, KAPASI, S, WANG, L S and BUTTON, B L, Measurement of temperature field in confined jet impingement using phase stepping video holography, *Proc. SPIE 1554A*, 1991, 772-780.

(6) WANG, L S, DOBBINS, B N, JAMBUNATHAN, K and WU, X P, Fibre optic shape measuring system using phase stepping speckle pattern interferometry, *Int. Conf. on Laser Dimensional Metrology: Recent Advances for Industrial Application, Brighton (Proc. SPIE* **2088**), 1993.

(7) DOBBINS, B N, HE, S P, KAPASI S, WANG, L S, BUTTON, B L, WU X P, Application of phase-stepping speckle interferometry to shape and deformation measurement of a 3D surface, *Proc. SPIE* **1554A**, 1991, 772-780.

(8) ROBINSON, D W and WILLIAMS, D C, Automatic fringe analysis in double exposure and live fringe holographic interferometry, *SPIE* **559**, 1985, 135-140.

(9) VROOMAN, H A and MAAS, A A M, Image processing algorithm for the analysis of phase shifted speckle interferometry patterns, *Appl. Opt.*, 1991, 30, 1636-1641.

(10) NAKADATE, S and SAITO, H, Fringe scanning speckle pattern interferometry, *Applied Optics*, 1985, **24**, 2172-2180.

(11) MACLEOD, N and TODD, R B, The experimental determination of wall-fluid mass transfer coefficients using plasticized polymer surface coating, *Int. J. of Heat Mass Transfer*, 1973, **16**, 485-504.

(12) SCHOLTZ, M T and TRASS, O, Mass transfer in laminar radial wall jet, *A. I. Chem. Eng. Journal*, July 1963, 548-554.

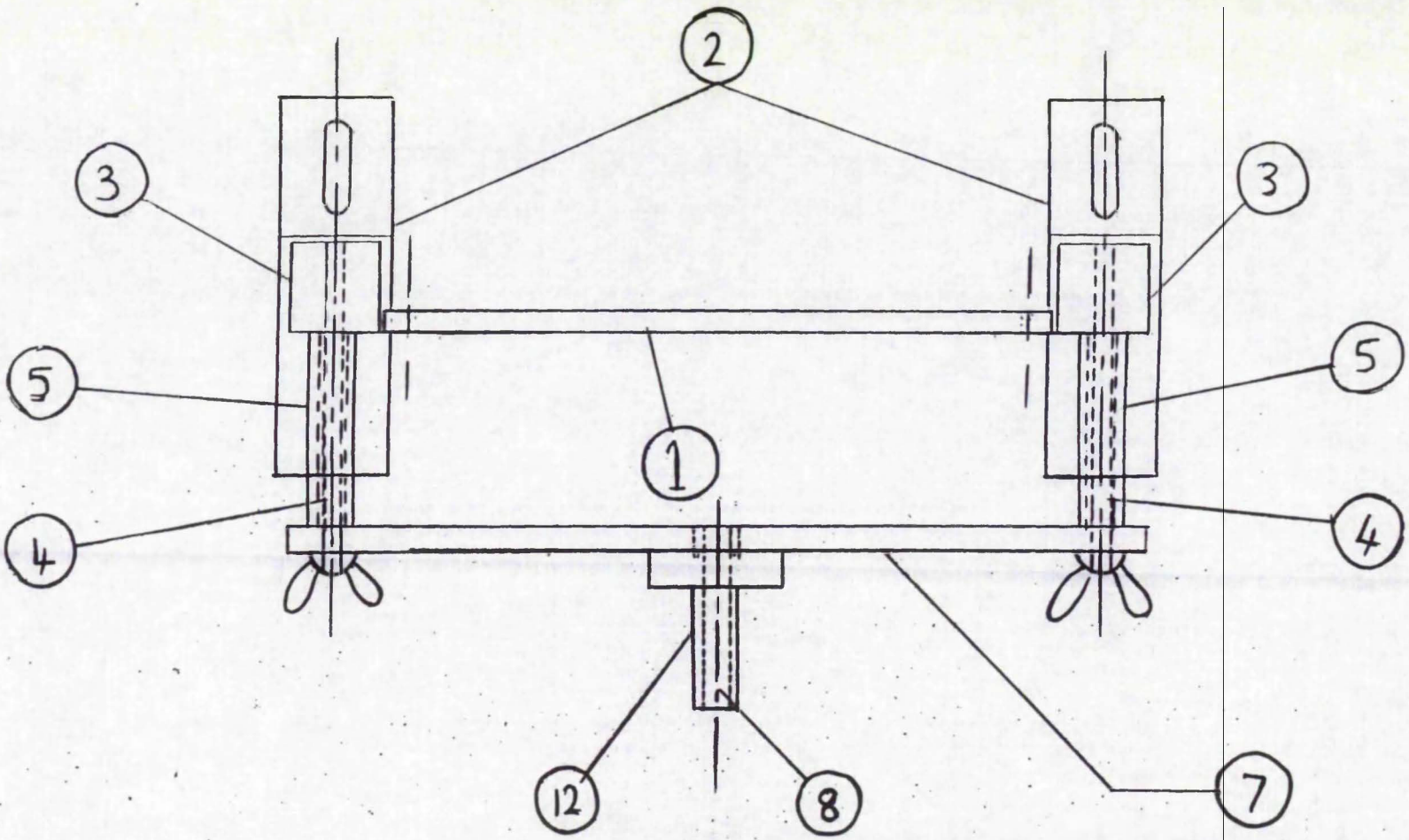

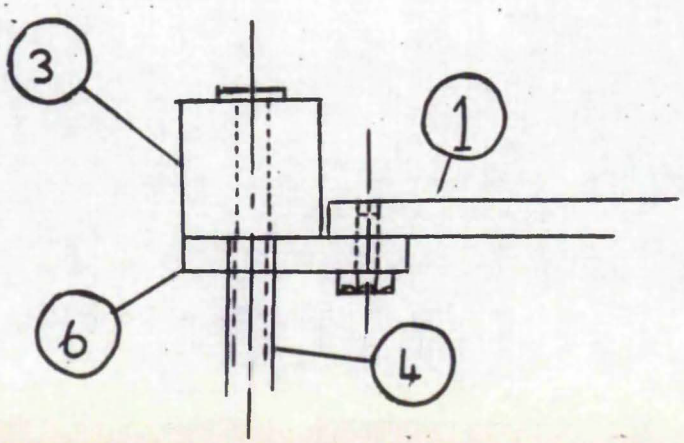

12	Nozzle locator	Alum
8	Nozzle	Stainle
7	Confinement plate	Mild
6	Removable aligner	Mild
5	Spacer	Alum
4	Spacer support	Mild
3	Strut	Mild
2	Strut support	Mild
1	Test plate	Alum
Part No	Name of Part	Mat

Fig. Experimental assembly of jet impingement

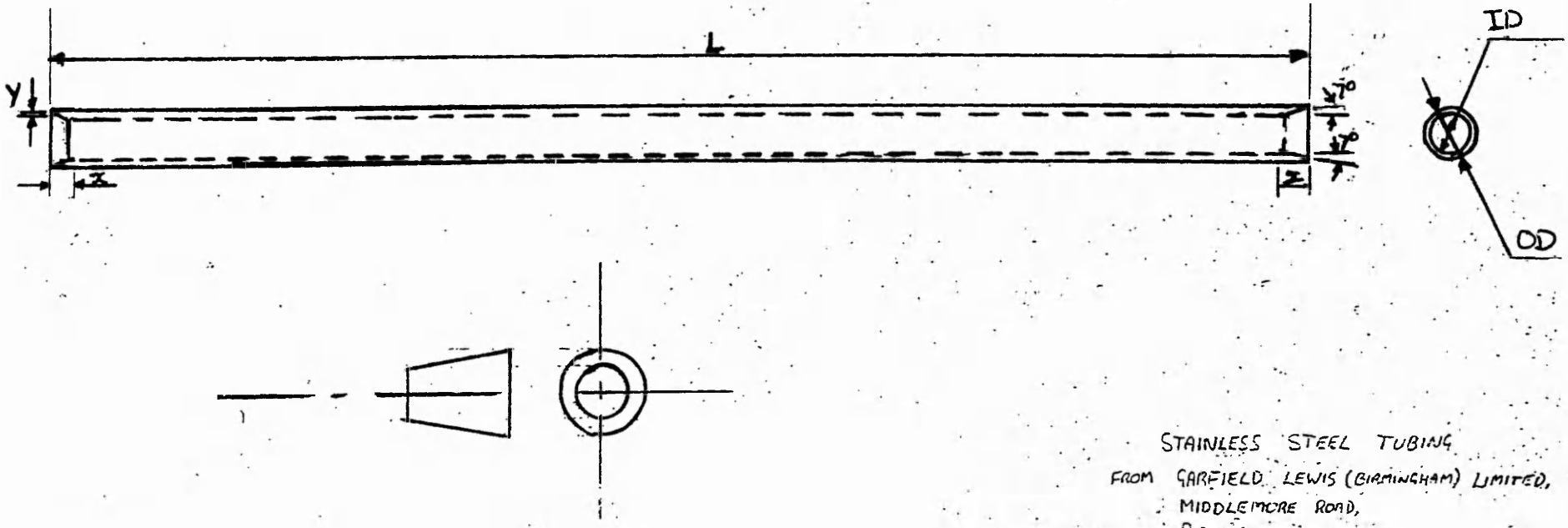

STAINLESS STEEL TUBING
FROM GARFIELD LEWIS (BIRMINGHAM) LIMITED,
MIDDLEMORE ROAD,
BIRMINGHAM,
B21 0BH.
TEL. 021 554 5242

Part No	L	ID	OD	No. off	X	Y
10	300	4.93	6.35	1	3	0.343
12	300	10.2	13.97	2	5	0.605
8	355	3.1	6.35	1	6	0.880

8-12	Nozzle	Stainless steel
Part No	Name of Part	Material

Nozzle tube dimensions

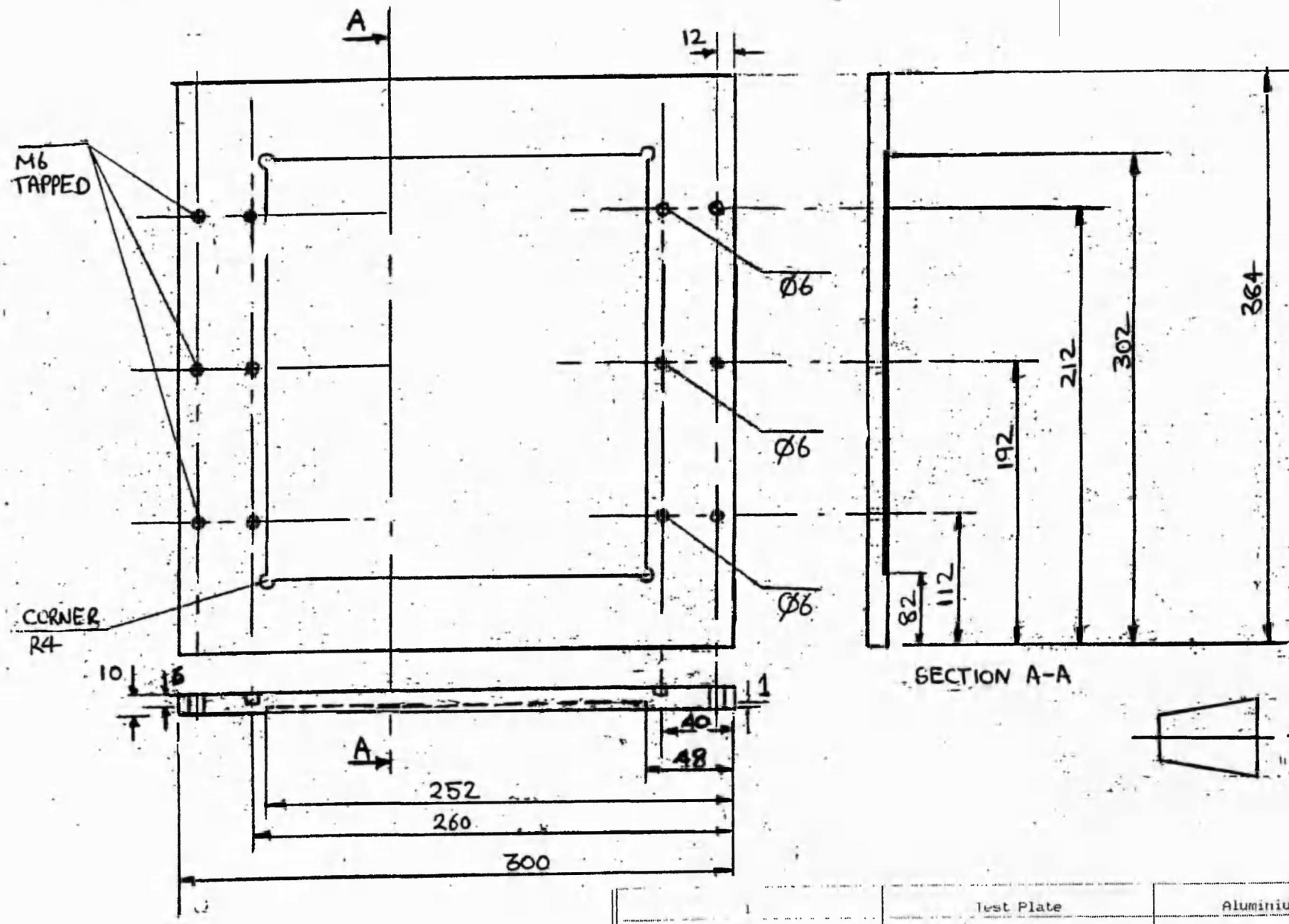

1	Test Plate	Aluminiu
Part No	Name of Part	Mate
test plate dimensions		